THE UNIVERSITY OF TULSA

THE GRADUATE SCHOOL

A STOCHASTIC SIMPLEX APPROXIMATE GRADIENT FOR PRODUCTION OPTIMIZATION OF WAG AND CONTINUOUS WATER FLOODING

by
Bailian Chen

A dissertation submitted in partial fulfillment of
the requirements for the degree of Doctor of Philosophy
in the Discipline of Petroleum Engineering

The Graduate School
The University of Tulsa

2017

THE UNIVERSITY OF TULSA

THE GRADUATE SCHOOL

A STOCHASTIC SIMPLEX APPROXIMATE GRADIENT FOR PRODUCTION OPTIMIZATION OF WAG AND CONTINUOUS WATER FLOODING

by
Bailian Chen

A DISSERTATION

APPROVED FOR THE DISCIPLINE OF

PETROLEUM ENGINEERING

By Dissertation Committee

Albert C. Reynolds, Chair

Albert C. Reynolds

William Coberly

Bill Coberly

Rami Younis

Fahim Forouzanfar

Fahim Forouzanfar

ABSTRACT

Bailian Chen (Doctor of Philosophy in Petroleum Engineering)

A Stochastic Simplex Approximate Gradient for Production Optimization of WAG and Continuous Water Flooding

Directed by Albert C. Reynolds

166 pp., Chapter 7: Conclusions

(531 words)

The objective of this research is to develop and implement an ensemble-based optimization technique named stochastic simplex approximate gradient (StoSAG) for both the water-alternating-gas (WAG) flooding and the continuous water flooding problem.

Poorly designed WAG parameters can result in sub-optimal WAG performance. In this work, we apply the StoSAG algorithm to estimate the optimal well controls which maximize life-cycle net-present-value (NPV) for the WAG flooding. The optimization methodology is applied to a synthetic, channelized-reservoir. The performances of optimized WAG flooding, optimized water flooding and optimized continuous CO_2 flooding are compared. Due to the similarity between WAG and surfactant-alternating-gas (SAG foam), we also optimize the SAG process and provide a more computationally efficient way to optimize the SAG process. The effect of gas and water injection time periods on the optimization of WAG is also investigated, and the conditions under which optimizing the injection time intervals of WAG significantly enhances the NPV of production and the conditions under which optimization of each injection period has a very small effect on the NPV are established.

Recently, intelligent or smart completions, such as Inflow Control Valves (ICVs), have been used to optimize well performance. When ICVs are installed in wells, it allows us to optimize the production/injection well controls of perforated segments along the wellbore to

maximize NPV or sweep efficiency and delay water and/or gas breakthrough. In this work, we consider smart completions for both injection and production wells. We optimize the well controls (rates or pressures) and ICV settings simultaneously and compare the NPV obtained by this process with the NPV obtained by optimizing only well controls and with the NPV generated by optimizing only ICV settings.

To account for reservoir geological uncertainty, robust optimization based on an ensemble of reservoir models is performed. When well controls and/or ICV settings are the optimization variables, EnOpt is the most popular ensemble-based algorithm for robust life-cycle production optimization. Recently, however, a superior algorithm, referred to here as StoSAG, was proposed. In this study, we provide a refined theoretical discussion on why EnOpt is generally inferior to StoSAG and provide two reasonable examples where StoSAG generates estimates of optimal well controls that give a life-cycle NPV from 15% to 60% higher than the NPV obtained from EnOpt. When there is a large variation in the ensemble of reservoir models used for robust life-cycle production optimization, the theory indicates StoSAG can be expected to radically outperform EnOpt.

We develop a framework based on the lexicographic method and the StoSAG algorithm to maximize the expected NPV and minimize the associated risk or uncertainty in robust life-cycle production optimization. With the lexicographic method, we first maximize the expectation of the life-cycle NPV value, then we minimize the risk using the resulting optimal value of expected NPV as a constraint. This constrained optimization problem is solved with the augmented Lagrangian method. The measures of risk considered include the standard deviation, the worst-case scenario (minimum NPV over the set of realizations) and conditional-value-at-risk (CVaR). Results obtained with different risk measures are benchmarked using two reservoir examples, namely, a channelized reservoir model and the well-known Brugge reservoir model in order to determine the effect of the choice of the risk measure.

ACKNOWLEDGEMENTS

I would like to express my deepest appreciation to my advisor, Dr. Albert C. Reynolds, for his insightful inputs for my research. He is smartknowledgeable, humorous and easygoing. He is very responsive to all of his students, and because of this, he is the busiest man in our department. I often see him work on weekends until very late. I guess my poorly written papers and reports have made him mad a lot of times, but he is always very patient to revise them word by word, sentence by sentence. I have experienced and learned a lot from him: his real love of research, his responsibility, his patience and a lot other good qualities will greatly influence my future career and my whole life. It is my greatest honor to have him as my advisor.

I would like to thank my committee members, Dr. Bill Coberly, Dr. Rami Younis and Dr. Fahim Forouzanfar, for serving as my committee members and for their helpful comments and suggestions. I would like to show my gratitude to my internship mentors, Jincong He, Raul-Mark Fonseca and Olwijn Leeuwenburgh. They helped a lot during my internships. I also would like to show my thanks and appreciations to Mrs Judy Teal and all my other colleagues and friends in Tulsa.

Finally, I would like show my greatest appreciation to family for their unconditional support and love. Words cannot express how grateful I am to my parents, Fuquan Chen and Jiafeng Zhang, and especially to my wife, Jiajia Wang. She gave birth to my lovely daughter, Alicia C. Chen, and sacrifices a lot to take care of our daughter. This work is dedicated to my parents, my wife and my daughter.

TABLE OF CONTENTS

LIST OF TABLES

LIST OF FIGURES

CHAPTER 1

INTRODUCTION

1.1 Background

Closed-loop reservoir management [49, 50] is a general framework that combines the process of model-based production optimization and data assimilation (assisted history matching). All the tasks involved in this loop are performed sequentially during the expected life of a reservoir with the aim of maximizing the reservoir performance, in terms of recovery or net-present-value (NPV). Fig. 1.1 presents the framework of the closed-loop reservoir management. "Reservoir Model(s)" which represent the current information about the reservoir is(are) first built through the geo-modeling process. Then, a set of optimal control settings (e.g., well flow rates, bottom hole pressure (BHP) and settings of inflow control valves (ICVs)) will be determined by a process called "Production Optimization". The optimized well control settings will then be applied to the real field. At the next stage, production data (e.g., well production rates and BHP) will be measured and the choice of yet-to-be-measured data is generally determined by a process called "Surveillance Optimization" [57, 56, 43, 44]. After the application of optimized surveillance strategies, new measurements are obtained from the reservoir. The collected data (measurements) are then incorporated into the reservoir model(s) by "Data Assimilation" [32, 33, 95, 31], whereby the uncertain model parameters are calibrated so that the reservoir simulation matches the observed data. The new model(s) is applied to predict the future performance of the reservoir and the loop as shown in Fig. 1.1 repeats. The focus of this study is only on the production optimization stage in the close-loop reservoir management.

Previous studies on production optimization mainly focus on optimizing reservoir performance under water flooding [10, 80, 4, 54, 47, 92, 21, 22, 70]; there are few studies on

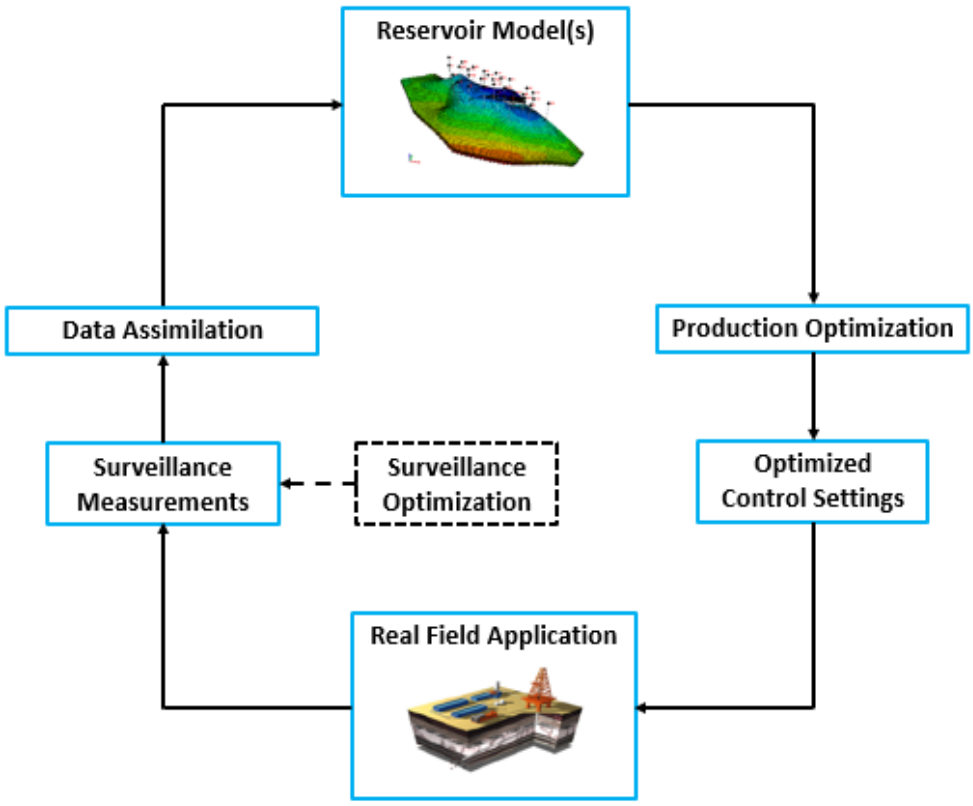

Figure 1.1: Schematic representation of closed-loop reservoir management.

optimization of enhanced oil recovery (EOR) processes, such as water-alternating-gas (WAG) and surfactant-alternating-gas (SAG) injection processes. The first focus of this study is to explore an efficient optimization algorithm which does not require a simulator's source code for the optimization of WAG injection process. The effect of gas and water injection intervals on the optimization of WAG flooding will also be investigated in this study.

When reservoir layers have significantly different petro-physical properties, WAG injection can result in early breakthrough of the injected water and/or injected gas in layers with unfavorable physical characteristics. Recently, intelligent or smart completions, such as Inflow Control Valves (ICVs), have been used to optimize well performance [67, 30, 5, 1, 2, 17]. When ICVs are installed in wells, they allow the optimization of the production/injection well controls of perforated segments along the wellbore to maximize NPV or sweep efficiency and water and/or gas breakthrough. In this study, we will consider smart completions for both injection and production wells and demonstrate the benefits of

simultaneous optimization of well controls (rates or pressures) and ICV settings.

In the reservoir production optimization community, geological uncertainties, such as uncertainty in permeability field, normally have significant impact on reservoir performance. Consequently, the optimal solution obtained based on a single reservoir model may deviate significantly from the actual optimum. To account for geological uncertainty, robust optimization is performed where the purpose is to mitigate the effect of uncertainties in the reservoir model [89, 24, 14, 16, 18, 35, 37]. Ensemble-based Optimization (EnOpt) is one of the most popular optimization algorithms for performing robust optimization [25]. Fonseca et al. [35] observed that original form of EnOpt, proposed by Chen et al. [25], does not always yield satisfactory results, and they formulated a modified ensemble-based robust optimization algorithm (motivated by a modified version of EnOpt developed by Do and Reynolds [29]). The new robust ensemble-based optimization algorithm was dubbed as StoSAG (stochastic simplex approximate gradient) by Fonseca et al. [37] and this terminology is used throughout this dissertation. Fonseca et al. [35, 37] showed that StoSAG generally yields a significantly higher value of the life-cyle NPV for the robust optimization problem than is obtained with the standard EnOpt algorithm. In this study, a theoretical understanding of why StoSAG outperforms EnOpt will be presented.

In robust life-cycle optimization, one typically maximizes the expectation of the NPV of production (or cumulative oil production) over a set of plausible reservoir realizations, where the expectation of the NPV (or cumulative oil production) is approximated by the average NPV (or cumulative oil production). However, if only the expectation is maximized, one may obtain a large variance in the set of plausible NPV values, and if the true reservoir description is close to the reservoir description that generates the worst NPV, then further exploitation of the reservoir may not be commercially feasible [64]. Therefore, it is important to consider also the minimization of risk or uncertainty, in the aforementioned life-cycle robust optimization. The last objective of this study is to investigate the possibility of using the newly developed StoSAG algorithm for the case where the two objectives are to maximize the life-cycle NPV of production under geological uncertainty and to minimize the risk.

1.2 Literature Review

1.2.1 Optimization of WAG Injection Process

WAG flooding is an enhanced oil recovery (EOR) method designed to improve sweep efficiency during gas injection by using the injected water to control the mobility of gas and to stabilize the gas front [26]. WAG injection is a cyclic method of injecting alternating cycles of gas (e.g., CO_2) followed by water and then repeating this process over a number of cycles. CO_2-WAG flooding is one of the successful EOR methods for a low permeability reservoir or a reservoir with fractures [61] because WAG results in better mobility control and higher microscopic miscible displacement efficiency compared to injecting water or CO_2 individually.

Poor recovery from the WAG technique can be caused by inappropriately-designed WAG parameters: e.g., the WAG ratio, the length and the number of WAG cycles, and the gas or water injection rate. Thus, the optimization of WAG injection is widely recognized as a viable technique for controlling mobility of gas and the miscible process in order to achieve a better recovery [23, 7]. The existing studies on WAG optimization are based in most cases on an experimental approach [6, 86, 82] or trial-and-error reservoir simulation work [52, 66, 99, 41, 9]. However, the well control parameters determined by an experimental approach or reservoir simulation experiments may not be close to an optimal solution. Thus, it is important to adaptively estimate the optimal WAG ratio, half-cycle length, well injection rates and optimal well controls for producers in an automatic way in order to achieve a better recovery or NPV.

Chen et al. [23] presented a hybrid technique that integrates the orthogonal array and Tabu techniques into a genetic algorithm a computationally expensive procedure to determine the optimum WAG production-injection parameters. However, the possible values of the control variables are preselected and discrete, and the authors did not provide any further information about how they chose those control variable values for each injector and producer and the WAG ratio. It is difficult to know whether the WAG production-injection

parameters obtained by using their hybrid technique are optimal.

Bahagio [7] used EnOpt method to optimize the injection process of CO_2-WAG where the length of each injection cycle is fixed to one year, i.e., each gas injection period lasts six months and each water injection period lasts six months. The author did not study the effect of the length of each injection cycle on the performance of CO_2-WAG EOR. Moreover, the WAG ratio for the case the author studied was fixed to a constant value which is not feasible in practice due to the reservoir heterogeneity, miscibility conditions, injection conditions and well operational parameters. In addition, the author did not estimate the optimal well controls for production wells, only for injection wells. Although the NPV obtained by the optimized strategy was higher than the one obtained by the base case strategy in the study of Bahagio, better results should be achievable if more control variables (e.g., well controls for production wells) are taken into consideration.

Hewson and Leeuwenburgh [45] applied an ensemble-based optimization algorithm to estimate optimal CO_2-WAG cycle lengths and well operating conditions (rates for injectors and BHP for producers) for a full-field model called "Chigwell Viking 'I' Pool". A single reservoir model was first used to demonstrate the benefits of simultaneous optimization of injection cycle lengths and well operating conditions over optimization of only well operating conditions with fixed injection cycle lengths. Then, the simultaneous optimization strategy was applied to an ensemble of model realizations for robust optimization. However, it is unclear whether the simultaneous optimization strategy still outperforms the strategy of only optimizing well operating conditions in the robust optimization scenario. In addition, a similar approach to the work of Fonseca et al. [35] for optimization of on/off inflow-control devices (ICDs) was applied to optimize the length and the number of WAG cycles. One of the drawbacks for this approach is the choice of "chopping"; that is, the total injection time intervals (T_{inj}) for any injection well will be chopped to reservoir lifetime if T_{inj} is larger than reservoir lifetime. This can cause some of the tailend WAG cycles to be removed from the injection process due to the stochastic properties of ensemble-based method, which could result in suboptimal solutions. In this study, we will develop a new algorithm to optimize

the WAG cycle lengths.

1.2.2 Optimization of Inflow-Control-Valves

Smart well completions, such as ICVs or ICDs, are designed to monitor downhole conditions, such as flow rate, pressure and temperature, and to control the inflow and outflow from multiple segments along the wellbore [3]. ICVs are widely used in the oilfield in order to maximize oil production and the recovery factor [67, 30, 5, 1, 2, 17]. ICVs can have settings which vary continuously between 0 and 1 (where zero indicates the valve is closed and one indicates the valve is fully open) or can be restricted to settings of either 0 or 1, i.e., either fully open or fully closed [68, 73, 35, 36], or can impose a small number of discrete settings. Many authors have used ICV settings to optimize the well performance on the basis of downhole-flow conditions or updated production data [60]; using either a true gradient or a stochastic gradient as the search direction in a steepest ascent algorithm [11, 68, 90, 3, 35, 36].

Brouwer and Jansen [11] developed a systematic dynamic optimization approach based on optimal control theory and investigated the scope for optimization under pressure- and rate-constrained operating conditions. They used "ICV settings" as the control variables in the pressure-constrained scenario where the flowing wellbore pressures were preselected, i.e., the flowing wellbore pressures were fixed throughout the optimization process. In the rate-constrained scenario, the authors chose water injection and liquid production rates in each well segment as control variables where the total field injection and production rates remained constant over time. Thus, the optimization problem simplified to a redistribution of flow rates over the well segments for the rate-constrained scenario.

Naus et al. [68] proposed an operational strategy for commingled production with ICVs using sequential linear programming (SLP), which is based on the simplex algorithm, where ICV settings were modeled as a multiplication factor of the productivity index (PI) with values between 0 and 1. van Essen et al. [90] implemented a gradient-based optimization technique to optimize the ICV settings of a field-scale reservoir. They proposed a dynamic

grouping approach based on the optimal ICV settings which were obtained at the first stage of their workflow. However, as observed by Fonseca et al. [35], having fewer ICVs results in a loss of controllability and, thus, an optimized strategy with a lower NPV. Alhuthal et al. [3] proposed an approach that relies on finite-difference or streamline-based models to estimate the production/injection rates of designated ICVs which maximize the waterflood sweep efficiency, where the optimization was performed under operational and facility constraints using a sequential quadratic programming approach. Li and Zhu [60] proposed a procedure which utilizes temperature-distribution data as feedback guidance to operate ICVs in order to achieve an approximately uniform flow distribution and to increase oil-flow rate and delay early water breakthrough.

Fonseca et al. [36] considered a waterflooding optimization problem where ICV settings of injection and production wells which maximize the NPV over the reservoir life are estimated. The well PI multipliers were used to model the ICV settings in the simulator with the values varying between 1×10^{-4} and 1. Recently, they proposed a new approach that changes a discrete control problem to a continuous control problem to estimate the on-off ICVs which maximize the NPV [35]. However, in both of these works, the authors only optimize the ICV settings with fixed well controls (rate or bottom-hole-pressure). On the other hand, if only well controls are optimized, we will generally obtain early water and/or gas breakthrough in high permeability layers. In this study, we will investigate the possibility of simultaneous optimization of ICV settings together with well controls and demonstrate the benefits by applying this methodology.

1.2.3 Optimization Under Geological Uncertainty

In the reservoir optimization community, geological uncertainties, such as uncertainty in the permeability field, normally have a significant impact on reservoir performance. Consequently, the optimal solution obtained based on a single reservoir model may deviate significantly from the actual optimum for the true reservoir. To incorporate geological uncertainty into the optimization framework, robust optimization has been performed where the purpose

is to mitigate the effect of uncertainties in the reservoir model [89, 24, 14, 16, 18, 35, 37].

van Essen et al. [89] performed robust optimization to optimize the expectation of net present value over an ensemble of reservoir realizations using steepest ascent with the gradient computed with the adjoint method. They compared the results obtained from the robust optimization procedure to those obtained from two alternative strategies (a nominal optimization and a reactive control strategy). The results showed that the robust optimization strategy yielded a much smaller variance than the alternatives. Moreover, the robust optimization strategy significantly improved the expected NPV compared to the alternatives. Capolei et al. [14] proposed a modified robust optimization strategy that inherits the features of both the reactive control and the robust optimization strategy which uses the adjoint method to generate the gradient. The results indicated that modified robust optimization strategy performed significantly better than the open-loop certainty strategy and the reactive control strategy. As can be observed, the adjoint-based method used in their work is a computationally efficient approach for the reservoir optimization problem, because it requires only one single forward simulation run and one adjoint simulation to generate a gradient of the objective function with respect to the control vector [59, 81, 51, 20, 38].

Unfortunately, implementing the adjoint method requires access to a reservoir simulator's source code which is not available for a commercial reservoir simulator. This limitation leads to the popularity of the stochastic gradient for optimization [91, 29, 19, 34, 35]. One of the these stochastic gradients, ensemble-based optimization (EnOpt), inspired by the Ensemble Kalman Filter (EnKF) method, was first introduced by Lorentzen et al. [65] and Nwaozo [69]. The standard formulation of the EnOpt algorithm for robust optimization was generated by Chen et al. [25]. It has been suggested that a one-to-one pairing of random control vectors and random geological reservoir models is capable of generating sufficiently accurate approximate gradients. However, other studies suggest that a straightforward one-to-one combination of control vectors and geological models is not always the best choice to be applied to robust optimization. Raniolo et al. [77] observed that standard EnOpt did not generate a good search direction for a polymer injection optimization problem. In order to

enhance the performance of standard EnOpt and avoid unacceptable computational costs, the authors selected 5 representative geological realizations from 100 geological models and coupled each geological realization with 20 perturbed controls. One imperfection of their work is that they did not benchmark their results to those obtained with standard EnOpt. Fonseca et al. [34] investigated the effect of different ratios of control perturbations to geological models by the use of hypothesis testing. They concluded that using higher ratios generate better quality gradient estimates. In one of their other studies [35], they observed that original form of EnOpt, proposed by Chen et al. [25], does not always yield satisfactory results, and they formulated a modified ensemble-based robust optimization algorithm (inspired by the modified version of EnOpt developed by Do and Reynolds [29]). The robust optimization procedure of Fonseca et al. [35, 37] is referred to throughout as stochastic simplex approximate gradient (StoSAG). Fonseca et al. [35, 37] showed that StoSAG generally yields a significantly higher value of the life-cyle NPV for the robust optimization problem than is obtained with the standard EnOpt algorithm. In this study, we will provide a theoretical understanding of why StoSAG algorithm is superior to EnOpt.

1.2.4 Risk Minimization in Robust Optimization

Much of the published work on life-cycle production optimization considers only a single reservoir model when maximizing the life-cycle NPV [12, 80, 55, 21, 13, 70, 97, 98]. However, the true description of a reservoir is never known, and thus, it is now common to consider multiple geological realizations to account for the geological uncertainty in the reservoir model [50, 25, 22, 83, 37, 42]. To account for the geological uncertainty, robust life-cycle production optimization is performed [89]. In robust life-cycle optimization, one typically maximizes the expectation of the NPV of production (or cumulative oil production) over a set of plausible reservoir realizations, where the expectation of the NPV (or cumulative oil production) is approximated by the average NPV (or cumulative oil production). However, if only the expectation is maximized, one may obtain a large variance in the set of plausible NPV values, and if the true reservoir description is close to the reservoir

description that generates the worst NPV, then further exploitation of the reservoir may not be commercially feasible [64]. Therefore, it is important to consider also the minimization of risk, or, uncertainty, in the aforementioned life-cycle robust optimization. In the oil and gas optimization community, the possibility of incorporating risk minimization in robust optimization has been investigated by several researchers. Some of the most relevant work is discussed below in order to put the methodology presented in this manuscript in proper context.

Bailey et al. [8] proposed an optimization framework based on a "downhill simplex" (also called amoeba or polytope) optimizer to maximize the expectation of the NPV over an ensemble of geological realizations and minimize its variance. The objective function that is maximized in their work is defined by $F_\lambda = \mu - \lambda\sigma$ where μ and σ denote, respectively, the mean and the standard deviation of the plausible NPV values, and λ is referred to as the risk aversion factor depending on the user's own risk preference. The efficient frontier (plot of the mean of the NPV values versus its standard deviation) was generated for risk and decision analysis. In fact, the efficient frontier defined by Bailey et al. is the Pareto front for the scenario where the two objectives are to maximize the expectation of NPV and minimize its variance, even though Bailey et al. did not use Pareto front or multiobjective optimization terminology.

Isebor and Durlofsky [46] applied a hybrid algorithm that combines the local convergence properties of Mesh Adaptive Direct Search (MADS) with the conceptually global search nature of Particle Swarm Optimization (PSO) method to simultaneously maximize the expectation and reduce the risk associated with the worst-case scenario. A general field-development optimization problem was considered in their work in which the number, type, locations and controls for a maximum of six wells were the optimization variables (36 optimization variables in total). A Pareto front was generated to depict the tradeoff between the expected NPV and the worst-case NPV. Optimization for a synthetic problem required a total of 795,340 simulation runs. With extensive parallelization, the equivalent computational cost was still over 24,000 simulation runs.

Liu and Reynolds [62] developed and implemented the weighted sum and normal boundary intersection (NBI) methods to solve biobjective optimization problem where the two objectives are to maximize the expected value of the life-cycle NPV and minimize the standard deviation of the NPV over the ensemble of geological realizations. They observed that the use of standard deviation as the risk measure is not wise because the reduction in risk/uncertainty is mainly achieved by reducing the largest possible NPV. Thus, Liu and Reynolds [63] applied the constrained weighted sum and constrained NBI methods to maximize the expected value of NPV and reduce the risk by maximizing the worst NPV; in this work, they also considered the presence of nonlinear field constraints. In the work of Liu and Reynolds [64], the lexicographic method also was used to maximize expectation and maximize the NPV of the worst-case scenario (or minimize the standard deviation). For the methods utilized in these papers of Liu and Reynolds, a gradient-based algorithm with the gradients computed by the adjoint method is used for the optimization. While gradient-based methods significantly enhance computational efficiency, adjoint solutions are not generally available in commercial simulators.

Capolei et al. [16] introduced a mean-variance approach to mitigate the risk in production optimization of oil reservoirs. The idea in their mean-variance approach is to compute the optimal solution for different values of the "return-risk trade-off parameter", $\lambda \in [0, 1]$, and select the parameter λ to obtain the best trade-off between return and risk. One way they suggested to choose a solution among the efficient pairs of risk-return pairs is to select the solution that maximizes the Sharpe ratio (the ratio of the mean to the standard deviation of the NPV over the ensemble of geological realizations). However, as pointed out in another paper [15], the mean-variance approach is more suitable to reduce the uncertainty (or standard deviation) of plausible NPV values than to reduce the risk of loss. This result is consistent with the result of Liu and Reynolds [62] who showed that minimization of the standard deviation of the NPV of production may lead to a non-negligible decrease in risk. The gradient used in the optimization process of Capolei et al. [16, 15] was computed by the adjoint method. The pros and cons of several different risk measures, e.g., worst-case

scenario, standard deviation, safety margin, mean-variance and conditional value at risk (CVaR), were discussed in the work of Capolei et al. [15] and the authors proposed the worst-case scenario and the CVaR as appropriate risk measures for risk minimization, which is consistent with the results of Liu and Reynolds [62, 64].

Siraj et al. [84] studied the mean-variance risk measure and an asymmetric mean-CVaR risk measure and considered economic uncertainty by varying oil price scenarios. The formula for the mean-CVaR approach is given by $J_{\mathrm{MCVaR}} = J_M - \omega J_{\mathrm{CVaR}}$, where J_{MCVaR} is the objective of mean-CVaR approach; J_M represents the mean value of all plausible NPV; ω is the weighting parameter; J_{CVaR} denotes the CVaR objective. Note that CVaR is conceptually identical to the approach used by Bailey et al. [8]. Siraj et al. [84] found that the mean-CVaR approach performs better than the mean-variance approach. Siraj et al. [85] applied the asymmetric mean-CVaR approach to minimize the risk involved in reservoir geology. They observed that the mean-CVaR approach improves the worst case(s) without highly compromising the best cases. As there are no well-defined rules on how to choose the weighting factor ω, different values should be investigated and thereby the computational cost is very expensive. The semi-variance risk measure was also investigated in the work of Siraj et al. [85], however, it does not provide an attractive solution as it reduces the risk of worst case(s).

As we can see, many of the previous approaches for reducing the risk in production optimization are either extremely computationally expensive or require the availability of a simulator that incorporates the adjoint method [8, 46, 62, 63, 64, 16, 15, 84, 85]. One of the main objectives in this study is to develop a framework that can be used to minimize the risk in robust life-cycle optimization without access to a simulator with adjoint solution capability and with acceptable computational cost.

1.3 Research Objectives and Dissertation Outline

1.3.1 Research Objectives

The objectives of this research are as follows:

1. Explore the applicability of EnOpt algorithm to adaptively determine the optimal well controls (for both injectors and producers) for each WAG cycle.

2. Incorporate the smart completion technique into the WAG injection optimization; propose a new approach which optimizes the well operating conditions (rates or pressures) and ICV settings simultaneously to maximize the life-cycle NPV.

3. Provide a theoretical understanding of why StoSAG algorithm outperforms EnOpt for robust optimization and demonstrate it with reasonable examples.

4. Apply the lexicographic method to investigate its applicability in combination with the StoSAG algorithm to maximize the expected value of NPV and reduce the risk in the robust life-cycle production optimization.

5. Develop a new optimization technique to estimate the length of WAG cycles and the optimal well controls for each cycle which maximize life-cycle NPV.

1.3.2 Dissertation Outline

This dissertation contains seven chapters that proceed as follows:

In Chapter 2, we first present the WAG optimization problem, which is followed by the description of the optimization methodology. Then, we present the results of CO_2-WAG optimization on a synthetic channelized reservoir example and make a comparison between WAG, continuous CO_2 and waterflooding techniques. Thereafter, we provide a more efficient method to optimize the Surfactant-Alternating-Gas (SAG foam) process.

In Chapter 3, we present the methodology of simultaneous optimization of well operating conditions and ICV settings. Then, we demonstrate the superiority of simultaneous

optimization over individual optimization (well controls or ICV settings only) for two synthetic reservoir examples.

In Chapter 4, we first describe the robust optimization problem followed by presentation which provides a new theoretical understanding of standard EnOpt and StoSAG. Thereafter, we show the superior performance of StoSAG compared to standard EnOpt with two reservoir models.

In Chapter 5, we first discuss a variety of risk measures, introduce the lexicographic method, and end with algorithms for the reduction of risk when the primary objective is to maximize the expectation of NPV under geological uncertainty. Then, we apply the proposed methodology to two reservoir examples.

In Chapter 6, we further explore the possibility of optimizing the lengths of WAG cycles together with the well controls. We adopt the augmented Lagrangian method which can handle both equality and inequality constraints to optimize the injection time intervals with and without well controls. The benefits of including WAG cycle lengths as optimization variables are demonstrated for both the deterministic and robust scenarios.

We summarize the main conclusions of this study in Chapter 7.

CHAPTER 2

ENSEMBLE-BASED PRODUCTION OPTIMIZATION OF THE WAG INJECTION PROCESS

In this Chapter, we apply an ensemble-based optimization (EnOpt) technique, which has been previously used in waterflooding optimization [65, 25, 87, 34, 36], to adaptively determine the optimal well controls (for both injectors and producers) for each WAG cycle during the presumed reservoir lifetime, without preselecting any control variables. In this Chapter, optimization is based on a single reservoir model but robust optimization is considered later in this work. By considering a single reservoir model, we can establish the applicability of our basic optimization algorithm as well as compare optimum WAG results with optimum results obtained by injecting only water or only gas. The EnOpt formula applied is the one suggested by Do and Reynolds [29] which invokes fewer assumptions in the underlying mathematical development than does the standard Chen et al. [25] formulation, but the difference between the performance of the two methods is negligible when optimization is based on a single reservoir model. Due to the similarity between WAG and surfactant-alternating-gas (SAG foam), we also can apply this optimization technique to the SAG process. However, the computational time required to estimate the optimal well controls for SAG injection is computationally expensive if we start the optimization directly from an initial guess that is far from optimal. The computational time required to run a SAG simulation is much longer than the time required to run a WAG simulation. The longer computational time is due to the incorporation of the chemical reactions necessary to model the generation of foam as well as foam collapse. In this Chapter, we illustrate that it is possible to radically reduce the computational costs of SAG optimization by setting the initial guess for the optimal well controls for SAG equal to the optimal well controls generated for

the WAG process.

2.1 WAG Injection Optimization Problem

The optimization problem we consider is how to estimate the well controls which maximize the NPV in a WAG EOR process. NPV is defined by

$$J(u) = \sum_{n=1}^{N_t} \left\{ \frac{\Delta t_n}{(1+b)^{\frac{t_n}{365}}} \left[\sum_{j=1}^{N_P} \left(r_o \cdot \overline{q_{o,j}^n} - c_w \cdot \overline{q_{w,j}^n} \right) - \sum_{k=1}^{N_I} \left(c_{wi} \cdot \overline{q_{wi,k}^n} + c_{gi} \cdot \overline{q_{gi,k}^n} \right) \right] \right\}, \quad (2.1)$$

where u is a N_u-dimensional column vector which contains all the well controls at all wells over the production lifetime; n denotes the nth time step of the reservoir simulator; N_t is the total number of time steps; the time at the end of the nth time step is denoted by t_n; Δt_n is the nth time step size; b is the annual discount rate; N_P and N_I denote the number of producers and injectors, respectively; r_o is the oil revenue, in \$/STB; c_w, c_{wi} and c_{gi}, respectively, denote the disposal cost of produced water, the cost of water injection and the cost of gas injection, in units of \$/STB; $\overline{q_{o,j}^n}$ and $\overline{q_{w,j}^n}$, respectively, denote the average oil production rate and the average water production rate at the jth producer for the nth time step, in units of STB/day; $\overline{q_{wi,k}^n}$ and $\overline{q_{gi,k}^n}$, respectively, denote the average water injection rate and the average gas injection rate at the kth injector for the nth time step, in units of STB/day. For the examples considered in this work, we neglect the revenue from hydrocarbon gas production and the disposal cost of injected gas (CO_2) that is produced.

We consider only bound constraints and let u_i^{low} and u_i^{up} denote the lower bound and upper bound for the ith control variable, respectively. Then, the problem of WAG optimization can be expressed as

$$\begin{cases} \underset{u \in R^{N_u}}{\text{maximize}} \ J(u), \\ s.t. \ u_i^{\text{low}} \leqslant u \leqslant u_i^{\text{up}}, i = 1, 2, 3, ..., N_u. \end{cases} \quad (2.2)$$

We apply a logarithm transformation [40] to each element of the control vector. The

ith component of the transformed control vector is given by

$$x_i = \ln\left(\frac{u_i - u_i^{\text{low}}}{u_i^{\text{up}} - u_i}\right), \tag{2.3}$$

where u_i denotes the ith component of u. Note that x_i varies from $-\infty$ to $+\infty$, and thus, after applying log-transformation to the control variables, the original constrained optimization problem is transformed to an unconstrained problem. Even though the log-transform converts the probem to an unconstrained problem, following Oliveira and Reynolds [70], in the log-domain, the variables are still truncated to the interval [-7, 7] in the optimization process. Then, the optimization is performed in terms of the transformed vector x, i.e., the optimization problem becomes $\underset{x}{\text{maximize}}\ J(x)$. After the optimal x is obtained, we apply the inverse log-transformation in order to transform x back to u in the original space, i.e.,

$$u_i = \frac{\exp(x_i) \cdot u_i^{\text{up}} + u_i^{\text{low}}}{1 + \exp(x_i)} = \frac{u_i^{\text{up}} + \exp(-x_i) \cdot u_i^{\text{low}}}{1 + \exp(-x_i)}. \tag{2.4}$$

2.2 Optimization Methods Considered

In this chapter, we apply a slight modification on the standard ensemble-based optimization (EnOpt) method [65, 25] to optimize the CO_2-WAG process. Note that this modified EnOpt is similar to foundational StoSAG for robust optimization which will be introduced in Chapter 4. In this section, we discuss the standard EnOpt method, the modified EnOpt method, and the hierarchical multiscale optimization (Hi-MO) method [70] which will be used to optimize the continuous CO_2 injection and continuous water flooding processes for the purpose of comparing the optimal NPVs obtained for these processes with the optimal NPV for CO_2-WAG injection.

2.2.1 EnOpt Algorithm

Assume that $J(x)$ is the NPV function we wish to maximize, where x is the vector related to the control vector u by Eqs. 2.3 and 2.4. Here, $J(x)$ is maximized using the

steepest descent form of the optimization algorithm given by

$$x_{k+1} = x_k + \alpha_k \left[\frac{d_k}{\|d_k\|_\infty} \right], \tag{2.5}$$

for $k = 0, 1, \ldots$ until convergence, where x_0 is the initial guess and x_k is the estimate of the optimal control vector at the kth iteration; α_k is the step size. The search direction vector d_k can be expressed as

$$d_k = \left[(d_k^1)^T, (d_k^2)^T, \ldots, (d_k^m)^T, \ldots, (d_k^{n_{\text{well}}})^T \right]^T, \tag{2.6}$$

where n_{well} is the total number of wells. The vector d_k^m represents "the search direction for well m," i.e., d_k^m is the subvector of d_k that produces changes in the components of x_k that correspond to the controls of well m when Eq. 2.5 is applied. All vectors and subvectors without a transpose sign refer to column vectors. To enumerate the components of a subvector d_k^m, we use the notation

$$d_k^m = \left[(d_k^m)_1, (d_k^m)_2, \ldots, (d_k^m)_{n_c} \right]^T, \tag{2.7}$$

for $m = 1, 2, \cdots, n_{\text{well}}$, where n_c is the number of control steps for each well. Here, each well has the same number of controls, i.e., n_c is the same for all the wells. To obtain the search direction d_k at iteration $k+1$, we first generate N_e samples of the Gaussian random vector X, where $X \sim N(x_k, C_X)$, i.e., the mean of X is equal to x_k and its covariance matrix is C_X. These samples can be generated from

$$x_k^j = x_k + LZ^j, \quad j = 1, 2, \ldots, N_e, \tag{2.8}$$

where L is the lower triangular matrix in the Cholesky decomposition of C_X and the component of Z^j are independent, standard, random-normal deviates, i.e., $Z^j \sim N(0, I_{N_x})$. LZ^j is a N_x-dimensional Gaussian random vector with mean equal to the N_x-dimensional zero

vector and covariance matrix, C_X, i.e., $LZ^j \sim N(0, C_X)$. As discussed later, C_X is chosen to control the temporal smoothness of the controls at each well.

The search direction used in this work is the one considered in Do and Reynolds [29] which at iteration $k+1$ is given by

$$d_k = \frac{1}{N_e} \sum_{j=1}^{N_e} (x_k^j - x_k)\big(J(x_k^j) - J(x_k)\big). \tag{2.9}$$

Do and Reynolds [29] show that

$$d_k \approx C_X \nabla_x J(x_k). \tag{2.10}$$

This search direction differs slightly from the one proposed by Chen et al. [25]. Chen et al. use the the mean of the samples in place of x_k and $J = (\sum_{j=1}^{N_e} J(x_k^j))/N_e$ in place of $J(x_k)$. When optimization is based on a single fixed reservoir model, Do and Reynolds [29] show that the difference between results generated from the two basic EnOpt algorithms is negligible even though the Do-Reynolds EnOpt formulation of Eq. 2.9 involves fewer approximations than does the Chen et al. formula. Thus, here when optimization is based on a single reservoir model, we will still simply refer to the modified EnOpt of Do and Reynolds as EnOpt. It is important to note that the Chen et al. algorithm was developed for robust optimization where one wishes to maximize the expected value of the NPV of life-cycle productions over an ensemble of reservoir models. Recently, Fonseca et al. [35] generalized Eq. 2.9 to the robust optimization case and found that with this generalization, one can obtain a significantly higher value of life-cycle NPV than is obtained with the Chen et al. version of EnOpt in the robust optimization case. More discussions on the comparison of the Fonseca et al. [35, 37] modification of EnOpt (referred to as "StoSAG") to standard EnOpt for robust optimization will be provided in Chapter 4. In this Chapter, we only focus on deterministic optimization which is based on single reservoir model.

In EnOpt [25], additional smoothing is typically performed by multiplying by C_X,

and if we do the same, the final EnOpt search direction, denoted by g_k, is given by

$$g_k = C_X d_k. \tag{2.11}$$

When using steepest ascent with the true gradient replaced by a stochastic gradient, the stochastic gradient may be quite rough. For the optimal well control problem, this rough gradient often results in controls at an individual well that vary rapidly in time and thus are not palatable in practice. Equally importantly, using a rough gradient at each iteration can result in very suboptimal estimates of the maximum achievable NPV. One way to control this is to smooth the stochastic gradient by multiplying the stochastic gradient by a covariance matrix which provides smoothing, and here EnOpt refers to the case where d_k is replaced by g_k in Eq. 2.5. See Do and Reynolds [29], Yan and Reynolds [93], Fonseca et al. [35] as well as the original work of Chen et al. [25].

When d_k of Eq. 2.9 is multiplied by C_X, the resulting algorithm is referred to here as EnOpt. If Eq. 2.5 gives a x_{k+1} such that $J(x_{k+1}) > J(x_k)$, the x_{k+1} is accepted as the new approximation to a x that maximizes NPV. If not, then the step size α_k is repeatedly reduced by a factor of 2 and x_{k+1} is recomputed with the reduced step size until Eq. 2.5 produces a x_{k+1} such that $J(x_{k+1}) > J(x_k)$ or the maximum number of step-size cuts has been reached. If with the maximum number of step-size cuts, we cannot find a x_{k+1} that increases the NPV, then we generate a new set of perturbed controls to try to find an uphill search direction and, if necessary, repeat the step-size cuts. If after N_{Res} consecutive resamplings of the perturbations to obtain a search direction, we still cannot find a x_{k+1} that increases $J(x)$ after the maximum number of allowable step-size cuts, then the algorithm is terminated. Also, if both of the following two equations hold:

$$\frac{J(x_{k+1}) - J(x_k)}{\max[J(x_k), 1.0]} \leqslant \varepsilon_J, \tag{2.12}$$

and

$$\frac{x_{k+1} - x_k}{\max[\|x_k\|_2, 1.0]} \leqslant \varepsilon_x, \tag{2.13}$$

the algorithm is terminated. Following the discussion of subsection 8.5.1 of Oliver et al. [72], we use $\varepsilon_J = 10^{-4}$ and $\varepsilon_x = 10^{-3}$. In total number of allowable simulation runs, N_R, is exceeded, we terminate the algorithm. Typically, we choose N_R between 1,000 and 5,000 depending on the computational resources available.

2.2.2 Adaptation of Modified EnOpt to WAG

To simulate WAG with a standard reservoir simulator, we represent each actual injection well by two injection wells, a gas injection well and a water injection well at the same location. The use of two wells is necessary because CMG's GEM [27], the simulator used to model WAG, does not allow us to switch a well back and forth from a water injector to a CO_2 injector. Each WAG injection cycle contains two half-cycles, a first half-cycle and a second half-cycle. Specifically, gas is injected during the first half-cycle, and water is injected during the second half-cycle. However, the water injection well is turned off (rate fixed at zero) during the first half-cycle of each cycle, and the gas injection well is turned off during the second half-cycle of each cycle. When an injection rate is fixed at zero during a half-cycle, we do not want to include the rate during this period as an optimization variable; thus, we fix both the associated rate and the corresponding search direction equal to zero. As discussed below, the use of two injection wells at the same location where each well alternates from open to closed at the end of each half-cycle requires only minor complications in our inhouse optimization code.

Here, n_{well} represents the number of wells where each physical injection well is modeled as two wells in the reservoir simulator, a water injection well and a gas injection well. Each of these two wells is represented by its own subvector in the form of Eq. 2.7, which also can be expressed in terms of the number of WAG cycles as

$$d_k^m = \left[(d_k^m)_{1,a}^T, (d_k^m)_{1,b}^T, (d_k^m)_{2,a}^T, (d_k^m)_{2,b}^T, \ldots, (d_k^m)_{n_{\text{cycle}},a}^T, (d_k^m)_{n_{\text{cycle}},b}^T\right]^T. \tag{2.14}$$

where n_{cycle} denotes the total number of WAG cycles; a and b represent the first half-cycle and the second half-cycle of each injection cycle, respectively. Note that each half-cycle may contain more than one control step. Here, for simplicity, we assume all the half-cycles contain the same number of control steps, n_{cs}, which means each entry of d_k^m given in the form of Eq. 2.14, has n_{cs} subentries, e.g., $(d_k^m)_{1,a}$ can be expressed as

$$d_k^m = \left[(d_k^m)_{1,a}^1, (d_k^m)_{1,a}^2, \ldots, (d_k^m)_{1,a}^{n_{cs}}\right]^T. \tag{2.15}$$

We see that n_c, the total number of control steps for each well, is equal to $2n_{cs}n_{\text{cycle}}$. To account for the fact that for all the first half-cycles, the water injection rates and their corresponding search directions are zero and for all the second half-cycles, the gas injection rates and their corresponding search directions are zero, we make the modifications discussed in steps 1, 2 and 3 below.

Step 1. For gas injectors, we set the even entries of d_k^m, i.e., $(d_k^m)_{1,b}$, $(d_k^m)_{2,b}$,..., $(d_k^m)_{n_{\text{cycle}},b}$ in Eq. 2.14, equal to zero in order to eliminate the entries that do not correspond to the design (optimization) variables. Similarly, for water injectors, we have to set the odd entries of d_k^m given in the form of Eq. 2.14 equal to zero,i.e., $(d_k^m)_{1,a} = (d_k^m)_{2,a} = \ldots = (d_k^m)_{n_{\text{cycle}},a} = 0$.

Step 2. Because we smooth the d_k of Eq. 2.9 by the covariance matrix C_X which is a block diagonal matrix to obtain the search direction, the search direction we use in our algorithm is first computed as

$$g_k = C_X d_k = \begin{pmatrix} C_X^1 & 0 & \ldots & 0 \\ 0 & C_X^2 & \ldots & 0 \\ \vdots & \vdots & \ddots & \vdots \\ 0 & 0 & \ldots & C_X^{n_{\text{well}}} \end{pmatrix} \begin{pmatrix} d_k^1 \\ d_k^2 \\ \vdots \\ d_k^m \\ \vdots \\ d_k^{n_{\text{well}}} \end{pmatrix} = \begin{pmatrix} C_X^1 d_k^1 \\ C_X^2 d_k^2 \\ \vdots \\ C_X^m d_k^m \\ \vdots \\ C_X^{n_{\text{well}}} d_k^{n_{\text{well}}} \end{pmatrix}, \tag{2.16}$$

where C_X^m, $m = 1,\ 2,\ \ldots,\ n_{\text{well}}$ is the covariance matrix used to force temporal smoothness on the well controls for well m. In this work, we use a spherical covariance function; i.e., denoting the (i, j) entry of C_X^m by $C_{i,j}^m$, we have

$$C_{i,j}^m = \sigma_m^2 \left(1 - \tfrac{3}{2}(\tfrac{|i-j|}{N_s^m}) + \tfrac{1}{2}(\tfrac{|i-j|}{N_s^m})^3\right), \tag{2.17}$$

if $|i - j| \leq N_s^m$, and $C_{i,j}^m = 0$ if $|i - j| > N_s^m$. Here, i and j denote the control step i and j, respectively; σ_m refers to the standard deviation; N_s^m is the number of control steps over which we wish the control at well m to be correlated. As discussed later, the choice of N_s^m at each refinement level of the Hi-MO algorithm [70] controls the degree of smoothing imposed on the well controls. Also see Wang et al. [91] and Yan and Reynolds [93] for the effect that the choice of N_s^m has on the temporal smoothness of the estimated optimal controls. Then the mth component of g_k, i.e., $g_k^m = C_X^m d_k^m$, can be expressed as

$$\begin{aligned} g_k^m = C_X^m d_k^m &= \begin{pmatrix} C_{11} & C_{12} & \ldots & C_{1n_c} \\ C_{21} & C_{22} & \ldots & C_{2n_c} \\ \vdots & \vdots & \ddots & \vdots \\ C_{n_c1} & C_{n_c2} & \ldots & C_{n_cn_c} \end{pmatrix} \begin{pmatrix} (d_k^m)_1 \\ (d_k^m)_2 \\ \vdots \\ (d_k^m)_{n_c} \end{pmatrix} \\ &= \begin{pmatrix} C_{11}(d_k^m)_1 + C_{12}(d_k^m)_2 + \ldots + C_{1n_c}(d_k^m)_{n_c} \\ C_{21}(d_k^m)_1 + C_{22}(d_k^m)_2 + \ldots + C_{2n_c}(d_k^m)_{n_c} \\ \vdots \\ C_{n_c1}(d_k^m)_1 + C_{n_c2}(d_k^m)_2 + \ldots + C_{n_cn_c}(d_k^m)_{n_c} \end{pmatrix} \\ &= \left((g_k^m)_1, (g_k^m)_1, \ldots, (g_k^m)_{n_c}\right). \end{aligned} \tag{2.18}$$

But g_k^m also can be expressed in terms of the number of WAG cycles as

$$g_k^m = \left[(g_k^m)_{1,a}^T, (g_k^m)_{1,b}^T, (g_k^m)_{2,a}^T, (g_k^m)_{2,b}^T, \ldots, (g_k^m)_{n_{\text{cycle}},a}^T, (g_k^m)_{n_{\text{cycle}},b}^T\right]^T. \tag{2.19}$$

Note that d_k^m and g_k^m in Eq. 2.18 are expressed in the form of Eq. 2.7 not in the form of

Eq. 2.14 in order to show the matrix multiplication by C_X^m more clearly.

Step 3. From Eqs. 2.16, 2.18 and 2.19, we see that a zero entry of d_k^m in the form of Eq. 2.14 does not imply that the corresponding entry of g_k^m in the form of Eq. 2.19 is zero. Thus, for gas injectors, we again set the even entries of the subvector g_k^m in the form of Eq. 2.19 equal to zero; for water injectors, we set the odd entries of g_k^m in the form of Eq. 2.19 equal to zero. This gives the final g_k^m, and hence the g_k which we use as the EnOpt search direction.

After the above modifications, the ensemble-based optimization techniques that have been developed for life-cycle waterflooding optimization can be adapted to optimize the design variables for the WAG injection process.

2.2.3 Hi-MO Method

In this Chapter, the performances of continuous CO_2 flooding and waterflooding are studied for the purpose of comparing their performance with that of CO_2-WAG technique. The algorithm applied to optimize the process of continuous CO_2 flooding and waterflooding is the adaptive hierarchical multiscale optimization (Hi-MO) algorithm [70], which can yield a higher NPV than is obtained by applying the standard procedure of EnOpt. The objectives of the Hi-MO algorithm are to reduce the number of control variables used in order to generate a set of less ill-conditioned optimization problems, and improve computational efficiency without compromising the optimal value of the life-cycle NPV obtained. The Hi-MO method can be applied with any optimization algorithm, but here, we only consider its application with the EnOpt method.

In the multiscale approach, we start with a small number of control steps and find the optimal controls by maximizing $J(x)$; then, we select the new set of control steps for the next level of parametrization based on two main procedures: merging and splitting. The control steps are selected to be merged if the following control variation criterion holds:

$$\frac{|u_i^w - u_{i,\mathrm{ref}}^w|}{u_i^{\mathrm{up},w} - u_i^{\mathrm{low},w}} < \varepsilon_u^*, \tag{2.20}$$

where ε_u^* is the control variation tolerance for merging well controls; $u_i^w$is the ith control at well w, and $u_{i,\text{ref}}^w$ is a reference value corresponding to the average of all the consecutive controls at well w previous to the ith control which were merged; $u_i^{\text{up},w}$ and $u_i^{\text{low},w}$ denote the upper bound and lower bound of ith control at well w, respectively. Although the log-transform is used to handle the bound constraints, the control variation criterion is checked in the original control space instead of the log-transformed control space.

All control steps that are not selected to be merged are split into n_{split} (2 or 4) new control steps of uniform length. Here, h denotes the parametrization level; $h_{\max}$ represents the number of refinement levels; x^h is related to u^h which is the optimal control vector at parameterization level h by Eqs. 2.3 and 2.4. The basic Hi-MO iteration loop is shown below:

For parametrization level $h = 0, 1, 2, \cdots, h_{\max}$.

Step 1. Solve the optimization problem (EnOpt method).

Use x^h as the initial guess, ϵ_J^h and ϵ_x^h as the convergence tolerances in Eqs. 2.12 and 2.13, and $n_s^{\max,h}$ as the maximum number of allowable simulation runs at step 1 of level h, obtain

$$x^h = \underset{x}{\text{argmax}}\ J(x). \tag{2.21}$$

Step 2. Check convergence.

If both of the following equations hold:

$$\frac{J(x^h) - J(x^{h-1})}{\max\{J(x^{h-1}), 1.0\}} \leq \varepsilon_J^*, \tag{2.22}$$

and

$$\frac{\|x^h - x^{h-1}\|_2}{\max\{\|x^{h-1}\|_2, 1.0\}} \leq \varepsilon_x^* \tag{2.23}$$

then set $x_{\text{opt}} = x^h$ and terminate the algorithm. If the total allowable simulation runs, $n_s^{\max}$, are reached, i.e., $n_s > n_s^{\max}$ then set $x_{\text{opt}} = x^h$ and terminate the optimization algorithm. Here ε_J^* and ε_x^* are the final convergence tolerance for the change of objective function and control variables, respectively; n_s is the counter for the number of reservoir simulation runs.

Step 3. Reparameterization: redefine the control steps for each well, $w = 1, 2, \cdots, n_{\text{well}}$.

Perform the splitting and merging procedure: for each control step $i = 1, 2, 3, \cdots, n_c^w$ of each well, determine whether the ith control should be either merged or split using Eq. 2.20, where n_c^w denotes the number of control steps for well w.

Step 4. Updating the covariance matrix.

Decrease the temporal correlation length used to define C_X between the control variables for the optimization step for the next level by multiplying the current correlation length, T^h , by a decreasing factor β, where $0 < \beta < 1$, i.e.,

$$T^{h+1} = \max\{\beta T^h, T_{\min}\}, \tag{2.24}$$

where $T_{\min}$ is the minimum correlation length which may be zero. Then generate the covariance matrix, C_X^{h+1}, for the next level.

Step 5. Updating convergence tolerances.

Tighten the tolerance for the optimization step for the next level by applying the following equations:

$$\varepsilon_J^{h+1} = \max\{\gamma\varepsilon_J^h, \varepsilon_J^*\}, \tag{2.25}$$

$$\varepsilon_x^{h+1} = \max\{\gamma\varepsilon_x^h, \varepsilon_x^*\}, \tag{2.26}$$

where γ is the tolerance-tightening factor. More total simulation runs for the next refinement level can be allowed by multiplying the total $n_s^{\max,h}$ by a user chosen factor greater than one. Then, set $h = h + 1$ and go to step 1.

End (**For**)

We wish to start with a very few controls and long control steps because there exist cases where one can obtain an optimal solution with a small number of control steps, e.g., case where bang-bang controls are optimal [96]. Thus, we choose two initial control steps of equal length. We assume n_{split}=2 is based on the computational experiments of Oliveira [71], but choosing n_{split}=4 is not expected to yield radically different results. Once n_{split} is

chosen, $h_{\max}$ is chosen so that

$$\Delta t_{\min} = \frac{T}{n_{\text{split}}^{h_{\max}}}, \tag{2.27}$$

where T is the total production lifetime and $\Delta t_{\min}$ is the minimum allowable length of a control step. For example, if T=2,048 days and $\Delta t_{\min}$=32 days, then Eq. 2.27 yields $h_{\max}$=6. It is of course possible for the algorithm to terminate prior to reaching the sixth refinement.

2.3 Computational Results

The reservoir model studied in this work is a three-layer synthetic reservoir with a $25 \times 25 \times 3$ grid with the grid block dimensions given by $\Delta x = \Delta y = 100$ ft and $\Delta z = 20$ ft. It contains 4 injectors and 9 producers. The horizontal log-permeability distribution of the first layer is shown in Fig. 2.1. Note the reservoir has three high permeability channels. The other two layers have the same horizontal permeability distribution as the first layer. The porosity is homogeneous with $\phi = 0.2$. The rock and water compressibility are equal to 6.103×10^{-5} and 3.3×10^{-6} psi^{-1}, respectively. The initial reservoir pressure is 4,300 psi, and the minimum miscibility pressure is equal to 4,150 psi. The reservoir lifetime is set equal to 2,048 days. A compositional reservoir simulator, GEM (Version 2009.10) [27] from Computer Modeling Group Ltd., is used in reservoir simulation for WAG injection. There are 7 pesudo components used to describe the oil and gas: CO_2, N_2, C_1, C_2-C_4, C_5-C_6, C_7-C_{18} and C_{19}-C_{43}.

The control variables at each gas injector are the injection rates with an upper bound of 20 MM scf/D and a lower bound of 0 MM scf/D; the control variables at each water injector are the injection rates with an upper bound of 4,000 STB/D and a lower bound of 0 STB/D; each producer operates under BHP control with an upper bound of 4,500 psi and a lower bound of 1,500 psi. The initial guess for rate controls of each water injector is set equal to 2,000 STB/D; the initial guess for rate controls of each gas injector is equal to 10 MM scf/D and the initial guess for BHP controls for each producer is equal to 3,500 psi.

To optimize the NPV, the oil price is set equal to \$80.0/STB ; the water injection cost is \$5.0/STB; the gas injection cost is \$1.5/Mscf; the cost of disposing produced water is

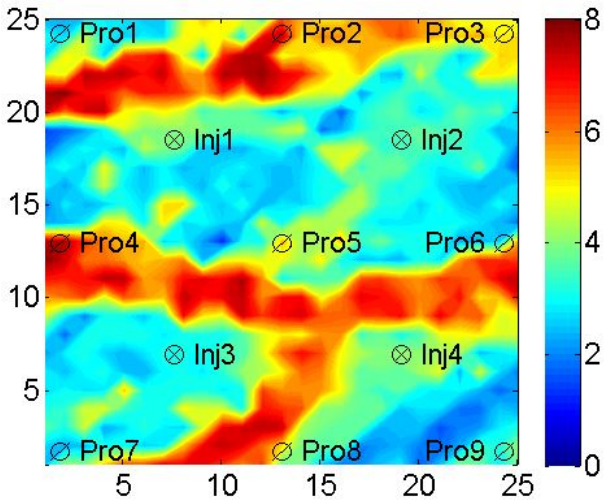

Figure 2.1: Log-permeability distribution of the first layer, three channel case.

\$5.0/STB; the annual discount rate is 0.1. Here, we neglect the revenue of hydrocarbon gas production and the cost of disposing of breakthrough injection gas. For the optimization of the SAG process, the cost of injecting water containing dissolved surfactant is set equal to \$8.0/STB.

We apply the log-transformation to handle the bound constraints for all the optimization methods considered in this paper. For the EnOpt method, we set the number of samples for gradient averaging to $N_e = 10$; the maximum number of step-size cuts is set equal to 5 and the maximum number of resamples is specified as $N_{\text{res}} = 5$; the initial step size is 1.0; the time correlation length is 512 days; the perturbation size is equal to 1.0; the maximum number of allowable simulation runs is 1,000. When the Hi-MO method used to optimize the processes of continuous CO_2 flooding and waterflooding, we specify the maximum number of refinement levels as $h = 6$; the minimum control step length is 32 days; we use 2 initial control steps and the number of splits is given by $n_{\text{split}} = 2$; the control tolerance for lumping steps is 0.01; the initial control correlation length is $T^1 = 2,048$ with a decreasing factor of 2 for each optimization level; the tolerance tightening factor is set equal to 0.5; the maximum number of allowable simulation runs of level 1 is set equal to $n_s^{\max,1} = 100$ and this number increases by a factor of 2 at each level; the total maximum allowable simulation runs is 1,000.

2.3.1 Comparison among Different WAG Cycles

In order to compare the performance of WAG with different number of cycles, we set up four cases with 4 cycles, 8 cycles, 16 cycles and 32 cycles. The number of control steps for each well, n_c, is set equal to 64 regardless of the number of cycles, and the length of each control step is 32 days. When the total number of WAG cycles is equal to 4, we set the length of each of the eight half-cycles equal to 256 days and each of the half-cycle contains 8 control steps. For 8 cycles, the length of each half-cycle is equal to 128 days and each of the half-cycle contains 4 control steps, and so on. Table 1 presents the summary of the initial NPV, final NPV (estimate of optimal NPV) and cumulative oil production for the different cases. From the results in Table 2.1, the final NPV in all of the cases is increased compared to the initial NPV. We see that the initial NPV, the estimated optimal (final) NPV and cumulative oil production increase as the number of cycles increases (cycle time decreases), but they are fairly close for the 16 cycle and 32 cycle cases.

Table 2.1: Summary, comparison among different WAG cycles.

Number of Cycles	Initial NPV $\times 10^8$\$	Final NPV $\times 10^8$\$	Cumulative Oil $\times 10^6$ bbl
4 cycles	3.073	4.480	7.606
8 cycles	3.300	4.692	7.953
16 cycles	3.410	4.756	8.009
32 cycles	3.436	4.793	8.066

Fig. 2.2 shows the remaining oil saturation as a function of the number of cycles (or cycle time). The color scale corresponds to the oil saturation with the darkest blue representing the lowest oil saturation and the darkest red color representing the highest oil saturation. For the same layer (layer 1 or layer 3 in Figure 2), as the number of cycles increases, the remaining oil saturation decreases. Note that regardless of the number of cycles, the upper layer has less remaining oil than the bottom layer because the gravity segregation of injected water and gas causes CO_2 , which has a higher displacement efficiency, to move to the upper layer while water, which has a lower displacement efficiency, moves to the bottom layer.

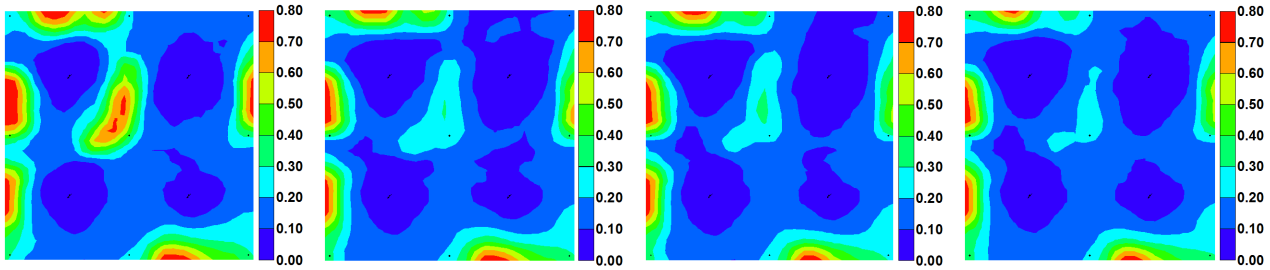

(a) 4 cycles, layer 1 (b) 8 cycles, layer 1 (c) 16 cycles, layer 1 (d) 32 cycles, layer 1

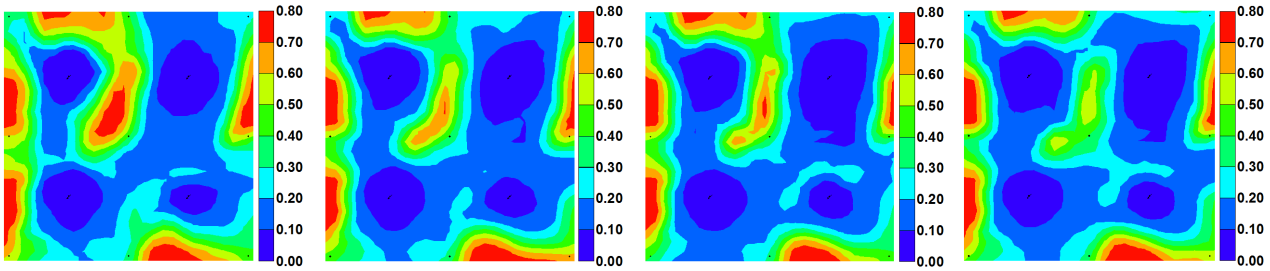

(e) 4 cycles, layer 3 (f) 8 cycles, layer 3 (g) 16 cycles, layer 3 (h) 32 cycles, layer 3

Figure 2.2: Remaining oil saturation distribution of different cycle cases.

The estimated optimal controls for all the production wells and injection wells can be obtained by applying the EnOpt algorithm. Fig. 2.3 presents the well controls of producers for the case with 32 WAG cycles. As can be seen in Fig. 2.1, producer Pro1 is separated from injectors by one of the three high-permeability channels, which we refer to here as channel 1. When the injected water or gas reaches channel 1, most of the injected fluid will move towards Pro2 through this channel. Thus, it is reasonable to expect Pro1 to operate at close to minimum allowable BHP (1,500 psi) throughout the production lifetime, but Pro2 can operate at close to minimum allowable BHP only at the early times when it is still economic but is shut in from 500 to 1,700 days, as shown in Fig. 2.3(a). Pro3, Pro4, Pro5 and Pro6 are located either in a channel or close to a channel, all of which operate at close to minimum allowable BHP at the early times and thereafter they are almost shut in, as shown in Fig. 2.3(b) and (c). Pro7 is shut in at the early times and thereafter operates at close to minimum allowable BHP. Pro8 is located close to the high-permeability channel so that the estimated control for this producer is close to the minimum allowable BHP at the early control steps, but after injected gas and water breakthrough at this producer, its pressure increases (rate decreases), which occurs at about 1,000 days. Pro9 is located far

from the channel and the injectors and is separated from Inj4 by a low permeability region, so it operates at close to minimum allowable BHP during the whole production lifetime, as shown in Fig. 2.3(d). The estimated optimal well controls for injection wells for the case with 32 WAG cycles are shown in Fig. 2.4. Note that the rates plotted correspond to the half cycle rates for the different cycles. Various factors affect the gas and water injection rates, including the miscibility between CO_2 and oil, the channeling of injected fluid and the shut-in of some production wells during the production lifetime, all of which lead to the optimal well injection rates shown in Fig. 2.4.

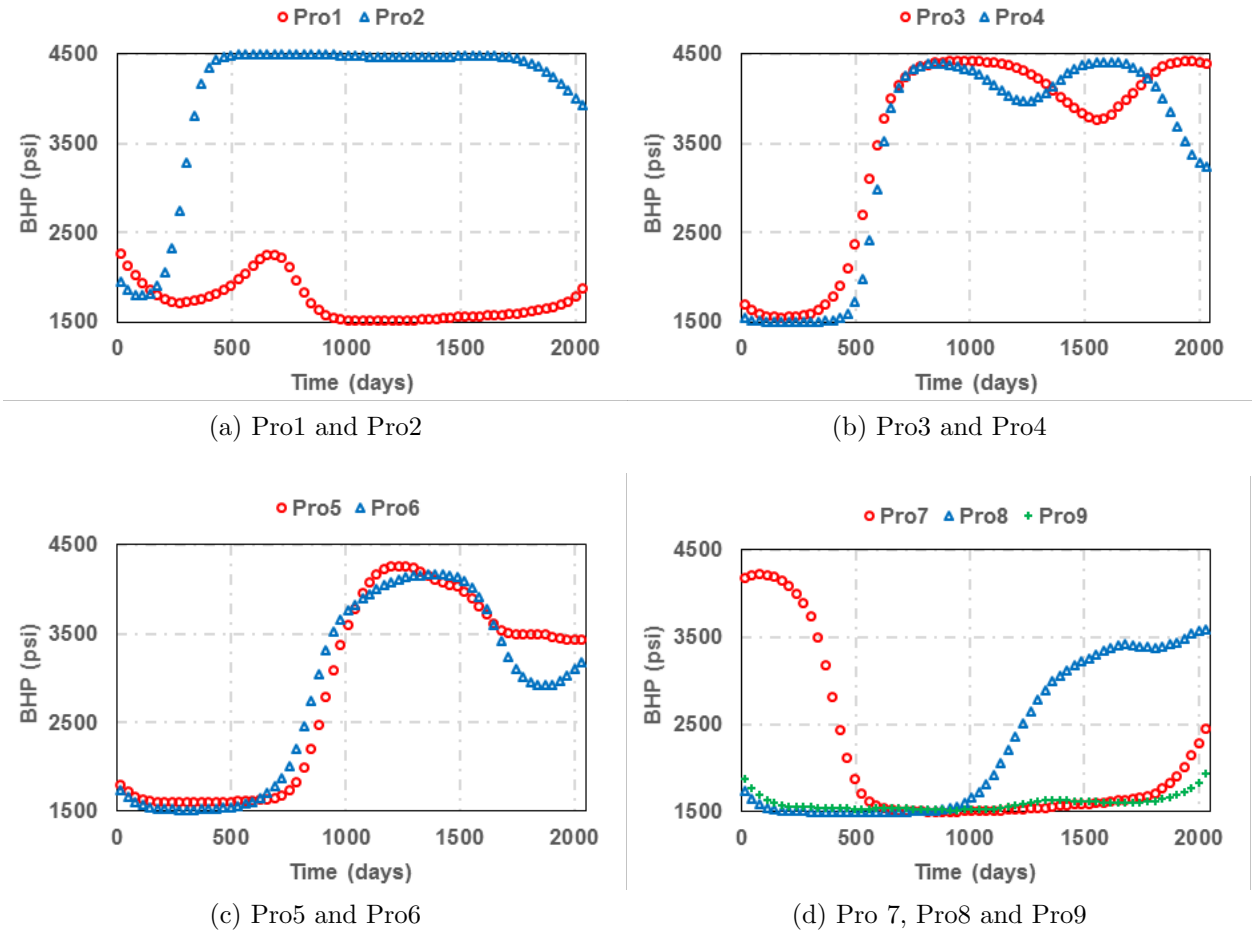

(a) Pro1 and Pro2

(b) Pro3 and Pro4

(c) Pro5 and Pro6

(d) Pro 7, Pro8 and Pro9

Figure 2.3: Estimated optimal well controls for production wells, 32 WAG cycles.

Fig. 2.5 shows the estimated optimal WAG ratio (volume of water injected divided by the volume of gas injected) for each cycle for the case with 32 cycles. The WAG ratio is affected by reservoir heterogeneity, miscibility conditions, injection conditions and well

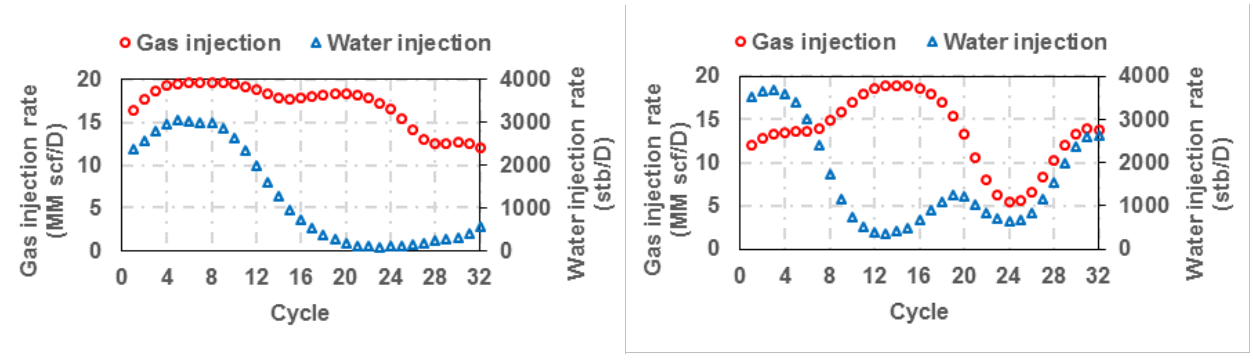

(a) Inj1

(b) Inj2

(c) Inj3

(d) Inj4

Figure 2.4: Estimated optimal well controls for injection wells, 32 WAG cycles; the rates plotted correspond to the half cycle rates for the different cycles.

operational parameters, so it is hard to explain why the estimated WAG ratio changes with the WAG cycle as shown in Fig. 2.5. However, there are some general ideas that can be obtained from the results of this figure. First of all, the WAG ratio starts with a relatively high value at the early injection times for the purpose of injecting more water into the reservoir to block the high-permeability zone and increase gas miscibility by increasing pressure. Thereafter, the WAG ratio decreases to a lower value in order to have more gas injected to obtain a better microscopic displacement of oil. Finally, the WAG ratio increases at the end of the reservoir life. From above analysis, we can see that it is inappropriate to fix the WAG ratio for WAG injection process in practice although for most cycles, the WAG ratio is less than 0.2. Note that we implicitly optimize the WAG ratio for different cycles by optimizing the well controls.

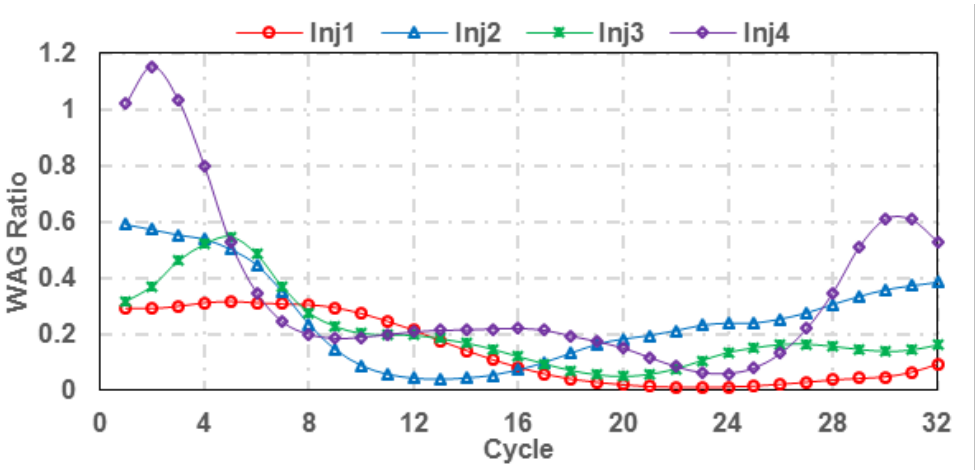

Figure 2.5: Estimated optimal WAG ratio of each cycle, 32 WAG cycles.

2.3.2 Comparison of WAG, Continuous CO_2 Injection, and Continuous Waterflooding

In order to compare the efficiency of CO_2-WAG, continuous CO_2 and continuous water flooding, we consider the following three subcases, all of which pertain to the three-layer reservoir.

(1) WAG with 32 cycles using modified EnOpt for optimization;

(2) Continuous CO_2 using Hi-MO (2 initial control steps; n_{split}=2) for optimization;

(3) Water flooding using Hi-MO (2 initial control steps; n_{split}=2) for optimization.

For continuous CO_2 and water flooding, we apply the Hi-MO algorithm [70] with 2 initial control steps and 2 splits to optimize the processes and obtain the final NPV and cumulative oil produced. Because Hi-MO adaptively selects the duration and length of the time steps and is designed to mitigate the effects of ill conditioning, Hi-MO is generally able to provide a higher NPV than is obtained by fixing the number and length of the control steps a priori. We have not developed a version of the Hi-MO algorithm applicable for the WAG process, but it is likely that such an algorithm would yield higher optimized values of NPV than the ones given in this paper for the WAG process.

Table. 2.2 presents the summary of the initial NPV, final NPV and cumulative oil produced for the three techniques. From the results in Table. 2.2, all the final NPVs are improved compared to the initial NPVs. Most importantly, the optimized WAG process yields significantly more oil production and a higher NPV than those obtained by optimizing continuous CO_2 or water flooding.

Table 2.2: Summary, comparison among three techniques.

Techniques	Initial NPV $\times 10^8$\$	Final NPV $\times 10^8$\$	Cumulative Oil $\times 10^6$ bbl
32 WAG cycles	3.436	4.793	8.066
Continuous CO_2	2.335	3.907	6.510
Water flooding	1.667	3.121	5.026

Figs. 2.6 and 2.7 display the CO_2 concentration in the bottom layer (layer 3) and the pressure distribution for the middle layer (layer 2), respectively. These two figures compare results from WAG flooding with those from continuous CO_2 flooding after 1,440 days of production and 2,048 days of production. In Fig. 2.6, the color scale corresponds to CO_2 concentration with the darkest red color representing the highest CO_2 concentration (1.00) and the darkest blue representing the lowest concentration (0.00). In Fig. 2.7, the color scale corresponds to pressure with the darkest red color representing the highest pressure (5,500 psi) and the darkest blue representing the lowest pressure (1,500 psi); the upper two figures show the pressure distribution for layer 2 for WAG flooding at 1,440 days and 2,048 days and the bottom two figures show the pressure distribution for layer 2 of continuous CO_2 flooding

at 1,440 days and 2,048 days.

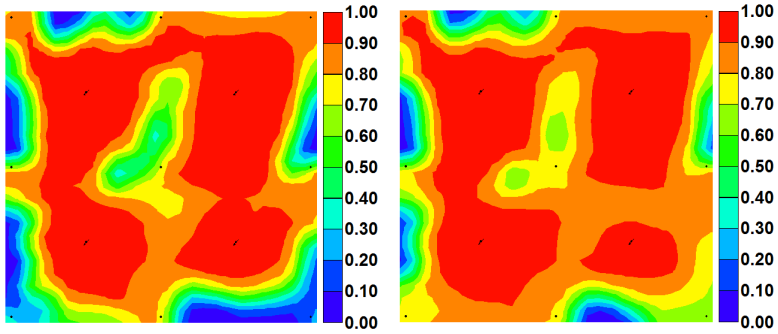

(a) 1,440 days (WAG) (b) 2,048 days (WAG)

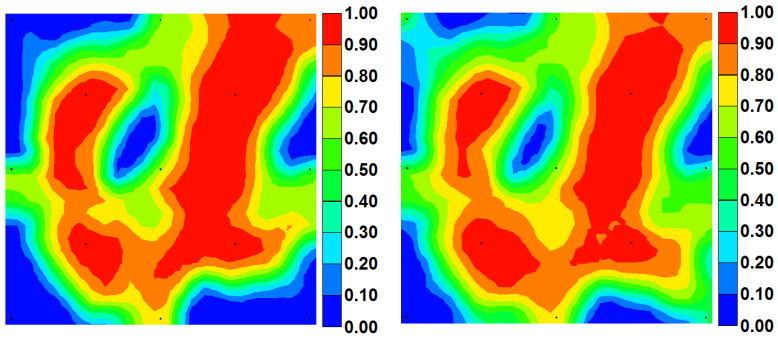

(c) 1,440 days (CO_2) (d) 2,048 days (CO_2)

Figure 2.6: CO_2 concentration in layer 3 from WAG flooding and continuous CO_2 flooding.

From Fig. 2.6, we see that WAG flooding yields a higher CO_2 concentration distribution in the bottom layer than does continuous CO_2 flooding, i.e., more oil is displaced from layer 3 using WAG than is displaced using only CO_2 flooding. This is because the water injected in the WAG process can control the mobility of CO_2 by blocking the high-permeability channel or zones and reducing the effects of gravity segregation which keeps more injected CO_2 in the bottom layer, which in turn improves the sweep efficiency and results in higher oil production. Fig. 2.7 shows that WAG flooding yields a higher pressure distribution than continuous CO_2 flooding; this is because the water injected in the WAG process helps to maintain a higher reservoir pressure because water is immiscible and has a relatively low compressibility. The higher pressure also enhances the miscibility of CO_2 and oil and hence improves the microscopic displacement efficiency.

Fig. 2.8 shows the layer 1 and layer 3 oil saturation distribution at 2,048 days obtained

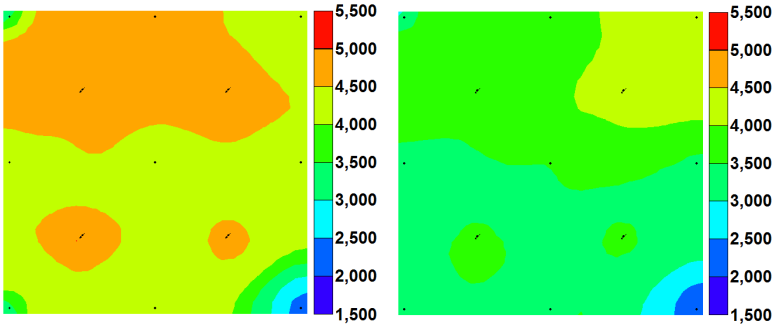

(a) 1,440 days (WAG) (b) 2,048 days (WAG)

(c) 1,440 days (CO_2) (d) 2,048 days (CO_2)

Figure 2.7: Pressure distribution for layer 2 of WAG flooding and continuous CO_2 flooding.

for the three processes. The color scale corresponds to oil saturation. From Fig. 2.8, we can conclude that compared to the other two techniques, WAG flooding yields the lowest remaining oil saturation both in the upper layer and the bottom layer. This statement also holds for the second layer although the results are not shown. For continuous CO_2 flooding, more oil is produced from the upper layer (layer 1) because of the segregation of CO_2 to the upper layer; however, for water flooding, the bottom layer achieves a lower oil saturation because of water segregation to the bottom layer. Comparing the remaining oil saturation distribution for layer 1 and layer 3 of the WAG case, we also can conclude that CO_2 does have better microscopic displacement efficiency than water.

2.3.3 Optimization of SAG Injection Process

The surfactant-alternating-gas (SAG foam) injection process is very similar to WAG. Thus, the modified ensemble-based algorithm still can be applied to optimize the SAG injection process. Generally, the SAG model is simulated using the STARS simulator [79] which

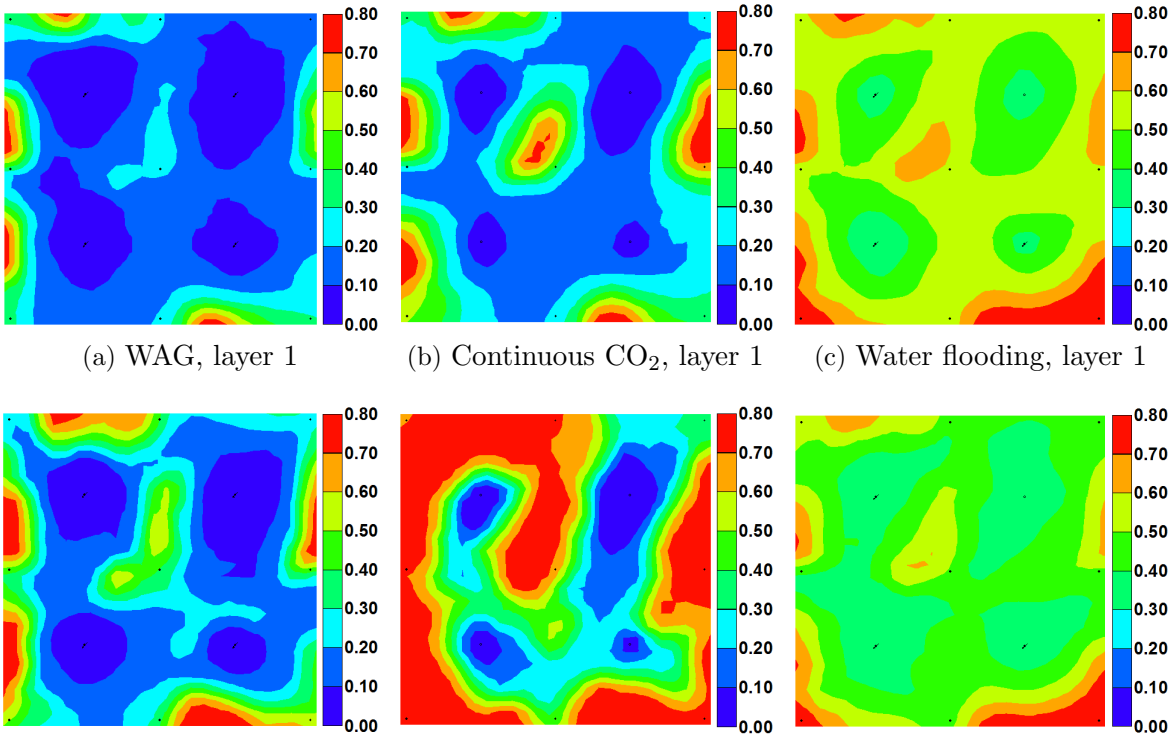

(a) WAG, layer 1 (b) Continuous CO_2, layer 1 (c) Water flooding, layer 1

(d) WAG, layer 3 (e) Continuous CO_2, layer 3 (f) Water flooding, layer 3

Figure 2.8: Remaining oil saturation distribution for three different techniques.

is also from Computer Modeling Group Ltd. STARS is CMGs advanced reservoir simulator which includes options to simulate processes which GEM does not consider. These processes include foam injection and chemical flooding. In this part of the Chapter, we first compare the performance of the two simulators (GEM and STARS) and thereafter move forward to the optimization of the SAG injection process using as initial guesses the optimized well controls obtained by the optimization of WAG injection.

Fig. 2.9 presents plots of NPV values versus the number of simulation runs of SAG and WAG injection for the cases with 16 cycles and 32 cycles. Both Figs. 2.9(a) and 2.9(b) show that WAG injection implemented by GEM yields a much higher final NPV than SAG injection implemented by STARS. However, the cases are such that we believe that SAG should achieve a better NPV or oil recovery factor than WAG because of additional EOR mechanisms generated by surfactant and foam. In order to understand this discrepancy, we perform optimization of the WAG process with STARS as well as GEM, where the initial

guess for the vector of well controls is the same for both simulators. For the case with 16 cycles, the final NPV obtained by optimizing WAG with GEM is 18.28% higher than the NPV obtained by optimizing WAG with STARS; for the 32 cycles WAG case, the final NPV obtained by optimizing WAG with GEM is 18.58% greater than the NPV obtained by optimizing WAG with STARS. Our explanation is that this is because STARS uses k-values to model compositional effects whereas GEM uses an equation of state (EOS) based phase equilibrium package for multiphase PVT calculations. However, it is well known that the liquid-gas phase envelope can change dramatically as the CO2 concentration increases. Thus, it is unfair to compare the performance of the WAG injection implemented by GEM with the performance of the SAG injection implemented by STARS. We have to choose the same simulator in order to compare the performances of the SAG and WAG for the same reservoir case. As seen in Fig. 2.9, SAG injection yields a higher final NPV than WAG injection when both WAG and SAG cases are optimized using STARS as the forward model. As we have mentioned above, GEM cannot model the process of SAG injection, so we cannot compare the performance of WAG and SAG using GEM.

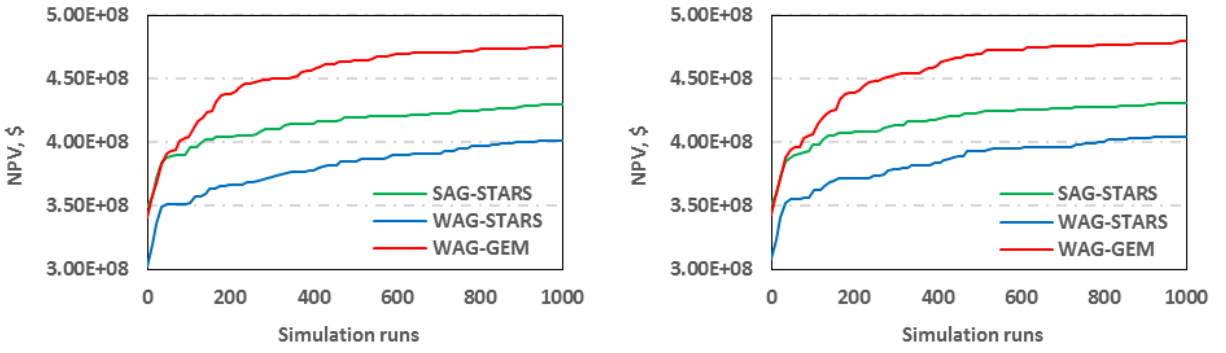

(a) 16 cycles (b) 32 cycles

Figure 2.9: NPV values versus the number of simulation runs for SAG and WAG injection.

Table 2.3 lists the computational time required for the optimization of SAG and WAG processes with different simulators for the two different cases. Note that for the same reservoir case, the computational time for the WAG optimization using GEM is less than that of WAG simulation using STARS and SAG simulation using STARS. For the case with

32 cycles, SAG optimization implemented by STARS utilizes the most computational time (241 hrs). WAG optimization with GEM requires the least computational time (80 hrs), less than one third the computational time of SAG optimization with STARS. Thus, if we optimize the SAG process by directly starting with the original initial guess of the vector of optimal well controls (initial guess for rate controls of each water injector is 2,000 STB/D, initial guess for rate controls of each gas injector is 10 MM scf/D and initial guess for BHP controls for each producer is 3,500 psi), even though we can finally obtain optimal controls and NPV by directly optimizing the SAG process, the optimization could be prohibitively computationally expensive, especially for a real field case. One possible way to reduce the computational time for the SAG optimization would be to optimize the reservoir for WAG and then use the WAG optimal controls as the initial guess for optimization of the SAG process. Hopefully, by generating a better initial guess by doing the WAG optimization first, we can reduce the overall computational time required for the SAG optimization. In a sense, this means that the WAG process can serve as a proxy for optimization of SAG.

Table 2.3: Summary, computational time for SAG and WAG for control optimization with different simulators.

Case	Injection Type	Simulator	Computational Time (hrs)
16 cycles	SAG	STARS	232
16 cycles	WAG	STARS	101
16 cycles	WAG	GEM	75
32 cycles	SAG	STARS	241
32 cycles	WAG	STARS	117
32 cycles	WAG	GEM	80

Fig. 2.10 shows the performance of SAG optimization with three different initial guesses for the case with 16 cycles. The first initial guess is the original initial guess that was used in previous cases; the second initial guess is the WAG optimal control vector obtained using GEM; the third initial guess is the WAG optimal control vector obtained with STARS. Table 2.4 presents the initial NPV, final NPV, simulation runs and the computational time for SAG optimization with the three different initial guesses. From Fig. 2.10 and Table 2.4, we

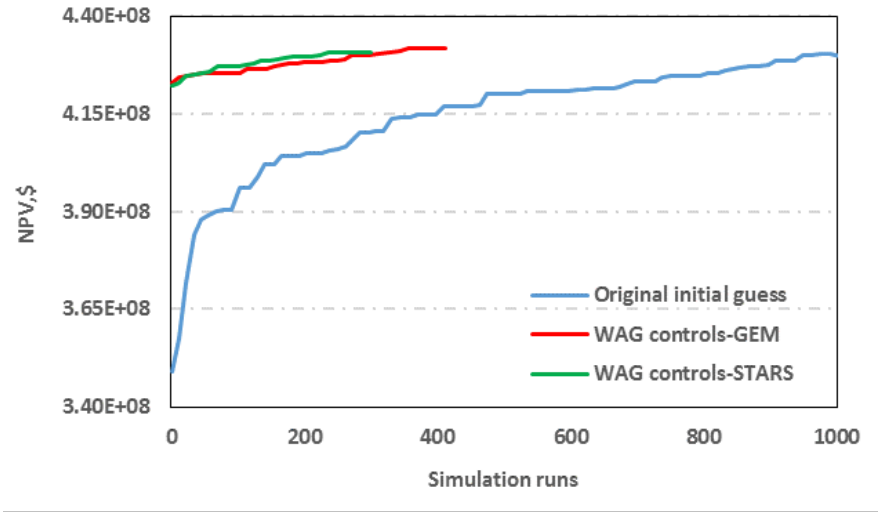

Figure 2.10: Performance of SAG optimization with different initial guesses, 16 WAG cycles.

see that much faster convergence is obtained when the initial guess for the SAG optimization corresponds to the WAG optimal well controls.

The total computational times in Table 2.4 are calculated as follows: for the original initial guess case, we run 1,000 simulations with SAG and the total computational time is 232 hrs. For the second initial guess case, we first run 1,000 simulations with GEM to obtain the optimal WAG controls as the initial guess for SAG; the computational time required is 75 hrs. Thereafter, we run 411 simulations for SAG optimization requiring a computational time of 80 hrs, so the total computational time is 155 hrs. For the third initial guess case, we first run 1,000 simulations with STARS to obtain the optimal WAG controls (this optimization requires 101 hrs) and thereafter run 299 SAG simulations which require a computational time of 48 hrs, so the total computational time is 149 hrs.

Table 2.4: SAG optimization with different initial guess, 16 WAG cycles.

Initial Guess	Initial NPV	Final NPV $\times 10^8$\$	Simulation Runs	Total Computational Time (hrs)
Original	3.491	4.296	1,000	232
WAG controls-GEM	4.230	4.316	411	155
WAG controls-STARS	4.221	4.307	299	149

From the above analysis, we can see that optimizing the WAG process to obtain

initial guesses for the optimization of the SAG process improves computational efficiency.

2.3.4 Effect of Random Seed and Ensemble Size

Due to the stochastic nature of the gradient estimate, it is important to consider the effect of the random seed and the ensemble size (the number of perturbations used to compute the stochastic gradient) on the optimization results. For all the cases studied above, we ran a few random seeds and choose the result which achieves the highest final NPV. Table 2.5 lists the final NPV calculated from five different random seeds for the 16 and 32 cycle WAG cases. Note that both the mean NPV and highest NPV achieved from the 32 cycle case are higher than those obtained from 16 cycle case.

Table 2.5: Final NPV's calculated from different random seeds, cases with 16 cycles and 32 cycles.

Case	Final NPV ($\times 10^8$ \$)						
	Seed 1	Seed 2	Seed 3	Seed 4	Seed 5	Mean	Highest
16 cycles case	4.756	4.685	4.671	4.619	4.722	4.691	4.756
32 cycles case	4.793	4.688	4.728	4.620	4.750	4.716	4.793

In order to quantify the impact of ensemble size on the optimization results, we compare the final NPVs achieved from an ensemble size equal to 30 with an ensemble size equal to 10. For both ensemble sizes, we ran with 5 different seeds. For the ensemble size equal to 30, the maximum allowable simulation runs is set equal to 1,500, while for the ensemble size equal to 10, the maximum allowable simulation runs is equal to 1,000 as before. Table 2.6 presents the final NPV's achieved from the 32 cycle case with two different ensemble sizes (10 and 30). As we can see from Table 2.6, the mean value of NPV achieved from the ensemble size equal to 30 is not significantly higher than the NPV achieved with an ensemble size equal to 10, and the highest value obtained from the ensemble size equal to 30 is even lower than that obtained with the ensemble size equal to 10 even though we allow 50% more simulation runs when the ensemble size is 30. As demonstrated by Fonseca et al. [34], the quality of gradient can be improved with a relatively large ensemble size. However,

for the compositional simulation, it is computational expensive to use a large ensemble size with more allowable maximum simulation runs. As can be seen in Table 2.6, at least for this problem, an ensemble size equal to 10 is sufficient to obtain a good gradient and to achieve a reasonable final NPV.

Table 2.6: Final NPV's calculated from 32 WAG cycle case with ensemble size equal to 10 and 30.

Ensemble Size	Final NPV ($\times 10^8$ \$)						
	Seed 1	Seed 2	Seed 3	Seed 4	Seed 5	Mean	Highest
10	4.793	4.688	4.728	4.620	4.750	4.716	4.793
30	4.760	4.713	4.749	4.759	4.732	4.743	4.760

CHAPTER 3

OPTIMAL CONTROL OF ICV'S AND WELL OPERATING CONDITIONS FOR WAG

Inflow-control valves (ICVs) are widely used to control the inflow and outflow from multiple segments along the wellbore. As introduced in Chapter 1, the existing studies on the optimization of ICV settings are done with fixed well controls (rates or BHPs). On the other hand, if only well controls are optimized, we will generally obtain early water and/or gas breakthrough in high permeability layers. In this Chapter, instead of optimizing well controls only or optimizing ICV settings only, we propose an approach in which well controls and ICV settings are simultaneously optimized in order to maximize the NPV of production from a WAG injection project.

3.1 Methodology

In this section, we first briefly discuss the underlying mathematical formulation behind the proposed approach. The well model correlates the reservoir flow rate of phase j ($j = g$ or $j = w$ for an injector and $j = o$, g or w for a producer) to the bottom-hole pressure and the pressure at gridblocks intersected by the well via the following relationship:

$$q_j^n = \sum_l \mathrm{PI}_l^n \lambda_{j,l}^n (p_o^n - p_{wf,l}^n), \tag{3.1}$$

where

$$\mathrm{PI}_l = 2\pi\alpha_l k_l h_l \frac{\mathrm{wfrac}_l}{\ln(r_e/r_w) + s}. \tag{3.2}$$

Here, q_j is the flow rate of phase j; n denotes the nth time step of the reservoir simulator; PI_l is the well productivity index at layer l; $\lambda_{j,l}$ is the total mobility of phase j in the well

gridblock at layer l; p_o is the oil pressure at the grid block; $p^n_{wf,l}$ is the bottom-hole pressure at the perforation of layer l at time t_n and is related p^n_{wf}, the bottom hole pressure at datum at time t_n by the specific weight of the wellbore fluid which accounts for gravity effects; α_l is the fraction of the well that is completed in gridblock l and is more generally representing the PI multiplier for perforation l; wfrac is the well fraction which is governed by areal geometry; k is the effective permeability in the plane perpendicular to the well direction; h is the gridblock thickness in the well direction; r_w and r_e, respectively, denote wellbore radius and effective radius, and s is the skin factor.

Regardless of whether the control for a well is a rate or a pressure, we can optimize the well control together with the PI multipliers of each segment of this well, to adjust injection and production in each layer in order to avoid early breakthrough. This means that ICV settings are effectively modeled by PI multipliers. Thus, for each well at each control step, we can use both PI multipliers and total rate or a phase rate as optimization variables. Instead of flow rate, we can also use the flowing bottom-hole pressure (BHP) of the wells as optimization variables. However, as pointed out by Leeuwenburgh [58] if all controls are BHP's, and there are lower and upper bounds on each BHP control, then intuitively one should be able to obtain the identical optimal NPV that can be found by optimizing both BHP's and ICV settings by simply optimizing only ICV settings with all producer BHP's fixed at their lower bounds and all injector BHP's fixed at their upper bounds. Whether the same optimal NPV can be obtained by the two methods, however, may depend on other factors such as the surface of the objective functions for the two problems.

Here, for simplicity, we assume that an ICV is assigned to each perforated geological layer, and equate the adjustment of the PI multiplier of the layer to the adjustment of the ICV. Then, PI multipliers are used to simulate the use of ICVs where a value of zero corresponds to a fully closed valve; a value of one corresponds to a fully open valve and a value between zero and one corresponds to a partially open valve. It is important to note however that the active relationship between ICV settings and PI multipliers is unknown.

In this work, we consider optimizing the well controls and ICV settings simultane-

ously so that the control vector contains both well controls and ICV settings. The question we wish to address is whether significant gains can be obtained by optimizing both the well ICV settings (PI multipliers) and the well controls (BHPs or rates) as opposed to, for example, simply setting well controls to a bound and using only ICV settings to maximize the life-cycle NPV value of production. In order to investigate the relative performance of simultaneous optimization of well controls and ICV settings, we set up two reference approaches for comparison. Reference approach #1: Optimize well controls only with all ICV settings set equal to 1, i.e., PI multipliers are equal to 1. Reference approach #2: Optimize ICV settings only with fixed well controls. For reference approach #2, we consider two subsets, namely: (a) set each well control equal to the average of its upper and lower bounds and (b) set well controls at injectors equal to their upper bounds and BHP well controls at producers equal to their lower bounds.

The EnOpt algorithm (modified by Do and Reynolds [29] and referred to as foundational StoSAG in robust optimization) used in the Chapter 2 is applied to optimize WAG injection process using smart well completions. We consider the same optimization problem of Eq. 2.2 as in the Chapter 2.

Assume that $J(u)$ is the NPV function we wish to maximize, where u is the control vector (e.g., BHP, well rates, and/or ICV settings over time). The ith component of control vector u, u_i, is transformed to x_i in log-domain by Eq. 2.3. Then, the optimization is performed in terms of the transformed vector x. At kth iteration of optimization, the control vector, x_k, can be expressed as

$$x_k = \left[(x_k^1)^T, (x_k^2)^T, \ldots, (x_k^m)^T, \ldots, (x_k^{n_{\text{well}}})^T\right]^T, \tag{3.3}$$

where n_{well} is the total number of wells. The vector x_k^m represents "the controls of well m at iteration k." All vectors and subvectors without a transpose sign refer to column vectors.

To enumerate the components of a subvector x_k^m, $m = 1, 2, \ldots, n_{\text{well}}$, we use the notation

$$x_k^m = \left[\left((x_k^m)^{\text{WC}} \right)^T, \left((x_k^m)^{\text{ICV}_1} \right)^T, \ldots, \left((x_k^m)^{\text{ICV}_j} \right)^T \ldots, \left((x_k^m)^{\text{ICV}_{n^m}} \right)^T \right]^T, \tag{3.4}$$

where $(x_k^m)^{\text{WC}}$ contains the well controls for well m at all control steps; n^m is the number of control valves at well m; $(x_k^m)^{\text{ICV}_j}$, $j = 1, 2, \ldots, n^m$, contains the ICV settings of the jth control valve for well m at all control steps. If we assume that each component of x_k^m has the same number of controls, then $(x_k^m)^{\text{ICV}_j}$ can be expressed as

$$(x_k^m)^{\text{ICV}_j} = \left[(x_k^m)_1^{\text{ICV}_j}, (x_k^m)_2^{\text{ICV}_j}, \ldots, (x_k^m)_{n_c}^{\text{ICV}_j} \right]^T, \tag{3.5}$$

where n_c is the number of control steps for each component of x_k^m in Eq. 3.4.

If we optimize only well controls, then x_k^m is equal to $(x_k^m)^{\text{WC}}$. If we optimize only ICV settings, $(x_k^m)^{\text{WC}}$ is deleted from the set of optimization variables in Eq. 3.4. Note the partitioning (ordering) of d_k must be identical to that of x_k given in Eqs. 3.3, 3.4 and 3.5. The algorithm implementation procedure is the same as introduced in Chapter 2.

3.2 Example 1: Channelized Reservoir

3.2.1 Problem Description

We first consider a three-channel synthetic reservoir simulation model with a $25 \times 25 \times 3$ grid with the grid block dimensions given by $\Delta x = \Delta y = 100$ ft and $\Delta z = 30$ ft. The reservoir contains 4 injectors and 9 producers. The horizontal log-permeability distribution for the first layer is shown in Fig. 3.1. Note there are three layers of this channelized reservoir. The second and third layers have the same heterogeneity features as the first layer, but the permeability field of layer 2 is equal to the permeability field of layer 1 multiplied by 0.6, and the permeability field of layer 3 is equal to the permeability field of layer 1 multiplied by 0.3. The vertical permeability is equal to one tenth of the horizontal permeability. The porosity is homogeneous with $\phi = 0.2$. The initial reservoir pressure is 4,500 psi. The reservoir lifetime

is equal to 2,880 days. A compositional reservoir simulator, GEM (Version 2009.10) from Computer Modeling Group Ltd. [27], is used for all reservoir simulation runs in both this and the second example.

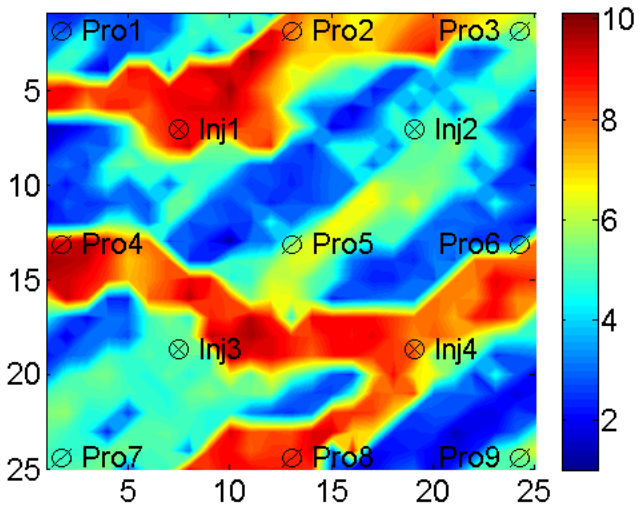

Figure 3.1: Log-permeability distribution, three-channel reservoir case.

The control variables at injectors during gas injection are the injection rates with an upper bound of 20 MM scf/D and a lower bound of 0 MM scf/D; the control variables at injectors during each water injection half-cycle are the water injection rates with an upper bound of 4,000 STB/D and a lower bound of 0 STB/D; each producing well operates under BHP control with an upper bound of 4,500 psi and a lower bound of 2,500 psi; each ICV setting for both producers and injectors has an upper bound of 1 and a lower bound of 0. In simultaneous optimization of operating well controls and ICV settings, the initial guess for the rate controls of each water injection rate is set equal to 2,000 STB/D; the initial guess for rate controls of each gas injection rate is equal to 10 MM scf/D; the initial guess for BHP controls for each producer is equal to 3,500 psi, and the initial guess for each ICV setting (PI multiplier) is equal to 0.5. It is important to note, however, that the ICV settings are set equal to 1 when we do well control optimization only, while when we optimize only the ICV settings, each well control is set equal to either its averages, i.e., the average value of the lower and upper bounds or equal to the "bound", where herein "bound" means the upper

bounds for injectors and the lower bounds for producers. Also note the ICV setting j is for layer j, where layer 1 is the top layer which has the highest permeability.

To optimize the NPV, the oil price is set equal to \$80.0/STB; the water injection cost is \$5.0/STB; the gas injection cost is \$1.5/Mscf; the cost of disposal of produced water is \$5.0/STB; the annual discount rate is 0.1. Here, we neglect the revenue due to the sale of produced hydrocarbon gas and the disposal cost of injected gas that is produced, i.e., the NPV function is again the one given by Eq. 2.1. In the implementation of EnOpt, the number of perturbations used to estimate the EnOpt search direction is 10; the perturbation size, σ, is set equal to 0.1 and the time correlation length is set equal to 720 days, both of which are used for computing the covariance matrix, C_X; see Chapter 2 for the calculation formula of C_X. The total number of WAG cycles for this case is set equal to 8 and the time length of each half-cycle is equal to 180 days. Thus, each well contains 16 control steps, with the length of each control step equal to 180 days. The total number of allowable simulation runs for the optimization process is set equal to 2,000.

3.2.2 Computational Results

Table 3.1 shows the initial NPV, the final (estimated optimal) NPV, the cumulative oil produced, the cumulative water injected/produced and the cumulative gas injected based on using different optimization approaches (optimize well controls only, optimize ICV settings only, and optimize both simultaneously) for WAG flooding. Note that all the values in Table 3.1 are averages of the values obtained from the optimization processes with three different starting random seeds. From Table 3.1, we can see that the final NPVs that we obtain using the different optimization approaches are significantly greater than the initial NPVs. The simultaneous optimization approach achieves the highest final NPV, while optimizing ICV settings only with fixed "average" well controls yields the lowest final NPV. The final NPV and cumulative oil achieved by using the simultaneous optimization approach are, respectively, 9.36% and 6.00% higher than the ones obtained by using our previous approach which optimizes well controls only. Meanwhile, the cumulative water and gas

injected, as well as the cumulative water produced, using simultaneous optimization are lower than those obtained by using well control optimization only. The approach which optimizes ICV settings only with well controls fixed at one of their bounds yields a higher cumulative oil production than the simultaneous optimization approach, but with much larger amounts of gas injected, water injected and water produced, which results in a significantly lower final NPV than is obtained via simultaneous optimization. Thus, we see that the gain in NPV obtained with the simultaneous approach is due to a combination of more oil produced and smaller injection and disposal costs.

Table 3.1: Comparison among different approaches of WAG flooding, Example 1.

Terms	Opt. well controls	Opt. ICV (averages)	Opt. ICV (bounds)	Opt. simultaneous
Initial NPV($\times 10^6$\$)	363.4	364.5	339.6	364.5
Final NPV($\times 10^6$\$)	550.4	499.1	522.5	601.9
Cum. oil prod.($\times 10^6$stb)	9.65	9.22	10.49	10.23
Cum. water inj.($\times 10^6$stb)	5.44	11.40	19.96	4.97
Cum. water prod.($\times 10^6$stb)	1.72	5.72	13.17	1.36
Cum. gas inj.($\times 10^9$scf)	66.56	54.51	86.86	61.67

Fig. 3.2 shows the NPV versus the number of reservoir simulation runs for different optimization approaches with three different initial starting random seeds. From Fig. 3.2, it is clear that the approach using simultaneous optimization achieves the highest average final NPV while the approach using optimization of only ICV settings yields the lowest NPV. For each optimization approach, different initial seeds result in different values of NPV, but the differences are not highly significant for the optimizing well controls only approach and the simultaneous approach.

Next, we choose the cases that generate the highest final NPV and show the corresponding estimated optimal well controls and/or ICV settings and the remaining oil saturation distribution. Fig. 3.3 shows the estimated well controls obtained by optimizing well controls only compared to those generated with the simultaneous optimization approach. Figs. 4.15 and 4.16, respectively, show the estimated ICV settings for producers and injec-

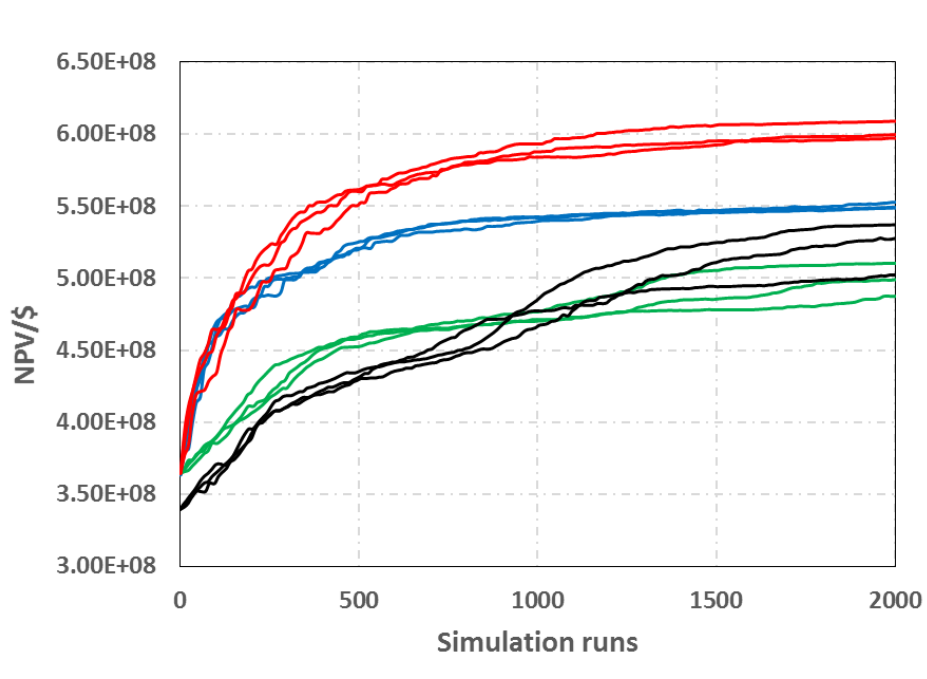

Figure 3.2: NPV versus simulation runs for different optimization approaches with three different starting random seeds; blue curves: optimization of only well controls; green curves: optimization of only ICV settings with fixed "average" well controls; black curves: optimization of only ICV settings with fixed "bound" well controls; red curves: simultaneous optimization, Example 1.

tors calculated with the simultaneous optimization approach. Note that the reservoir model is a three-layer case, so each well contains three ICVs, i.e., each well has three PI multipliers to estimate via the optimization process. For the axis titles in Fig. 3.3 and similar figures, "Control steps" is the control step indicator (16 control steps) where the control step indicator is ordered in terms of time; the "WAG cycle index" represents different WAG cycles (8 cycles); the "Producer index" represents the index of production wells, i.e., Pro1 through Pro9; and "Injector index" denotes different injection wells, namely, Inj1, Inj2, Inj3 and Inj4.

Not surprisingly, the results of Fig. 3.3 indicate that the estimated well controls obtained from these two approaches are different for most of the wells. The differences in the estimated optimal well controls generated with the two approaches are caused by including ICV in the simultaneous optimization approach. For the well control only optimization approach (Fig. 3.3(a)), Pro1 and Pro9, which are neither in nor close to the channel, operate at close to the minimum allowable BHP throughout the production lifetime. Pro2 is in the

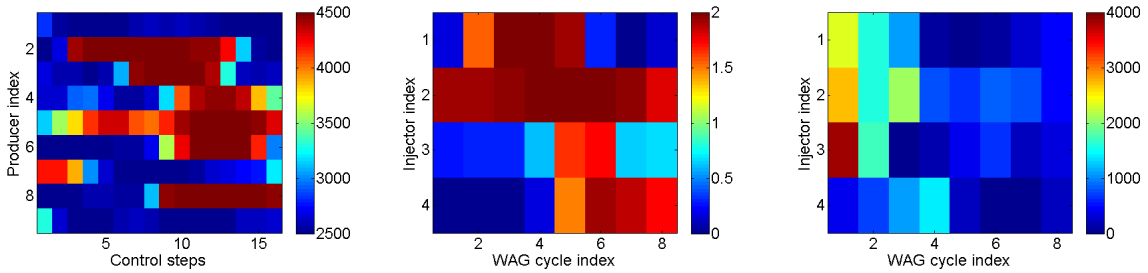

(a) Opt. well control only, producers (psi)

(b) Opt. well control only, gas injectors ($\times 10^7$scf/d)

(c) Opt. well control only, water injectors (stb/d)

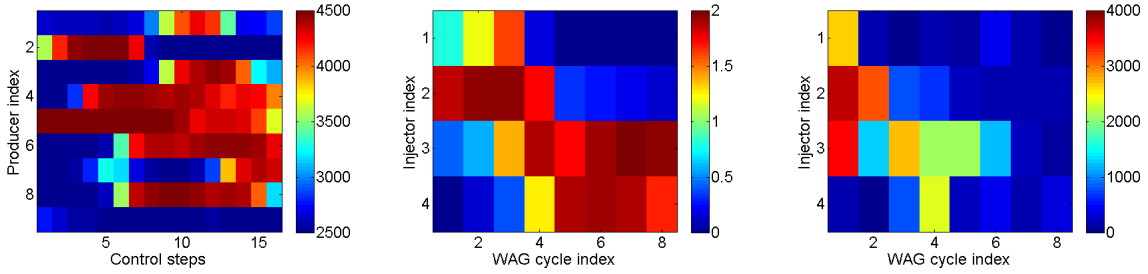

(d) Opt. simultaneously, producers (psi)

(e) Opt. simultaneously, gas injectors ($\times 10^7$scf/d)

(f) Opt. simultaneously, water injectors (stb/d)

Figure 3.3: Estimated well controls at different control steps/WAG cycle from two different approaches: well control optimization only ((a), (b), (c)) and simultaneous optimization ((d), (e), (f)), Example 1.

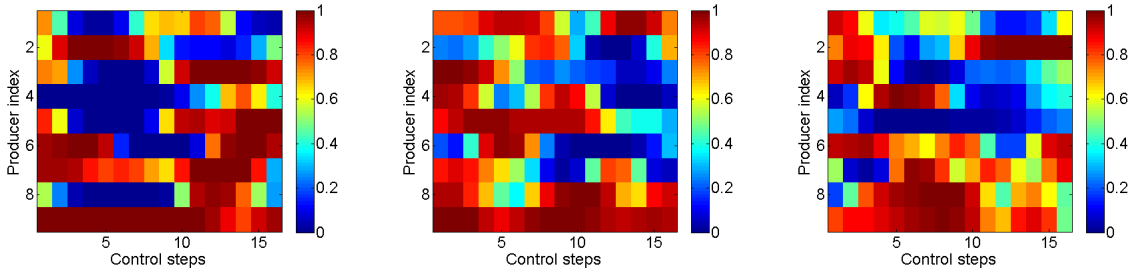

(a) Producers, ICV 1

(b) Producers, ICV 2

(c) Producers, ICV 3

Figure 3.4: Estimated ICV settings of all the production wells at different perforated segments; simultaneous optimization approach, Example 1.

channel and operates at a relatively low BHP only at the first two control steps; thereafter it is shut in until it is reopened during the last few control steps at which time Inj1 is closed. Pro4, Pro6 and Pro8 are in the channel and they operate at close to minimum allowable BHP at the first few control steps, and then they are shut in when the injected gas and/or water breaks through; Pro5 is connected to Inj2, Inj3 and Inj4 by high permeability channels,

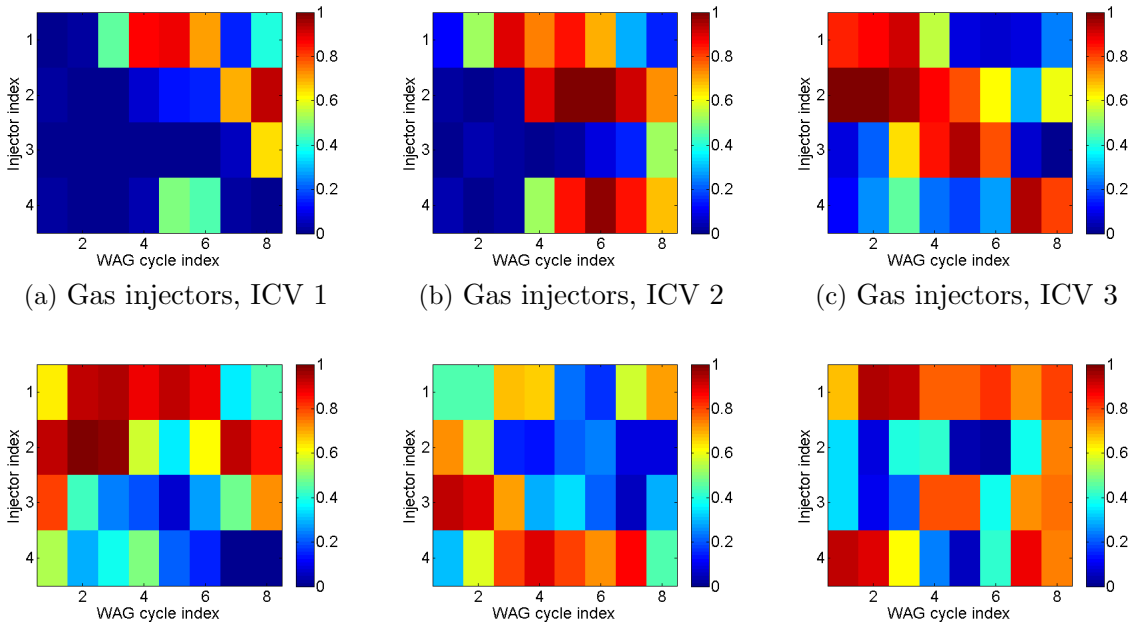

(a) Gas injectors, ICV 1 (b) Gas injectors, ICV 2 (c) Gas injectors, ICV 3

(d) Water injectors, ICV 1 (e) Water injectors, ICV 2 (f) Water injectors, ICV 3

Figure 3.5: Estimated ICV settings of all the injection wells at different perforated segments; simultaneous optimization approach, Example 1.

so Pro5 is shut in or operates at a pressure that results in little production throughout the reservoir life in order to prevent the production of injected gas and water.

For the simultaneous optimization approach, we need to consider both the estimated well controls and the ICV settings in order to explain the well performance. If a well is shut in, we do not need to consider the corresponding ICV settings because when a well is shut in, the ICV settings have no influence. Thus, we can refine the ICV settings plot by setting the values of ICVs equal to 0 when the corresponding well is shut in. Figs. 3.6 and 3.7 show the oil, water and gas production rates of all the producers during the production lifetime, and these results clearly display the shut-in periods. The cause of the spikes in the production profiles is due to a dramatic change in operating BHP pressure from one control step to the next. In practice, the change in operating BHP would not be a discontinuous but would change gradually from the optimal BHP at one control step to the operating BHP at the next step.

By setting all ICV settings to zero during a shut-in period, the ICV settings for all

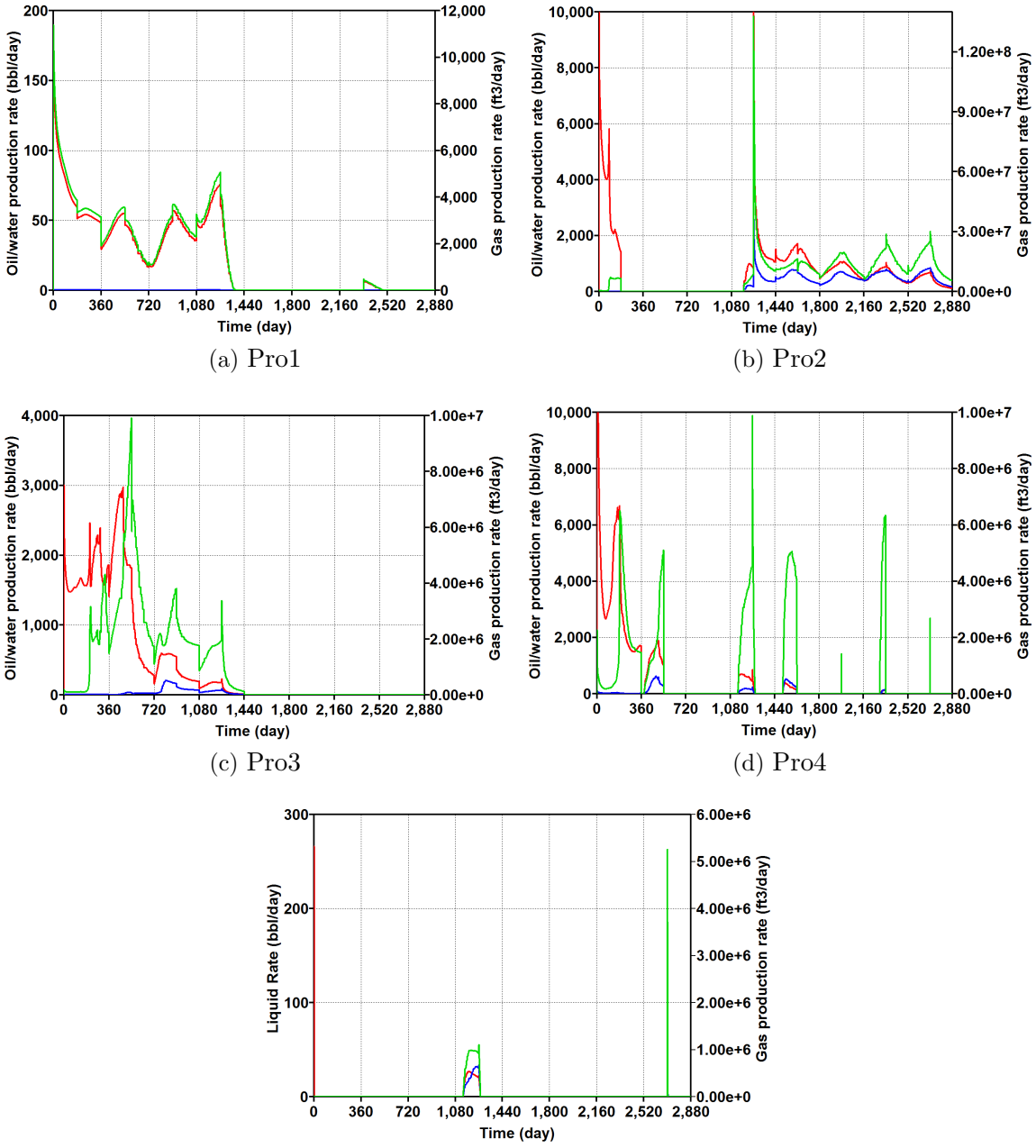

(a) Pro1 (b) Pro2

(c) Pro3 (d) Pro4

(e) Pro5

Figure 3.6: Production rates of Pro1 through Pro5 based on optimal controls for the simultaneous optimization approach; red curve denotes oil rate, blue curve denotes water rate and green curve denotes gas rate; Example 1.

producers shown in Fig. 3.4 are modified to obtain Fig. 3.8. In Fig. 3.8, we see that in layer 1, which is controlled by the ICVs of segment 1, far more producer ICV settings are zero or very close to zero than is the case for segments 2 and 3, respectively. This is due to the fact that layer 1 is the highest permeability layer. When more ICVs in layer 1 are closed

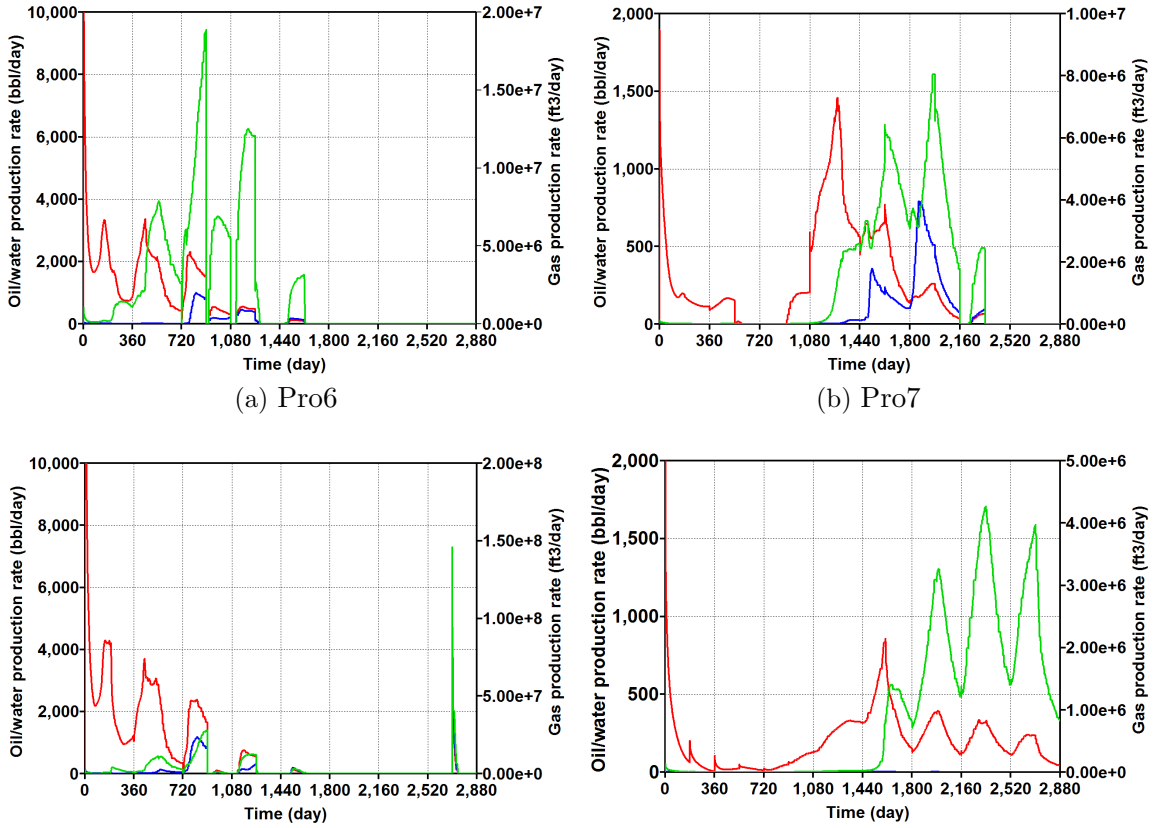

(a) Pro6 (b) Pro7

(c) Pro8 (d) Pro9

Figure 3.7: Production rates of Pro6, Pro7, Pro8 and Pro9 based on optimal controls for the simultaneous optimization approach; red curve denotes oil rate, blue curve denotes water rate and green curve denotes gas rate; Example 1.

or almost closed during production lifetime, the water and/or gas breaking through from the high permeability layer is prevented or delayed. As is evident from Fig. 3.6(e), Pro5 is shut-in for most control steps and consequently most ICV settings for Pro5 are recorded as zero in Fig. 3.8. This indicates that virtually all of the oil is swept toward the boundary of the reservoir, and the drilling and completion of Pro5 was a wasted expense.

From a careful examination of the numerical results pertaining to Figs. 3.3(e) and 3.3(f), we find that no injector is fully shut-in for any control step even though at some control steps, injection rates may be very low as indicated by a dark blue color in Figs. 3.3(e) and 3.3(f). For gas injection wells, there are more ICV settings close to 1 (fully open) in the bottom segment (bottom layer) than in the upper segment (Figs. 4.16(a), 4.16(b) and 4.16(c)), especially for Inj2 and Inj3, which results in more gas injected into the bottom layer (see

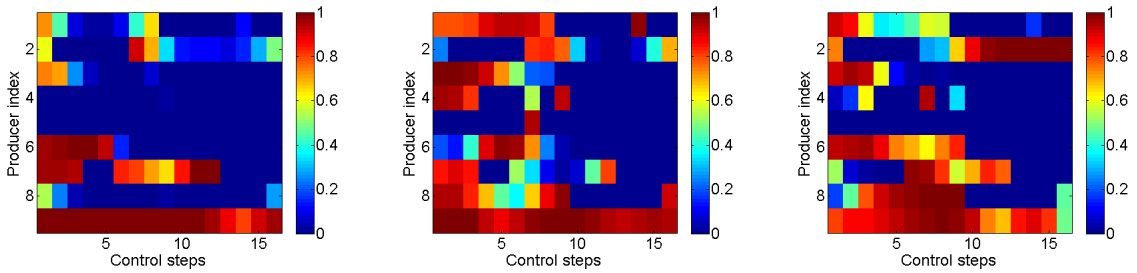

(a) Producers, ICV 1 (b) Producers, ICV 2 (c) Producers, ICV 3

Figure 3.8: Refinement of estimated ICV settings of all producers at different perforated segments using a simultaneous optimization approach, Example 1.

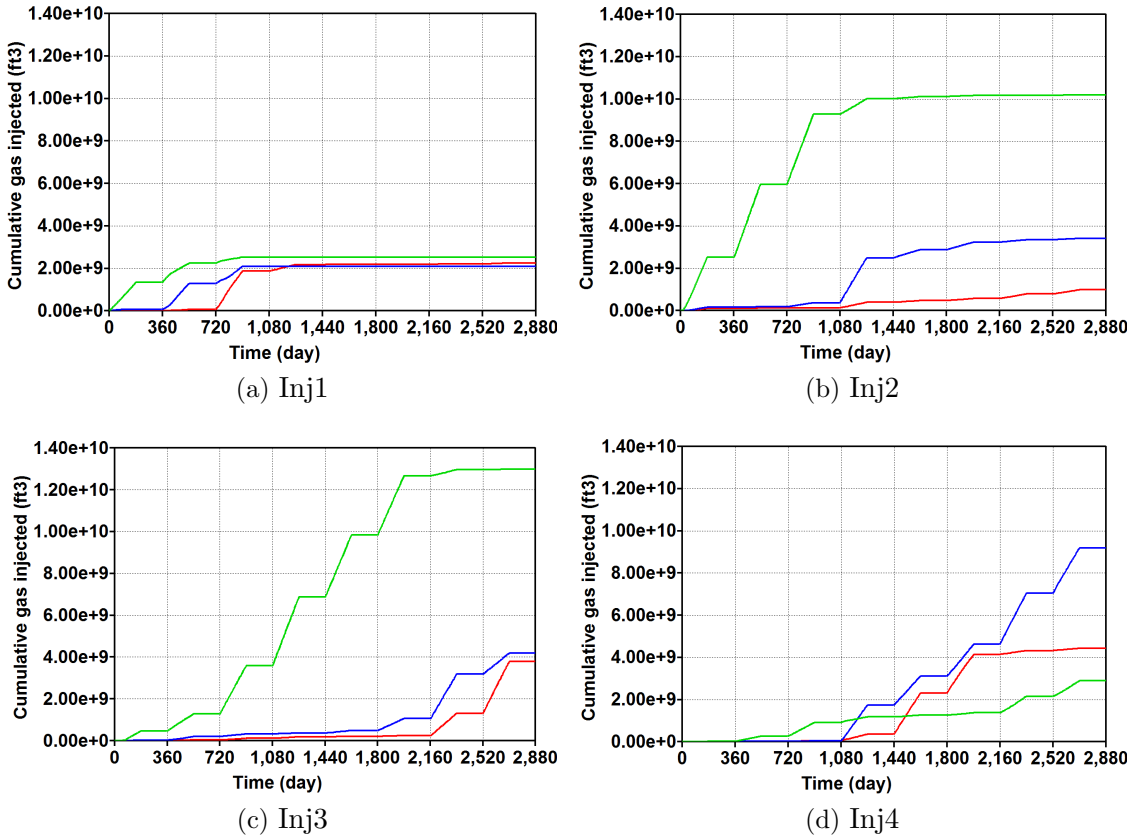

(a) Inj1 (b) Inj2

(c) Inj3 (d) Inj4

Figure 3.9: Cumulative gas injection of four injectors into three different layers using simultaneous optimization approach; red curve denotes layer 1, blue curve denotes layer 2 and green curve denotes layer 3, Example 1.

Fig. 3.9). As injected gas has a tendency to rise to the top, injecting more gas in the bottom layer displaces more oil than would be the case if gas were injected only in the top layer in which case the gas would displace oil mainly from the top layer.

Fig. 3.10 shows the cumulative gas injected into the three layers for each of the four

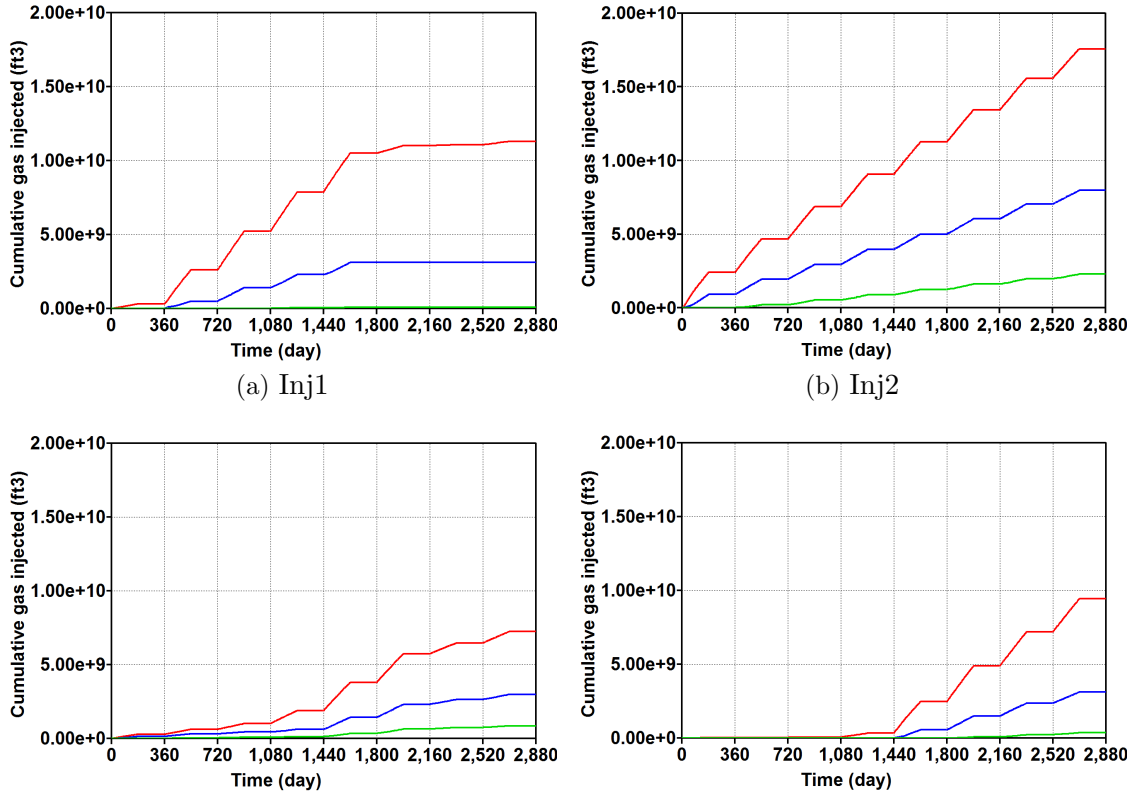

(a) Inj1 (b) Inj2

(c) Inj3 (d) Inj4

Figure 3.10: Cumulative gas injection of four injectors into three different layers using only well controls optimization approach; red curve denotes layer 1; blue curve denotes layer 2 and green curve denotes layer 3, Example 1.

injectors based on the optimal well controls computed using only well control optimization approach. Compared to the cumulative gas injected into the three layers through the four injectors with the simultaneous optimization approach (see Fig. 3.9), more gas is injected into the top layer when optimizing only well controls. Thus more oil is displaced from the top layer when optimizing well controls; the oil saturation distribution is shown later.

The results of Fig. 3.3(f) obtained from simultaneous optimization indicate that water injection wells operate at a rate lower than 1,000 stb/day for most of the production lifetime. Water is injected mainly through Inj2 within the first two WAG cycles and through Inj3 within the first six WAG cycles. Table 3.2 shows the cumulative water injected into the three different layers for the simultaneous optimization and the well controls only optimization approaches. It can be seen that more water is injected into the top layer for both of these

two optimization approaches. Due to the gravity segregation, injected water has a tendency to move to the bottom; thus, injecting more water in the top layer displaces more oil than would be the case if water were injected only in the bottom layer.

Table 3.2: Cumulative water injected at the end of the reservoir life (2,880 days) into three different layers for simultaneous optimization and well controls only optimization approaches, Example 1.

Terms	Layer 1 $\times 10^6$stb	Layer 2 $\times 10^6$stb	Layer3 $\times 10^6$stb
Optimize simultaneously	2.333	1.917	1.204
Optimize well controls only	2.504	1.785	0.650

The results of With the optimized injection/production strategy from simultaneous optimization of well controls and ICV settings, controlling the ICV settings enables more displacement of oil from the lower permeability layers (layers 2 and 3) with less gas and/or water production from the high permeability layer (layer 1) compared to the case where only well controls are optimized.

Fig. 3.11 shows the remaining oil saturation distribution for the three different optimization approaches. Although the results of Table 3.1 and Fig. 3.11 indicate that the most oil is produced for the case where we optimize both well controls and ICV settings, the case where we optimize only well controls is interesting when we compare the remaining distribution of oil obtained (Figs. 3.11(a), 3.11(b) and 3.11(c)) with that obtained when optimizing only ICV settings. For the case where we optimize only ICV's, the remaining oil saturation map is almost the same in all layers whereas when only well controls are optimized, only the high permeability layer, layer 1, is well swept by the injected fluid, which is consistent with the results on the cumulative oil produced from each layer shown in Fig. 3.12. Recall that the layers all have the same initial pore volume and hence the same number of RB of oil initially in place. It is interesting to note that for all three optimization approaches, much of the original oil in the region near Pro1 has not been produced (see Fig. 3.11) even though Pro1 operates near its minimum allowable BHP during most of the "reservoir life," see Figs. 3.3(a) and 3.3(d). The fact that a large amount of oil remains in the vicinity of Pro1

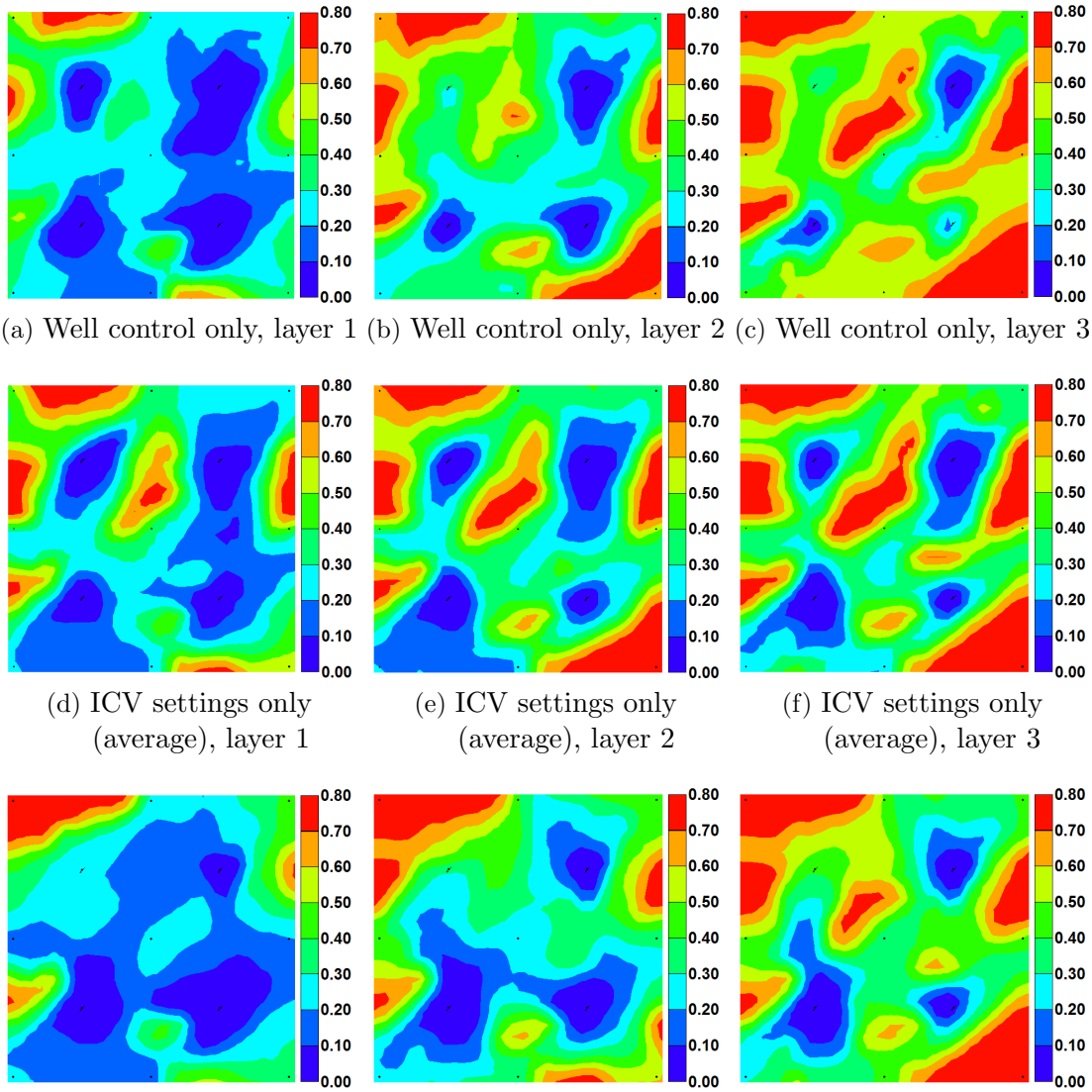

(a) Well control only, layer 1 (b) Well control only, layer 2 (c) Well control only, layer 3

(d) ICV settings only (average), layer 1 (e) ICV settings only (average), layer 2 (f) ICV settings only (average), layer 3

(g) Simultaneous, layer 1 (h) Simultaneous, layer 2 (i) Simultaneous, layer 3

Figure 3.11: Remaining oil saturation distribution for different approaches, Example 1.

at the end of the "reservoir life" is primarily a consequence of the fact that Pro1 is located in a very low permeability region, but it is also due partially to the fact that the nearest injector, Inj1, operates at rates close to zero during most of the last four WAG cycles.

3.2.3 Investigation of Perturbation Size and Initial Guesses

In this subsection, we investigate the effect of the perturbation size and initial guesses on the EnOpt optimization results. Three different perturbation sizes are considered, namely, σ=1, 0.1 and 0.01. These three perturbation sizes are considered for the three different

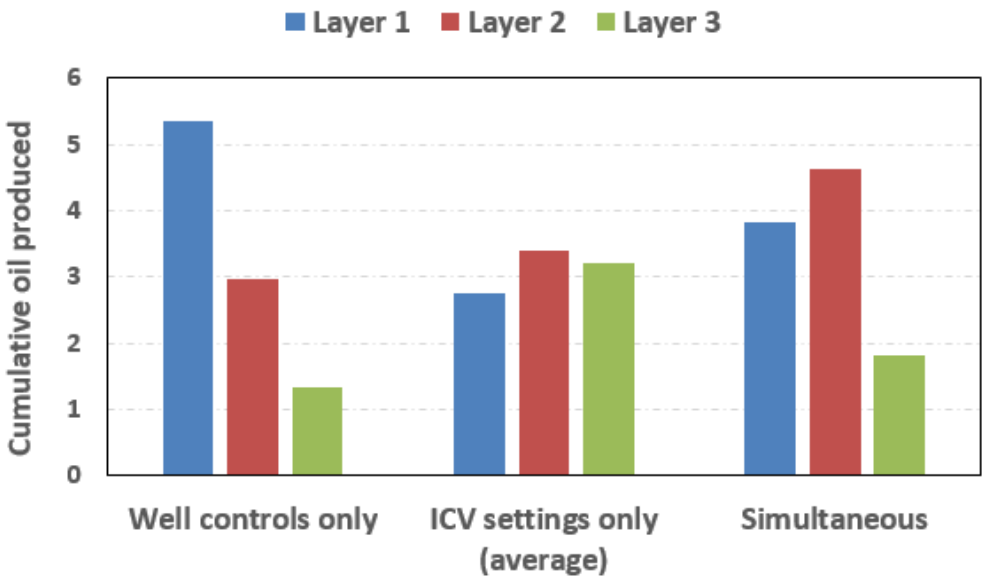

Figure 3.12: Cumulative oil produced from each layer in millions of STB, Example 1.

optimization approaches. Fig. 3.13 shows the effect of the perturbation size on the NPV. The cases used to study the effect of perturbation size are run with the same initial seed. From Fig. 3.13, we can see that σ=0.1 yields the best final NPV, especially for the simultaneous optimization approach.

Table 3.3 shows the optimization results obtained by simultaneous optimization of well controls and ICV settings for different initial guesses. Initial guess 1 is the original initial guess discussed previously, i.e., each well control is set equal to the average of its upper and lower bounds and all ICV settings are equal to 0.5. With this initial guess, we apply simultaneous optimization using 2,000 total reservoir simulation runs. Initial guess 2 uses all ICV settings equal to 0.5 but sets the initial well controls equal to those obtained from the well control optimization only approach after 500 simulation runs. With these initial guesses, we run another 1,500 simulations using simultaneous optimization. Initial guess 3 starts with each well control equal to the average of its bounds but uses the estimated values for ICV settings obtained by optimizing the ICV settings using 500 simulation runs, and with these new initial guesses, we run another 1,500 simulations. Initial guess 4 uses the estimated values for well controls obtained from the well control optimization only approach after 500 simulation runs and the estimated values for ICV settings obtained from the ICV settings

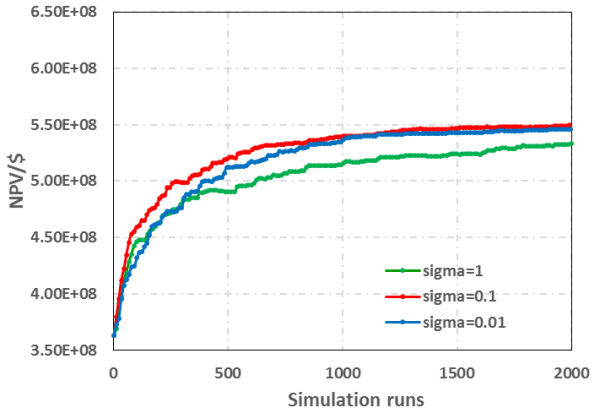

(a) Well control optimization only

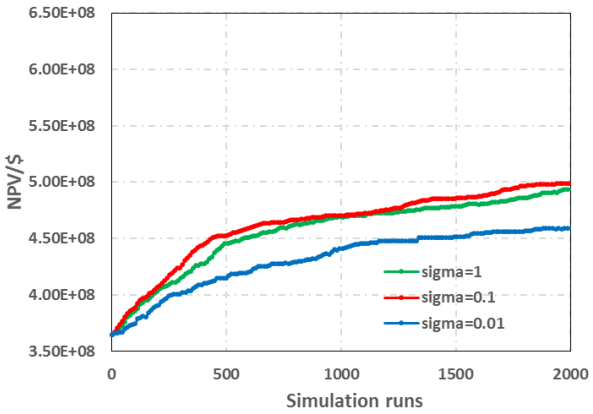

(b) ICV settings optimization only

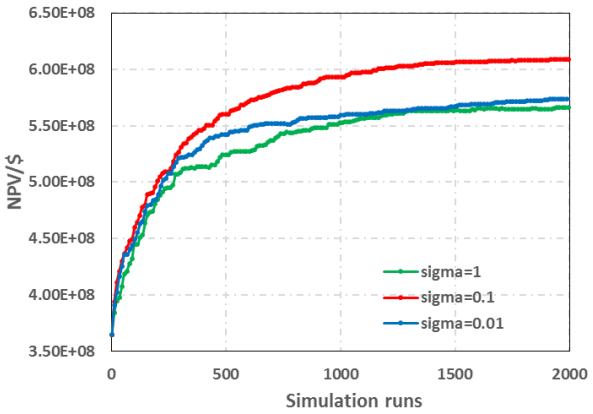

(c) Simultaneous optimization

Figure 3.13: Effect of perturbation size on optimization results for three optimization approaches.

optimization only after 500 simulation runs, and with these new initial guesses, we run another 1,000 simulations. Note that the total simulation runs for all the four optimizations under different initial guesses are the same, i.e., 2,000 simulation runs. All the cases are run with three different initial seeds, and the table shows the average of the three runs. From Table 3.3, we note that the final NPV and cumulative oil produced under different initial guesses are practically identical but there is some variation in the values of the other outputs. In terms of NPV and cumulative oil produced, the simultaneous optimization approach is robust with regard to the initial guess.

Table 3.3: Comparison of optimization results with different initial guesses; simultaneous optimization of well controls and ICV settings.

Terms	Initial 1	Initial 2	Initial 3	Initial 4
Final NPV($\times 10^6$\$)	601.9	600.9	604.3	603.3
Cum. oil prod.($\times 10^6$stb)	10.229	10.285	10.248	10.352
Cum. water inj.($\times 10^6$stb)	4.968	4.983	5.310	5.305
Cum. water prod.($\times 10^6$stb)	1.360	1.533	1.531	1.645
Cum. gas inj.($\times 10^9$scf)	61.67	64.55	59.72	64.78

3.3 Example 2: Anisotropic Reservoir

3.3.1 Problem Description

The second example is based on a reservoir simulation model defined on a $25 \times 25 \times 3$ grid with the grid block dimensions given by $\Delta x = \Delta y = 100$ ft and $\Delta z = 30$ ft. Fig. 3.14 displays the horizontal log-permeability distribution for the first layer, which is generated from a spherical anisotropic variogram model with a major correlation length of 1,700 ft (corresponding to the width of 17 gridblocks) and a minor correlation length of 500 ft (i.e., 5 gridblocks). The direction of maximum continuity is equal to 135 degrees measured from the positive x-axis. The mean of the log-permeability field is 5.0 and the standard deviation of log-permeability is set equal to 0.3. The reservoir contains four injectors and five producers in a nine-spot pattern as shown in Fig. 3.14. Note there are three layers. The second and third layers have the same heterogeneity features as the first layer, but the permeability field of layer 2 is equal to the permeability field of layer 1 multiplied by 0.5, and the permeability field of layer 3 is equal to the permeability field of layer 1 multiplied by 0.3. The vertical permeability is set equal to one tenth of the horizontal permeability. The reservoir lifetime is equal to 2,160 days. The total number of WAG cycles for this case is set equal to 6 and the time length of each half-cycle is equal to 180 days. Thus, each well contains 12 control steps, with the length of each control step equal to 180 days. The time correlation length is 540 days, which means three consecutive control steps are correlated.

In this example, each producer operates under BHP control with an upper bound of

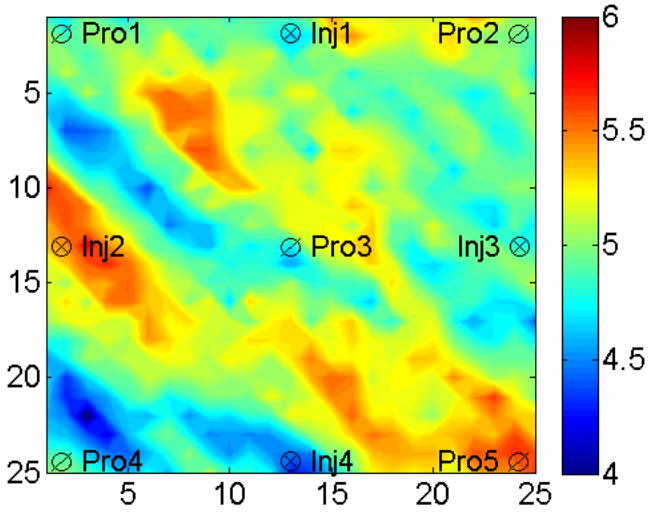

Figure 3.14: Log-permeability distribution.

4,500 psi and a lower bound of 1,500 psi. All the other problem specifications, including the bounds of control variables for injectors and the economic parameters, are the same as those in Example 1.

Table 3.4: Comparison among different approaches of WAG flooding, Example 2.

Terms	Opt. well controls	Opt. ICV (average)	Opt. ICV (bound)	Opt. simultaneous
Initial NPV($\times 10^6$\$)	497.3	471.0	497.1	471.0
Final NPV($\times 10^6$\$)	614.5	607.7	660.8	687.0
Cum. oil prod.($\times 10^6$stb)	10.84	10.57	11.67	11.79
Cum. water inj.($\times 10^6$stb)	4.93	8.24	11.95	5.39
Cum. water prod.($\times 10^6$stb)	0.94	1.95	5.08	1.39
Cum. gas inj.($\times 10^9$scf)	79.48	40.98	68.92	70.54

3.3.2 Computational Results

Table 3.4 shows the initial NPV, the final NPV, the cumulative oil produced, the cumulative water injected/produced and cumulative gas injected based on using different optimization approaches for WAG flooding. Note that all the values in Table 3.4 are averages of the values obtained from the optimization processes with three different starting random seeds. From Table 3.4, we can see that the final values of NPV using the three optimization

approaches increase significantly compared to the initial values of NPV. As in Example 1, the simultaneous optimization approach achieves the highest final NPV and cumulative oil produced, while optimizing ICV settings only with "average" well controls yields the lowest final NPV and cumulative oil produced. The final NPV and cumulative oil achieved by using the simultaneous optimization approach are, respectively, 11.80% and 8.77% higher than the ones obtained by optimizing well controls only. Meanwhile, the cumulative gas injected using simultaneous optimization is lower than that obtained by optimizing only well controls. Thus, we see that the significant gain in final NPV obtained with the simultaneous approach over optimizing only well controls is due to a combination of more oil produced and less gas injected while the simultaneous optimization value of NPV attained is superior to the NPV obtained by only optimizing ICV settings with "bound" well controls primarily because less water is injected and less water is produced when the values of design variables obtained with simultaneous optimization are applied.

Fig. 6.8 shows the NPV versus the number of reservoir simulation runs for different optimization approaches with three different initial random seeds for Example 2. From Fig. 6.8, it is clear that the approach using simultaneous optimization achieves the highest average final NPV as in Example 1.

Fig. 3.16 displays the estimated well controls and ICV settings of gas injectors at different WAG cycles from the simultaneous optimization approach. It can be seen from Fig. 3.16(a) that all the gas injectors operate at close to the maximum injection rate (20 million scf/day) for most of the WAG cycles. For gas injection wells, there are more ICV settings close to 1 (fully open) in the bottom segment (ICV 3) than in the upper segment (Figs. 3.16(b), 3.16(c) and 3.16(d)), and thus, more gas is injected into the bottom layer (see Fig. 3.17). Again, as injected gas has a tendency to rise to the top, injecting more gas in the bottom layer displaces more oil than would be the case if gas were injected only in the top layer, in which case the gas would displace oil mainly from the top layer. Fig. 3.18 shows the cumulative gas injected into each layer from three different optimization approaches. Compared to the cumulative gas injected into each layer through the four injectors with the

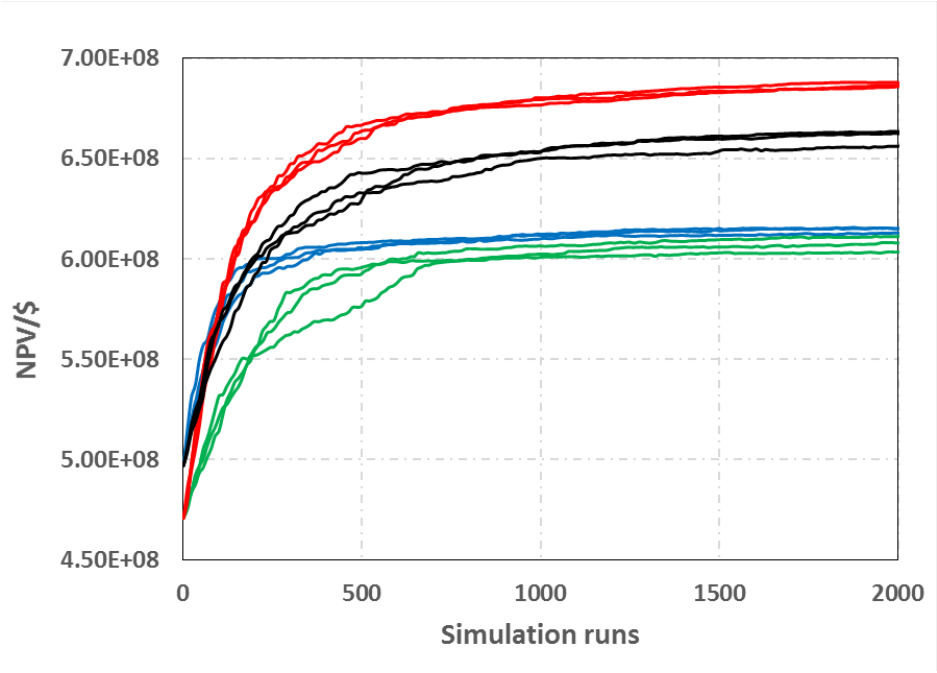

Figure 3.15: NPV versus simulation runs for different optimization approaches with three different starting random seeds; blue curves: optimization of only well controls; green curves: optimization of only ICV settings with fixed "average" well controls; black curves: optimization of only ICV settings with fixed "bound" well controls; red curves: simultaneous optimization, Example 2.

simultaneous optimization and ICV settings only (with "bound" well controls) optimization approaches, more gas is injected into the top layer when optimizing only well controls, thus significant more oil is displaced from the top layer.

Fig. 3.19 shows the estimated well controls and ICV settings of water injectors at different WAG cycles from the simultaneous optimization approach. We can see from Fig. 3.19(a) that all four water injection wells operate at a relatively high rate (around 2,000 stb) within the first four WAG cycles while they are almost shut in at the last two WAG cycles. From Figs. 3.19(b), 3.19(c) and 3.19(d), it can be seen that there are more ICV settings close to 1 (fully open) in the upper segment (ICV 1) than in the other two segments, and thus, more water injected into top layer. Due to the gravity segregation, injected water has a tendency to move to the bottom. Thus, injecting more water into the top layer displaces more oil than would be the case if water were injected only into the bottom layer. Fig. 3.20 shows the cumulative water injected into each layer from three different

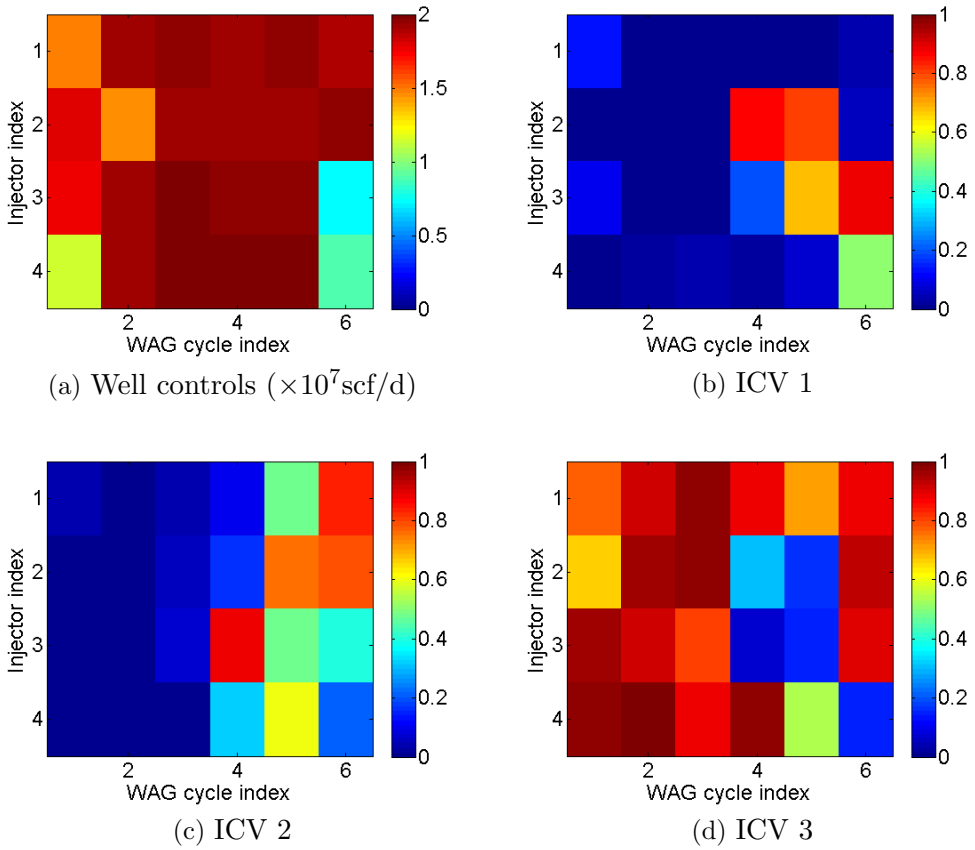

(a) Well controls ($\times 10^7$scf/d) (b) ICV 1

(c) ICV 2 (d) ICV 3

Figure 3.16: Estimated well controls and ICV settings of gas injectors at different WAG cycles from simultaneous optimization approach, Example 2.

optimization approaches. Note the plots for "ICV settings only" in this figure pertain to the approach where we optimize ICV settings only with all well controls fixed to one of their bounds. The results of Fig. 3.20 indicate that, for all the three optimization approaches, more water is injected into the top layer than the other two layers. Note that a similar result was obtained in Example 1.

Fig. 3.21 shows the estimated optimal well controls and ICV settings of producers obtained at different WAG cycle from the simultaneous optimization approach. From Fig. 3.21(a), we can see that only Pro1 and Pro3 operate at close to the minimum allowable BHP throughout the reservoir life.

Fig. 3.22 shows the remaining oil saturation distribution for the three different optimization approaches at the end of the assumed reservoir life. Fig. 3.22 indicates that the

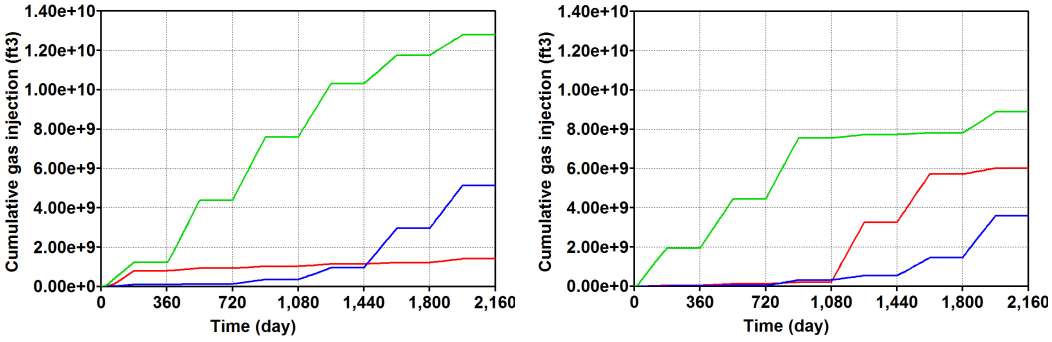

(a) Simultaneously: Inj1

(b) Simultaneously: Inj2

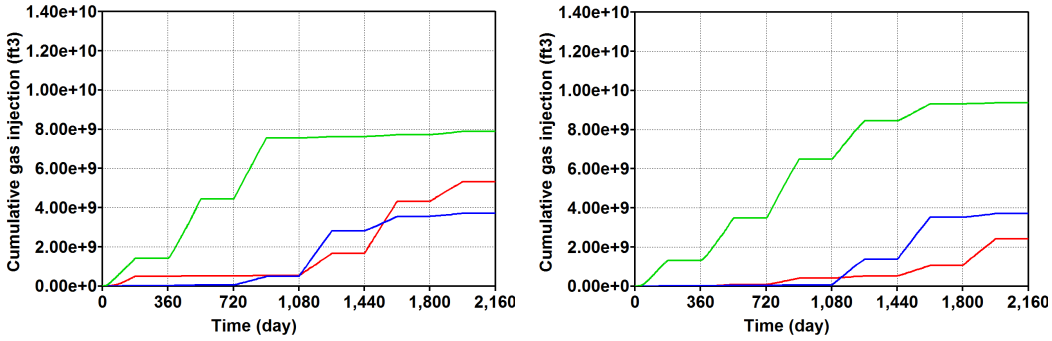

(c) Simultaneously: Inj3

(d) Simultaneously: Inj4

Figure 3.17: Cumulative gas injected into each layer using simultaneous approach; red curve: layer 1, blue curve: layer 2; green curve: layer 3, Example 2.

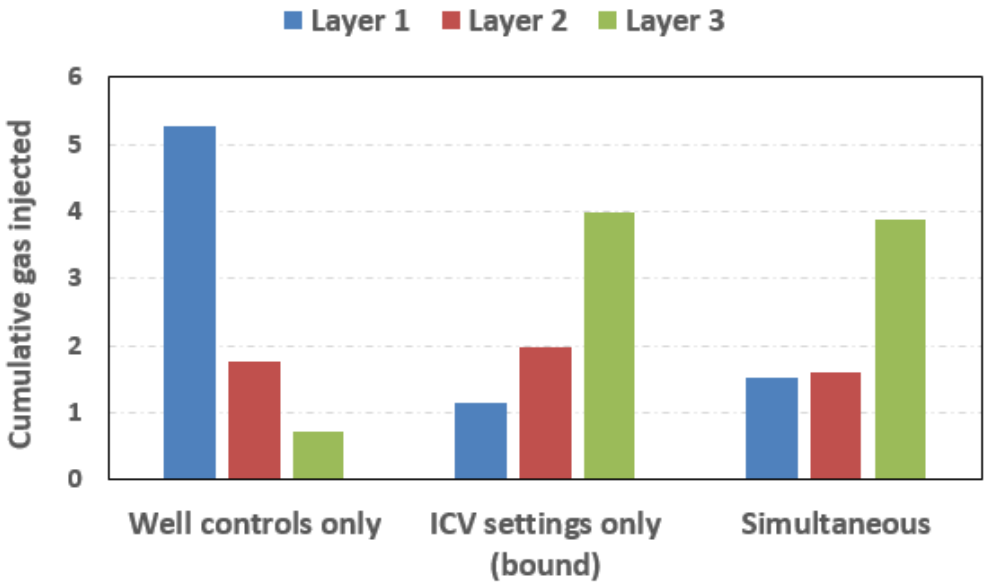

Figure 3.18: Cumulative gas injected into each layer ($\times 10^{10}$ ft^3), Example 2.

least oil remains, or, equivalently, the most oil is produced for the case where we optimize both well controls and ICV settings while the case where we optimize ICV settings with fixed

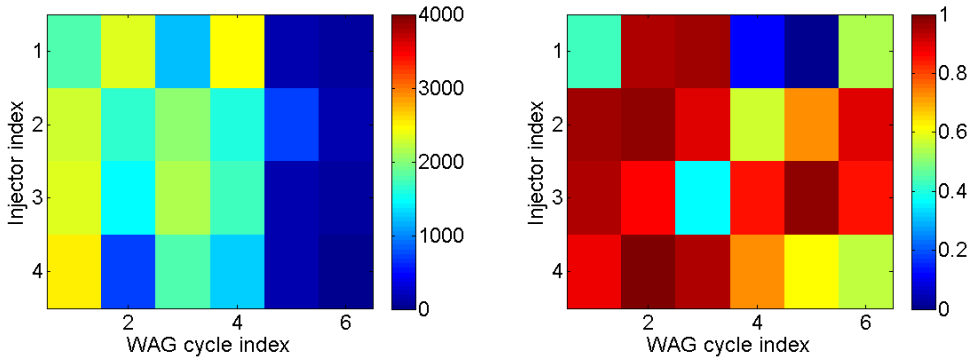

(a) Well controls (stb/d) (b) ICV 1

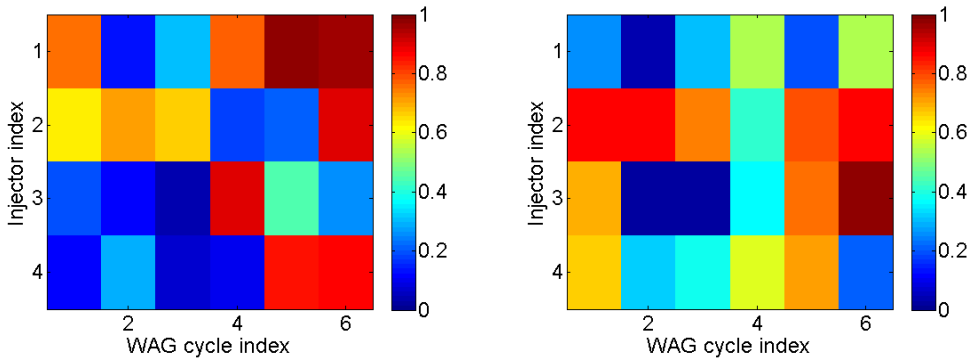

(c) ICV 2 (d) ICV 3

Figure 3.19: Estimated well controls and ICV settings of water injectors at different WAG cycles from simultaneous optimization approach, Example 2.

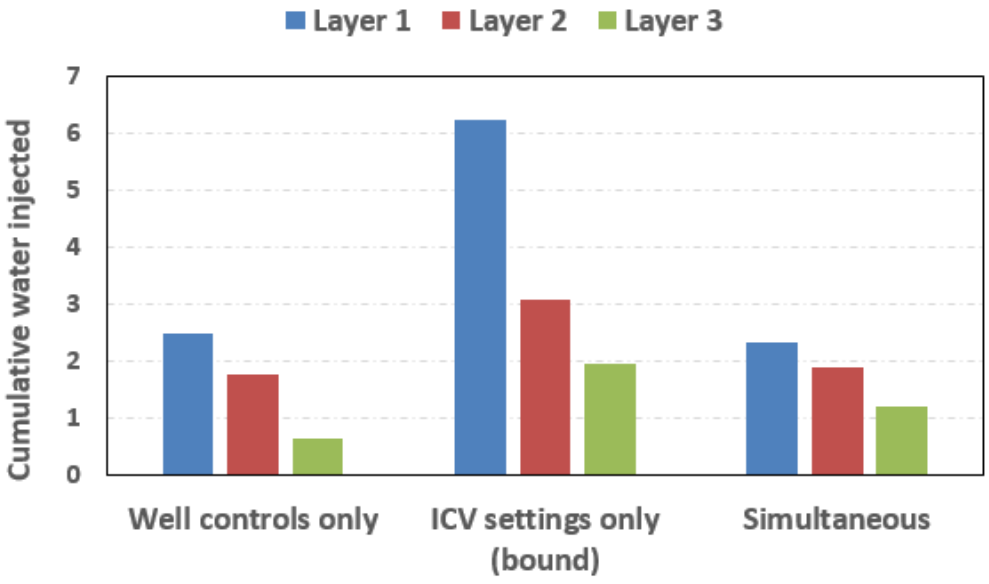

Figure 3.20: Cumulative water injected into each layer in millions of STB, Example 2.

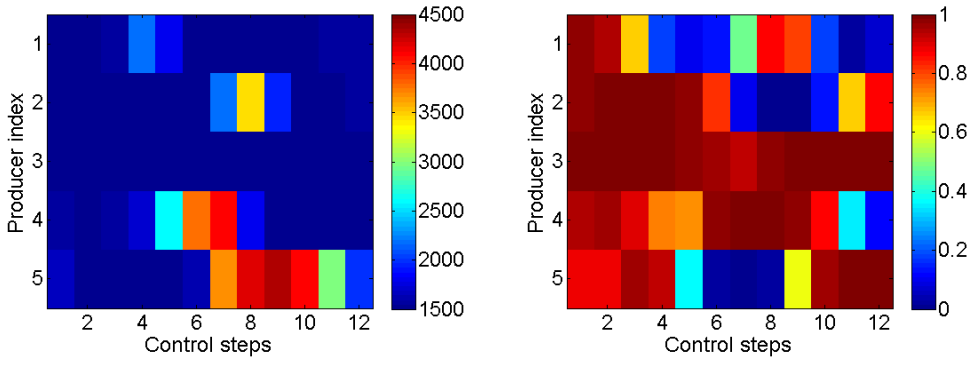

(a) Well controls (psi)

(b) ICV 1

(c) ICV 2

(d) ICV 3

Figure 3.21: Estimated well controls and ICV settings of producers at different control steps from simultaneous optimization approach, Example 2.

"average" values of the well controls yields the smallest oil production (most oil remaining). This result is consistent with the results of Table 3.4.

3.4 Comments

We provide a discussion here to address three issues: (a) the perturbation size and number of perturbations used to calculate the stochastic gradient, (b) whether simultaneous optimization of well controls and ICV settings yields a higher NPV than is obtained by ICV settings for the scenario where all well controls are BHP's and (c) the impact of the reservoir lifetime on the estimated life-cycle NPV.

3.4.1 Perturbations

The perturbation size affects the accuracy of the search direction as a stochastic

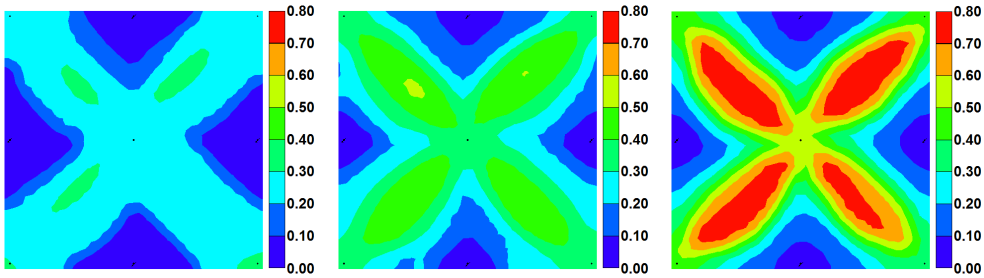

(a) Well control only, layer 1 (b) Well control only, layer 2 (c) Well control only, layer 3

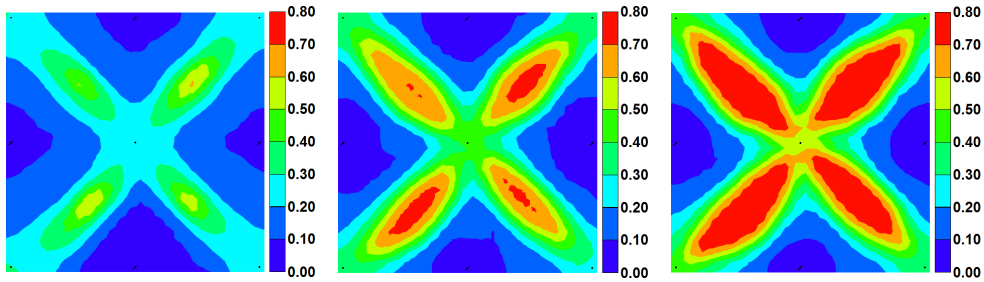

(d) ICV settings only (average), layer 1 (e) ICV settings only (average), layer 2 (f) ICV settings only (average), layer 3

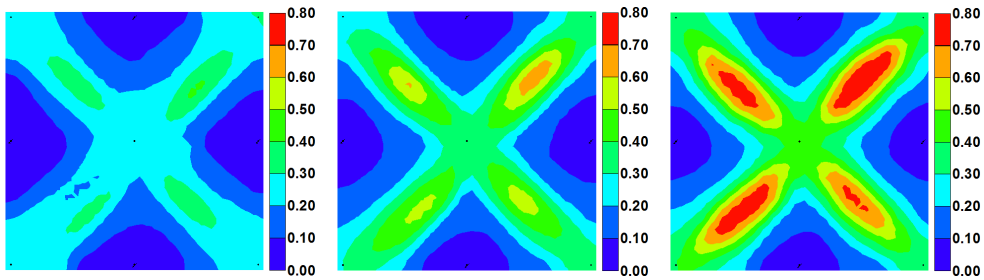

(g) ICV settings only (bound), layer 1 (h) ICV settings only (bound), layer 2 (i) ICV settings only (bound), layer 3

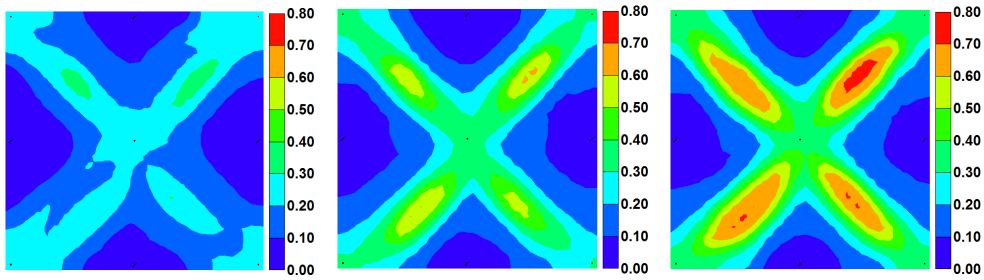

(j) Simultaneous, layer 1 (k) Simultaneous, layer 2 (l) Simultaneous, layer 3

Figure 3.22: Remaining oil saturation distribution for different optimization approaches at end of assumed reservoir life, Example 2.

approximation of the true gradient in a similar fashion as the approximation of a partial derivative by a finite-difference approximation. If the perturbation size is too small, the

approximation is totally corrupted by round off error, and when the perturbation size is too large, the approximation is highly inaccurate due to truncation error. Via a large set of computational experiments, [34] show that both the number of perturbations used to compute the stochastic gradient and the size of the perturbations affect the quality of the stochastic gradient (its direction compared to the direction of the true gradient) and hence affects the estimate of the optimal values of the design (optimization) variables. Unfortunately, there exists no known way to determine a priori the best choice for either the number of perturbations or the perturbation size. However, when we eliminate bound constraints by a log-transformation of the design variables, results presented here as well as other computational experiments not shown indicate that a perturbation size of 0.1 generally yields an optimal NPV of a similar or better quality than NPV values obtained with other perturbations. For the case where optimization is done on a single reservoir model, the stochastic gradient computed with 10-20 perturbations at each iteration generally give reasonable estimates of the optimal NPV although Fonseca et al. [34] have shown that to obtain a good estimate of the gradient at each iteration of steepest ascent may requires several dozens of perturbations. For the case of robust optimization where one estimates the expected NPV over a set of 10-100 reservoir models which represent geological uncertainty, computation of the stochastic gradient using one perturbation of the vector of optimization variables per reservoir model to compute a stochastic gradient results for use in steepest ascent, results in an algorithm which appears to obtain a good approximation of the optimal NPV. This algorithm, which was first introduced by Fonseca et al. [34] and is now referred to as StoSAG generally performs better than EnOpt, the first ensemble-based optimization algorithm [25]. Fonseca et al. [37] provide a theoretical explanation of why StoSAG outperforms EnOpt when the variation in the ensemble of reservoir models is large.

3.4.2 Simultaneous Optimization for BHP Controlled Wells

In cases like those considered here where injection wells are rate-controlled, it is intuitively clear that the optimization problem where both rates and ICV settings are used

as optimization variables has a higher optimal life-cycle NPV of production than does the problem where injection rates are fixed at their upper bounds and only ICVs settings are used as optimization variables. This is because when the injection rate is fixed, one can redistribute flow among zones by adjusting ICV settings but one cannot reduce the injection rate if the amount of fluid injected at the maximum rate leads to a suboptimal NPV. The same argument applies if flow rates are fixed at their maximum allowable values at producers. As pointed out by [58], however, the optimization problem where the flowing BHP's at producers are fixed equal to their lower bounds, injection pressures are fixed at their upper bounds, and only ICV settings are used as design variables should have the same value of optimal life cycle NPV as the problem where we use both BHPs and ICV settings as optimization variables. The validity of the previous statement seems clear because when BHPs are fixed at their bounds, the total injection rate at a well or the total production rate at a well can be reduced by simply lowering the ICV settings (reducing the PI multipliers) without changing the preset BHP's. We will illustrate the veracity of Leeuwenburgh's insight with the example presented next.

Fig. 3.23 shows the NPV versus simulation runs for the two approaches for the situation where both injectors and producers are under BHP control and upper and lower bounds are specified on the BHPs where the bounds, reservoir model and other parameters are identical to those specified in Example 2. In Fig. 3.23, the results for bound controls pertain to the case where producer BHPs are fixed at the lower bounds and injector operating BHPs are fixed at their upper bounds and these results are compared with the case where both BHP controls and ICV settings are optimized; this latter case is referred to as "simultaneous optimization." As we use a stochastic gradient, results for the two sets of design variables are generated for three different initial random seeds. Note from about 1500 reservoir simulation runs onward, the two sets of results are practically identical. Table 3.5 displays the results from the two optimization problems where all the values in Table 3.5 are averages of the values obtained from the optimization processes with three different starting random seeds. Although the estimated optimal BHPs (not shown) from the simultaneous

optimization approach are different from the BHP "bounds" and the ICV settings from the two optimization problems are different, the results of Table 3.5 indicate that the total amount of gas injected, the cumulative water injected, the total amount of produced water and cumulative oil production obtained from the two sets of results are very close.

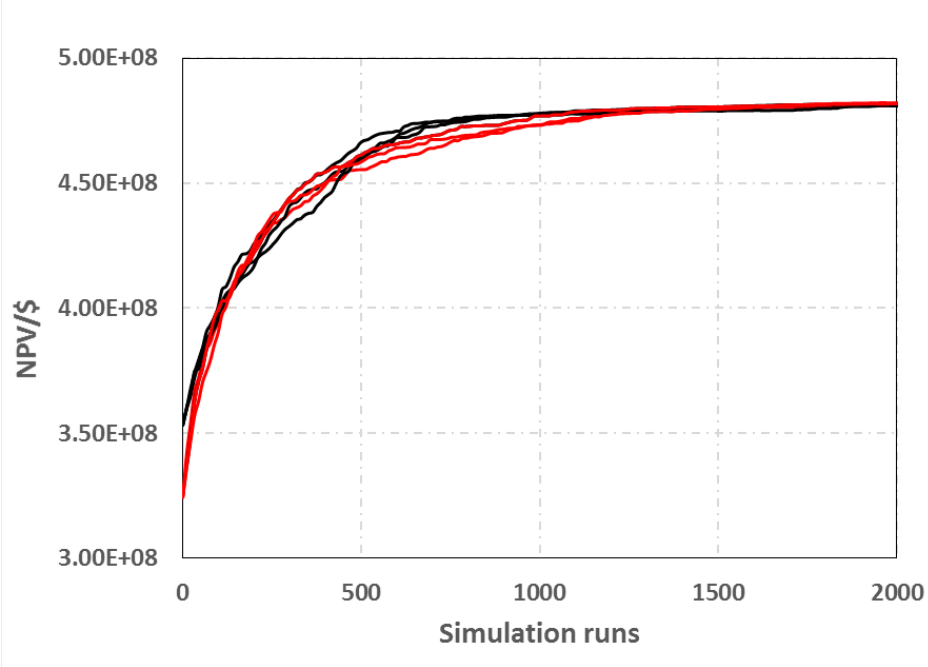

Figure 3.23: NPV versus simulation runs for three different starting random seeds; black curves: optimization of only ICV settings with fixed "bound" well controls; red curves: simultaneous optimization of both BHP controls and ICV settings.

Table 3.5: Comparison among different approaches with BHP controlled wells.

Terms	Opt. ICV only	Opt. simultaneous
Initial NPV($\times 10^6$\$)	353.3	324.4
Final NPV($\times 10^6$\$)	481.3	481.7
Cum. oil prod.($\times 10^6$stb)	7.80	7.83
Cum. water inj.($\times 10^6$stb)	5.98	5.99
Cum. water prod.($\times 10^6$stb)	2.04	2.15
Cum. gas inj.($\times 10^9$scf)	83.04	81.43

Considering the results discussed in the previous paragraph, it is perhaps worthwhile to note that very recent work of [42] indicates that optimization using rate control is more robust to uncertainty. The authors also note that in practice, it may be easier to implement

rate control at injectors where single-phase flow injection rates can be measured reasonably well. For producers, accurate individual well phase flow rate measurements are not generally available and in this case it is more practical to implement pressure controls at producing wells.

3.4.3 Impact of Reservoir Lifetime

To investigate the influence of reservoir lifetime on the estimated optimal life-cycle NPV, we reconsider Example 2, where we specify a priori two alternate reservoir lifetimes, namely 1,080 days and 4,320 days. With these lifetimes, we then perform simultaneous optimization of ICV settings and well controls where the well controls are rates at injectors and BHPs at producers. The reservoir model and other parameters are the same as those applied in Example 2. Fig. 3.24 displays the NPV versus simulation runs obtained for three different reservoir lifetimes. As can be seen, the NPV obtained from the reservoir lifetime of 1,080 days is much lower than the NPV values obtained from the two longer reservoir lifetimes but increasing the reservoir lifetime from 2,160 days to 4,320 days did not result in a significant gain in life-cycle NPV because the increased cost due to more gas and water injected and more water produced essentially offsets the revenue due to an increase in the barrels produced oil; see Table 3.6. Fig. 3.25 shows the estimated well controls for producers and their corresponding oil production rates for the case where the reservoir lifetime is equal to 4,320 days. As can be observed with the exception of producer "PRO-03," the other producers produce at a high pressure (low rate) for most of the time period after 2,160 days and a careful examination of the simulator run outputs indicates producers "PRO-01" and "PRO-02" are totally shut-in after about 2,700 days (15 control steps); and that producers "PRO-04" and "PRO-05" are shut-in during the time period from 2,700 days until 3,960 days. The corresponding NPV after 2,160 days of the optimization results for the case where the reservoir lifetime is equal to 4,320 days is 682.4 million USD, which indicates that 99% of the estimated NPV is obtained within 2,160 days (half of reservoir lifetime). If the operating expenses were known and taken into account, it is possible that production from

the reservoir would not be commercially viable beyond 2,160 days. At least for this example, the results indicate that it is far better to overestimate the reservoir lifetime when doing computer-based optimization. One can then recalibrate the reservoir life-time based on the optimization results.

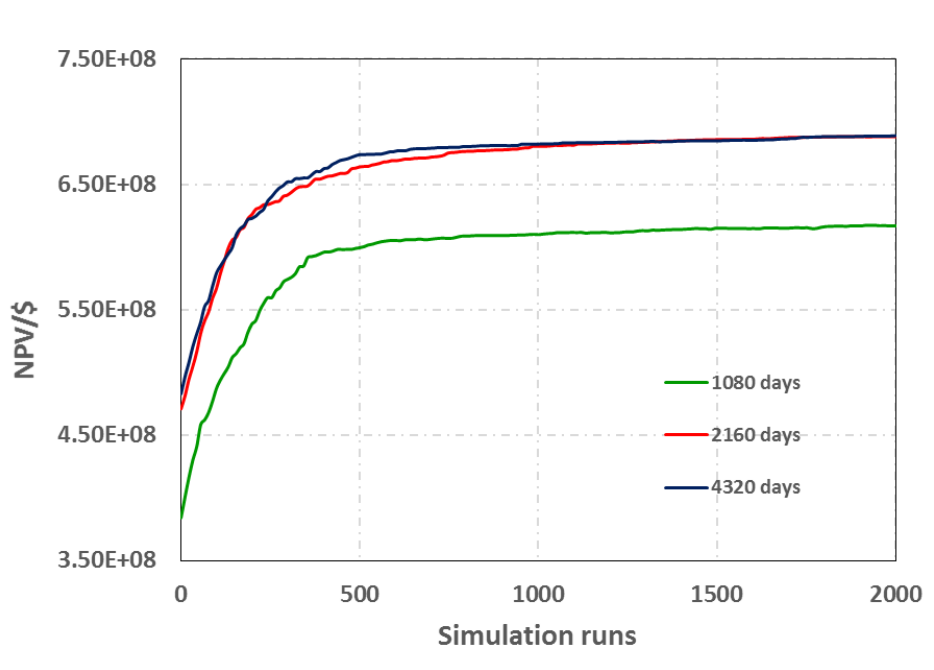

Figure 3.24: NPV versus simulation runs obtained from different reservoir lifetimes.

Table 3.6: Results obtained from different reservoir lifetimes.

Terms	1,080 days	2,160 days	4,320 days
Initial NPV($\times 10^6$\$)	384.2	471.0	482.9
Final NPV($\times 10^6$\$)	617.0	688.0	689.0
Cum. oil prod.($\times 10^6$stb)	9.62	11.80	12.12
Cum. water inj.($\times 10^6$stb)	4.44	5.23	6.26
Cum. water prod.($\times 10^6$stb)	0.52	1.53	1.63
Cum. gas inj.($\times 10^9$scf)	34.15	70.27	87.49

Finally, we ran the example with the reservoir lifetime specified as 4,320 days but production terminated when the field water cut reaches 94.11%, i.e., when the cost of water disposal becomes equal to the revenue from oil production. Although not shown, the NPV results obtained by using field water cut as a constraint is almost identical to the one obtained from the scenario where the field water cut is not incorporated as a constraint because

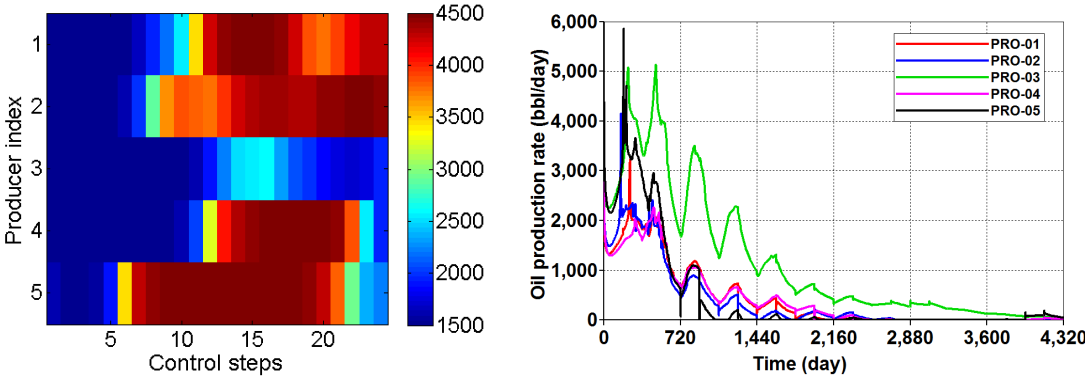

(a) Estimated BHP for producers (b) Corresponding oil production rate

Figure 3.25: Estimated well controls for producers and their corresponding oil production rates for the reservoir lifetime equal to 4,320 days.

the water cut of all the producers where we impose the field water cut constraint does not reach 94.11% until very near the end of the simulation.

CHAPTER 4

A STOCHASTIC SIMPLEX APPROXIMATE GRADIENT (STOSAG) FOR ROBUST LIFE-CYCLE PRODUCTION OPTIMIZATION

Due to geological uncertainties, such as uncertainty in the permeability and porosity field, the optimal solution obtained based on a single reservoir model may deviate significantly from the actual optimum. To account for geological uncertainty, robust optimization is typically performed to mitigate the effect of uncertainties in the reservoir model [89]. As mentioned in the introduction, EnOpt is one of the most popular optimization algorithms that can be used to perform robust optimization [25]. However, Fonseca et al. [35] observed that original form of EnOpt, proposed by Chen et al. [25], does not always yield satisfactory results, and they formulated a modified ensemble-based robust optimization algorithm, referred to here as stochastic simplex approximate gradient (StoSAG) and showed that StoSAG generally yields a significantly higher value of the life-cycle NPV for the robust optimization problem than is obtained with the standard EnOpt algorithm. In this Chapter, we provide a theoretical understanding of why StoSAG is superior to EnOpt in robust optimization, provide new insight on different forms of StoSAG algorithms, and demonstrate the outperformance of StoSAG over EnOpt with two reasonable examples.

4.1 Robust Optimization

In robust optimization, we consider the problem of finding u which maximizes the expectation over m of a nonlinear functional of the form $J = J(m, u, y(m, u))$, where m is a random vector with a known probability density function (pdf), u is a vector of system inputs (well control variables) and $y = y(m, u)$ is the output vector which is, in turn, a function of the system response to input vector u for a given model m [48]. Throughout

we assume that the uncertainty in m can be represented by sampling its pdf to obtain an ensemble of N_e realizations (i.e. geological models in our setting), m_i, $i = 1, 2, \cdots N_e$ and then we can approximate the expectation of J with respect to m as the mean of the set $\{J(m_i, u)\}_{i=1}^{N_e}$, i.e.,

$$J_E(u) = \frac{1}{N_e} \sum_{i=1}^{N_e} J(m_i, u), \tag{4.1}$$

where $J_E(u)$ denotes the approximation of the expectation of life-cycle NPV. The robust optimization problem is then stated as

$$\begin{aligned} \max_u J_E(u) = \max_u \tfrac{1}{N_e} \sum_{i=1}^{N_e} J(m_i, u), \\ \text{s.t.} \quad u^{\text{low}} \leq u \leq u^{\text{up}}, \end{aligned} \tag{4.2}$$

where u^{low} and u^{up}, respectively, denote the vector of lower bounds and the vector of upper bounds. Note that only bound constraints are considered in this work.

4.2 Theoretical Understanding on Ensemble Robust Optimization

To solve the robust optimization problem of Eq. 4.2, we use the steepest ascent algorithm which is given by Eq. 2.5. The gradient-based robust optimization technique where the gradient is computed by the use of adjoint formulation is the most computationally efficient method [89, 22], but the implementation of the adjoint method requires access to the source code of a reservoir simulator which is not publicly available for commercial reservoir simulators, and therefore various alternative optimization methods are being used. One of these, a non-code-intrusive approximate gradient method known as Ensemble-based Optimization (EnOpt), has gained considerable popularity over the past years in the reservoir optimization community following the pioneering work of Chen et al. [25].

In EnOpt, an ensemble of randomly perturbed control vectors is used to approximate a gradient of the objective function with respect to the control vector. The standard EnOpt

search direction is given by

$$d_{k,\text{EnOpt}} = \frac{1}{N_e - 1} \sum_{i=1}^{N_e} (\hat{u}_{k,i} - \overline{\hat{u}_k}) \Big(J(m_i, \hat{u}_{k,i}) - \overline{J(m, u_k)} \Big), \tag{4.3}$$

where

$$\overline{\hat{u}_k} = \frac{1}{N_e} \sum_{i=1}^{N_e} \hat{u}_{k,i} \tag{4.4}$$

and

$$\overline{J(m, u_k)} = \frac{1}{N_e} \sum_{i=1}^{N_e} J(m_i, \hat{u}_{k,i}). \tag{4.5}$$

Here, each control perturbation $\hat{u}_{k,i}$, $i = 1, 2, \cdots N_e$, at iteration k is generated from the distribution $\mathcal{N}(u_k, C_U)$, where C_U is a predefined covariance matirx which is kept constant throughout the optimization procedure. Note that this standard EnOpt formulation uses a one-to-one combination of random control perturbations and random geological models, i.e., one control perturbation for each geological model. The standard implementation of EnOpt of Chen et al. [25], which multiplies the search direction in Eq. 4.3 by C_U, is

$$d_{k,s,\text{EnOpt}} = C_U \left(\frac{1}{N_e - 1} \sum_{i=1}^{N_e} (\hat{u}_{k,i} - \overline{\hat{u}_k})(J(m_i, \hat{u}_{k,i}) - \overline{J(m, u_k)}) \right). \tag{4.6}$$

In order to demonstrate that $d_{k,\text{EnOpt}}$ defined in Eq. 4.3 can be approximated by C_U times the true gradient $\nabla_u J_E(u_k)$, i.e.,

$$d_{k,\text{EnOpt}} \approx C_U \nabla_u J_E(u_k), \tag{4.7}$$

Chen et al. [25] make the following two assumptions:

$$\overline{\hat{u}_k} = \frac{1}{N_e} \sum_{i=1}^{N_e} \hat{u}_{k,i} \approx u_k \tag{4.8}$$

and

$$\overline{J(m, u_k)} = \frac{1}{N_e} \sum_{i=1}^{N_e} J(m_i, \hat{u}_{k,i}) \approx J(m, \overline{\hat{u}_k}) \approx J(m, u_k). \tag{4.9}$$

Although $\hat{u}_{k,i}$, $i = 1, 2, \cdots, N_e$, are samples generated from $\mathcal{N}(u_k, C_U)$, the approximation in Eq. 4.8 may be inaccurate for the bound-constrained problem when the lower and/or upper bounds on u force truncation of the samples. The second assumption suggests that for any realization m_i of m, $J(m_i, u_k) \approx \overline{J(m, u_k)}$, which is clearly an invalid approximation unless the variance in the prior geological models is sufficiently small so that when the control vector u_k is applied to each of these models, the same value of NPV is obtained. Because of these two questionable assumptions, the quality of search direction obtained from Eq. 4.3, i.e., the quality of the approximation of Eq. 4.7 may not be good if there is a large variance in the prior geological models and/or the bound truncation issue arises for a nonneglible number of perturbations.

The generally invalid assumption that Eq. 4.9 holds implies that

$$\overline{J(m, u_k)} = J(\overline{m}, u_k), \tag{4.10}$$

where $\overline{m}$ is the mean of the m_i's or the mean of the underlying probability density function (pdf) for m. Using Eq. 4.10 and the assumption that Eq. 4.8 holds in the EnOpt formula of Eq. 4.3 gives

$$d_{k,\text{EnOpt-mod}} = \frac{1}{N_e} \sum_{i=1}^{N_e} (\hat{u}_{k,i} - u_k) \Big(J(m_i, \hat{u}_{k,i}) - J(\overline{m}, u_k) \Big), \tag{4.11}$$

where the additional subscript 'mod' indicates 'modified'. In Eq. 5.10, we have replaced the factor $1/(N_e - 1)$ in the original basic EnOpt formation by $1/N_e$ because we no longer approximate the mean of the distribution for u.

For simplicity in discussing EnOpt, we assume u and m are one dimensional. Denote $\delta m_j = m_j - \overline{m}$, $\delta \hat{u}_{k,i} = \hat{u}_{k,i} - u_k$. Assume that all derivatives of J are continuous and bounded, then the Taylor series expansion is

$$J(m_i, \hat{u}_{k,i}) = \sum_{n=0}^{\infty} \sum_{\ell=0}^{\infty} (\delta \hat{u}_{k,i})^n (\delta m_i)^\ell \frac{\partial^{n+\ell} J(\overline{m}, u_k)}{\partial u^n \partial m^\ell}. \tag{4.12}$$

Expanding the first three terms, i.e., the terms where '$n = 0, \ell = 0$', '$n = 1, \ell = 0$' and

'$n = 0, \ell = 1$', then we can rewrite Eq. 4.12 as

$$J(m_i, \hat{u}_{k,i}) = J(\overline{m}, u_k) + \sum_{n=1}^{\infty} (\delta\hat{u}_{k,i})^n (\delta m_i)^0 \frac{\partial^{n+0} J(\overline{m}, u_k)}{\partial u^n \partial m^0} + \sum_{\ell=1}^{\infty} (\delta\hat{u}_{k,i})^0 (\delta m_i)^\ell \frac{\partial^{0+\ell} J(\overline{m}, u_k)}{\partial u^0 \partial m^\ell} + \sum_{n=1}^{\infty}\sum_{\ell=1}^{\infty} (\delta\hat{u}_{k,i})^n (\delta m_i)^\ell \frac{\partial^{n+\ell} J(\overline{m}, u_k)}{\partial u^n \partial m^\ell}. \quad (4.13)$$

Subtracting $J(\overline{m}, u_k)$ on both sides of Eq. 4.13 and multiplying by $\delta\hat{u}_{k,i}$ give

$$(\delta\hat{u}_{k,i})\Big(J(m_i, \hat{u}_{k,i}) - J(\overline{m}, u_k)\Big) = \sum_{n=1}^{\infty} (\delta\hat{u}_{k,i})^{n+1} \frac{\partial^n J(\overline{m}, u_k)}{\partial u^n} + \sum_{\ell=1}^{\infty} (\delta\hat{u}_{k,i})^1 (\delta m_i)^\ell \frac{\partial^\ell J(\overline{m}, u_k)}{\partial m^\ell} + \sum_{n=1}^{\infty}\sum_{\ell=1}^{\infty} (\delta\hat{u}_{k,i})^{n+1} (\delta m_i)^\ell \frac{\partial^{n+\ell} J(\overline{m}, u_k)}{\partial u^n \partial m^\ell}. \quad (4.14)$$

Expanding the first term and combining the last two terms on the RHS of Eq. 4.14, we obtain

$$(\delta\hat{u}_{k,i})\Big(J(m_i, \hat{u}_{k,i}) - J(\overline{m}, u_k)\Big) = (\delta\hat{u}_{k,i})^2 \frac{\partial J(\overline{m}, u_k)}{\partial u} + \sum_{n=2}^{\infty} (\delta\hat{u}_{k,i})^{n+1} \frac{\partial^n J(\overline{m}, u_k)}{\partial u^n} + \sum_{n=0}^{\infty}\sum_{\ell=1}^{\infty} (\delta\hat{u}_{k,i})^{n+1} (\delta m_i)^\ell \frac{\partial^{n+\ell} J(\overline{m}, u_k)}{\partial u^n \partial m^\ell}. \quad (4.15)$$

Taking the expectation of Eq. 4.15 with respect to u gives

$$\begin{aligned} E_u\Big[(\delta\hat{u}_{k,i})\Big(J(m_i, \hat{u}_{k,i}) - J(\overline{m}, u_k)\Big)\Big] &= C_U \frac{\partial J(\overline{m}, u_k)}{\partial u} + \sum_{n=2}^{\infty} E_u\Big[(\delta\hat{u}_{k,i})^{n+1} \frac{\partial^n J(\overline{m}, u_k)}{\partial u^n}\Big] \\ &\quad + \sum_{n=0}^{\infty}\sum_{\ell=1}^{\infty} E_u\Big[(\delta\hat{u}_{k,i})^{n+1} (\delta m_i)^\ell \frac{\partial^{n+\ell} J(\overline{m}, u_k)}{\partial u^n \partial m^\ell}\Big] \\ &= C_U \frac{\partial J(\overline{m}, u_k)}{\partial u} + \mathcal{O}\Big[(\delta\hat{u}_{k,i})^3\Big] + \mathcal{O}\Big[(\delta\hat{u}_{k,i})(\delta m_i)\Big], \end{aligned} \quad (4.16)$$

where $E_u[\cdot]$ denotes the expectation with respect to u. Note that we used the fact the expectation of $(\delta\hat{u}_{k,i})^2$ is equal to C_U. Taking the Taylor expansion of $\partial J(m_i, u_k)/\partial u$, we get

$$\frac{\partial J(m_i, u_k)}{\partial u} = \frac{\partial J(\overline{m}, u_k)}{\partial u} + \sum_{\ell=2}^{\infty} (\delta m_i)^\ell \frac{\partial^\ell J(\overline{m}, u_k)}{\partial m^\ell}. \quad (4.17)$$

Rearranging Eq. 4.17 generates

$$\frac{\partial J(\overline{m},u_k)}{\partial u}=\frac{\partial J(m_i,u_k)}{\partial u}-\sum_{\ell=2}^{\infty}(\delta m_i)^{\ell}\frac{\partial^{\ell}J(\overline{m},u_k)}{\partial m^{\ell}}=\frac{\partial J(m_i,u_k)}{\partial u}+\mathcal{O}\Big[(\delta m_i)^2\Big]. \tag{4.18}$$

Substituting Eq. 4.18 into Eq. 4.16 gives

$$E_u\Big[(\delta\hat{u}_{k,i})\Big(J(m_i,\hat{u}_{k,i})-J(\overline{m},u_k)\Big)\Big]=C_U\frac{\partial J(m_i,u_k)}{\partial u}+\mathcal{O}\Big[(\delta m_i)^2\Big]+\mathcal{O}\Big[(\delta\hat{u}_{k,i})^3\Big]+\mathcal{O}\Big[(\delta\hat{u}_{k,i})(\delta m_i)\Big]. \tag{4.19}$$

Taking the expectation of the modified EnOpt of Eq. 4.11, we obtain

$$E_u\Big[d_{k,\text{EnOpt-mod}}\Big]=\frac{1}{N_p}\sum_{i=1}^{N_p}E_u\Big[(\hat{u}_{k,i}-u_k)\Big(J(m_i,\hat{u}_{k,i})-J(\overline{m},u_k)\Big)\Big], \tag{4.20}$$

Substituting Eq. 4.19 into Eq. 4.20, it follows easily that

$$\begin{aligned}E_u\Big[d_{k,\text{EnOpt-mod}}\Big]&=C_U\frac{1}{N_p}\sum_{i=1}^{N_p}\frac{\partial J(m_i,u_k)}{\partial u}+\mathcal{O}\Big[\max_i\{(m_i-\overline{m})^2\}\\&\quad+\max_i\{(\hat{u}_{k,i}-u_k)^3\}+\max_i\{(\hat{u}_{k,i}-u_k)(m_i-\overline{m})\}\Big]\\&=C_U\nabla_u J_E(u_k)+\mathcal{O}\Big[\max_i\{(m_i-\overline{m})^2\}\\&\quad+\max_i\{(\hat{u}_{k,i}-u_k)^3\}+\max_i\{(\hat{u}_{k,i}-u_k)(m_i-\overline{m})\}\Big].\end{aligned} \tag{4.21}$$

The error terms $\mathcal{O}\Big[\max_i\{(\hat{u}_{k,i}-u_k)^3\}\Big]$ and $\mathcal{O}\Big[\max_i\{(\hat{u}_{k,i}-u_k)(m_i-\overline{m})\}\Big]$ go to zero as the magnitude of the perturbations goes to zero, that is, as $\hat{u}_{k,i}\to u_k$. On the other hand, the ensemble of m's reflect the geological uncertainty and if the uncertainty is large, i.e., $\|m_i-\overline{m}\|$ is large, then the error term $\mathcal{O}\Big[\max_i\{(m_i-\overline{m})^2\}\Big]$ can be large, and it can be seen that with the increase in geological uncertainty, the error in this term will be even larger. It is important to point out that the standard EnOpt in the form of Eq. 4.3 introduces even more approximations than the modified EnOpt in the form of Eq. 4.11 as it assumes that the approximations of Eqs. 4.8 and 4.10 are accurate.

4.3 StoSAG Algorithm for Robust Optimization

As can be seen from above discussion, approximations of Eqs. 4.8 and 4.9 are potentially unreliable under some circumstances, thus it would be better to find a search direction that does not depend on these assumptions. Do and Reynolds [29] proposed a modified formulation of EnOpt which requires fewer assumptions to generate a search direction than the one used in standard EnOpt. They used the current distribution mean, u_k, in place of the mean of the samples, $\overline{\hat{u}_k}$, and $J(m, u_k)$ in place of $\overline{J(m, u_k)}$. When production optimization is based on a deterministic reservoir model, they show that this modified formulation generates very similar results with the one proposed by Chen et al. [25]. However, in a robust optimization scenario where several geological reservoir models are considered, Fonseca et al. [35] observed that one can obtain a substantially higher value of life-cycle NPV with a generalization of modified EnOpt formulation than is achieved with the Chen et al. [25] version of EnOpt. This improved algorithm is referred to as the Stochastic Simplex Approximate Gradient (StoSAG) [37]. Following Fonseca et al. [37], a foundational StoSAG search direction (referred to as f-StoSAG) is defined by

$$d_{k,f,sto} = \frac{1}{N_e}\sum_{i=1}^{N_e}\Big(\frac{1}{N_p}\sum_{j=1}^{N_p}(\hat{u}_{k,j} - u_k)(J(m_i, \hat{u}_{k,j}) - J(m_i, u_k))\Big). \tag{4.22}$$

As observed by Fonseca et al. [34], using higher ratios of randomly perturbed controls to each geological realization generates a better quality gradient estimate. However, in this study, we only select $N_p = 1$, i.e., one perturbed control vector pairing with one geological realization, to obtain a StoSAG algorithm that requires the same computational effort as standard EnOpt algorithm to achieve a search direction at each iteration of the steepest ascent algorithm. The foundational StoSAG search direction with one perturbed control per geological realization is then given by

$$d_{k,f,sto} = \frac{1}{N_e}\sum_{i=1}^{N_e}(\hat{u}_{k,i} - u_k)(J(m_i, \hat{u}_{k,i}) - J(m_i, u_k)). \tag{4.23}$$

Assume that all second derivatives of J are continuous and bounded, then a first-order Taylor series approximation of $J(m_i, \hat{u}_{k,i}) - J(m_i, u_k)$ gives

$$J(m_i, \hat{u}_{k,i}) - J(m_i, u_k) = (\delta\hat{u}_{k,i})^T \nabla_u J(m_i, u_k) + \mathcal{O}\Big(\|\delta\hat{u}_{k,i}\|_2^2 \Big), \tag{4.24}$$

for $i = 1, 2, \cdots N_e$, where $\delta\hat{u}_{k,i} = \hat{u}_{k,i} - u_k$. Using the first order Taylor series of Eq. 4.24, Eq. 4.23 then can be written as

$$d_{k,f,sto} = \frac{1}{N_e} \sum_{i=1}^{N_e} \delta\hat{u}_{k,i} \Big[(\delta\hat{u}_{k,i})^T \nabla_u J(m_i, u_k) + \mathcal{O}\Big(\|\delta\hat{u}_{k,i}\|_2^2 \Big) \Big]. \tag{4.25}$$

Taking expectation of Eq. 4.25 with respect to u gives

$$\begin{aligned} E_u[d_{k,f,sto}] &= \frac{1}{N_e} \sum_{i=1}^{N_e} E_u \Big[\delta\hat{u}_{k,i} (\delta\hat{u}_{k,i})^T \Big] \nabla_u J(m_i, u_k) + e \\ &= C_U \Big(\frac{1}{N_e} \sum_{i=1}^{N_e} \nabla_u J(m_i, u_k) \Big) + e = C_U \nabla_u J_E(u_k) + \mathcal{O}\Big(\max_i \{ \|\delta\hat{u}_{k,i}\|_2^3 \} \Big). \end{aligned} \tag{4.26}$$

From Eq. 4.26, we can observe that expectation of StoSAG search direction contains only one error term, i.e., $\mathcal{O}\Big(\max_i \{ \|\delta\hat{u}_{k,i}\|_2^3 \} \Big)$, which goes to zero as the perturbation size goes to zero. Moreover, the uncertainty in the prior model for m has no influence on the quality of the StoSAG search direction, i.e., on the error term. However, the expectation of the EnOpt search direction given in Eq. 4.21 has two additional error terms, i.e., $\mathcal{O}\Big[\max_i \{ (m_i - \overline{m})^2 \} \Big]$ and $\mathcal{O}\Big[\max_i \{ (\hat{u}_{k,i} - u_k)(m_i - \overline{m}) \} \Big]$ compared to the StoSAG error term. It is easy to follow that the larger the geological uncertainty in reservoir model, the better performance of StoSAG search direction over the EnOpt search direction given in Eq. 4.11.

When the vectors $\hat{u}_{k,i}$ used in Eq. 4.23 are forced to be truncated, then

$$E_u \Big[\delta\hat{u}_{k,i} (\delta\hat{u}_{k,i})^T \Big] \neq C_U, \tag{4.27}$$

and Eq. 4.26 is no longer valid. However, one still obtain an approximation of $C_U \nabla_u J_E(u_k)$

by first using a simplex gradient [29, 34, 35] to approximate $\nabla_u J_E(u_k)$ and multiplying this simplex gradient by C_U. Using the first order Taylor series of Eq. 4.24, we can obtain

$$\delta\hat{u}_{k,i}[J(m_i,\hat{u}_{k,i}) - J(m_i,u_k)] \approx \delta\hat{u}_{k,i}(\delta\hat{u}_{k,i})^T\nabla_u J(m_i,u_k). \tag{4.28}$$

From Eq. 4.28, a stochastic simplex approximate gradient, referred to as StoSAG, then is given by

$$d_{k,i} = [\delta\hat{u}_{k,i}(\delta\hat{u}_{k,i})^T]^+\delta u_{k,i}[J(m_i,\hat{u}_{k,i}) - J(m_i,u_k)] \approx \nabla_u J(m_i,u_k), \tag{4.29}$$

where the superscript '+' on a matrix denotes the Moore-Penrose pseudo-inverse [39]. With the simplex gradient of Eq. 4.29, the search direction for maximizing the expected NPV is given by

$$d_{k,sto} = \frac{1}{N_e}\sum_{i=1}^{N_e} d_{k,i} = \frac{1}{N_e}\sum_{i=1}^{N_e}[\delta\hat{u}_{k,i}(\delta\hat{u}_{k,i})^T]^+\delta u_{k,i}[J(m_i,\hat{u}_{k,i}) - J(m_i,u_k)]. \tag{4.30}$$

It follows that

$$d_{k,sto} \approx \frac{1}{N_e}\sum_{i=1}^{N_e}\nabla_u J(m_i,u_k) = \nabla_u J_E(u_k). \tag{4.31}$$

If we perform singular value decomposition on $\delta\hat{u}_{k,i}$ and use the first order Taylor series of Eq. 4.24, Eq. 4.30 can be simplified as

$$d_{k,sto} = \frac{1}{N_e}\sum_{i=1}^{N_e}\frac{\delta\hat{u}_{k,i}}{\|\delta\hat{u}_{k,i}\|_2^2}[J(m_i,\hat{u}_{k,i}) - J(m_i,u_k)] \approx \frac{1}{N_e}\sum_{i=1}^{N_e}\frac{\delta\hat{u}_{k,i}(\delta\hat{u}_{k,i})^T}{\|\delta\hat{u}_{k,i}\|_2^2}\nabla_u J(m_i,u_k). \tag{4.32}$$

Taking a closer look at the foundational StoSAG search direction $d_{k,f,sto}$ in Eq. 4.25 and the StoSAG search direction $d_{k,sto}$ in Eq. 4.32, we can see that the difference of these two search directions is that each component of $d_{k,sto}$ in Eq. 4.32 is normalized by its corresponding $\|\delta\hat{u}_{k,i}\|_2^2$. It is important to note that $\delta\hat{u}_{k,i}$ satisfies the same distribution for $i = 1, 2, \cdots N_e$; that is, $\delta\hat{u}_{k,i} \sim \mathcal{N}(0, {C_U}^{1/2}Z^i)$, where the components of Z^i are independent, standard, random-normal deviates, i.e., $Z^i \sim \mathcal{N}(0, I_{N_u})$. When the dimension of $\delta\hat{u}_{k,i}$ goes to a suffi-

ciently large value, the following equation will hold:

$$\|\delta\hat{u}_{k,1}\|_2^2 = \|\delta\hat{u}_{k,2}\|_2^2 = \cdots = \|\delta\hat{u}_{k,i}\|_2^2 = \cdots = \|\delta\hat{u}_{k,N_e}\|_2^2, \tag{4.33}$$

which indicates that when applying the StoSAG search direction in Eq. 4.32 to the steepest ascent algorithm in Eq. 2.5, where the final search direction is normalized by its infinite norm, one can achieve a similar result to the one obtained with foundational StoSAG. The results obtained from the provided example also confirms this conjecture; see Fig. 4.12.

When using a stochastic gradient for steepest ascent algorithm, the gradient may be quite rough and additional smoothing is typically enforced by multiplying the search direction by C_u [29, 93, 35]. After multiply the foundational StoSAG search direction (Eq. 4.23) and the StoSAG search direction (Eq. 4.30) by C_u, respectively, the following two search directions can be obtained:

$$d_{k,sf,sto} = C_u d_{k,f,sto}, \tag{4.34}$$

and

$$d_{k,ss,sto} = C_u d_{k,sto}, \tag{4.35}$$

where $d_{k,sf,sto}$ and $d_{k,ss,sto}$, respectively, denote the smoothed foundational search direction (referred to as sf-StoSAG) and singly smoothed StoSAG (referred to as ss-StoSAG).

4.4 Numerical Examples

The first example that we consider in this chapter is to estimate simultaneously the well controls (pressures and/or flow rates) and downhole inflow control valve (ICV) settings in a three-phase (oil-gas-water) reservoir to maximize the expectation of an economic objective function in a CO_2 WAG EOR process. The objective function for a specific reservoir model, m_i, is defined by

$$J_i(m_i, u) = \sum_{n=1}^{N_t} \left\{ \frac{\Delta t_n}{(1+b)^{\frac{t_n}{365}}} \left[\sum_{j=1}^{N_P} \left(r_o \cdot \overline{q_{o,j}^n} - c_w \cdot \overline{q_{w,j}^n} \right) - \sum_{k=1}^{N_I} \left(c_{wi} \cdot \overline{q_{wi,k}^n} + c_{gi} \cdot \overline{q_{gi,k}^n} \right) \right] \right\}, \tag{4.36}$$

for $i = 1, 2, \cdots N_e$. All the notations in the above equation are the same as in Eq. 2.1.

The second example considered in this Chapter pertains to estimating the well controls and ICV settings in a two-phase (oil-water) reservoir to maximize the expectation of the NPV in a waterflood production scenario and in this case, the term for gas injection cost is deleted from the objective function of Eq. 4.36.

In this work, five types of search directions are used to estimate the optimal well controls and ICV settings which maximize the $J_E(u)$. The five types of search directions are:

1. standard implementation of EnOpt, $d_{k,s,\text{EnOpt}}$, defined in Eq. 4.6;
2. the foundational search direction $d_{k,f,sto}$ defined in Eq. 4.23 (referred to as f-StoSAG);
3. the smoothed foundational search direction $d_{k,sf,sto}$ defined in Eq. 4.34 (referred to as sf-StoSAG);
4. unsmoothed StoSAG, $d_{k,sto}$, defined in Eq. 4.30 (referred to as StoSAG);
5. singly smoothed StoSAG, $d_{k,ss,sto}$ defined in Eq. 4.35, (also referred to as ss-StoSAG).

4.4.1 Example 1: 3D Fluvial Reservoir

We consider the optimization of WAG flooding for a 3D synthetic reservoir where the injected gas is carbon dioxide, CO_2. The reservoir simulation model is on a $25 \times 25 \times 3$ grid with grid block dimensions given by $\Delta x = \Delta y = 100$ ft and $\Delta z = 30$ ft. For robust optimization, we generate 15 geological realizations (models) to represent the uncertainty in the reservoir description. Fig. 4.1 shows six realizations of the log-permeability distribution for the first layer. The second and third layers have the same heterogeneity features as the first layer but with the permeability field of layer 2 equal to the permeability field of layer 1 multiplied by 0.6; the permeability field of layer 3 is equal to the permeability field of layer 1 multiplied by 0.3. The reservoir contains 4 injection wells and 9 producers. All wells are vertical fully penetrating wells (i.e. being open to flow over the entire reservoir height) and their locations are shown in the realizations of the permeability fields that are displayed in

Fig. 4.1. Each of the wells is equipped with an ICV in each of the three layers. The porosity is homogeneous with $\phi = 0.2$. No capillary pressures are included and the reservoir rock is assumed to be incompressible. The initial reservoir pressure is 4,500 psi at the top of the reservoir. The producing reservoir lifetime is set equal to 2,880 days. A compositional reservoir simulator, GEM (Version 2009.10) [27] is used for reservoir simulation.

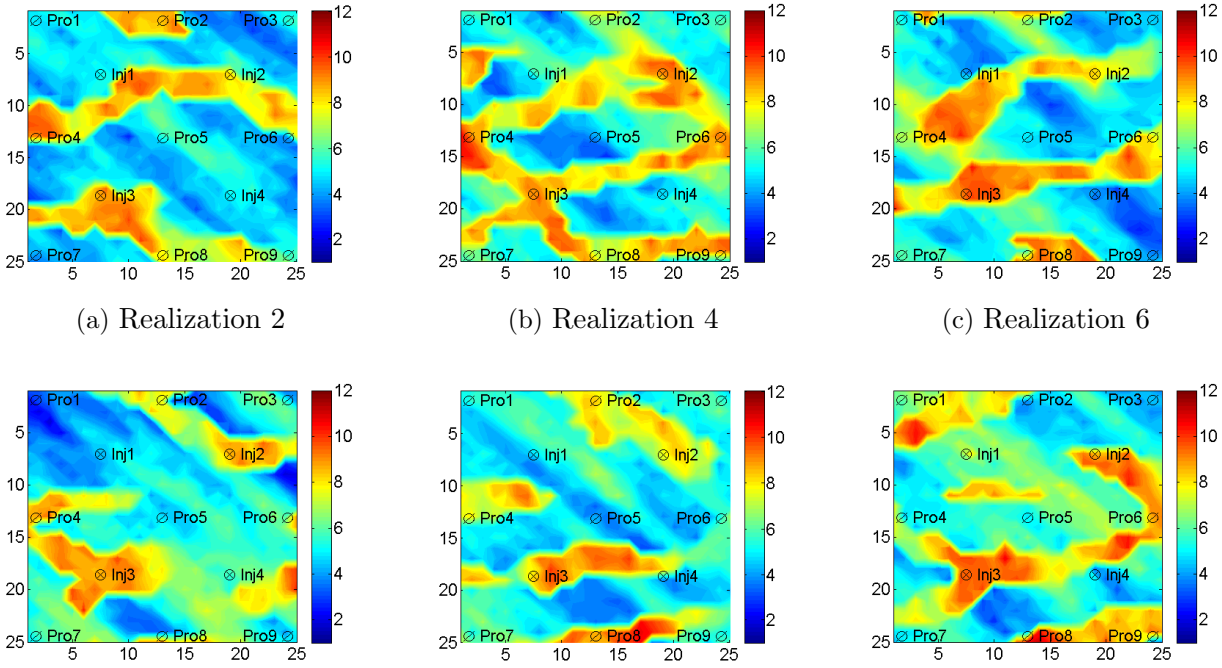

(a) Realization 2 (b) Realization 4 (c) Realization 6

(d) Realization 8 (e) Realization 10 (f) Realization 12

Figure 4.1: Log-permeability distribution of six realizations for the first layer.

Because of the density difference between water, oil and CO_2, phase segregation will occur resulting in "over ride" and "under ride" of the injected CO_2 and water respectively, resulting in early "break through" of these undesirable fluids in the production wells. The ICVs can partly counteract these "gravity segregation" effects, and the physical mechanisms that drive the optimization are therefore both the heterogeneity in the permeability and density difference between the reservoir fluids. To optimize $J_E(u)$, the oil price is set equal to \$80.0/STB; the water injection cost is \$5.0/STB; the gas injection cost is \$1.5/Mscf; the disposal cost of produced water is \$5.0/STB; the annual discount rate is 0.1. Here, we neglect the revenue of hydrocarbon gas production and the cost of disposing of injected CO_2 gas that

is produced. Within the producing lifetime we can change each well control and ICV setting 16 times in control intervals of $2880/16 = 180$ days. We let u^o denote the n_0-dimensional column vector ($n_o = (9+4) \times 16 = 208$) of all well controls (rates or pressures) and u^v denote the n_v-dimensional column vector of ICV settings ($n_v = (9+4) \times 3 \times 16 = 624$) so that the vector of all control settings is

$$u = \begin{bmatrix} u^o \\ u^v \end{bmatrix}. \tag{4.37}$$

In the EnOpt and StoSAG algorithms, we generate perturbations from a covariance matrix. This covariance matrix is block diagonal and has the form

$$C_u = \begin{bmatrix} C_u^o & O \\ O & I \end{bmatrix}, \tag{4.38}$$

where the O's denote null matrices and I is the $n_v \times n_v$ identity matrix. The matrix C_u^o is a block diagonal matrix where each kth submatrix in the diagonal block is denoted by $C_{u_k^o}$ and is associated with the subvector, u_k^o of u^0 that contains all the well controls for well k. Here, to impose some temporal smoothness on the the well controls (rates or pressures) for well k, $C_{u_k^o}$ is generated from a spherical covariance function [53] with variance equal to $(0.1)^2$ and time correlation length equal to 720 days which is equivalent to four control steps. However, gas injection rates are not correlated with water injection rates and so effectively, when sampling from $\mathcal{N}(u_k, C_u)$, only two consecutive water rates are correlated and only two consecutive gas rates are correlated. The appearance of the identity matrix in Eq. 4.38 indicates that there is no correlation between ICV settings. As discussed in the section 2.1 of Chapter 2, we apply a logarithm transformation [40] to each element of the control vector.

We use a steepest ascent optimization algorithm with a simple backtracking line search. At iteration k of the steepest ascent, we generate $N_e = 15$ samples of the Gaussian random control vector u with each sample corresponding to one geological model, where $\hat{u}_{k,i} \sim \mathcal{N}(u_k, C_u)$. In steepest ascent, the initial step size is 1.0, and the maximum number

of step-size cuts (each with a factor 0.5) is set equal to 5. If five steps sizes do not yield an increase in J_E, we set the new estimate, u_{k+1} of the optimal u equal to the u that gave the largest value of J_E obtained during the line search. We allow a maximum of 4,000 total reservoir simulation runs. For this relatively small example, about 3.5 minutes per simulation run is required so that the entire optimization procedure could be performed sequentially. For more realistic, large-scale reservoir simulations, which may have run times in the order of several hours, parallel processing will be a practical necessity. Fortunately the StoSAG algorithm, just like the EnOpt algorithm, is embarrassingly parallel.

Fig. 4.2 shows the expectation of NPV (Eq. 4.1) versus the number of reservoir simulation runs using the five different search directions. It is clear that standard EnOpt generates the lowest expected NPV while the unsmoothed StoSAG search direction proposed by Fonseca et al. [34, 35] and sf-StoSAG generate the highest average NPV. Note that although both sf-StoSAG and standard EnOpt impose the same degree of smoothing, sf-StoSAG results in a much higher NPV than is obtained with standard EnOpt.

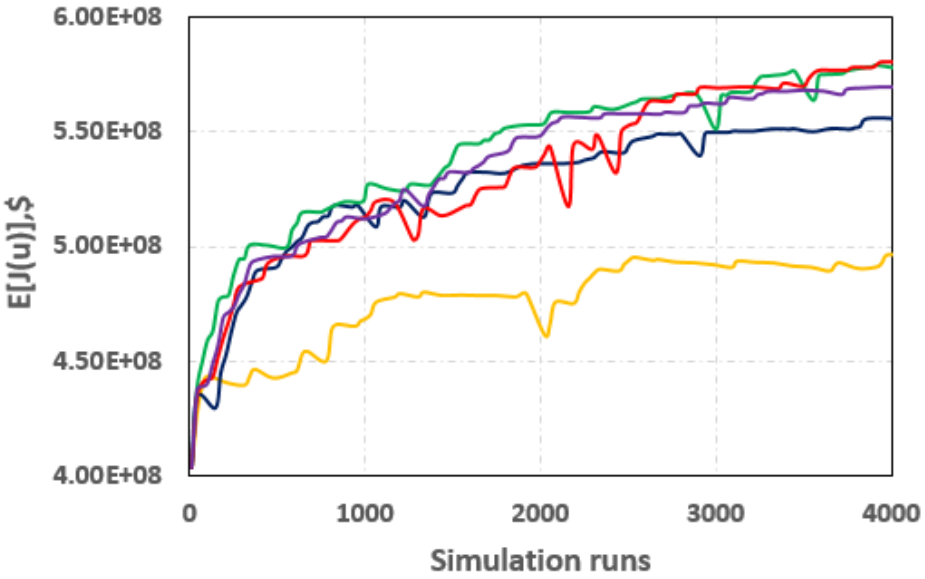

Figure 4.2: Expectation of NPV versus number of simulation runs for different search direction formulations; yellow: standard EnOpt; purple: f-StoSAG; red: sf-StoSAG; green: StoSAG; dark blue: ss-StoSAG.

It is curious to note that unsmoothed StoSAG which uses a stochastic approximation to the gradient as the search direction and sf-StoSAG which utilizes an approximation of C_u^2

times the gradient as the search direction yield very similar final values of NPV. However, as expected the well controls and ICV settings obtained with smoothed foundational StoSAG are much smoother than those obtained with unsmoothed StoSAG; see Figs. 4.3-4.8. In these figures, the vertical axes refer to the well number (recall that there are 9 producers and 4 injectors), while the horizontal axis in Figs. 4.3 and 4.6 refer to the control interval (16 in total). In Figs. 4.4, 4.5, 4.7 and 4.8 the horizontal axis has a related but slightly different interpretation: Although there are 16 control intervals, at injection wells the well controls are gas injection rates at odd numbered control steps and water injection rates at even numbered time steps, so only 8 control steps (referred to as "WAG cycles") are shown in Figs. 4.4, 4.5 and 4.7. The color scale in Fig. 4.3 corresponds to the pressures (at the top of the reservoir) in the production wells, while the color scales in Fig. 4.4 refer to the gas rates in the injection wells. In Figs. 4.6, 4.7 and 4.8, ICV j refers to the ICV setting of layer j which $j = 1$ is the top layer with the highest permeability distribution; see the discussion of the permeability fields of Fig. 4.1.

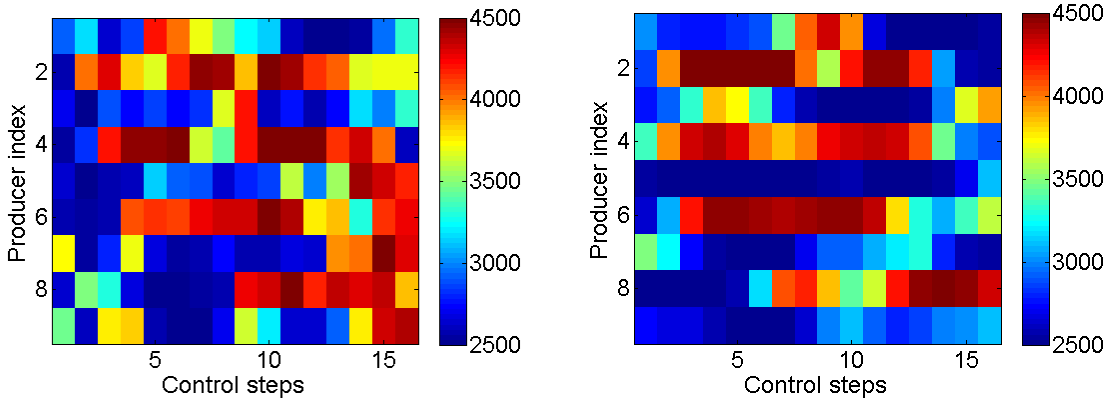

(a) Unsmoothed StoSAG (b) sf-StoSAG

Figure 4.3: Estimated well controls for producers at different control steps calculated from unsmoothed StoSAG and sf-StoSAG; units are psi.

In order to quantify the smoothness of the controls at an individual well, the total variation of the function representing well controls is calculated on a well-by-well basis. As the control function at a well is a piecewise constant function, its total variation is given by the sum of the absolute values of the differences between two consecutive well controls. The

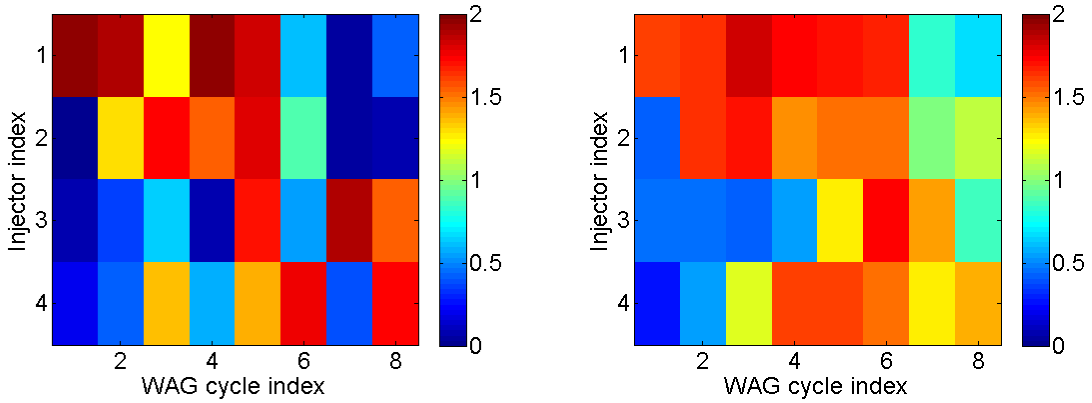

(a) Unsmoothed StoSAG (b) sf-StoSAG

Figure 4.4: Estimated well controls for gas injectors at different WAG cycles calculated from unsmoothed StoSAG and sf-StoSAG; units are $\times 10^7$ scf/day.

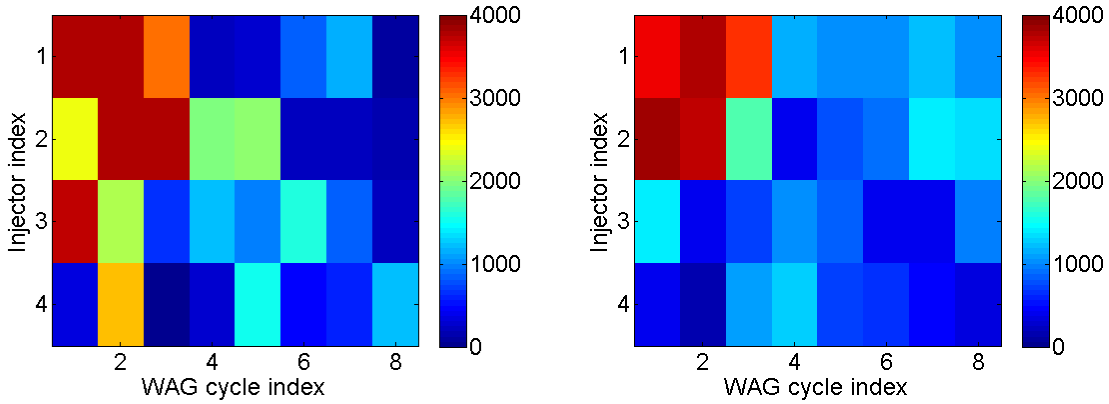

(a) Unsmoothed StoSAG (b) sf-StoSAG

Figure 4.5: Estimated well controls for water injectors at different WAG cycles calculated from unsmoothed StoSAG and sf-StoSAG; units are STB/day.

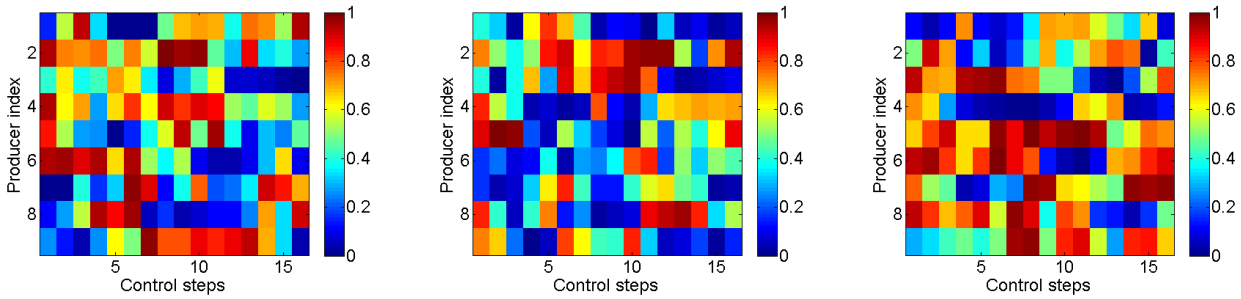

(a) Unsmoothed StoSAG, ICV 1 (b) Unsmoothed StoSAG, ICV 2 (c) Unsmoothed StoSAG, ICV 3

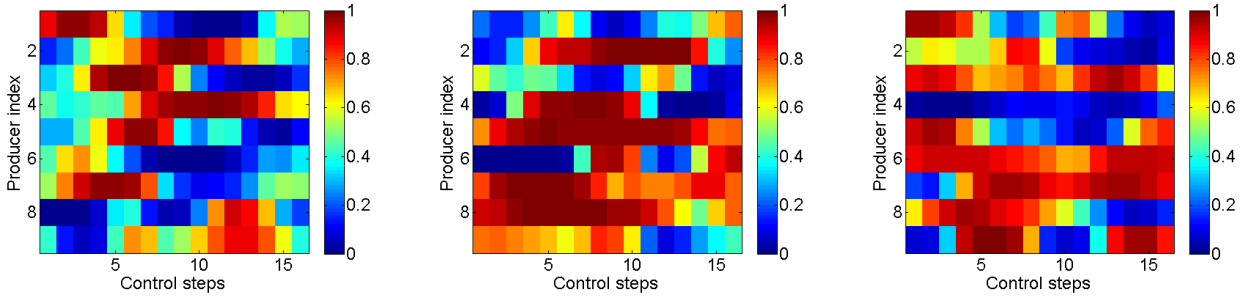

(d) sf-StoSAG, ICV 1 (e) sf-StoSAG, ICV 2 (f) sf-StoSAG, ICV 3

Figure 4.6: Estimated ICV settings for producers at different control steps calculated from unsmoothed StoSAG and sf-StoSAG on a scale from closed (0) to fully open (1).

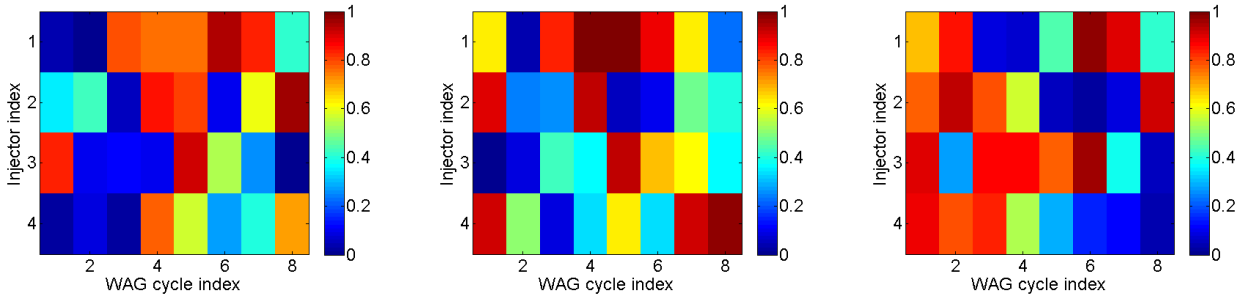

(a) Unsmoothed StoSAG, ICV 1 (b) Unsmoothed StoSAG, ICV 2 (c) Unsmoothed StoSAG, ICV 3

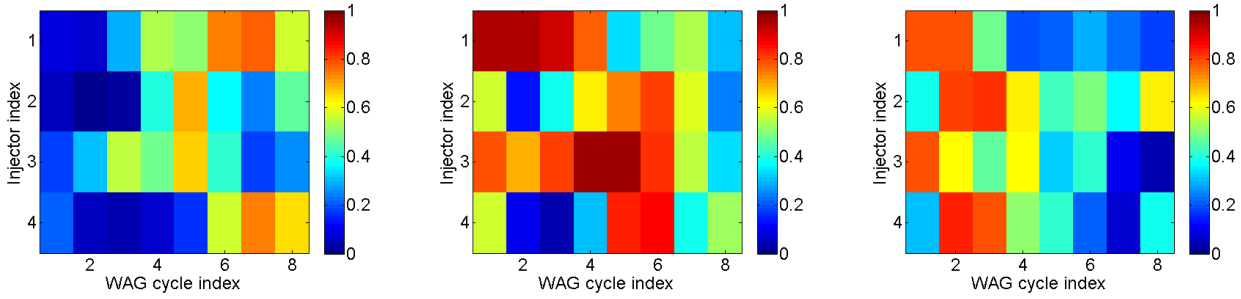

(d) sf-StoSAG, ICV 1 (e) sf-StoSAG, ICV 2 (f) sf-StoSAG, ICV 3

Figure 4.7: Estimated ICV settings for gas injectors at different WAG cycles calculated from unsmoothed StoSAG and sf-StoSAG on a scale from closed (0) to fully open (1).

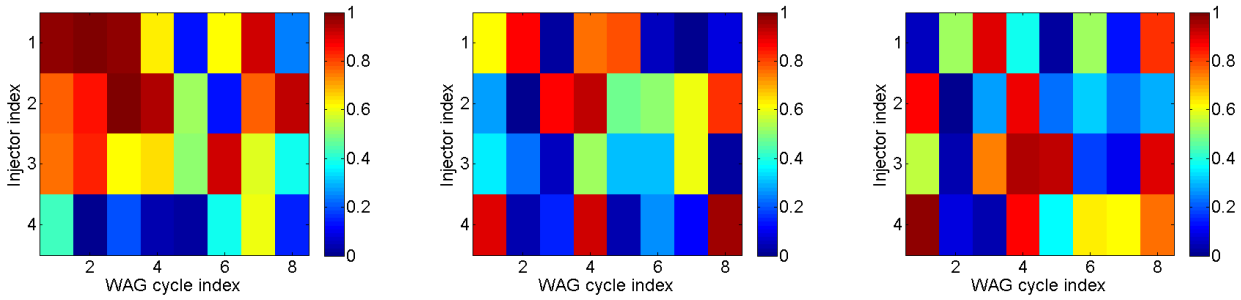

(a) Unsmoothed StoSAG, ICV 1 (b) Unsmoothed StoSAG, ICV 2 (c) Unsmoothed StoSAG, ICV 3

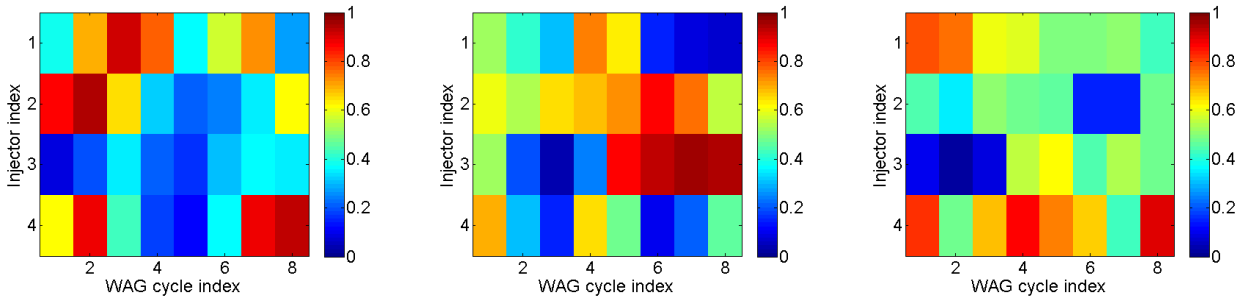

(d) sf-StoSAG, ICV 1 (e) sf-StoSAG, ICV 2 (f) sf-StoSAG, ICV 3

Figure 4.8: Estimated ICV settings for water injectors at different WAG cycles calculated from unsmoothed StoSAG and sf-StoSAG on a scale from closed (0) to fully open (1).

total variation of the function representing each well's ICV settings can be calculated on a well-by-well basis in a similar manner. As illustrated in Tables 4.1-4.6, the total variations of a well's optimized controls and ICV settings are lower when the optimized values are computed from sf-StoSAG than when the optimized values are estimated from unsmoothed StoSAG. Note the average total variation is also given in Tables 4.1-4.6. Overall, the average total variation of each sf-StoSAG result is roughly one-half of the corresponding average total variation for the unsmoothed StoSAG result. On average, each total variation computed from EnOpt results that are not shown is within 10% of the corresponding total variation obtained from sf-StoSAG. Although smoother controls and ICV settings are simpler to implement operationally, as noted earlier, too much smoothing can lead to suboptimal results.

Table 4.1: Total variation of the estimated well controls for different producers and average total variation across all the producers; unsmoothed StoSAG and sf-StoSAG.

Prod. index	StoSAG ($\times 10^3$ psi)	sf-StoSAG ($\times 10^3$ psi)
1	4.82	3.66
2	5.19	5.35
3	5.46	3.87
4	6.33	3.49
5	4.57	0.78
6	4.31	3.90
7	5.99	2.50
8	4.89	3.62
9	7.27	1.50
Average	5.42	3.19

Table 4.2: Total variation of the estimated well controls for gas injectors and average total variation across all the gas injectors; unsmoothed StoSAG and sf-StoSAG.

Inj. index	StoSAG ($\times 10^7$ scf/day)	sf-StoSAG ($\times 10^7$ scf/day)
1	3.73	1.39
2	3.92	2.30
3	5.64	2.17
4	5.89	1.81
Average	4.79	1.92

Table 4.3: Total variation of the estimated well controls for water injectors and average total variation across all the water injectors; unsmoothed StoSAG and sf-StoSAG.

Inj. index	StoSAG ($\times 10^3$ stb/day)	sf-StoSAG ($\times 10^3$ stb/day)
1	5.55	3.45
2	5.26	4.61
3	5.86	2.77
4	8.33	2.30
Average	6.25	3.28

Table 4.4: Total variation of the estimated ICV settings for producers; unsmoothed StoSAG and sf-StoSAG.

Prod. index	StoSAG ICV 1	sf-StoSAG ICV 1	StoSAG ICV 2	sf-StoSAG ICV 2	StoSAG ICV 3	sf-StoSAG ICV 3
1	3.77	1.64	2.86	1.90	3.37	2.11
2	3.43	1.54	3.15	1.62	4.23	1.43
3	2.51	1.78	3.63	1.95	2.24	1.15
4	2.96	1.07	3.10	2.04	2.34	0.46
5	4.03	2.07	3.87	0.50	1.98	1.83
6	3.16	1.40	3.18	2.67	2.57	0.52
7	4.47	1.76	2.79	0.88	2.80	1.22
8	3.83	2.38	4.23	0.89	3.42	1.32
9	2.73	2.23	3.53	1.54	3.15	2.84
Average	3.43	1.76	3.37	1.55	2.90	1.43

Table 4.5: Total variation of the estimated ICV settings for gas injectors; unsmoothed StoSAG and sf-StoSAG.

Inj. index	StoSAG ICV 1	sf-StoSAG ICV 1	StoSAG ICV 2	sf-StoSAG ICV 2	StoSAG ICV 3	sf-StoSAG ICV 3
1	1.54	1.00	2.34	1.06	2.40	0.79
2	2.84	1.39	2.69	1.67	1.96	1.28
3	2.50	1.18	1.58	0.99	2.40	1.26
4	1.80	0.97	2.30	1.98	0.94	1.60
Average	2.17	1.14	2.23	1.43	1.92	1.23

Table 4.6: Total variation of the estimated ICV settings for water injectors; unsmoothed StoSAG and sf-StoSAG.

Inj. index	StoSAG ICV 1	sf-StoSAG ICV 1	StoSAG ICV 2	sf-StoSAG ICV 2	StoSAG ICV 3	sf-StoSAG ICV 3
1	2.32	1.81	2.72	1.32	3.10	0.50
2	1.86	1.14	2.00	0.72	2.50	1.05
3	1.41	0.59	1.87	1.43	2.83	1.12
4	1.81	1.72	3.82	1.95	2.47	1.73
Average	1.85	1.32	2.60	1.36	2.73	1.10

4.4.2 Example 2: Burgge Test Case

Brugge field was developed by TNO as a benchmark case to test different methods for closed-loop reservoir management. The top structure of the Brugge filed with well locations is shown in Fig. 4.9. There are 30 vertical wells (20 production wells and 10 injection wells), and each well is equipped with ICVs to control flow into three different well segments. The original model of Brugge field consists of 20 million gridblocks and then was upscaled to a 450,000 gridblock model which was used as true reservoir to provide production data for history matching. Using the information from well logs and facies maps, 104 geological realizations were generated by TNO. These realizations upscaled to a 60,000 gridcell model were created on the same scale as the true reservoir and provided to participants.

Three different type of geostatistical modeling methods were applied to generate the 104 realizations of the property fields (permeability, porosity, net-to-gross and connate water saturation). The three geostatistical modeling techniques that we used are sequential Gaussian cosimulation, object-based modeling and sequential indicator simulation. Here, seven different realizations are randomly chosen from each of the three geological modeling methods to obtain 21 reservoir realizations which we use to characterize the reservoir uncertainty. Fig. 4.10 shows the log-permeability in the x-direction for all nine layers of three typical realizations. Realization 1 is generated from sequential Gaussian simulation; Realization 32 is created from channel object-based modeling; Realization 70 is obtained from a sequential indicator simulation. The Brugge reservoir consists of four geological formations and nine

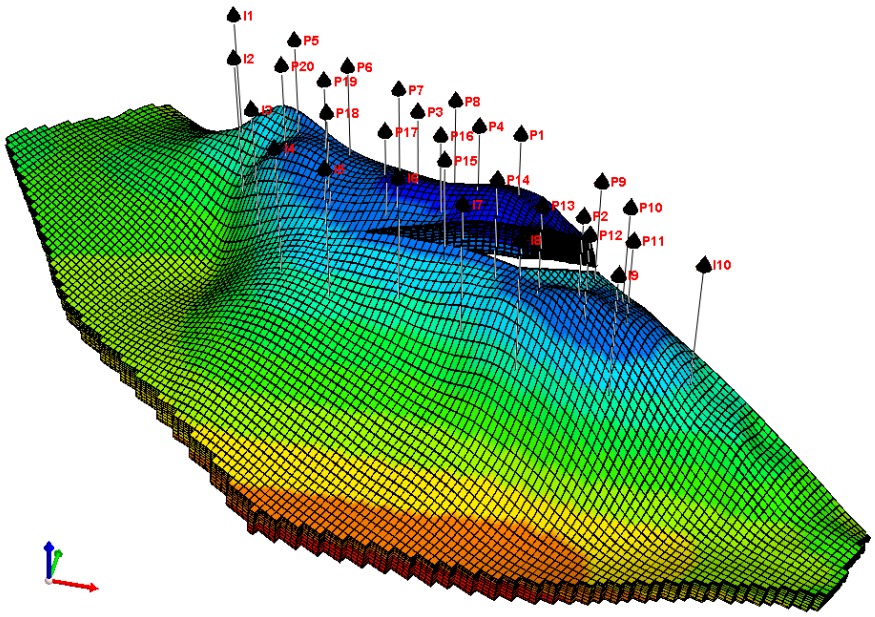

Figure 4.9: The top structure of Brugge.

reservoir simulation layers, each with a 139×48 grid. As can be seen from Fig. 4.11, the Schelde formation corresponds to the top two layers; the Maas formation corresponds to the layers 3, 4 and 5; the Waal formation corresponds to layers 6, 7 and 8; and the Schie formation corresponds to layer 9. Three inflow control valves are assigned to the first three well segments of each well (both injection wells and production wells), where one well segment corresponds to one geological formation (geological layer). A more detailed description of the Brugge reservoir model can be found in Peters et al. [74].

In previous studies on Brugge field, most of the authors [74, 24, 21] considered a 30 year production lifetime. They assimilated the observed production and interpreted seismic data during the first 10 years, and then optimized the NPV for years 10-30 by adjusting the well control variables. In this study, we do not consider the first 10 year data assimilation process. Instead, we estimate the optimal well controls for the first fifteen years of the reservoir life using robust optimization. The ICVs are assigned to the corresponding well segments at the beginning to control the flow in different formations. We equate the adjustment of the productivity index (PI) multiplier of each segment of a well, to adjust injection and production in each formation. Note that there is exactly one PI multiplier used

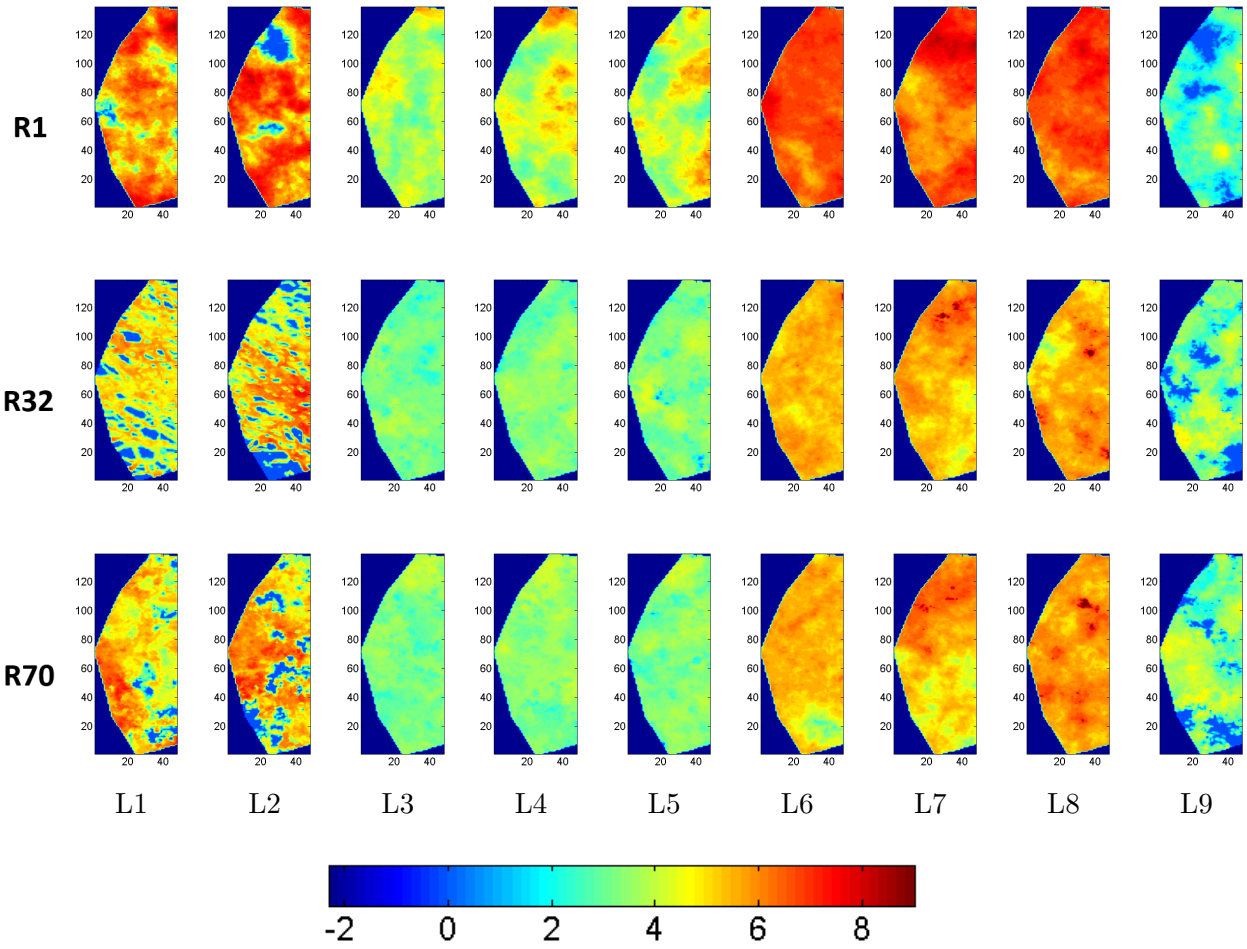

Figure 4.10: The log-permeability in the x direction for all nine layers of three typical realizations: R1, sequential Gaussian simulation; R32, channel objects; R70, sequential indicator simulation.

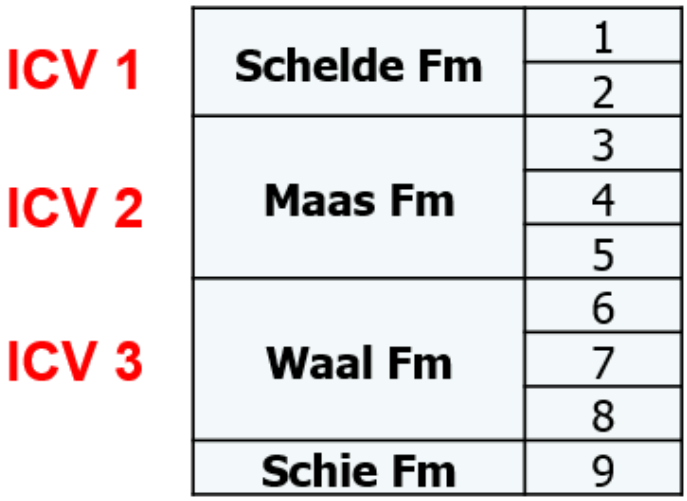

Figure 4.11: Four different formations with its corresponding reservoir simulation model layers and assigned ICV settings.

for each of the top three geological layers (Fig. 4.11). The optimization problem we consider in this work is to estimate simultaneously the well controls (injection rates for injectors and BHP for producers) and downhole ICV settings which maximize the expectation of NPV at the end of 15 years.

It is important to note that we use only one well control (rate or BHP) and three ICV settings per well, whereas others [24, 21] replaced each actual well by three wells with one of these three pseudo wells completed in each of the top three geological layers. By using three pseudo wells per actual well, they could control the rate at each pseudo well thus roughly mimicking the effect of ICV settings. This process can yield unreliable results as the BHP's as a function of time can vary radically from pseudo well to pseudo well which is not representative of the behavior of the one actual well. As we use PI multipliers to represent ICV settings, we have no need to replace one actual well by three pseudo wells. Moreover, with our approach, we can use BHP control at each well with the ICV setting of each well in each zone represented by a PI multiplier. In fact, in our example, for each injection well, the control variables contain injection rate and three ICV settings at each control step; for each production well, the control variables contain BHP plus three ICV settings at each control step. As discussed in the section 2.1 of Chapter 2, we apply a logarithm transformation [40]

to each element of the control vector.

Table 4.7 shows the initial guesses, lower and upper bounds for the three types of control variables. The well control variables at each injector are the injection rates with an upper bound of 4,000 STB/D and a lower bound of 0 STB/D; each producer operates under BHP control with an upper bound of 2,465 psi and a lower bound of 725 psi; each ICV setting for both producers and injectors has an upper bound of 1 and a lower bound of 0. Taking initial guess 2 as an example, the initial guess for the rate controls of each water injector is set equal to 3,000 STB/D; the initial guess for BHP controls for each producer is equal to 1,140 psi and the initial guess for all ICV settings are equal to 0.75. The intial reservoir pressure is 2,465 psi. Note the ICV setting j is for formation j where formation 1 is the Schelde formation.

Table 4.7: The initial guesses, lower and upper bounds for the three types of design variables.

Terms	Units	Initial guess 1	Initial guess 2	Initial guess 3	Lower bound	Upper bound
Rate-Inj	STB/D	2000	3000	3775	0	4000
Pressure-Prod	psi	1595	1140	850	725	2465
ICVs	\	0.5	0.75	0.9	0	1

It is assumed that only oil and water flow in the reservoir throughout the reservoir production life. To optimize the expectation of NPV, the oil price is set equal to \$80.0/STB; the water injection cost is \$5.0/STB; the cost of disposing produced water is \$5.0/STB; the annual discount rate is 10%. For the implementation of standard EnOpt and StoSAG methods, we use a one-to-one combination of random control perturbations and random geological models with the size of ensemble equal to 21 as discussed previously. The perturbation size is set equal to 0.1; the maximum number of step-size cuts is set equal to 5; the initial step size is 1.0; the time correlation length is 1,825 days which is one third of the reservoir life; the maximum number of allowable simulation runs is 3,000. Each well contains 30 control steps, with the length of each control step equal to 182.5 days (half a year). The CMG's IMEX [28] is used to perform the reservoir simulation.

Five types of search directions (e.g., standard EnOpt, f-StoSAG, sf-StoSAG, StoSAG and ss-StoSAG) for the steepest ascent optimization algorithm are applied to estimate the optimal well controls and ICV settings which maximize the $E[J(m,u)]$. Table 4.8 shows the optimized expectation of NPV obtained by using five different types of search direction in the steepest ascent algorithm. From Table 4.8, we can see that the optimized average NPVs generated from each of the five search directions is much higher than the initial average NPVs, especially for the four StoSAG search directions. The StoSAG algorithm results in 40%-70% higher expected NPV than is obtained with standard EnOpt.

Table 4.8: Optimized expectation of NPV obtained by five different types of search directions; in units of billion $.

Terms	Initial guess 1	Initial guess 2	Initial guess 3
Initial E[J]	3.118	4.262	4.875
Optimized E[J], EnOpt	4.969	5.838	5.771
Optimized E[J], f-StoSAG	8.394	8.393	8.273
Optimized E[J], sf-StoSAG	8.470	8.518	8.309
Optimized E[J], StoSAG	8.430	8.367	8.356
Optimized E[J], ss-StoSAG	8.384	8.523	8.346

Fig. 4.12 shows the expectation of NPV versus the number of reservoir simulation runs using the five different search directions in the steepest ascent method with three different initial guesses with the same initial starting random seeds. From Fig. 4.12, it is clear that standard EnOpt generates the lowest expected NPV while each of the other four StoSAG search directions generate a much higher average NPV. Taking a closer look at the four NPV curves calculated from the various StoSAG algorithms in all three figures (Figs. 4.12a, b and c), we can observe that the red curve almost overlaps with the green curve and the purple curve nearly overlaps with the yellow curve, which confirms that if we start from a same initial random seed to generate the same initial ensembles, one can achieve a fairly close results by using f-StoSAG and StoSAG or using sf-StoSAG and ss-StoSAG; see the theoretical analysis in the section of "StoSAG Algorithm for Robust Optimization".

Figs. 4.13 and 4.14, respectively, show the estimated well controls for production and

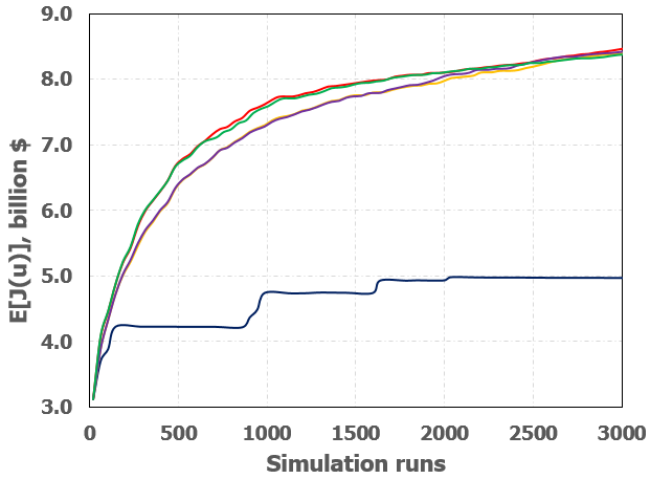

(a) Initial guess 1

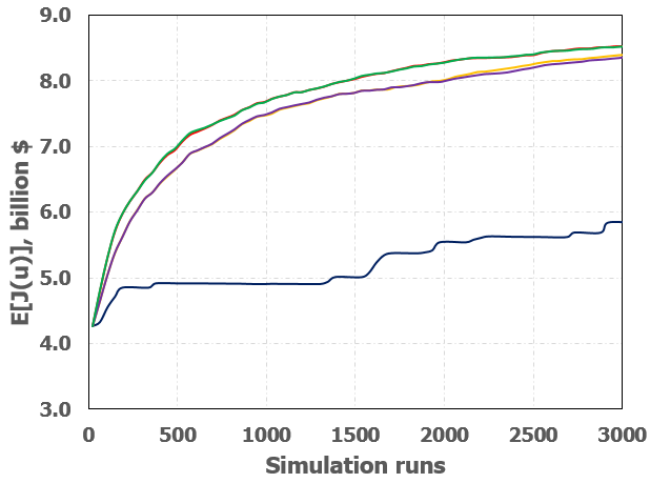

(b) Initial guess 2

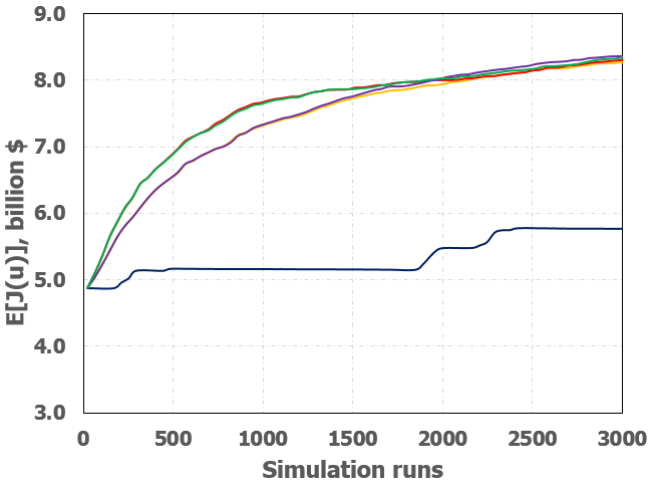

(c) Initial guess 3

Figure 4.12: Expectation of NPV versus number of simulation runs for different search direction formulations; dark blue: standard EnOpt; yellow: f-StoSAG; red: sf-StoSAG; purple: StoSAG; green: ss-StoSAG.

injection wells at different control steps obtained from the different algorithms. In these figures, the horizontal axes "Control steps" refer to the control interval (30 in total), while the vertical axes "Producer index" or "Injector index" represent the well number (recall that there are 20 producers and 10 injectors). The color scales in Fig. 4.13 refers to the pressures (psi) in the production wells, while the color scales in Fig. 4.14 correspond to the water injection rate (stb/day). As expected the well controls obtained with the smoothed standard EnOpt, sf-StoSAG and ss-StoSAG are much smoother than those obtained with f-StoSAG and StoSAG. It can be seen that the well controls calculated from sf-StoSAG and ss-StoSAG are very similar; see Figs. 4.13c and 4.13e as well as 4.14c and 4.14e, whereas the well controls obtained from standard EnOpt are obviously different from those calculated from sf-StoSAG or ss-StoSAG. For the estimated production-well controls achieved from sf-StoSAG or ss-StoSAG, it is clear that producers "P1", "P4", "P6", "P7" and "P8" operate at close to minimum allowable BHP, and this is because these production wells are far from the injection wells; whereas producers "P12", "P14", "P15", and "P20" are close to the corresponding water injection wells, so they are shut in during most of the production life; producers "P9" and"P10" operate at close to maximum allowable BHP at the early times, and then they switch to a minimum allowable BHP control. For the remaining production wells, e.g., "P17" and "P18", they operate at close to minimum allowable BHP at early times, and then they are either shut in or operate with a very small production rate (high pressure) after the injected water break through. From the estimated injection-well controls calculated from sf-StoSAG or ss-StoSAG, it can be seen that the all the injectors operate at close to maximum allowable injection rate during the reservoir production life except for injectors "I1", "I7" and "I10" at last few control steps. However, the well controls calculated from standard EnOpt search direction formulation are completely different from those obtained from StoSAG search direction formulations.

Figs. 4.15 and 4.16, respectively, show the estimated ICV settings of all the production wells and injection wells for the three top geological formation calculated from using the different search direction formulations in the steepest ascent algorithm. In these figures, ICV j

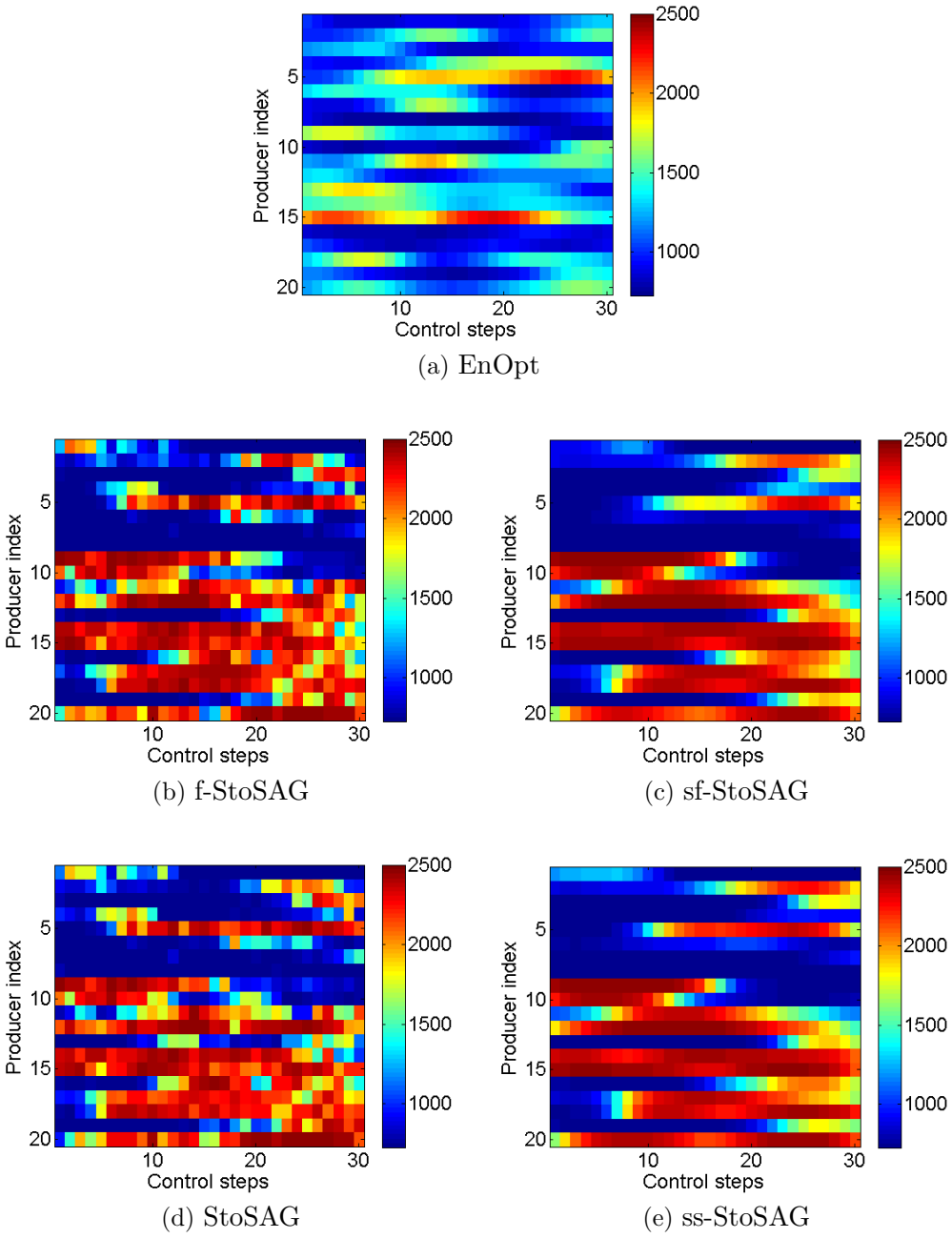

(a) EnOpt

(b) f-StoSAG

(c) sf-StoSAG

(d) StoSAG

(e) ss-StoSAG

Figure 4.13: Estimated well controls for producers at different control steps calculated from different search direction formulations; units are psi; initial guess 2.

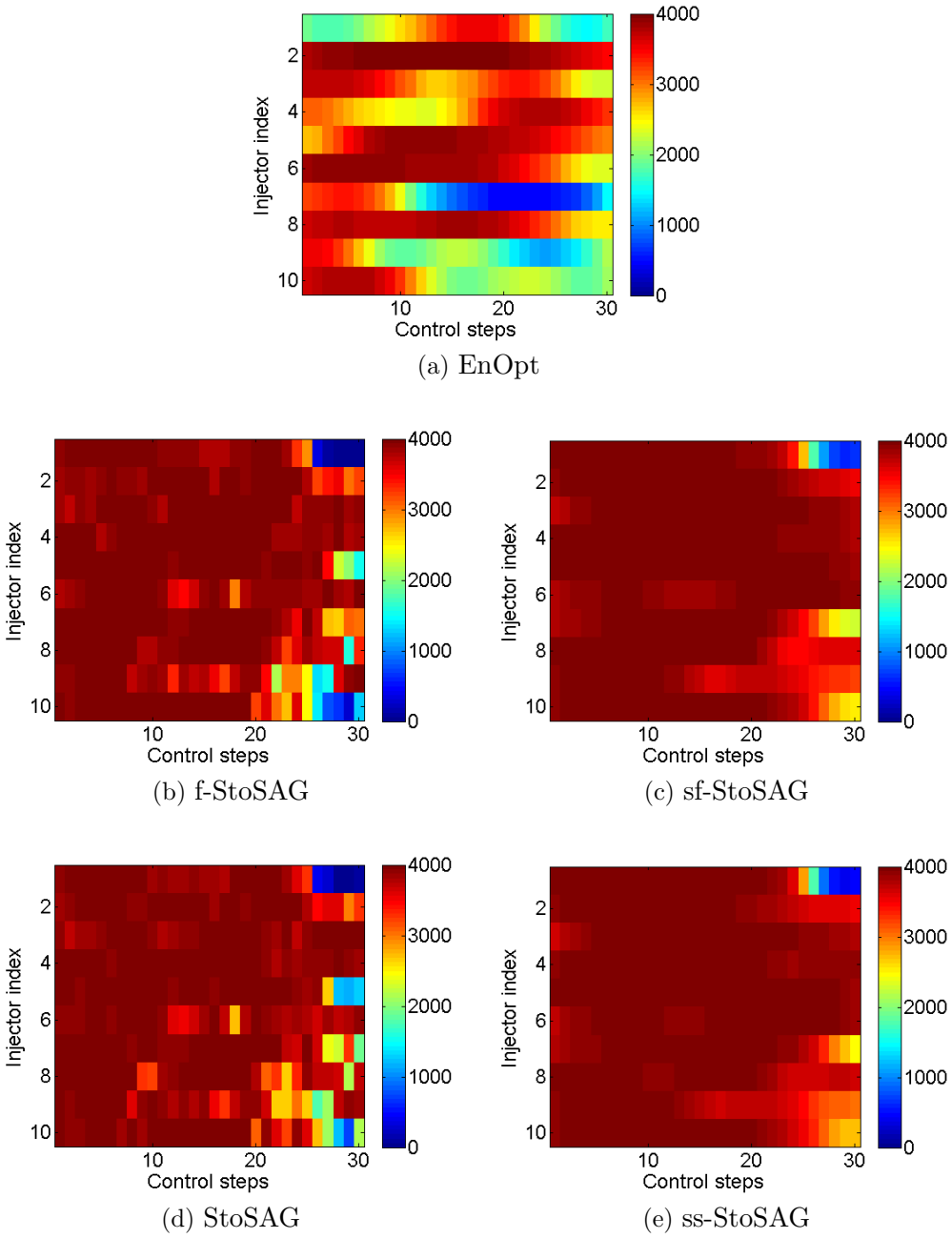

(a) EnOpt

(b) f-StoSAG

(c) sf-StoSAG

(d) StoSAG

(e) ss-StoSAG

Figure 4.14: Estimated well controls for injectors at different control steps calculated from different search direction formulations; units are STB/day; initial guess 2.

corresponds to the ICV setting of formation j where $j = 1$ is the top formation (i.e., Schelde), and a color-scale value equal to 1 refers to a fully open ICV and a color-scale value equal to 0 refers to a closed ICV. As shown in Figs. 4.15 and 4.16, the sf-StoSAG and ss-StoSAG search direction formulations give very similar estimated ICV settings, which are totally different from those calculated from the standard EnOpt search direction. The estimated ICV settings obtained from f-StoSAG and StoSAG are quite rough (unsmooth) compared to those obtained from the other three types of search directions. From Figs. 4.15(g), 4.15(h) and 4.15(i), we observe that in formation "Waal" , which is controlled by the ICVs of segment 3, far more ICV settings are zero or very close to zero than is the case for segments 1 and 2, respectively. This is probably due to the fact that "Waal" is the highest permeability formation. With more ICV settings close to zero, one can delay water breakthrough from the highest permeability formation "Waal".

Fig. 4.17 shows the initial oil saturation distribution, and the remaining oil saturation distribution of layer 6 at years 7.5 and 15 calculated from standard EnOpt, sf-StoSAG and ss-StoSAG. It is clear that more oil can be produced from layer 6 by sf-StoSAG and ss-StoSAG search directions than the one obtained by standard EnOpt. sf-StoSAG and ss-StoSAG achieve almost the same oil saturation distribution at the end of production life. From Fig. 4.17(e) or 4.17(g), we can observe that the oil is swept from southwest to northeast. Moreover, the fact that a large amount of oil remains in the vicinity of producer "P1" at the end of the production life is primarily a consequence of the fact that the fault blocks the oil moving from west to east direction, but is also due partially to the fact that there is no production well located close to the right-end of the fault.

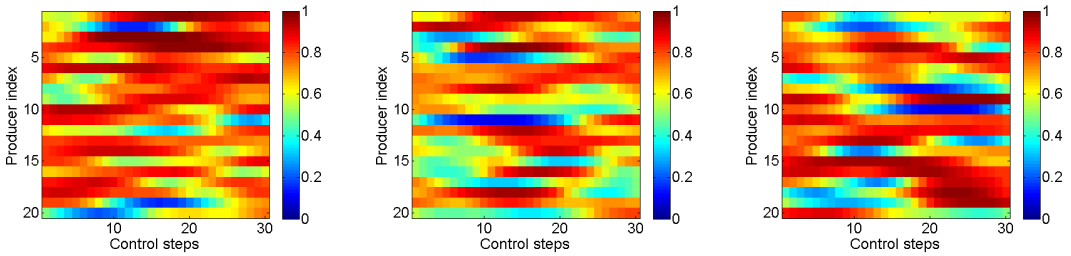

(a) EnOpt, ICV 1 (b) EnOpt, ICV 2 (c) EnOpt, ICV 3

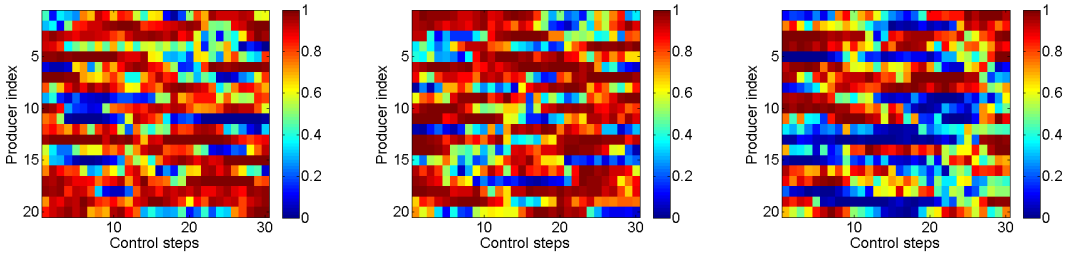

(d) f-StoSAG, ICV 1 (e) f-StoSAG, ICV 2 (f) f-StoSAG, ICV 3

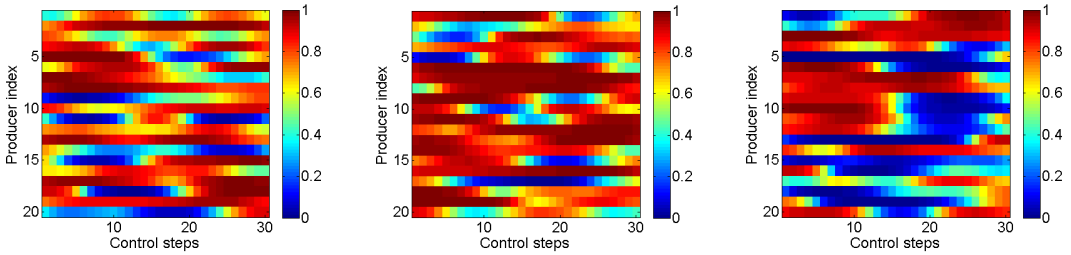

(g) sf-StoSAG, ICV 1 (h) sf-StoSAG, ICV 2 (i) sf-StoSAG, ICV 3

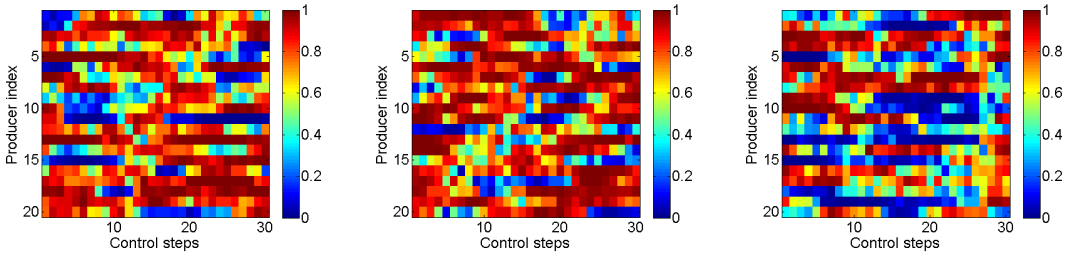

(j) StoSAG, ICV 1 (k) StoSAG, ICV 2 (l) StoSAG, ICV 3

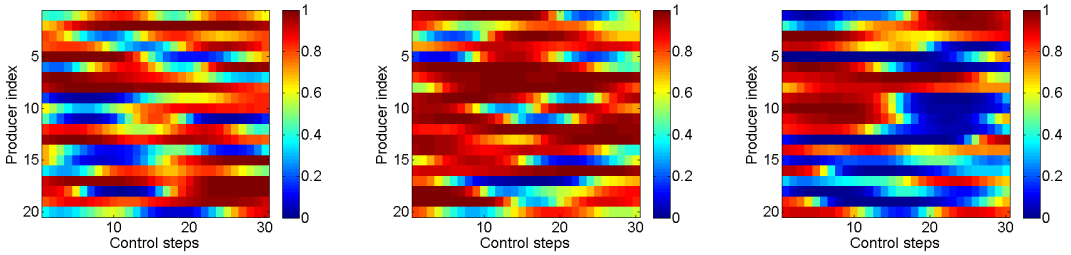

(m) ss-StoSAG, ICV 1 (n) ss-StoSAG, ICV 2 (o) ss-StoSAG, ICV 3

Figure 4.15: Estimated ICV settings of all the production wells at different perforated segment calculated from different search direction formulations on a scale from closed (0) to fully open (1); initial guess 2.

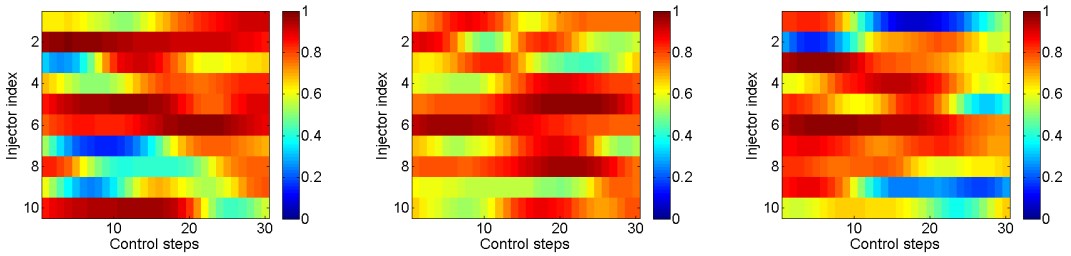

(a) EnOpt, ICV 1 (b) EnOpt, ICV 2 (c) EnOpt, ICV 3

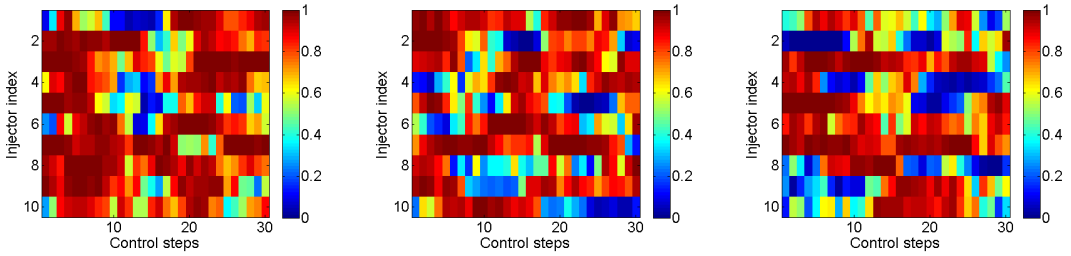

(d) f-StoSAG, ICV 1 (e) f-StoSAG, ICV 2 (f) f-StoSAG, ICV 3

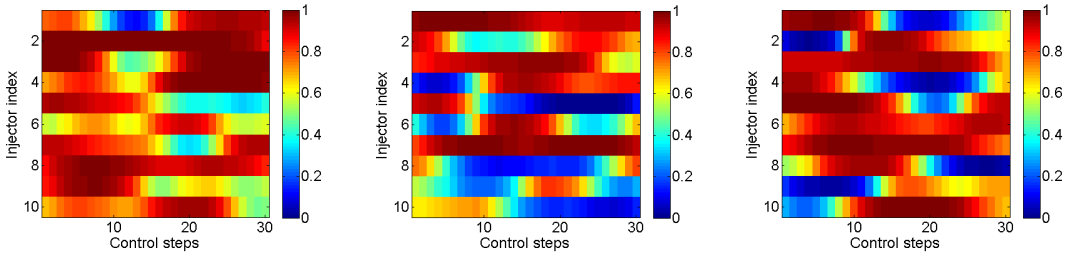

(g) sf-StoSAG, ICV 1 (h) sf-StoSAG, ICV 2 (i) sf-StoSAG, ICV 3

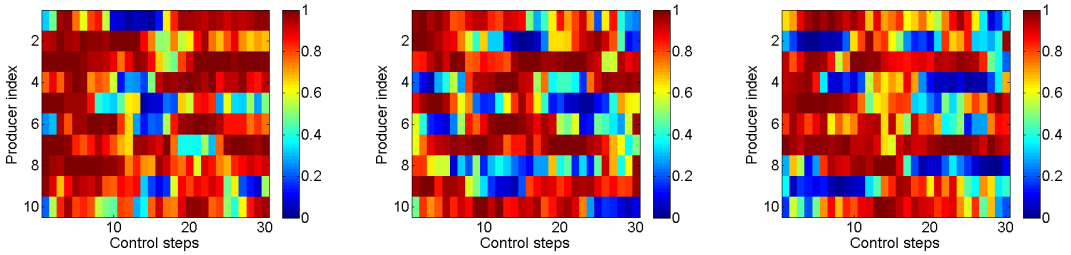

(j) StoSAG, ICV 1 (k) StoSAG, ICV 2 (l) StoSAG, ICV 3

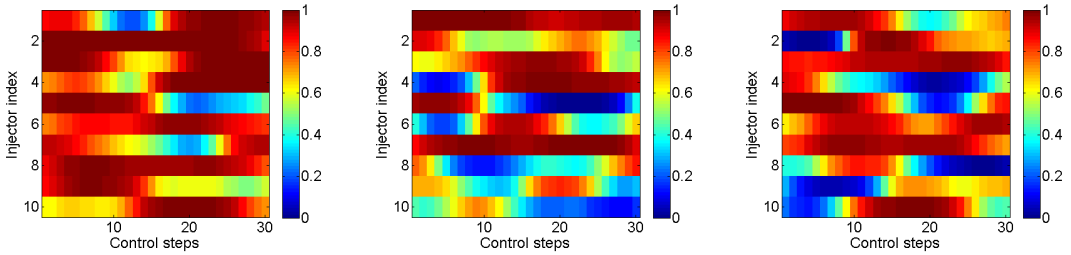

(m) ss-StoSAG, ICV 1 (n) ss-StoSAG, ICV 2 (o) ss-StoSAG, ICV 3

Figure 4.16: Estimated ICV settings of all the injection wells at different perforated segment calculated from different search direction formulations on a scale from closed (0) to fully open (1); initial guess 2.

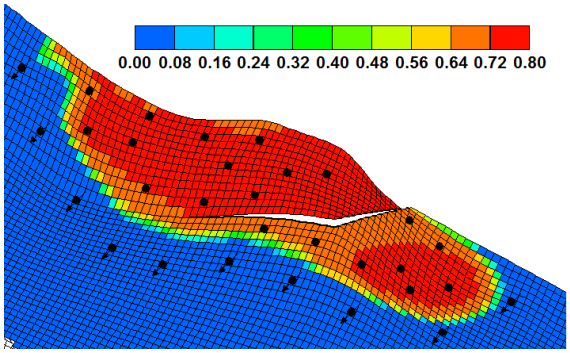

(a) Initial

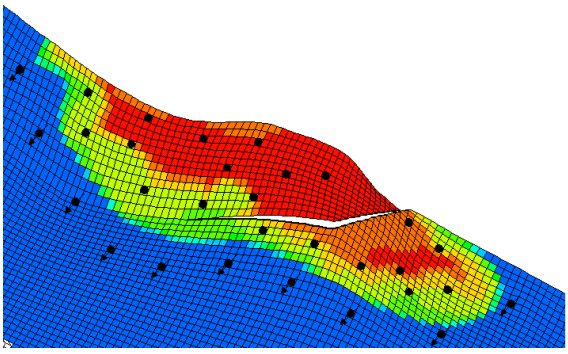

(b) EnOpt, 7.5 years

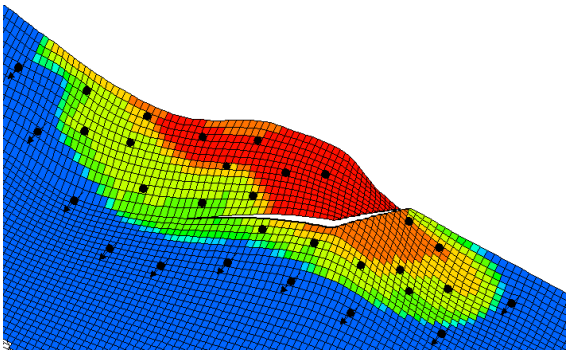

(c) EnOpt, 15 years

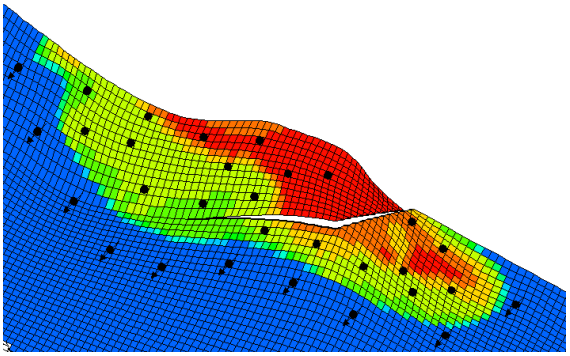

(d) sf-StoSAG, 7.5 years

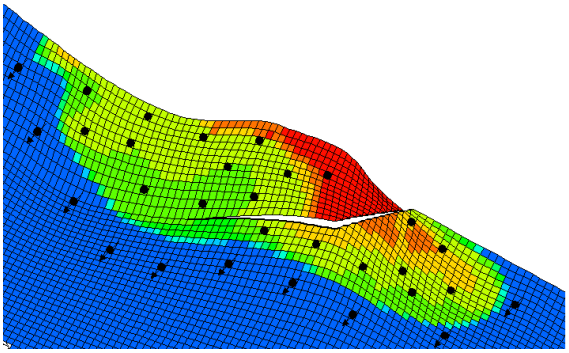

(e) sf-StoSAG, 15 years

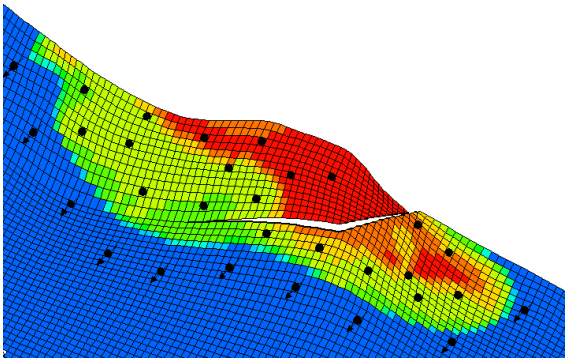

(f) ss-StoSAG, 7.5 years

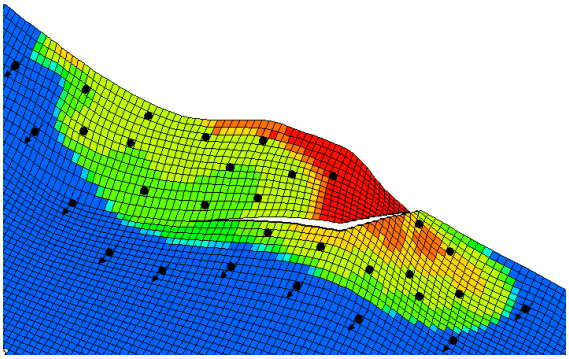

(g) ss-StoSAG, 15 years

Figure 4.17: Initial oil saturation distribution, and remaining oil saturation distribution at years 7.5 and 15 calculated from EnOpt, sf-StoSAG and ss-StoSAG; Layer 6; initial guess 2.

CHAPTER 5

RISK MINIMIZATION IN ROBUST LIFE-CYCLE PRODUCTION OPTIMIZATION

In this Chapter, we investigate the possibility of using the newly developed StoSAG algorithm for the case where the two objectives are to maximize the life-cycle NPV of production under geological uncertainty and to minimize the risk. To solve the bi-objective optimization problem, a workflow based on the lexicographic method is proposed. Then, the proposed workflow is applied to two reservoir examples: a fluvial reservoir and the Brugge reservoir model.

5.1 Methodology

5.1.1 Risk Measures

If only robust optimization is performed, i.e., only the average NPV value is maximized, the variance in the set of NPV values over the set of geological realizations is often large. As noted in the introduction, if the true reservoir description is close to the reservoir description that generates the worst NPV, then further exploitation of the reservoir may not be commercially feasible, i.e., there may be considerable commercial risk in implementing the estimated optimal well controls in practice. Therefore, it is also important to attempt to reduce risk and the hope is that risk can be mitigated without a significant decrease in the expected value of life-cycle NPV. Commonly used risk measures in the oil and gas community include standard deviation or variance, the worst-case scenario (minimum NPV over the set of geological models), safety margin, mean-variance, value at risk (VaR) and conditional value at risk (CVaR), which is also known as the expected shortfall. Liu and Reynolds [62] found that standard deviation is not a good measure for risk minimization. Capolei

et al. [15] also pointed out that, except for the worst-case scenario and CVaR, most of the risk measures are not satisfactory. Here, the mathematical formula for the risk measures of worst-case and CVaR are presented. The formulation for standard deviation is also provided here and will be benchmarked with the worst-case and CVaR scenarios for the reduction of risk later.

Worst-Case Scenario. The NPV of worst case, denoted by $J_W(u)$, is the minimum (worst) NPV obtained from all geological realizations; that is

$$J_W(u) = \min_i \{J(u, m_i)\}_{i=1}^{N_e}. \tag{5.1}$$

Conditional Value at Risk (CVaR). The CVaR (also known as the Expected Shortfall, Tail VaR, or Mean Excess Loss) is one of the most widely used risk measures in financial risk measurement [78, 76]. It was first introduced to the oil community by Valladao et al. [88]. The CVaR at q percentile is defined as the average value of the worst $q\%$ NPV values. For an estimated optimal control vector u, we order the set of geological models $\{m_i\}_{i=1}^{N_e}$, so that, $J(u, m_1) \leq J(u, m_2) \leq \cdots \leq J(u, m_{N_e})$. Then, the CVaR, denoted by $J_C(u)$, at q% is approximated by

$$J_C(u) \approx \frac{\sum_{i=1}^{N_Q} J(u, m_i)}{N_Q}, \tag{5.2}$$

where $N_Q = N_e \times q\%$. Note that, given N_e, we always choose q to make N_Q an integer or, given q, we choose N_e to make N_Q an integer. It is easy to see that the worst NPV J_W defined in Eq. 5.1 corresponds to the CVaR at the specific q which is equal to $100/N_e$ percentile. Note this risk measure was also used by Liu and Reynolds [64] where it was referred to as expected shortfall.

Standard Deviation. Standard Deviation, denoted by $J_D(u)$, is given by

$$J_D(u) = \sqrt{\frac{\sum_{i=1}^{N_e} \left(J(u, m_i) - J_E(u)\right)^2}{(N_e - 1)}}. \tag{5.3}$$

In the oil industry, standard deviation has been used previously as a risk/uncertainty measure by Yeten et al. [94], Bailey et al. [8], Alhuthal et al. [3], Liu and Reynolds [62] and Capolei et al. [16].

5.1.2 Lexicographic Method

If we wish to both reduce risk and maximize the expected value of the NPV of life-cycle production, then we encounter a bi-objective optimization problems where the two objectives, maximize the expectation of the life-cycle NPV of production and minimize the risk, are generally in conflict. This bi-objective optimization problem is conveniently stated as

$$\begin{aligned} &\max_{u \in R^{N_u}} \left\{J_E(u), J_x(u)\right\}, \\ &\text{s.t.} \quad u_i^{\text{low}} \leq u_i \leq u_i^{\text{up}}, \quad i = 1, 2, \cdots N_u, \end{aligned} \tag{5.4}$$

where $J_x(u)$ can be one of the risk measures of interest, e.g., $J_W(u)$, $J_C(u)$ or $-J_D(u)$. Note that $-J_D$ is used in place of J_D as we wish to frame the problem in terms of maximizing two objective functions and maximizing $-J_D$ is equivalent to minimizing J_D. As they had a simple reservoir simulator with adjoint capability, Liu and Reynolds [62, 63, 64] applied the weighted sum method, the NBI method and the lexicographical method for simultaneously maximizing the expectation and minimizing the risk using gradient-based optimization, but due to the limitations of their adjoint framework, they were also able to consider fairly simple reservoir models. Due to the computational cost of using the weighted sum method and NBI method to generate the Pareto front when the correct gradient cannot be computed with an adjoint method, we focus here on the computationally more efficient lexicographical method to optimize the objectives where we use StoSAG as the optimization algorithm.

The lexicographic method requires the user to order all objective functions by their

relative importance. The most important objective function will be optimized first. Then, the first optimized objective will be treated as an additional constraint when optimizing the second most important objective; this process is repeated until the least important objective is optimized. In Eq. 5.4, we have two objectives, $J_E(u)$ and $J_x(u)$. Here, we choose to maximize $J_E(u)$ first to find the estimate, u^*, of the optimal control vector and the corresponding value of the objective function, $J_E(u^*)$. Then using the optimal value $J_E(u^*)$ as a constraint, we optimize $J_x(u)$ in a second optimization where we solve

$$\begin{aligned} &\max_{u \in R^{N_u}} J_x(u), \\ \text{s.t.} \quad &\begin{cases} J_E(u) \geqslant \gamma J_E(u^*), \\ u_i^{\text{low}} \leq u_i \leq u_i^{\text{up}}, \quad i = 1, 2, \cdots N_u. \end{cases} \end{aligned} \tag{5.5}$$

Note that, in the preceding problem, $J_E(u)$ corresponds to the calculated value of the average NPV obtained based on the value of u obtained during the maximization of $J_x(u)$. In Eq. 5.5, $0 < \gamma \leq 1$, but typically we wish to choose γ very close to unity. If u^{opt} denotes the vector of control that represents the solution of Eq. 5.5, then, the choice of γ effectively determines how close $J_E(u^{\text{opt}})$ is to $J_E(u^*)$. Even if we choose $\gamma = 1$, however, $J(u^{\text{opt}})$ may not satisfy the constraint of Eq. 5.5 because the optimization problem specified by Eq. 5.5 is solved by the augmented Lagrangian method which forces the constraint to be satisfied up to 1% at convergence. Because of this tolerance, in the examples, we use $\gamma = 1$ in Eq. 5.5. Note, however, the problem could be repeated with a sequence of values of γ, e.g., $\gamma = 1$, $\gamma = 0.98$, $\gamma = 0.95$, $\gamma = 0.9$ to obtain alternate trade-off solutions, i.e., to construct a portion of the Pareto front.

To solve the sub-problem shown in Eq. 5.5, the constraint is handled by the augmented Lagrangian method. Define $c_E(u) = \big(J_E(u)/J_E(u^*)\big) - 1.0$ so that the constraint of Eq. 5.5 can be rewritten as $c_E(u) = \frac{J_E(u)}{J_E(u^*)} - 1.0 \geqslant 0$. Then the augmented Lagrangian function can be written as

$$\mathcal{L}(u, \lambda^k, \mu^k) = J_x(u) - \varphi(u, \lambda^k, \mu^k), \tag{5.6}$$

where

$$\varphi(u,\lambda^k,\mu^k)=\begin{cases}-\lambda^k c_E(u)+\frac{c_E^2(u)}{2\mu^k}, & \text{if } c_E(u)\leqslant\mu^k\lambda^k,\\ -\frac{\mu^k}{2}(\lambda^k)^2, & \text{otherwise,}\end{cases}\tag{5.7}$$

and λ^k is the Lagrangian multiplier and μ^k the penalty parameter at the kth outer loop. Taking the derivative of Eq. 5.6 with respect to u and evaluating it at $u=u_\ell$ gives

$$\nabla_u\mathcal{L}(u_\ell,\lambda^k,\mu^k)=\nabla_u J_x(u_\ell)-\nabla_u\varphi(u_\ell,\lambda^k,\mu^k).\tag{5.8}$$

In this work, the gradients, $\nabla_u J_x(u_\ell)$ and $\nabla_u\varphi(u_\ell,\lambda^k,\mu^k)$, are replaced by stochastic gradients which are calculated individually. $J_x(u)$ is one of the risk measures of interest, i.e., equal to $J_W(u)$, $J_C(u)$ or $J_D(u)$, with gradients at u_ℓ, respectively, denoted by $\nabla_u J_W(u_\ell)$, $\nabla_u J_C(u_\ell)$ and $\nabla_u J_D(u_\ell)$. The general formulation for the stochastic gradient, StoSAG, is given by

$$d_\ell=\nabla_u J_E(u)=\frac{1}{N_e}\sum_{i=1}^{N_e}\nabla_u J\left(u,m_i\right),\tag{5.9}$$

where $\nabla_u J\left(u,m_i\right)$ is replaced by the stochastic approximation

$$\nabla_u J\left(u,m_i\right)\approx\frac{1}{N_p}\sum_{j=1}^{N_p}\Big(\delta\hat{u}_{\ell,j}(\delta\hat{u}_{\ell,j})^T\Big)^+\delta\hat{u}_{\ell,j}\Big(J(\hat{u}_{\ell,j},m_i)-J(u_\ell,m_i)\Big)\tag{5.10}$$

to obtain

$$\nabla_u J_E(u)\approx\frac{1}{N_e}\sum_{i=1}^{N_e}\Big[\frac{1}{N_p}\sum_{j=1}^{N_p}\Big(\delta\hat{u}_{\ell,j}(\delta\hat{u}_{\ell,j})^T\Big)^+\delta\hat{u}_{\ell,j}\Big(J(\hat{u}_{\ell,j},m_i)-J(u_\ell,m_i)\Big)\Big]\equiv d_\ell,\tag{5.11}$$

where N_p is the number of perturbations of u_ℓ used.

In Eqs. 5.10 and 5.11, the superscript "+" on a matrix denotes the Moore-Penrose pseudo-inverse, $\delta\hat{u}_{\ell,j}=\hat{u}_{\ell,j}-u_\ell$, and N_p represents the number of control perturbations. Each control perturbation $\hat{u}_{\ell,j}$, $j=1,2,\cdots N_p$ at iteration ℓ is generated from the distribution $\mathcal{N}(u_\ell,C_U)$ and C_U is a predefined covariance matrix.

Then, the stochastic gradients of $\nabla_u J_W(u_\ell)$ and $\nabla_u J_C(u_\ell)$, respectively, can be easily

generated from Eq. 5.10 with J replaced by $J_W(u_\ell)$ and $J_C(u_\ell)$. Letting m_w denote the realization that gives the lowest NPV where the current estimate of the optimal controls, u_ℓ, are imposed, we then use the stochastic gradient formula of Eq. 5.10 to obtain

$$\nabla_u J_W(u_\ell) \approx \frac{1}{N_p}\sum_{j=1}^{N_p}\Big(\delta\hat{u}_{\ell,j}(\delta\hat{u}_{\ell,j})^T\Big)^+\delta\hat{u}_{\ell,j}\Big(J(\hat{u}_{\ell,j},m_w)-J(u_\ell,m_w)\Big). \tag{5.12}$$

Similarly, taking the gradient of Eq. 6.7 and using the stochastic gradient formula of Eq. 5.10 to approximate the term $\nabla_u J(u_\ell, m_i)$ gives

$$\nabla_u J_C(u_\ell) \approx \frac{1}{N_Q}\sum_{i=1}^{N_Q}\Big[\frac{1}{N_p}\sum_{j=1}^{N_p}\Big(\delta\hat{u}_{\ell,j}(\delta\hat{u}_{\ell,j})^T\Big)^+\delta\hat{u}_{\ell,j}\Big(J(\hat{u}_{\ell,j},m_i)-J(u_\ell,m_i)\Big)\Big], \tag{5.13}$$

where the N_Q models in Eqs. 6.7 and 5.13 correspond to the ones that generate the $q\%$ lowest NPV values at the current iterate u_ℓ.

Here, the derivation for the gradient of standard deviation, $J_D(u)$ given by Eq. 5.3, is provided. We first write $\nabla_u J_D(u)$ in terms of an equivalent expression and then differentiate to obtain

$$\begin{aligned}\nabla_u J_D(u_\ell) &= \left(\frac{1}{2J_D(u)}\nabla_u J_D^2(u)\right)_{u=u_\ell} = \left(\frac{1}{2(N_e-1)J_D(u)}\nabla_u\left[\sum_{i=1}^{N_e}\left(J(u,m_i)-J_E(u)\right)^2\right]\right)_{u=u_\ell}\\ &= \frac{1}{(N_e-1)J_D(u_\ell)}\left[\sum_{i=1}^{N_e}\left(J(u_\ell,m_i)-J_E(u_\ell)\right)\left(\nabla_u J(u_\ell,m_i)-\nabla_u J_E(u_\ell)\right)\right].\end{aligned} \tag{5.14}$$

For simplicity, $J(u_\ell, m_i)$ is replaced by J_i and $J_E(u_\ell)$ is replaced by J_E, then Eq. 5.14 can

be written as

$$\begin{aligned}
\nabla_u J_D(u_\ell) &= \frac{1}{(N_e-1)J_D(u_\ell)}\left[\sum_{i=1}^{N_e}\left(J_i - J_E\right)\left(\nabla J_i - \nabla J_E\right)\right] \\
&= \frac{1}{(N_e-1)J_D(u_\ell)}\left[\sum_{i=1}^{N_e}\left(J_i\nabla J_i - J_i\nabla J_E - J_E\nabla J_i + J_E\nabla J_E\right)\right] \\
&= \frac{1}{(N_e-1)J_D(u_\ell)}\left[\sum_{i=1}^{N_e} J_i\nabla J_i - \sum_{i=1}^{N_e} J_i\nabla J_E - \sum_{i=1}^{N_e} J_E\nabla J_i + \sum_{i=1}^{N_e} J_E\nabla J_E\right] \\
&= \frac{1}{(N_e-1)J_D(u_\ell)}\left[\sum_{i=1}^{N_e} J_i\nabla J_i - \nabla J_E\sum_{i=1}^{N_e} J_i - J_E\sum_{i=1}^{N_e}\nabla J_i + \sum_{i=1}^{N_e} J_E\nabla J_E\right] \\
&= \frac{1}{(N_e-1)J_D(u_\ell)}\left[\sum_{i=1}^{N_e} J_i\nabla J_i - \nabla J_E N_e J_E - J_E N_e\nabla J_E + \sum_{i=1}^{N_e} J_E\nabla J_E\right] \\
&= \frac{1}{(N_e-1)J_D(u_\ell)}\left[\sum_{i=1}^{N_e} J_i\nabla J_i - \nabla J_E N_e J_E - N_e J_E\nabla J_E + N_e J_E\nabla J_E\right] \\
&= \frac{1}{(N_e-1)J_D(u_\ell)}\left[\sum_{i=1}^{N_e} J_i\nabla J_i - N_e J_E\nabla J_E\right] \\
&= \frac{1}{(N_e-1)J_D(u_\ell)}\left[\sum_{i=1}^{N_e} J(u_\ell, m_i)\nabla_u J(u_\ell, m_i) - N_e J_E(u_\ell)\nabla_u J_E(u_\ell)\right], \qquad (5.15)
\end{aligned}$$

or

$$\nabla_u J_D(u_\ell) = \frac{1}{(N_e-1)J_D(u_\ell)}\sum_{i=1}^{N_e}\left[J(u_\ell, m_i)\nabla_u J(u_\ell, m_i) - J_E(u_\ell)\nabla_u J_E(u_\ell)\right]. \qquad (5.16)$$

Taking the derivative of Eq. 5.7 with respect to u and evaluating it at $u = u_\ell$ gives

$$\nabla_u\varphi(u_\ell, \lambda^k, \mu^k) = \begin{cases} \left(-\lambda^k + \frac{c_E(u_\ell)}{\mu^k}\right)\nabla_u c_E(u_\ell), & \text{if } c_E(u_\ell) \leqslant \mu^k\lambda^k; \\ 0, & \text{otherwise.} \end{cases} \qquad (5.17)$$

Eq. 5.17 provides the expression used to evaluate the second term on the right-hand-side of Eq. 5.8. Recall that $c_E(u) = J_E(u)/J_E(u^*) - 1.0$, so

$$\nabla_u c_E(u) = \nabla_u J_E(u)/J_E(u^*). \qquad (5.18)$$

Substituting the expression for $\nabla_u J_E(u)$ provided by the second equality of Eq. 5.11 into Eq. 5.18 and evaluating at $u = u_\ell$ yields

$$\nabla_u c_E(u_\ell) = \frac{1}{N_e \times J_E(u^*)} \sum_{i=1}^{N_e} \Big[\frac{1}{N_p} \sum_{j=1}^{N_p} \Big(\delta\hat{u}_{\ell,j} (\delta\hat{u}_{\ell,j})^T \Big)^+ \delta\hat{u}_{\ell,j} \Big(J(\hat{u}_{\ell,j}, m_i) - J(u_\ell, m_i) \Big) \Big]. \tag{5.19}$$

Thus, we have developed all equalities needed to compute the stochastic gradient of the augmented Lagrangian function (Eq. 5.6) at each steepest ascent iteration (Eq. 6.3) in the inner loop of the augmented Lagrange method.

In all examples, we use a 1:1 ratio of control perturbations to geological realizations, i.e., $N_p = 1$, to compute the gradient of $\nabla_u c_E(u_\ell)$. However, as $J_W(u_\ell)$ involves only one reservoir model at iteration of the optimization algorithm, using $N_p = 1$ is equivalent to computing a stochastic gradient with one perturbation which would typically give a very poor approximation of the true gradient [34]. Thus, we use 15 perturbations of u_ℓ ($N_p = 15$) when computing $\nabla_u J_W(u_\ell)$ with Eq. 5.12. We also use $N_p = 15$ as the base case when computing $\nabla_u J_C(u_\ell)$ with Eq. 5.13

The lexicographic framework for reducing the risk in the optimization under uncertainty by solving the constrained problem of Eq. 5.5 by application of the augmented Lagrange method is summarized below:

1. Primary optimization

First, we maximize $J_E(u)$ (Eq. 4.1) to find the estimate of the optimal control vector u^* and its corresponding expectation, $J_E(u^*)$. In primary optimization, the StoSAG search direction in Eq. 5.11 is applied, and we use one control perturbation paired with one geological realization (ratio of 1:1), i.e., $N_p = 1$ in Eq. 5.11, to calculate the StoSAG gradient; refer to Fonseca et al. [37] for more discussion.

2. Second-step optimization

2(a) Set the outer loop index $k = 0$, $u_0 = u^*$, $\lambda^0 = 0$, $\mu^0 = \frac{1}{2\times 0.1\times|J_x(u^*)|}$, $\eta^0 = 0.1$, $\varepsilon_u^0 = 0.1$, $\varepsilon_f^0 = 0.1$.

2(b) Inner Loop: With k, λ^k and μ^k fixed, we solve the subproblem in Eq. 5.6 to find the solution, u_{opt}^{k+1}. At the kth outer loop, the convergence criteria for the inner loop are

$$\frac{|\mathcal{L}(u_{\ell+1}) - \mathcal{L}(u_\ell)|}{\max[|\mathcal{L}(u_\ell)|, 1.0]} \leqslant \varepsilon_f^k, \tag{5.20}$$

and

$$\frac{\|u_{\ell+1} - u_\ell\|_2}{\max[\|u_\ell\|_2, 1.0]} \leqslant \varepsilon_u^k, \tag{5.21}$$

where ℓ is the inner loop index. If Eqs. 5.20 and 5.21 hold, set $u_{\text{opt}}^{k+1} = u_{\ell+1}$.

2(c) Outer Loop: At the kth outer loop iteration, update λ^k and μ^k based on the constraint violation factor, σ_{cv}, which is given by

$$\sigma_{cv} = \sqrt{\{\min(0, c_E(u_{\text{opt}}^{k+1}))\}^2}. \tag{5.22}$$

If $\sigma_{cv} < \eta^k$, goto step 2(d), otherwise goto step 2(e). The augmented Lagrangian method loops through each inner loop and then outer loop until the convergence criteria given below are reached

$$\frac{\left|\mathcal{L}(u_{\text{opt}}^{k+1}) - \mathcal{L}(u_{\text{opt}}^k)\right|}{\max[\left|\mathcal{L}(u_{\text{opt}}^k)\right|, 1.0]} \leqslant \varepsilon_f^*, \tag{5.23}$$

$$\frac{\|u_{\text{opt}}^{k+1} - u_{\text{opt}}^k\|_2}{\max[\left\|u_{\text{opt}}^k\right\|_2, 1.0]} \leqslant \varepsilon_u^*, \tag{5.24}$$

and the constraint-violation factor is acceptable (i.e., $\sigma_{cv} \leq \eta^*$). We terminate the augmented Lagrangian method if the maximum allowable simulation runs is reached.

2(d) Update Lagrangian multiplier λ^k and tighten the convergence criteria.

$$\begin{aligned}
\lambda^{k+1} &= \max\{0, \lambda^k - \tfrac{c_E(u_{\text{opt}}^{k+1})}{\mu^k}\}, \\
\mu^{k+1} &= \mu^k, \\
\eta^{k+1} &= \max\{\eta^k \times \min(\mu^\beta, 0.5), \eta^*\}, \\
\varepsilon_u^{k+1} &= \max\{\varepsilon_u^k \times \min(\mu^\beta, 0.5), \varepsilon_u^*\}, \\
\varepsilon_f^{k+1} &= \max\{\varepsilon_f^k \times \min(\mu^\beta, 0.5), \varepsilon_f^*\}.
\end{aligned} \tag{5.25}$$

2(e) Update penalty parameter μ^k and tighten the convergence criteria.

$$\begin{aligned}
\lambda^{k+1} &= \lambda^k, \\
\mu^{k+1} &= \tau \times \mu^k, \\
\eta^{k+1} &= \max\{\eta^k \times \min(\mu^\alpha, 0.5), \eta^*\}, \\
\varepsilon_u^{k+1} &= \max\{\varepsilon_u^k \times \min(\mu^\alpha, 0.5), \varepsilon_u^*\}, \\
\varepsilon_f^{k+1} &= \max\{\varepsilon_f^k \times \min(\mu^\alpha, 0.5), \varepsilon_f^*\}.
\end{aligned} \tag{5.26}$$

2(f) Set k equal to $k = k + 1$ and goto step 2(b).

End

In our example applications, the final convergence tolerances for the augmented Lagrangian method are $\varepsilon_u^* = 10^{-3}$ and $\varepsilon_f^* = 10^{-4}$; the tolerance for the constraint violation at convergence, η^*, is set equal to 0.01; the rate of decrease for the penalty parameter, τ, is equal to 0.25; $\beta = 0.2$ and $\alpha = 0.1$.

5.2 Numerical Examples

5.2.1 Example 1: 3D Fluvial Reservoir

Problem Description. In the first example, the simulation model is defined on a $25 \times 25 \times 3$ grid with the grid block dimensions given by $\Delta x = \Delta y = 100$ ft and $\Delta z = 30$ ft. The reservoir

contains 4 water injectors and 9 producers. Note this example pertains to waterflooding optimization. Fifteen geological realizations of a Gaussian random field are generated to represent the uncertainty in the reservoir description. Fig. 5.1 displays six realizations of the log-permeability distribution for the first layer. The second and third layers have the same heterogeneity features as the first layer but with the permeabilities field of layer 2 is equal to the permeability field of layer 1 multiplied by 0.6 and the permeability field of layer 3 is equal to the permeability field of layer 1 multiplied by 0.3. The porosity is homogeneous with $\phi = 0.2$. The initial reservoir pressure is 3,800 psi; the reservoir lifetime is 2,880 days.

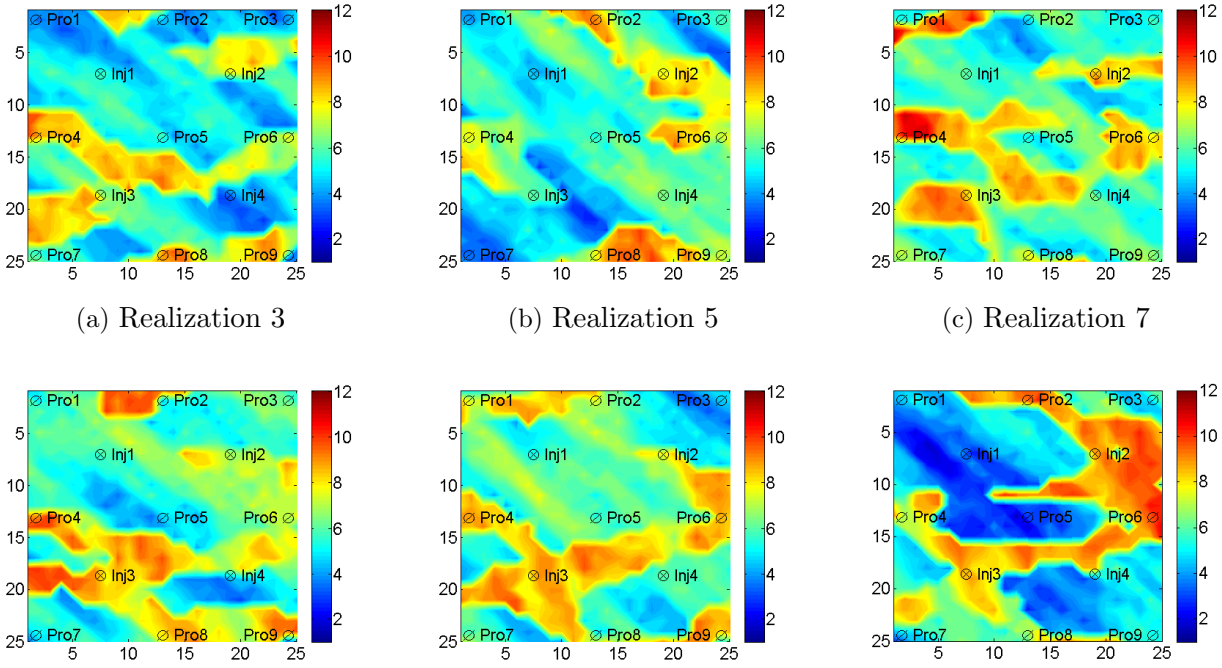

(a) Realization 3 (b) Realization 5 (c) Realization 7

(d) Realization 9 (e) Realization 11 (f) Realization 13

Figure 5.1: Log-permeability distribution of six realizations for the first layer, channelized reservoir.

Here, both well controls (rates or pressures on predefined control steps) and settings of ICVs are considered as the control variables where the two objectives are to maximize the expected NPV, $J_E(u)$, and minimize the risk, $J_x(u)$, where $J_x(u)$ is equal to either $J_W(u)$ or $J_C(u)$. The control variables at each water injector are the injection rates with an upper bound of 4,000 STB/D and a lower bound of 0 STB/D; each producer operates under BHP control with an upper bound of 3,800 psi and a lower bound of 1,500 psi; each ICV setting

for both producers and injectors has an upper bound of 1 and a lower bound of 0. The initial guess for the rate controls of each water injector is set equal to 2,000 STB/D; the initial guess for BHP controls for each producer is equal to 2,650 psi and the initial guess for all ICV settings are equal to 0.5. The oil price is set equal to \$ 50.0/STB; the water injection cost is \$5.0/STB; the cost of disposing produced water is \$5.0/STB; the annual discount rate is 0.1.

For the implementation of the StoSAG algorithm in the primary optimization (i.e., maximization of only expectation), we use a one-to-one combination of random control perturbations and random geological models (ratio of 1:1) with the size of the ensemble of reservoir models (log-permeability fields) equal to 15. The total number of controls steps is 16, with the length of each control step equal to 180 days. The perturbation size σ_w in Eq. 4.13 is set equal to 0.1; N_s^w is equal to 4, i.e., the controls at each well at 4 consecutive control steps (720 days) are correlated. In the second-step optimization, where the worst NPV (J_W) or the CVaR (J_C) is considered as risk measure, a 15:1 ratio of control perturbations to geological realization(s) is used to compute $\nabla_u J_W$ and $\nabla_u J_C$, and a 1:1 ratio is used to calculate $\nabla_u c_E$ in Eq. 5.19 for finding $\nabla_u \varphi$, in Eq. 5.8. However, a 1:1 ratio is used to compute the gradient when the standard deviation J_D is considered as the risk measure. The maximum number of allowable simulation runs for both primary optimization and the second-step optimization, is set equal to 3,000, i.e., a total of 6,000 simulation runs is required. A black-oil reservoir simulator, IMEX (Version 2009.10) [28] from Computer Modeling Group Ltd., is used for reservoir simulation.

Results. Fig. 5.2 shows the plot of the expected NPV (J_E) obtained during the primary optimization. Fig. 5.3 shows the values of the "second" objective function for each of the three risk measures (J_D, J_W, J_C) plotted versus the number of reservoir simulation runs when the second objective function is minimized using the lexicographic method. Note that J_C (i.e., CVaR) considered here is the average value of the 20% lowest NPV values. Fifteen realizations are used to represent the geological uncertainty, thus, J_C at 20% is the

expectation of the worst 3 NPV values. The results of Fig. 5.3 indicate that the standard deviation (J_D) is greatly decreased and both J_W and J_C are significantly improved, while the changes in the value of J_E is quite small during the secondary optimization because the optimal value of J_E is imposed as a constraint when each risk measure is optimized.

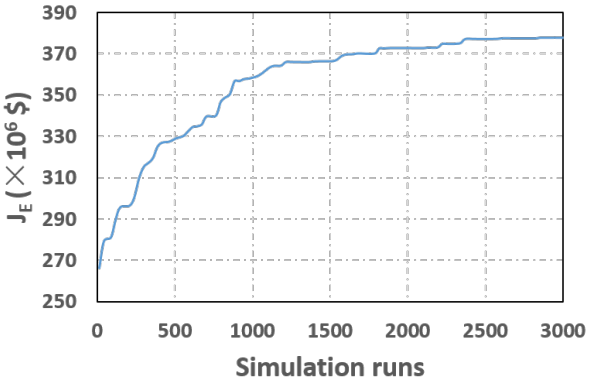

Figure 5.2: Primary objective (J_E) versus number of simulation runs, channelized reservoir.

Table 5.1 records the average NPV (J_E), the standard deviation (J_D), the values of the minimum (worst) NPV, the maximum NPV and the average value of 20% lowest NPV values (CVaR at 20%) obtained at the end of the secondary optimization with different risk measures, as well as those values obtained from the primary optimization (i.e., maximization of only expectation). It can be observed from Table 5.1 that the decrease of the corresponding expectation, J_E, obtained with the risk measure J_D in the secondary optimization is within 1% of the optimal value of J_E computed from the primary optimization. The corresponding expectations obtained when using the risk measures J_W and J_C are both slightly higher (within 0.5%) than the J_E value (377.8 million USD) obtained during primary optimization, which indicates that when we optimize the second objective function, the inequality constraint in the problem of Eq. 5.5 was strictly satisfied,. i.e., we found a strictly feasible solution. When using J_D (the standard deviation) as the risk measure in the lexicographic procedure, we obtained a value of J_D that is 30.77% lower than the value obtained when optimizing only the expected NPV. However, as shown in Table 5.1, after minimizing J_D, the worst (minimum) NPV is only increased 4.3 million USD above the value obtained from primary optimization, but the highest NPV is decreased 8.9 million USD below the highest

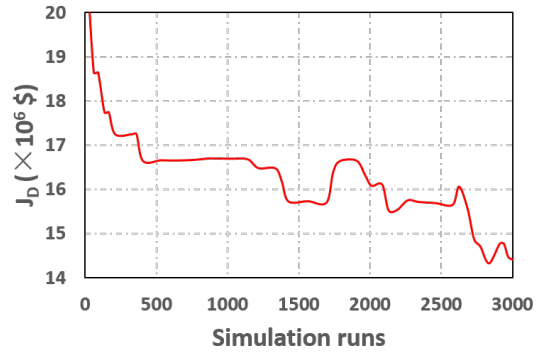

(a) Second objective, J_D

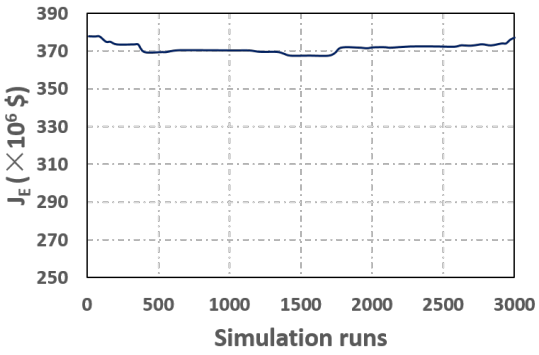

(b) J_E in minimization of J_D

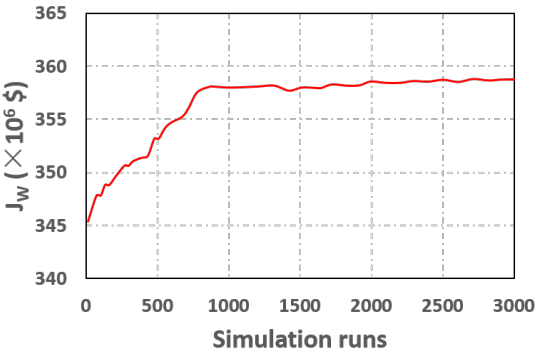

(c) Second objective, J_W

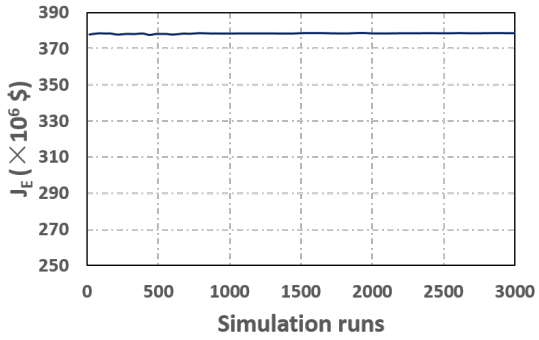

(d) J_E in maximization of J_W

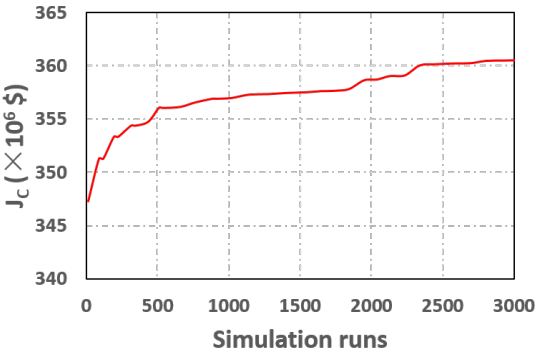

(e) Second objective, $J_C(20\%)$

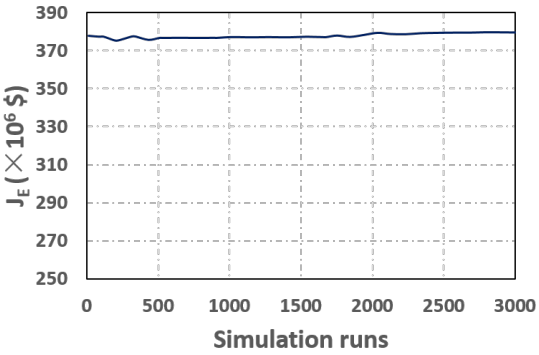

(f) J_E in maximization of $J_C(20\%)$

Figure 5.3: Second objectives (J_D, J_W and J_C at 20%) with their corresponding average NPVs (J_E) versus number of simulation runs, channelized reservoir.

NPV obtained during primary optimization. This indicates that the reduction in standard deviation is mainly achieved by markedly reducing the highest plausible NPV, a behavior that was first observed by Liu and Reynolds [64] when using an adjoint gradient-based optimization algorithm. On the other hand, as shown in Table 5.1, the minimum (worst) NPV

and CVaR at 20% obtained after maximizing either J_W or J_C is significantly higher than the value obtained by primary optimization. Moreover, the results of Table 5.1 indicate that when either J_W or J_C is used as the second objective in the lexicographic method, the final value of J_D is only slightly higher (17.3×10^6 USD or 17.0×10^6 USD) than the value (14.4×10^6 USD) obtained by minimizing the standard deviation objective (J_D) during the secondary optimization.

Table 5.1: Comparison of different risk measures, channelized reservoir.

Terms	J_E $\times10^6$ USD	J_D $\times10^6$ USD	Min. NPV $\times10^6$ USD	Max. NPV $\times10^6$ USD	CVaR (20%) $\times10^6$ USD
Primary : J_E	377.8	20.8	345.3	408.6	347.3
Secondary : J_D	377.1	14.4	349.6	399.7	351.8
Secondary : J_W	378.6	17.3	358.7	404.2	358.9
Secondary : $J_C(20\%)$	379.5	17.0	360.3	406.9	360.6

The cumulative distribution functions (CDFs) of the NPV values obtained by the lexicographic method with different risk measures, as well as the CDF obtained by maximizing the expectation only are displayed in Fig. 5.4. In this figure, the risk measure J_q represents the case where we wish to maximize the third lowest NPV. From the CDFs shown in Fig. 5.4, we can observe that the risk measure of J_C at 20% finds the solutions which increase the average value of the lowest 3 NPVs the most, while the risk measure of standard deviation finds the solutions which generate the lowest average value of the lowest 3 NPVs. It is interesting to note that when the NPV value at 20% (i.e., 3rd worst NPV) is considered as the objective of the second-step optimization, the 3rd lowest NPV can be greatly improved, but the two lowest NPV values cannot.

From above analysis, we can see that the CVaR (J_C) seems to be the best risk measure for use in the lexicographic method for this example in the sense that the estimated average value of the 3 lowest (20% lowest) NPV values is higher than the corresponding average value obtained with using other risk measures and is much higher than the corresponding value obtained by performing only robust optimization. However, the effect of the ratio of random perturbed controls to the number of geological models used to represent uncertainty

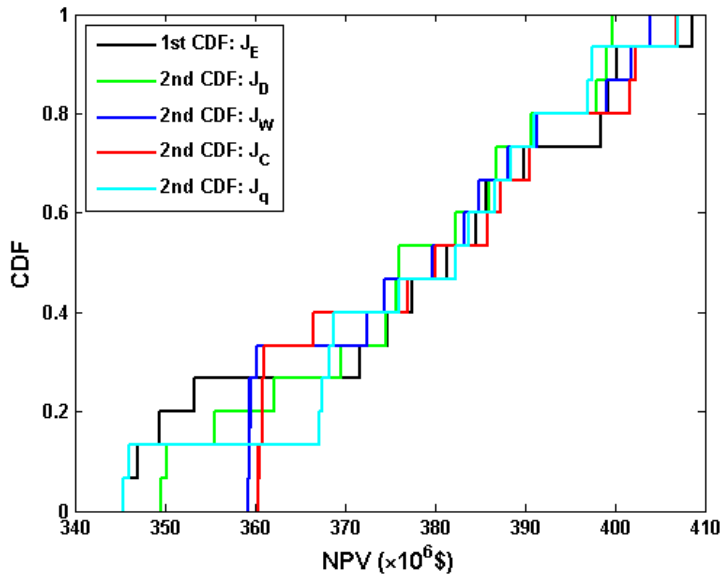

Figure 5.4: CDFs obtained by the lexicographic method with different risk measures; black: CDF obtained from primary optimization; green: CDF obtained using risk measure J_D; blue: CDF obtained using risk measure J_W; red: CDF obtained using risk measure J_C at 20%; cyan: CDF obtained using risk measure J_q at 20%; channelized reservoir.

is still unclear, so an additional investigation of CVaR is provided.

Fonseca et al. [37] show that one control perturbation paired with one geological model can generate a sufficiently good estimate of the gradient of the average value of NPV so that using this stochastic gradient in steepest ascent performs well, but we do not expect that will be the case if the number of reservoir models used to represent geological uncertainty is small. To investigate the effect of the number of perturbations used to compute the stochastic gradient of CVaR at 20%, we redo the example but now use different ratios of the number of perturbed controls to the the number of model realizations to compute $\nabla_u J_C(u)$. However, we continue to use one control perturbation for each of the fifteen ensemble models when compute $\nabla_u \varphi$ in Eq. 5.8. Fig. 5.5 shows results of CVaR obtained by using different ratios and the corresponding J_E values obtained when minimizing $J_C(u)$ in the second step of the lexicographic method. In Fig. 5.5, both J_C and J_E are plotted versus the number of reservoir simulation runs. It can be seen that, when computing $\nabla_u J_C$, a ratio of 15:1 achieves the highest CVaR while a ratio of 1:1 generates the lowest CVaR, but the corresponding J_E

values do not change significantly. Fig. 5.6 shows the CDF functions obtained from using different ratios when maximizing J_C. We can observe that, for all ratios, the average of the 3 lowest NPV values (20% worst NPVs) are improved above the corresponding average value obtained from the maximization of only expectation, and that the ratio of 15:1 performs the best.

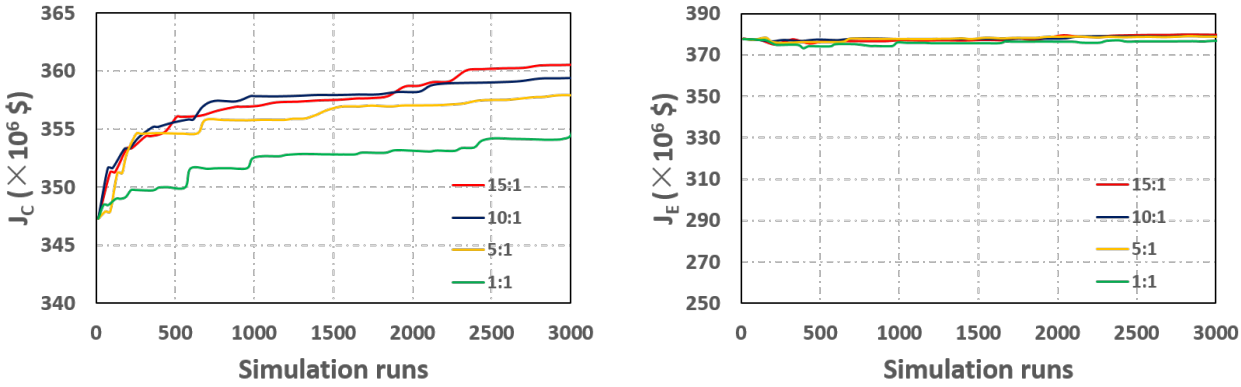

(a) J_C at 20%

(b) Corresponding J_E

Figure 5.5: Obtained J_C at 20% from different ratios and their corresponding J_E; red: ratio of 15:1; blue: ratio of 10:1; yellow: ratio of 5:1; green: ratio of 1:1; channelized reservoir.

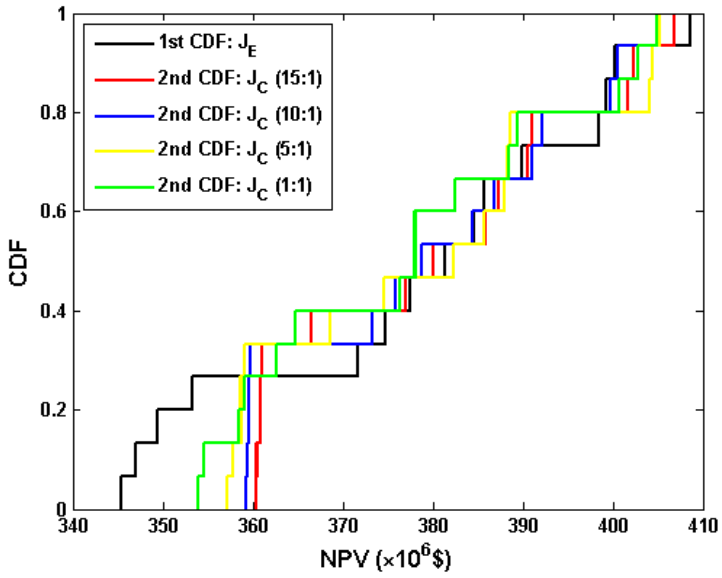

Figure 5.6: CDF functions obtained from different ratios for the optimization of J_C at 20%; red: ratio of 15:1; blue: ratio of 10:1; yellow: ratio of 5:1; green: ratio of 1:1; channelized reservoir.

CVaR at different percentiles represents different risk aversion levels. Fig. 5.7 shows CDF functions obtained from the risk measure of CVaR at different percentiles. For the channelized reservoir we use 15 reservoir models to represent the geological uncertainty, so the CVaR at 20%, 40%, 60%, 80% is equivalent to the average value of the lowest 3, 6, 9 and 12 plausible NPV values, respectively; 15 control perturbations for each geological realization (a ratio of 15:1) is used to estimate $\nabla_u J_C$. As expected, the results of Fig. 5.7 indicate that CVaR at 20% improves the average value of the 3 lowest NPVs the most. Table 5.2 displays the corresponding J_E, minimum NPV and maximum NPV obtained by using CVaR with different percentiles as the risk measure. Interestingly, Table 5.2 shows that the average NPV over all realizations, J_E, obtained from CVaR at 80% is 4.5 million USD higher than is obtained from CVaR at 20%, but the minimum NPV achieved from CVaR at 80% is 11.1 million USD lower than that computed from CVaR at 20%. From the view of reducing the risk, the CVaR at 20% is recommended as an optimal choice of risk measure.

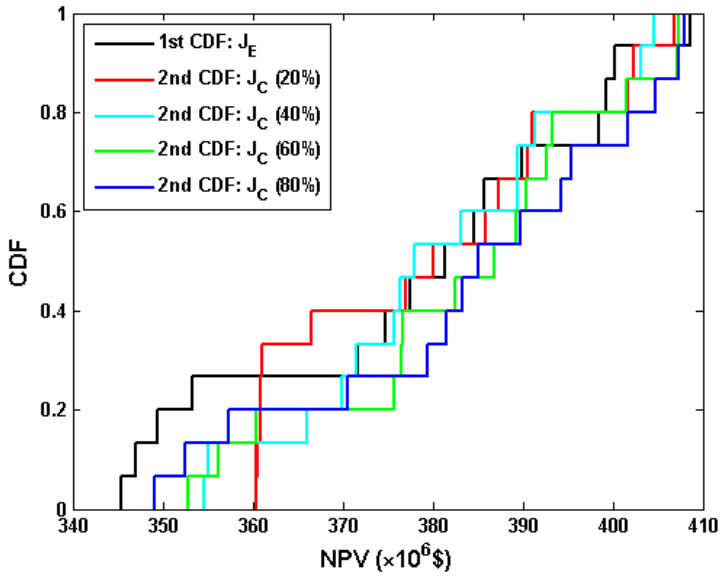

Figure 5.7: CDF functions obtained from different percentiles of worst cases for J_C optimization; black: CDF obtained from primary optimization; red: CDF obtained from J_C at 20%; cyan: CDF obtained from J_C at 40%; green: CDF obtained from J_C at 60%; blue: CDF obtained from J_C at 80%; channelized reservoir.

Fig. 5.8 shows the CDF functions obtained from the unconstrained (or one-step) CVaR optimization only and the two-step CVaR at 20% (i.e., lexicographic-based CVaR)

Table 5.2: Comparison of CVaR at different percentile, channelized reservoir.

Terms	J_E $\times 10^6$ USD	Minimum NPV $\times 10^6$ USD	Maximum NPV $\times 10^6$ USD
Primary opt. : J_E	377.8	345.3	408.6
Second opt. : $J_C(20\%)$	379.5	360.3	406.9
Second opt. : $J_C(40\%)$	380.7	355.1	404.6
Second opt. : $J_C(60\%)$	383.3	352.8	407.3
Second opt. : $J_C(80\%)$	384.0	349.2	408.1

approaches. Fig. 5.8 also includes the CDF function obtained by only performing robust optimization. Unconstrained CVaR is the approach where we only perform the CVaR optimization from the initial guess, i.e., maximize the worst case(s) at a certain percentile (20% in this example) without conducting the primary optimization. Note that for both CVaR at 20% approaches, we use a ratio of 15:1, i.e., 15 control perturbations for each geological realization, to compute the search direction $\nabla_u J_C(u_\ell)$ in Eq. 5.13. In the primary optimization of the two-step approach, we still use a 1:1 ratio to calculate the search direction. From Fig. 5.8, it can be observed that both the unconstrained and the two-step approaches can significantly improve the average of the three lowest NPV values compared to the scenario where we only perform robust optimization, i.e,. maximize J_E. However, the nine highest NPV values obtained from the unconstrained CVaR are much lower than can be obtained from the two-step CVaR, which results in the corresponding expectation of NPV value obtained from unconstrained CVaR is 6.6 million USD less than the expected NPV computed from two-step CVaR; see Table 5.3. We can see that the two-step or the lexicographic-based CVaR is better than the one-step or the unconstrained CVaR when reducing the risk is considered in the robust optimization.

5.2.2 Example 2: Brugge Test Case

Problem Description. The Brugge field was developed by TNO as a benchmark case to test different methods for closed-loop reservoir management [75]. The initial ensemble of reservoir models consists of 104 realizations of reservoir properties (permeability, porosity,

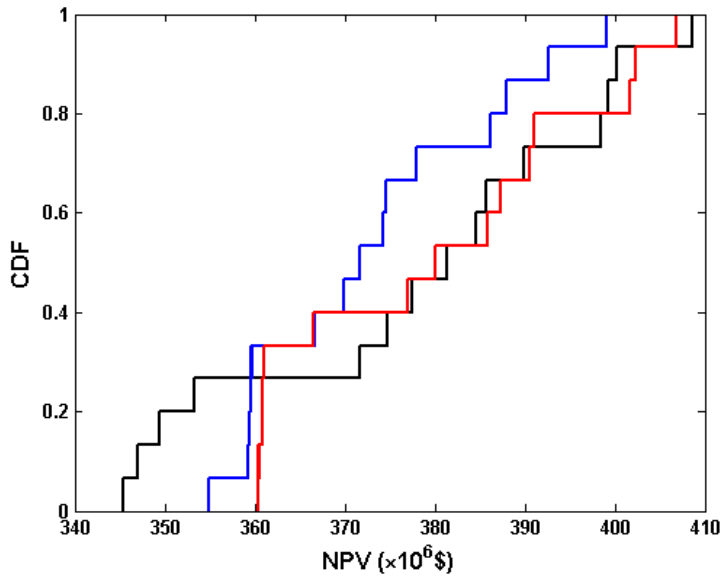

Figure 5.8: CDF functions obtained from unconstrained CVaR and two-step CVaR approaches; black: CDF obtained from primary optimization; blue: CDF obtained from unconstrained (one-step) CVaR; red: CDF obtained from two-step (lexicographic-based) CVaR; channelized reservoir.

Table 5.3: Comparison of the unconstrained CVaR and the two-step CVaR approaches, channelized reservoir.

Terms	J_E $\times 10^6$ USD	Minimum NPV $\times 10^6$ USD	Maximum NPV $\times 10^6$ USD
Primary opt. : J_E	377.8	345.3	408.6
Unconstrained CVaR	372.9	354.9	399.1
Two-step CVaR	379.5	360.3	406.9

net-to-gross and connate water saturation) upscaled to a 60,000 gridcell model; see Peters et al. [75]. Here, 15 reservoir realizations are randomly chosen to characterize the reservoir uncertainty. A more detailed description of the Brugge reservoir model can be found in Chapter 4 and in Peters et al. [75]. Note this is a two-phase flow (oil-water) waterflooding optimization example.

In their studies on Brugge field, Peters et al. [75], Chen and Oliver [24] and Chen et al. [21] considered a 30 year production lifetime. They assimilated the observed production and interpreted seismic data during the first 10 years, and then optimized the NPV for years 10-30 by adjusting the well control variables. In this study, we do not assimilate any data.

Instead, we estimate the optimal well controls for the first fifteen years of the reservoir life using robust optimization based on the fifteen selected models from the initial ensemble. The optimization problem is to estimate simultaneously the well controls (injection rates for injectors and BHP for producers) and downhole ICV settings which maximize the average NPV and minimize the risk over 15 years of production.

The well control variables at each injector are the injection rates with an upper bound of 5,000 STB/D and a lower bound of 0 STB/D; each producer operates under BHP control with an upper bound of 2,465 psi and a lower bound of 725 psi; each ICV setting for both producers and injectors has an upper bound of 1 and a lower bound of 0. The initial guess for the rate controls of each water injector is set equal to 2,500 STB/D; the initial guess for BHP controls for each producer is equal to 1,595 psi and the initial guess for all ICV settings are equal to 0.5. For each injection well, the control variables contain the injection rate at the well and three ICV settings at each control step; for each production well, the control variables contain BHP plus three ICV settings at each control step. The intial reservoir pressure is 2,465 psi.

Only oil and water flow in the reservoir throughout the reservoir production life. To maximize the expectation of NPV and minimize the risk, the oil price is set equal to \$60.0/STB. Each well contains 30 control steps, with the length of each control step equal to 182.5 days (half a year). The controls at each well are correlated over every 10 consecutive control steps (1,825 days); the maximum number of allowable simulation runs in the primary optimization and the second optimization are 6,000 and 3,000, respectively. All the other problem specifications are the same as those in Example 1.

Results. Fig. 5.9 shows the behavior of the average NPV (J_E) during the primary optimization procedure where the optimization was continued until approximately 6,000 reservoir simulation runs were done. The left column of plots in Fig. 5.10 corresponds to the secondary optimization in the lexicographic method, with each plot corresponding to one of the three risk measures, J_D (standard deviation), J_W (minimum or worst NPV) and J_C which here

is the conditional value at 20%. Each figure in the right column of plots in Fig. 5.10 corresponds to behavior of J_E during the optimization process shown in the plot to its left. Some related optimization results are shown in Table 5.4. These results are qualitatively similar to those of the first example. Note that during the constrained minimization of J_D, the value of J_E is decreased 5.88% from the value obtained from primary optimization (6.80×10^9 USD), i.e., decreases to 6.40×10^9 USD; see Table 5.4. This is due to the fact that, within the given 3,000 maximum allowable simulation runs in the secondary optimization, both the convergence criteria in Eqs. 5.23 and 5.24 and the acceptable constraint-violation factor ($\eta^* = 1\%$) in the outer loop of augmented Lagrangian method are not reached. The CDFs shown in Fig. 5.11 amplify the last result. In Fig. 5.11, we see that using J_D as the second objective barely increases this minimum value of NPV above the value obtained by optimizing only the expectation J_E but results in a decrease in the values of the highest NPV's below their values obtained by the primary optimization; this behavior is highly undesirable. The other two risk measures, J_W and J_C, as the second objectives gives results that conform to expected performance but also clearly indicate that CVaR at 20% (J_C) gives a more desirable posterior CDF than does J_W.

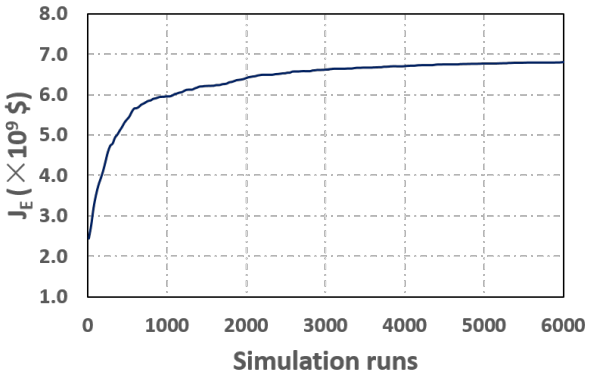

Figure 5.9: Primary objective (J_E) versus number of simulation runs, Brugge case.

The optimal well controls obtained by the primary optimization and secondary optimization are shown in Fig. 5.12. In these figures, the vertical axes refer to the well number (recall that there are 10 injectors and 20 producers), while the horizontal axes refer to the control interval (30 in total). It can be observed that several well controls for injector 5 in

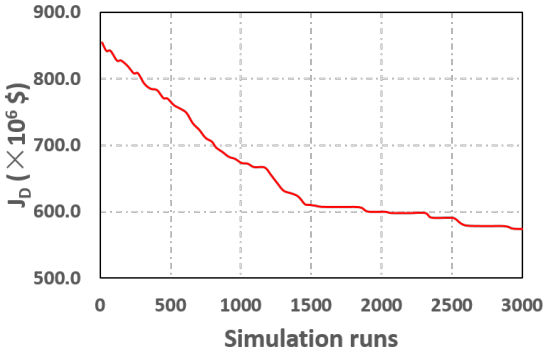

(a) Second objective, J_D

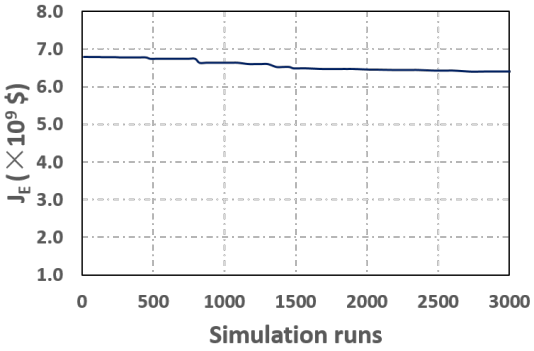

(b) J_E in optimization of J_D

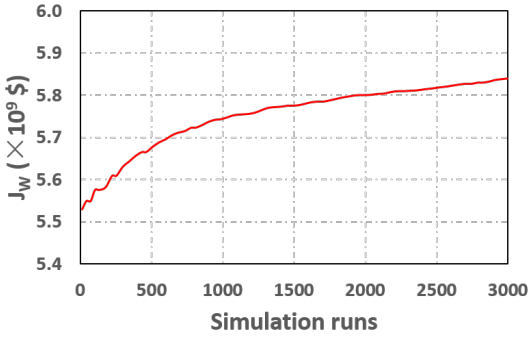

(c) Second objective, J_W

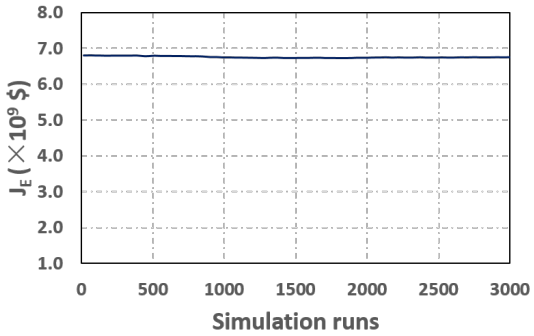

(d) J_E in optimization of J_W

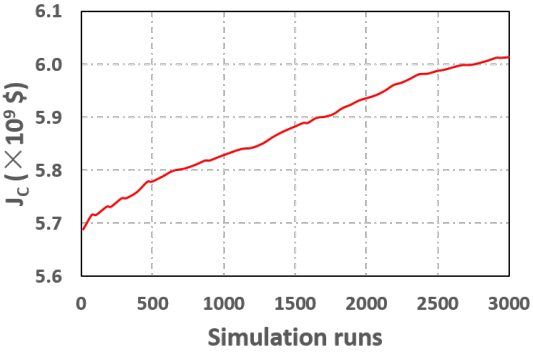

(e) Second objective, J_C

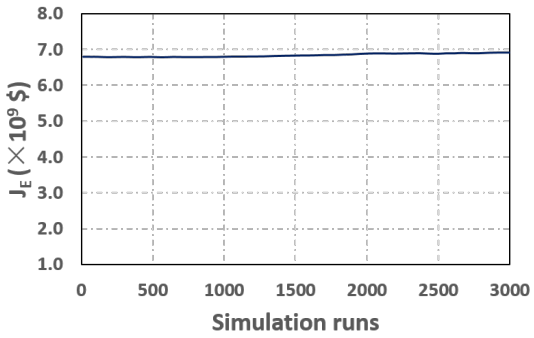

(f) J_E in optimization of J_C

Figure 5.10: Primary objective (J_E) and different second objectives (J_D, J_W, J_C) with their corresponding average NPV's (J_E) versus number of simulation runs, Brugge case.

Fig. 5.12(c) and producers 1, 2, 5 in Fig. 5.12(d) obtained by including the CVaR (J_C) at 20% as the second objective are quite different than the corresponding controls (Figures 5.12(a) and 5.12 (b)) obtained by simply maximizing the expected NPV (primary optimization).

Table 5.4: Comparison of different risk measures, Brugge case.

Terms	J_E $\times 10^9$ USD	J_D $\times 10^6$ USD	Min. NPV $\times 10^9$ USD	Max. NPV $\times 10^9$ USD	CVaR (20%) $\times 10^9$ USD
Primary : J_E	6.80	854.16	5.53	7.97	5.69
Secondary : J_D	6.40	575.72	5.59	7.29	5.65
Secondary : J_W	6.74	642.23	5.84	7.71	5.88
Secondary : $J_C(20\%)$	6.91	688.28	5.82	7.91	6.02

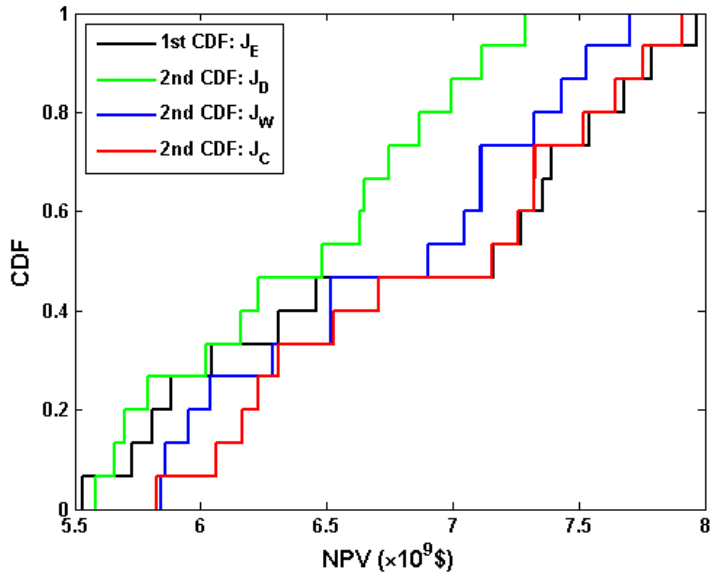

Figure 5.11: CDF functions obtained by the Lexicographic method with different risk measures; black: CDF obtained from primary optimization; green: CDF obtained using risk measure J_D; blue: CDF obtained using risk measure J_W; red: CDF obtained using risk measure J_C at 20%; Brugge case.

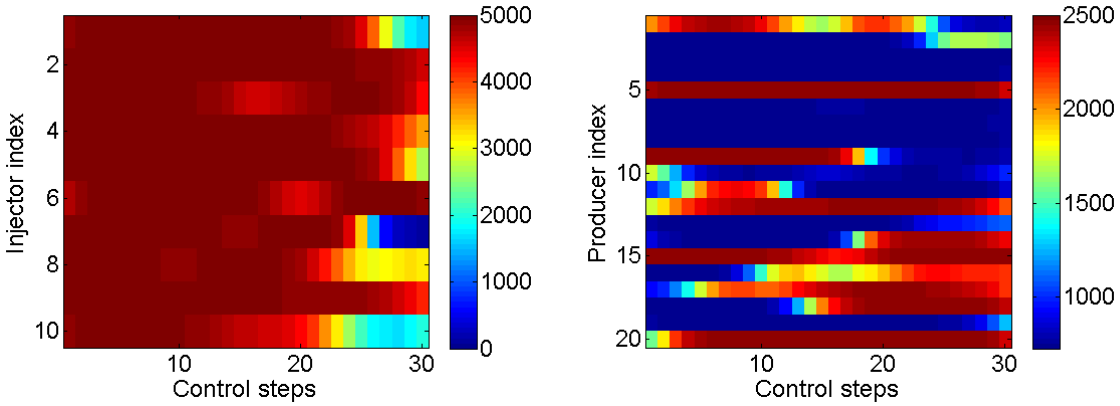

(a) Optimal injection rate, primary optimization

(b) Optimal production BHP, primary optimization

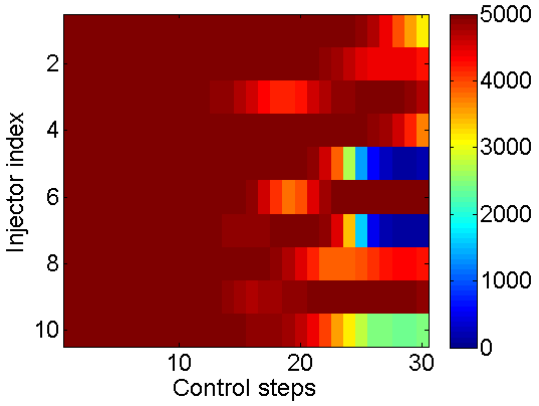

(c) Optimal injection rate, second optimization

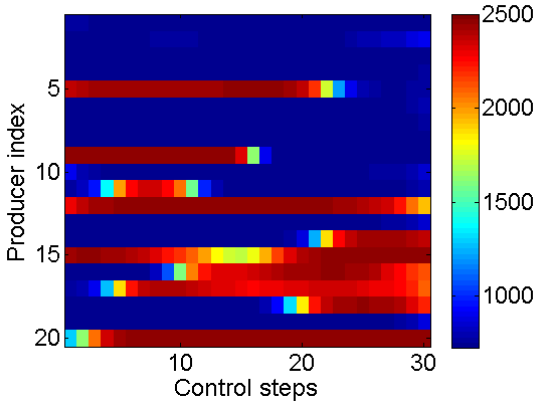

(d) Optimal production BHP, second optimization

Figure 5.12: Optimal well controls obtained by the primary optimization and the secondary optimization using J_C at 20% as the risk measure, Brugge case.

CHAPTER 6

ESTIMATION OF THE OPTIMAL LENGTH OF WAG CYCLES AND OPTIMAL WELL CONTROLS

In this Chapter, the length of the effect of gas and water injection time periods on the optimization of WAG is investigated. We set the sum of the gas and water injection time periods for each injector equal to reservoir lifetime and treat them as equality constraints. Then, the augmented Lagrangian method which can handle equality constraints is adopted to optimize the injection time periods. We provide examples to delineate the conditions under which optimizing the duration of each water injection period and each CO_2 injection period significantly enhances the NPV of production and the conditions under which optimization of each injection periods has a very small effect on the NPV.

6.1 Optimization Problem

The optimization problem we consider in this Chapter is how to estimate the injection time intervals of each WAG half-cycle with/without the well controls which maximize the NPV in a CO_2-WAG EOR process. Let N_{cycle} denote the total number of WAG cycles, and assume that the total gas/water injection time for each injector is equal to the reservoir production lifetime, T_{life}; that is

$$\delta t_1^j + \delta t_2^j + \cdots + \delta t_{2N_{\text{cycle}}}^j = T_{\text{life}}, \quad j = 1, 2, ..., n_{\text{inj}}, \tag{6.1}$$

where $\delta t_k^j, k = 1, 2, ..., 2N_{\text{cycle}}$, denotes the kth injection duration for jth injection well; n_{inj} represents the total number of injection wells. The time equality constraints of Eq. 6.1 can also be written as

$$e_j(u) = \delta t_1^j + \delta t_2^j + \cdots + \delta t_{2N_{\text{cycle}}}^j - T_{\text{life}} = 0, \quad j = 1, 2, ..., n_{\text{inj}}. \tag{6.2}$$

Here, $e_j(u)$ represents the jth time equality constraint which corresponds to the jth injection well. Let u_i^{low} and u_i^{up}, respectively, denote the lower bound and the upper bound for the ith control variable, the optimization problem then can be expressed as

$$\begin{aligned} &\max_u J_E(u) \\ \text{s.t.} \quad &u_i^{\text{low}} \leq u_i \leq u_i^{\text{up}}, \quad i = 1, 2, \cdots N_u, \\ &e_j(u) = 0, \quad j = 1, 2, ..., n_{\text{inj}}, \end{aligned} \tag{6.3}$$

where $J_E(u)$, defined in Eq. 4.1, denotes the approximation of the expectation of life-cycle NPV. Note that the control vector u contains injection time intervals for each injector and/or well controls for all the injection and production wells.

6.2 Handling Time Equality Constraint

To handle the equality constraints of injection time intervals in Eq. 6.3, the augmented Lagrangian method is applied. The augmented Lagrangian function can be written as

$$\mathcal{L}(u, \lambda, \mu) = J_E(u) - \sum_{j=1}^{n_{\text{inj}}} \lambda_j \frac{e_j(u)}{s_j} - \frac{1}{2\mu} \sum_{j=1}^{n_{\text{inj}}} \big(\frac{e_j(u)}{s_j}\big)^2, \tag{6.4}$$

where λ and μ, respectively, denote the Lagrangian multiplier and the penalty parameter; s_j denotes the scaling factor which is set equal to T_{life}. The two loops are involved in the augmented Lagrangian method are the same as discussed in Chapter 5 with the change discussed below:

Inner Loop: With k, λ^k and μ^k fixed, we solve the subproblem

$$\max_u \mathcal{L}(u) = \max_u \{\mathcal{L}(u, \lambda^k, \mu^k)\} \tag{6.5}$$

to find the solution, u_{opt}^{k+1}, where k is the outer loop index.

Outer Loop: At the kth outer loop iteration, update λ^k and μ^k based on the constraint violation factor, σ_{cv}, which is given by

$$\sigma_{cv} = \sqrt{\frac{1}{n_{\text{inj}}} \sum_{j=1}^{n_{\text{inj}}} (\frac{e_j(u_\ell)}{s_j})^2}. \tag{6.6}$$

If $\sigma_{cv} < \eta^k$, update Lagrangian multiplier λ^k and tighten the convergence criteria based on Eq. 5.25, otherwise update penalty parameter μ^k and tighten the convergence criteria based on Eq. 5.26. The augmented Lagrangian method loops through each inner loop and then outer loop until the convergence criteria given by Eqs. 5.23 and 5.24 are reached and the constraint-violation factor is acceptable (i.e., $\sigma_{cv} \leq \eta^*$). We terminate the augmented Lagrangian method if the maximum allowable simulation runs is reached. The settings, e.g., η^*, for the implementation of augmented Lagrangian method are the same as be used in subsection 5.1.2. To maximize the augmented Lagrangian function in Eq. 6.5 , we use the steepest ascent algorithm which is given by:

$$u_{\ell+1} = u_\ell + \alpha_\ell \left[\frac{d_\ell}{\|d_\ell\|_\infty} \right], \tag{6.7}$$

for $\ell = 0, 1, 2, ...$ until convergence, where u_0 is the initial guess and u_ℓ is the estimate of the optimal control vector at the ℓth iteration. As always, α_ℓ is the step size; d_ℓ denotes the search direction vector which in our work is a stochastic search direction. Here, foundational StoSAG algorithm with the search direction given by Eq. 6.8 below is applied to maximize the objective function in the form $\mathcal{L}(u, \lambda^k, \mu^k)$:

$$d_\ell = \frac{1}{N_e} \sum_{i=1}^{N_e} (u_{\ell,i} - u_\ell) \Big(\mathcal{L}(u_{\ell,i}) - \mathcal{L}(u_\ell) \Big). \tag{6.8}$$

Here, each control perturbation $u_{\ell,i}$, $i = 1, 2, \cdots N_e$, at iteration ℓ is generated from the distribution $\mathcal{N}(u_\ell, C_u)$, where C_u is a predefined covariance matrix which is kept constant throughout the optimization procedure. Note that the control vector u is transformed into

log-domain; see Chapter 2 for more details on log-transformation. Although the optimization is performed in the transformed log-domain, we still use u to represent the optimization control vector for simplicity. The control vector u contains injection time intervals and/or well controls (rates for injectors and BHP for producers) at each control step.

In the following two sections, we first apply the proposed methodology to optimize the injection time intervals for two deterministic examples, and then we apply the methodology to robust optimization.

6.3 Deterministic Optimization

6.3.1 Example 1: 3D Heterogeneous Reservoir

Problem Description. In the first example, the simulation model is defined on a $11 \times 11 \times 3$ grid with the grid block dimensions given by $\Delta x = \Delta y = 100$ ft and $\Delta z = 30$ ft. It contains 1 injector and 4 producers. Permeability distributions for three different layers, respectively, follow $\ln k_1 \sim \mathcal{N}(5.5, 0.3)$, $\ln k_2 \sim \mathcal{N}(4.5, 0.2)$ and $\ln k_3 \sim \mathcal{N}(5, 0.25)$. Figure 6.1 displays permeability distributions for three layers and well locations. The porosity is homogeneous; porosities for three layers, respectively, are $\phi_1 = 0.3$, $\phi_2 = 0.2$ and $\phi_3 = 0.25$. The initial reservoir pressure is 4,300 psi. Production lifetime is set equal to 4,320 days. We apply rate controls for injector and pressure controls for producers; the initial guess, lower bounds and upper bounds for different control variables are shown in Table 6.1.

For the StoSAG method, we set the number of samples for gradient averaging to 10; the maximum number of stepsize cuts is set equal to 5; the initial step size is 1.0; the perturbation size is equal to 0.05; the maximum number of simulation runs is 1,500. Violation tolerance for the total injection time at convergence is 10 days; 12 WAG cycles are specified, where each WAG cycle has two control steps (one for gas injection and one for water injection), but the length of the two control steps for each particular cycle may be different for each well. Thus, each injector contains 24 control steps with the time length for each control step equal to 180 days in the initial guess. The time length of each control step

for producers is fixed equal to 180 days.

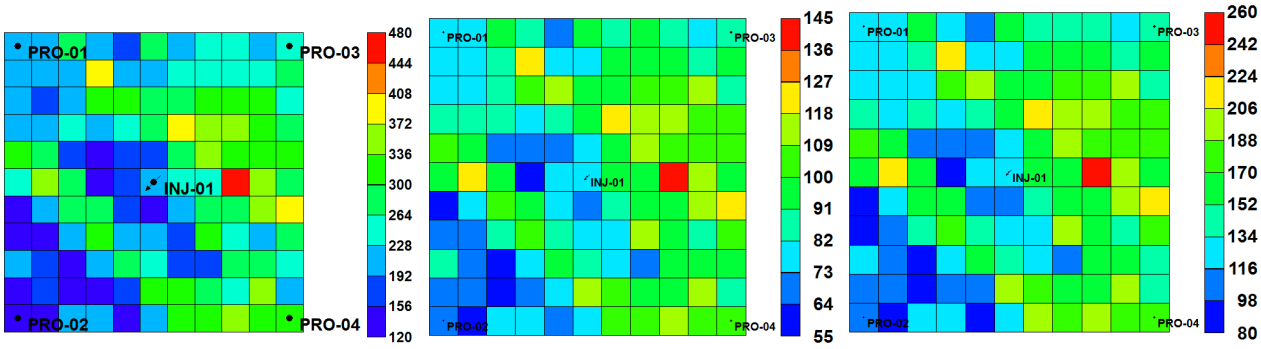

(a) Layer 1 (b) Layer 2 (c) Layer 3

Figure 6.1: Permeability distributions for three different layers and well locations.

Table 6.1: Initial guesses, lower bounds and upper bounds for different type of control variables, example 1.

Design variables	Units	Initial Guess	Lower Bound	Upper Bound
Pressure-Producer	psi	2,900	1,500	4,300
Rate-Gas Injector	MM scf/D	10	0	20
Rate-Water Injector	stb/D	2,000	0	4,000
Half-cycle length	day	180	1	360

Here, we consider four optimization strategies: (1) optimize the injection time intervals and well controls simultaneously; (2) optimize the well controls only with fixed injection time intervals (180 days); (3) optimize the injection time intervals only with well controls fixed at "bounds"; (4) optimize the injection time intervals only with well controls fixed at "averages". Note that "bounds" means injector operates at its maximum allowable rates (upper bounds) and producers operate at its minimum allowable BHP (lower bound); "averages" means both injector and producers operate at the mean value of upper and lower bounds.

Results. Figure 6.2 displays the NPV versus the number of simulation runs for different optimization strategies. The initial NPVs and final NPVs for different optimization strategies are shown in Table 6.2. It can be seen that the simultaneous optimization strategy generates the highest final NPV (923.2 million USD) which is 47 million dollars higher than the one

obtained from the strategy where we only optimize the well controls with fixed injection time intervals. The strategy where we optimize only injection time intervals with well controls fixed at "averages" generates the lowest NPV. The estimated NPV obtained from optimization of only injection time intervals with well controls fixed at "bounds" is almost the same as the one obtained from simultaneous optimization strategy.

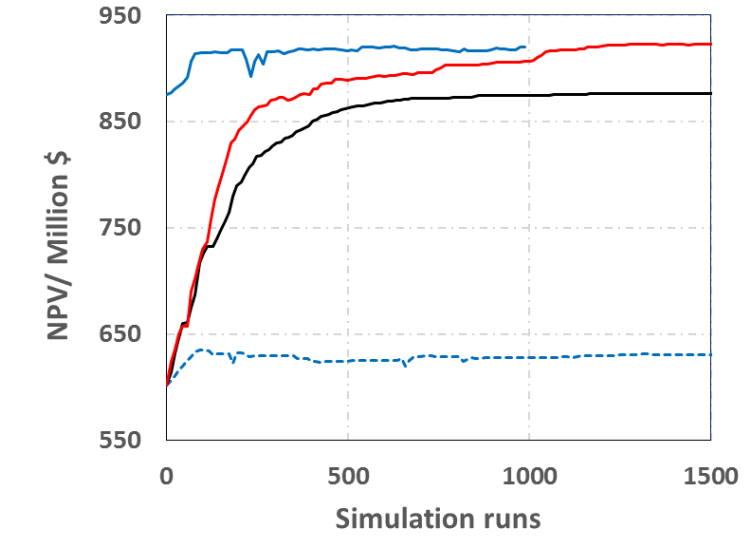

Figure 6.2: NPV versus number of simulation runs; dash blue: time only (averages); blue: time only (bounds); black: well control only; red: simultaneous, example 1.

Table 6.2: Initial NPVs and final NPVs for different optimization strategies, example 1.

Terms	Initial NPV, million $	Final NPV, million $
Time only (averages)	602.2	630.8
Time only (bounds)	875.1	920.2
Well control only	602.2	876.2
Simultaneous	602.2	923.2

Figure 6.3 shows the estimated well controls for producers obtained from well control only optimization and simultaneous optimization strategies. It can be seen that for both of the two optimization strategies, all the producers operate at close to the minimum allowable BHP throughout the reservoir lifetime expect for producers 3 and 4 operating at a high BHP for a few control steps due to the fact that these two producers are located in a relatively high permeability region.

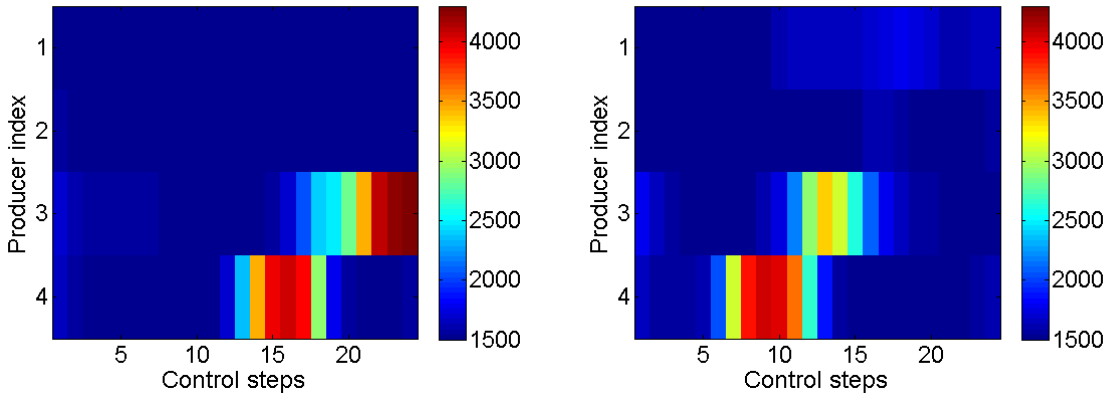

(a) Well control only (b) Simultaneous

Figure 6.3: Estimated well controls for producers obtained from well control only optimization and simultaneous optimization, example 1.

Figures 6.4 displays the estimated well controls for injector obtained from well control only optimization. Note that gas is injected at the "odd" numbered control steps and water is injected at the "even" numbered control steps. We can see that the injector operates at the maximum allowable gas injection rates for all the "odd" controls steps and operates at close to the maximum allowable water injection rates for the first several "even" numbered control steps but not for the last three "even" numbered control steps. This suggests that we can increase the NPV of life-cycle the reservoir production by injecting more gas. However, with the restrictions of fixed injection time intervals and upper bounds on rates, it is impossible to have significantly more gas injected. When adding the injection time intervals as optimization variables, it has more flexibility to control and adjust the total volume of gas and the total volume of water injected.

The estimated half-cycle lengths (injection time intervals) for simultaneous optimization strategy are shown in Figure 6.5. After adding the injection time intervals into control variables for simultaneous optimization, the results show that the total gas injection duration is 55.7% of the total injection time while the total water injection duration is only 44.3%. With the longer gas injection periods, the optimal gas injection rates is still fairly close to the upper bounds (see Figure 6.6(a)), but there has 1.73 billion more gas been injected into the reservoir for the simultaneous optimization strategy than for well control only optimization,

which results in a higher NPV obtained from simultaneous optimization strategy than can be obtained from well control only optimization strategy.

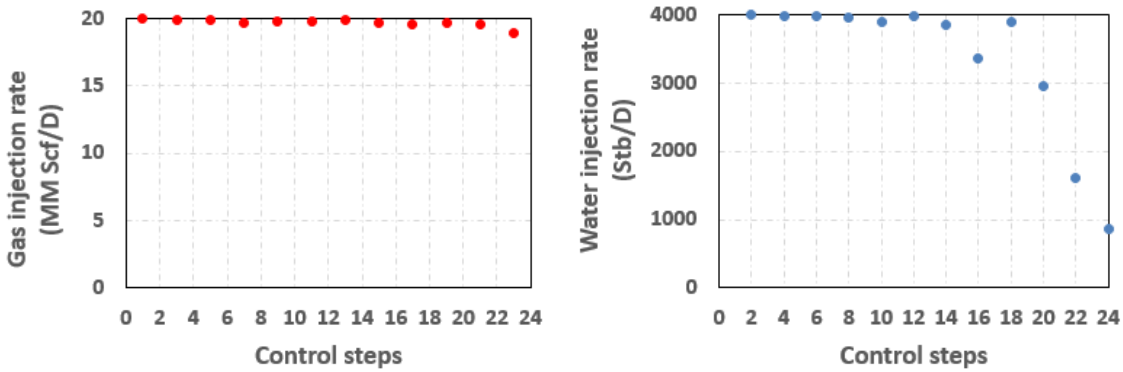

Figure 6.4: Estimated well controls for gas and water injection obtained from well control only optimization strategy, example 1.

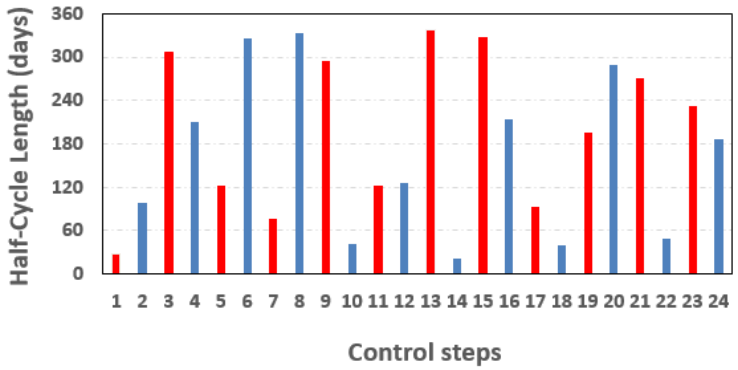

Figure 6.5: Estimated half-cycle lengths obtained from simultaneous optimization; 55.7% gas injection period; example 1.

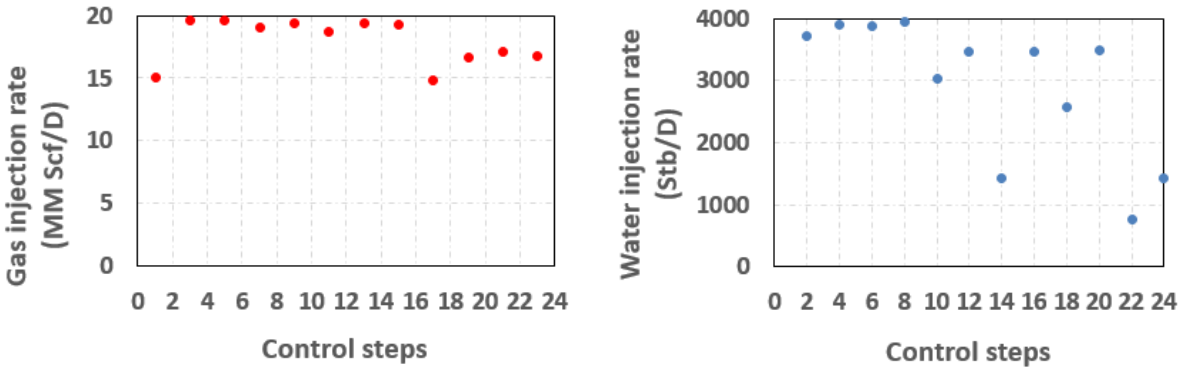

Figure 6.6: Estimated well controls for gas and water injection obtained from simultaneous optimization strategy, example 1.

Comments on Example 1. The results suggest that when the optimal well controls for injectors are close to the bounds (both upper bounds and lower bounds), optimizing the duration of each half cycle can significantly enhance the NPV of production.

6.3.2 Example 2: Channelized Reservoir

Problem Description. In the second example, the simulation model is defined on a $50 \times 50 \times 2$ grid with the grid block dimensions given by $\Delta x = \Delta y = 100$ ft and $\Delta z = 30$ ft. Figure 6.7 displays permeability distribution for the two layers and well locations. The initial reservoir pressure is 4,300 psi; reservoir lifetime is set equal to 3,600 days. We apply rate controls for injectors and pressure controls for producers; the initial guess, lower bounds and upper bounds for different control variables are shown in Table 6.3.

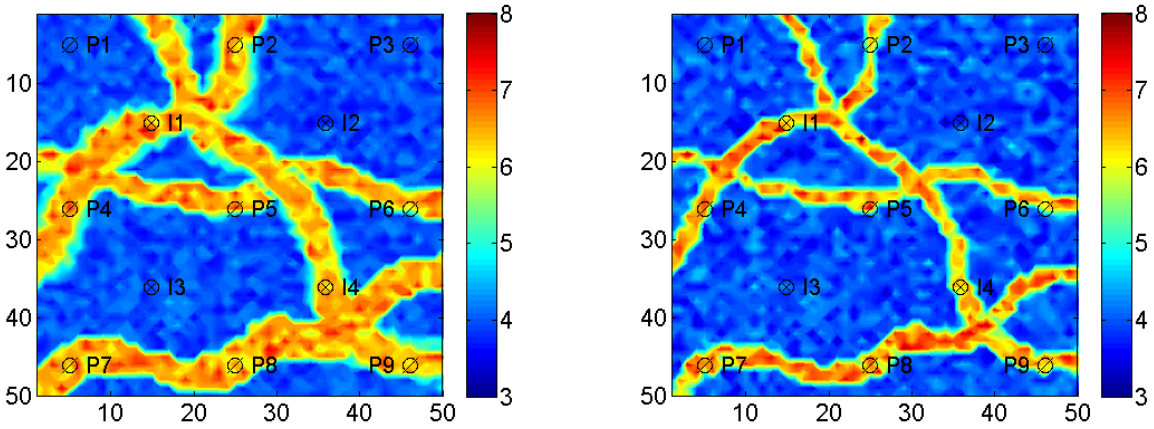

(a) Layer 1 (b) Layer 2

Figure 6.7: Log-permeability distributions for two different layers, example 2.

Table 6.3: Initial guesses, lower bounds and upper bounds for different type of control variables, example 2.

Design variables	Units	Initial Guess	Lower Bound	Upper Bound
Press-Prod	psi	3,500	2,500	4,500
Rate-Gas Inj	MM scf/D	10	0	20
Rate-Water Inj	STB/D	2,000	0	4,000
Half-cycle length	day	180	1	360

The violation tolerance for total injection time at convergence is 10 days. Ten WAG cycles are used. Each injector contains 20 control steps with the initial time length for each control step equal to 180 days. Time length of each control step for producers is equal to 180 days and fixed throughout the optimization process. All the other variables that are not mentioned here are the same as in Example 1.

Results. Figure 6.8 displays the NPV versus the number of simulation runs for different optimization strategies. The initial NPVs and final NPVs for different optimization strategies are shown in Table 6.4. It can be seen that the simultaneous optimization strategy and well control only optimization strategies generate the two highest final NPVs. The NPV is significantly improved by applying time only optimization strategy with well controls fixed at "averages" or fixed at "bounds", but it is not as high as the NPV obtained from simultaneous optimization or well control only optimization.

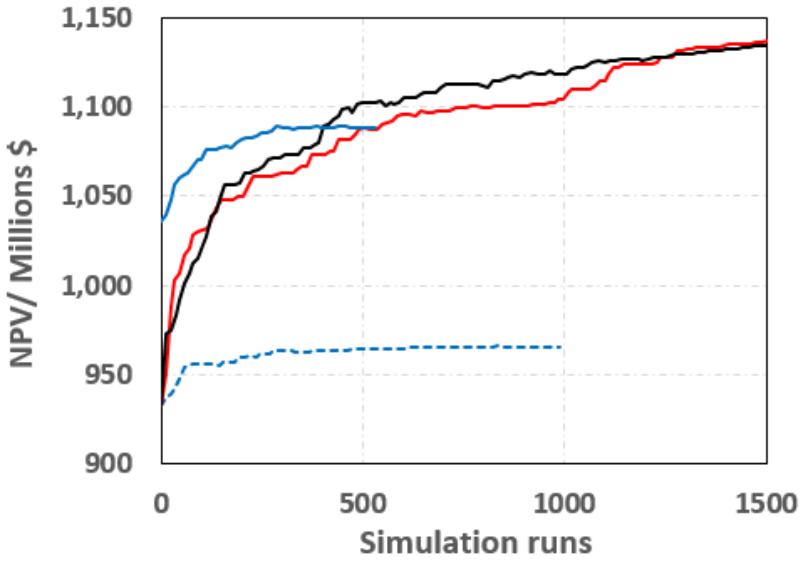

Figure 6.8: NPV versus the number of simulations; blue: time only (bounds); dash blue: time only (averages); red: well control only; black: simultaneous, example 2.

Figure 6.9 shows the estimated well controls for producers obtained from well control only optimization and simultaneous optimization strategies. Since producers 1 and 3 are not located at the high permeability channels, so they are operated at close to minimum BHP for most of the reservoir lifetime, while all the other producers operate at a relatively higher

Table 6.4: Comparison of different optimization strategies, example 2.

Terms	Initial NPV, million $	Final NPV, million $
Time only (averages)	932	966
Time only (bounds)	1,036	1,088
Well control only	932	1,136
Simultaneous	932	1,135

BHP for most of the control steps due to the fact that these producers are located at the channels.

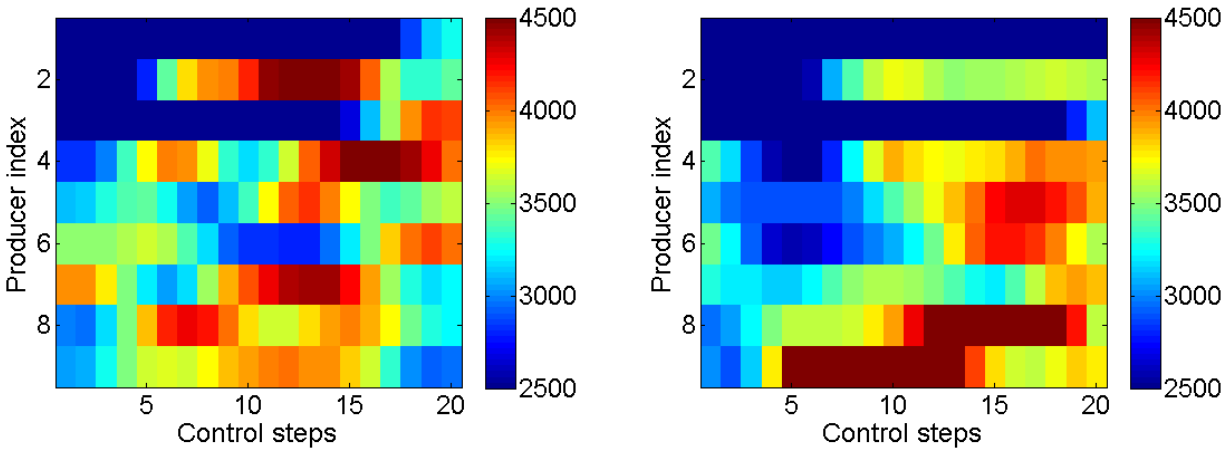

(a) Well control only

(b) Simultaneous

Figure 6.9: Estimated well controls for producers obtained from well control optimization only and simultaneous optimization.

Figures 6.10 and 6.11, respectively, display the estimated gas and water injection rates obtained from well control only optimization and simultaneous optimization strategies. We can see that the injectors 1 and 3 operate at the injection rates that are far from the bounds for both well control only and simultaneous optimization strategies; similar trends also can be observed from injectors 2 and 4 which are not shown here.

The estimated half-cycle lengths (injection time intervals) for simultaneous optimization strategy are shown in Figure 6.12. After adding the injection time intervals into control variables for simultaneous optimization, the results show that the total gas injection duration and the total water injection duration for injectors 1 and 3 are still very close; similar

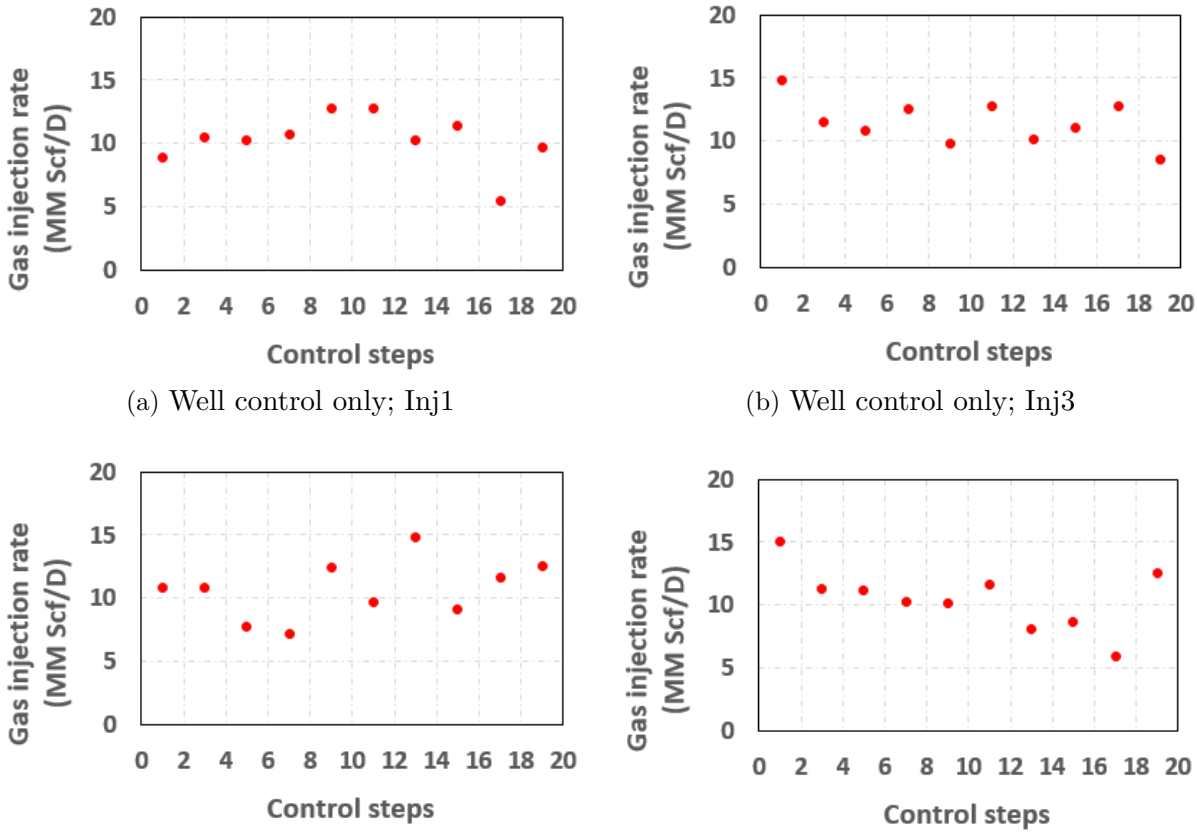

(a) Well control only; Inj1

(b) Well control only; Inj3

(c) Simultaneous; Inj1

(d) Simultaneous; Inj3

Figure 6.10: Estimated gas injection rates obtained from well control optimization only and simultaneous optimization, example 2.

trends can be observed from injectors 2 and 4 which are not shown here.

Comments on Example 2. When the optimal well controls for injectors is far from the bounds, optimizing the duration of each water injection period and each gas injection period has a very small effect on the NPV of production. Instead of optimizing the injection intervals together with well controls, one still can achieve a very comparable NPV to the one obtained from optimization of well controls and injection durations by optimizing only well controls.

6.4 Robust Optimization

6.4.1 Heterogeneous Reservoir

Problem Description. In the robust case, we consider reservoir model defined on a $25 \times 25 \times 3$ grid with the grid block dimensions given by $\Delta x = \Delta y = 100$ ft and $\Delta z = 30$

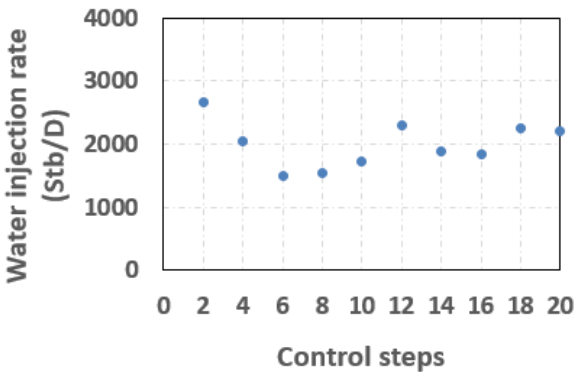

(a) Well control only; Inj1

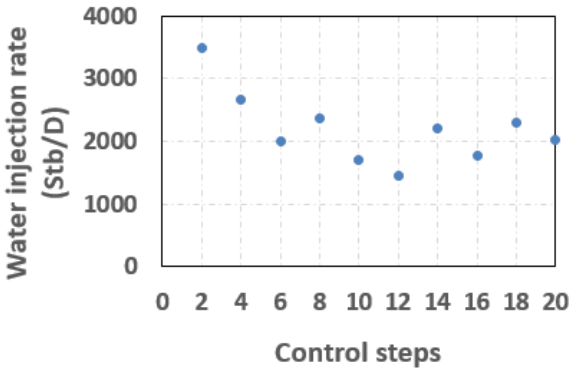

(b) Well control only; Inj3

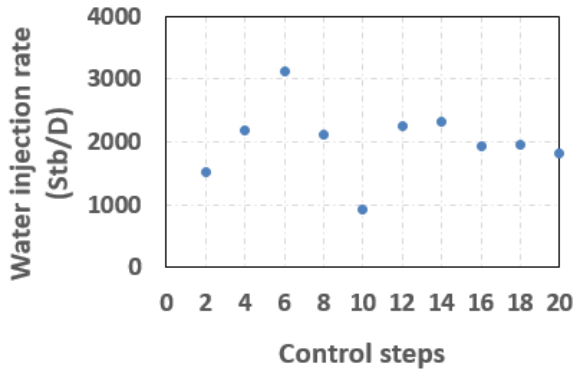

(c) Simultaneous; Inj1

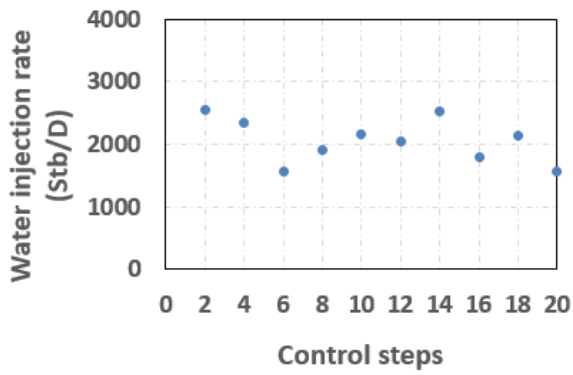

(d) Simultaneous; Inj3

Figure 6.11: Estimated water injection rates obtained from well control optimization only and simultaneous optimization, example 2.

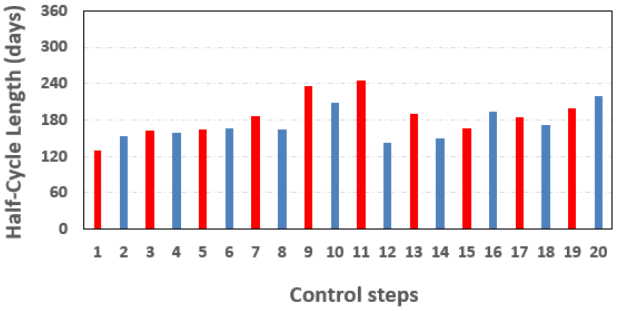

(a) Simul.; Inj 1; 52.9% gas injection period

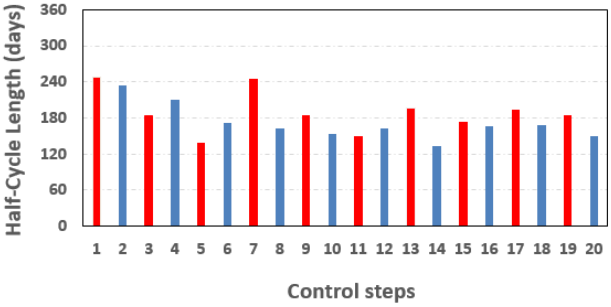

(b) Simul.; Inj 3; 51.8% gas injection period

Figure 6.12: Estimated WAG cycle lengths obtained from simultaneous optimization, example 2.

ft. Ten geological realizations of a Gaussian random field are generated to represent the uncertainty in the reservoir description. The reservoir contains 4 injectors and 9 producers. Fig. 5.1 displays three realizations of the log-horizontal permeability distribution for the

first layer. The second and third layers have the same permeability distribution as the first layer. The porosity is homogeneous with $\phi = 0.2$. The initial reservoir pressure is 4,300 psi. The production lifetime is set equal to 2,160 days. We apply rate controls for injectors and pressure controls for producers; the initial guess, lower bounds and upper bounds for different control variables are shown in Table 6.3.

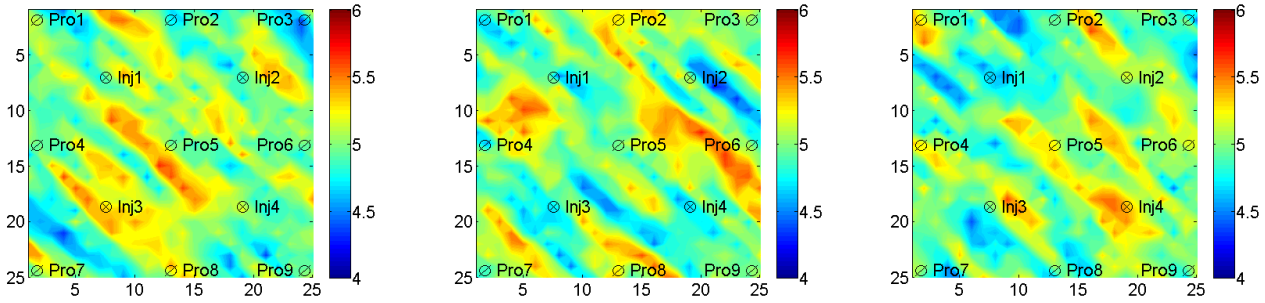

(a) Realization 1 (b) Realization 4 (c) Realization 7

Figure 6.13: Three realizations of log-horizontal permeability distribution for the first layer.

Table 6.5: Initial guesses, lower bounds and upper bounds for different type of control variables.

Design variables	Units	Initial Guess	Lower Bound	Upper Bound
Pressure-Producer	psi	2,000	1,500	4,500
Rate-Gas Injector	MM scf/D	4	0	5
Rate-Water Injector	STB/D	2,500	0	3,000
Half-cycle length	day	180	1	360

Results. In the robust optimization, we only consider the simultaneous optimization and well control only optimization strategies. Figure 6.14 displays the expected NPV versus the number of simulation runs for the two optimization strategies. It can be seen that the simultaneous optimization strategy generates 17 million dollars higher NPV than the one obtained from the strategy where we only optimize the well controls with fixed injection time intervals.

Figures 6.15 displays the estimated well controls for injectors obtained from well control only optimization strategy. We can see that all the injectors operate at close to the

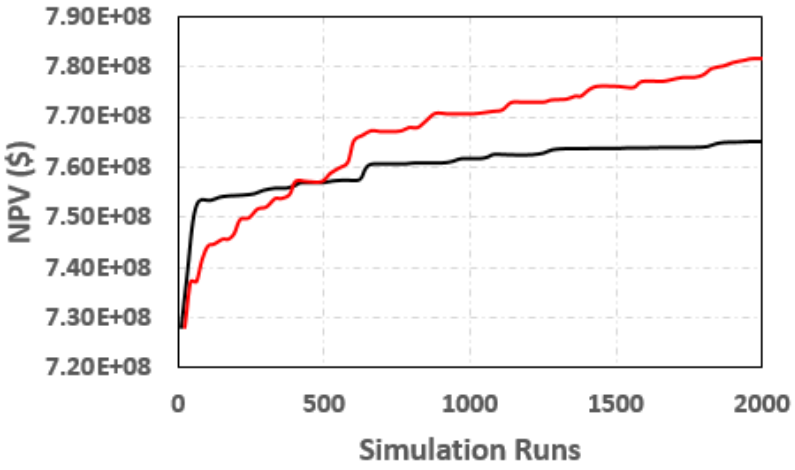

Figure 6.14: Expected NPV versus number of simulation runs; black: well control only; red: simultaneous.

maximum allowable gas injection rates expect for the injector 2 at last WAG cycle. Injectors 1 and 4 operate at close to the maximum allowable water injection rates for all the WAG cycles; injectors 2 and 3 operate at close to the maximum allowable water injection rates only at the first few cycles.

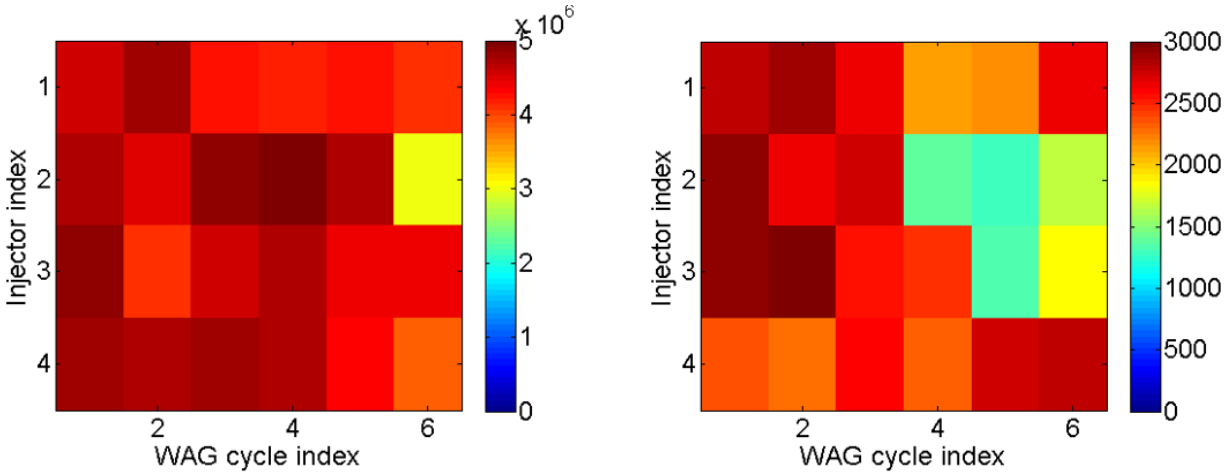

(a) Gas injection rates

(b) Water injection rates

Figure 6.15: Estimated well controls for gas and water injection obtained from well control only optimization strategy.

The estimated half-cycle lengths for the simultaneous optimization strategy are shown in Figure 6.16. After adding the injection time intervals into control variables for simultaneous optimization, the results show that the total gas injection durations for the four injectors

are over 58% of the total injection time while the total water injection durations for all the injectors are less than 42%. With much longer gas injection period and optimal gas injection rates close to the upper bounds for most of the WAG cycles (see Figure 6.17(a)), there is larger total amount of gas (more than 3.53×10^9 scf) injected into the reservoir for the simultaneous optimization than for the well control only optimization, which results in higher NPV obtained from the simultaneous optimization strategy.

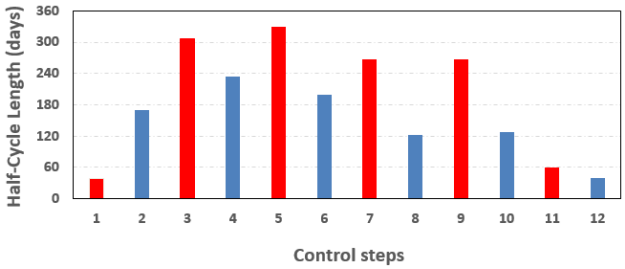

(a) Simul.; Inj 1; 58.74% gas injection period

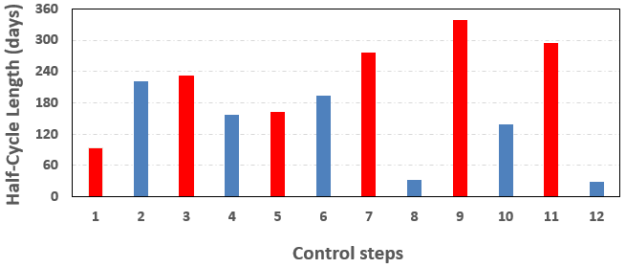

(b) Simul.; Inj 2; 64.84% gas injection period

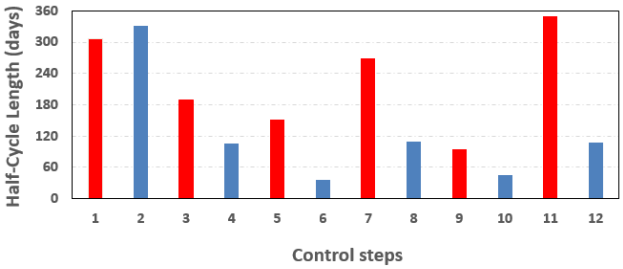

(c) Simul.; Inj 3; 64.39% gas injection period

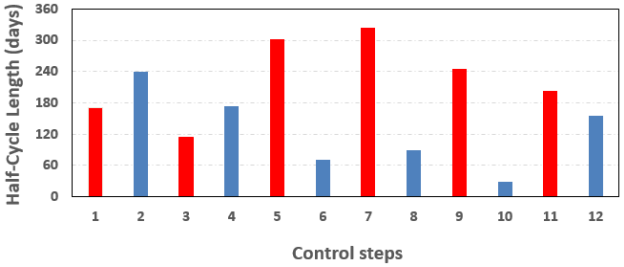

(d) Simul.; Inj 4; 64.18% gas injection period

Figure 6.16: Estimated WAG cycle lengths obtained from simultaneous optimization

Next, we increase the upper bounds for the gas and water injection rates, i.e., increase the maximum allowable gas and water injection rates. Specifically, we increase the upper bounds from 5 MM scf/day to 10 MM scf/day for gas injection and increase the upper bounds from 3,000 stb/day to 4,000 stb/day. All the other settings are kept the same as previous case. Figure 6.18 displays the expected NPV versus the number of simulation runs for different optimization strategies. It can be seen that with a higher upper bounds for gas and water injection rates, the simultaneous optimization strategy generates a comparable NPV to the one obtained from the strategy where we only optimize the well controls with fixed injection time intervals.

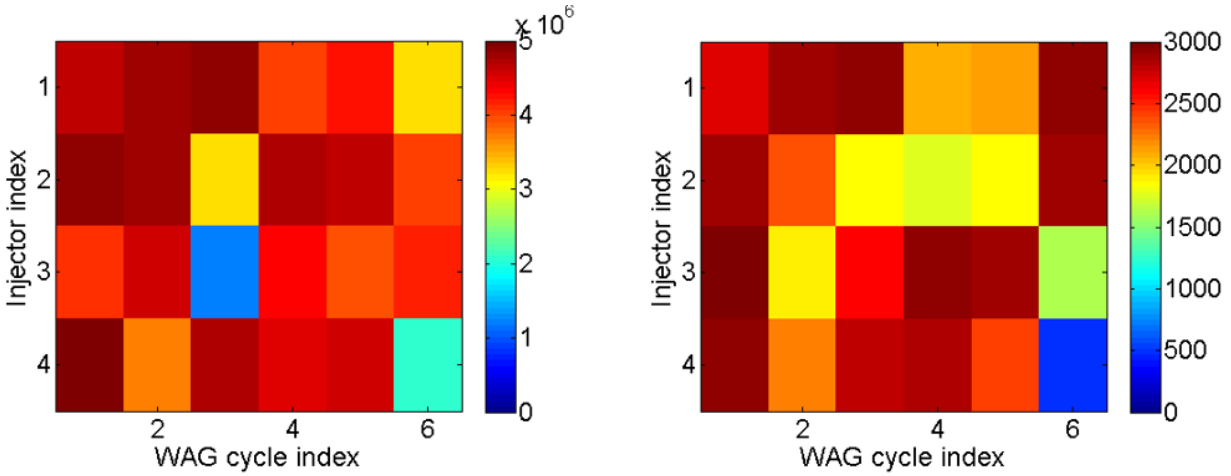

(a) Gas injection rates (b) Water injection rates

Figure 6.17: Estimated well controls for gas and water injection obtained from simultaneous optimization strategy.

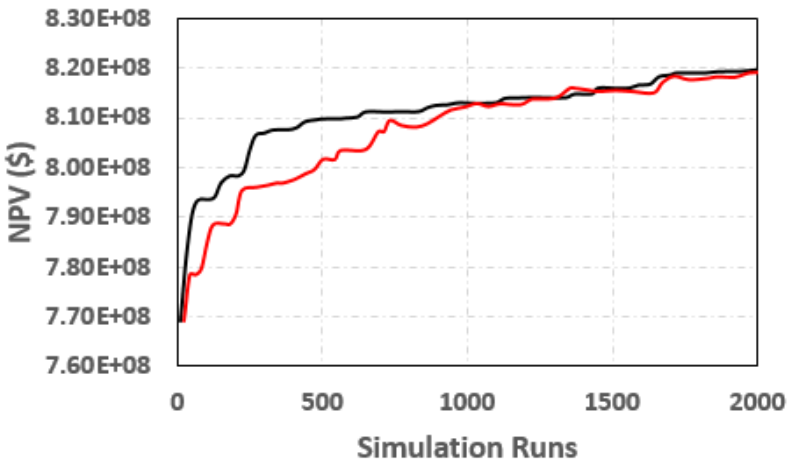

Figure 6.18: Expected NPV versus the number of simulation runs obtained from a larger upper bounds for gas and water injection; black: well control only; red: simultaneous.

CHAPTER 7

DISCUSSION AND CONCLUSIONS

In this work, we develop and apply a stochastic simplex approximate gradient (StoSAG) for ensemble-based optimization in order to address several problems of interest in life-cycle production optimization: the optimization of the WAG injection process, the optimization of inflow-control-valves (ICVs), the optimization under geological uncertainty (i.e., robust optimization) and risk minimization in the robust optimization.

For the optimization of the WAG injection process, this study suggests that the variety of ensemble-based optimization techniques that have been developed for life-cycle waterflooding optimization can be adapted to optimize the design variables for the WAG and SAG injection processes. An ensemble-based optimization algorithm can easily be coupled with any reservoir simulator. Thus, the ideas presented should lead to practical tools that allow a field engineer to decide whether waterflooding, continuous gas injection, WAG or SAG will lead to the highest NPV (or the highest oil recovery) and, at the same time, optimize the recovery process chosen. Several conclusions can be drawn based on the computational results. (i) The estimated optimal NPV of CO_2-WAG is improved significantly by applying production optimization. The initial NPV, final (estimated) NPV and cumulative oil production tend to increase with decreasing cycle time (increasing the number of cycles). (ii) For the channelized reservoir example considered, the optimized WAG flood results in significantly higher values of NPV and oil production than the values obtained with the well controls obtained by optimizing waterflooding or continuous CO_2 injection. (iii) If we wish to optimize the SAG injection process, we can first optimize the reservoir for WAG injection to obtain the optimal controls for WAG, and then treat the optimal controls for WAG as the initial guesses of the optimal well controls for the SAG process. This initialization procedure

can yield significant reduction in computational cost. (iv) Adding the lengths of each WAG half cycle to the set of optimization variables results in a significant improvement in NPV only when optimal well controls are very near their bounds. We established the conditions under which optimizing the injection time intervals of WAG significantly enhances the NPV of production and the conditions under which optimization of each injection periods has a very small effect on the NPV.

We implemented a procedure to optimize the well controls and ICV settings simultaneously in order to maximize the life-cycle NPV of production with a WAG injection process. The performance of the approach is compared with those where only well controls or only ICV settings are optimized. To assess the effectiveness of the proposed method, numerical results are presented for two examples where lower and upper bounds exist on the well controls. We consider two scenarios for well controls, one where the water and gas injection rates are used as controls at injection wells and BHPs are used as controls at producing wells and a second scenario where all wells, both injectors and producers, operate under BHP control. The following conclusions can be drawn. (i) For the case where injectors are rate controlled and producers operate under BHP control, the optimal NPV for the optimization problem where well controls and ICV settings are optimization variables is generally significantly greater than the optimal NPV for the problem where the well controls are the only optimization variables. (ii) For the case where injectors are rate controlled and producers operate under BHP control, the optimal NPV for the optimization problem where well controls and ICV settings are both included as optimization variables is generally significantly greater than the optimal NPV for the problem where the only optimization variables are the ICV settings and the injection rates are fixed equal to their upper bounds and the BHPs of producers are fixed equal to their lower bounds. (iii) For the case where both injectors and producers operate under BHP control, the optimal NPV for the optimization problem where the flowing BHPs at producers are fixed at their lower bounds and injection pressures are fixed equal to their upper bounds, and only ICV settings are used as design variables should be equal to the optimal life-cycle NPV for the problem where we use both BHPs and ICV

settings as optimization variables. (iv) The reservoir lifetime specified when doing optimization for any secondary or tertiary recovery project influences the optimal life-cycle NPV of production. The preliminary results presented here suggest that it is better to overestimate the reservoir lifetime when doing computer-based optimization.

For the robust optimization, we have provided a theoretical explanation and understanding as to the superior performance of StoSAG compared to standard EnOpt. When there is a large variation in the ensemble of reservoir models used for robust optimization, the theory indicates StoSAG can be expected to radically outperform EnOpt, and the Brugge case and the 3D fluvial case that we present confirm that.

For the risk minimization in robust optimization, a framework based on the lexicographic method and the StoSAG algorithm is proposed to maximize the expected NPV and minimize the associated risk in the life-cycle production optimization. Two reservoir examples are provided to demonstrate the robustness of the proposed framework. Through the numerical experiments, we observe that the proposed framework can be effectively used to minimize the risk in the robust optimization. The effect of the choice of different measure for the minimization of risk is investigated, and the results show that the conditional-value-at-risk (CVaR) (also called expected shortfall) is a better choice than the other two risk measures, i.e., the standard deviation and worst-case scenario. For the risk measure CVaR at 20%, a higher ratio of well control perturbations to geological realizations for the computation of $\nabla_u J_C(u)$ defined by Eq. 5.13 in the secondary optimization can achieve a relatively higher CVaR at 20% (average value of the 20% lowest plausible NPV values) with the same computational cost. The performance of the one-step (unconstrained) CVaR was compared with that of the two-step CVaR (i.e., lexicographic-based CVaR), and it was observed that the lexicographic-based CVaR performs much better than the unconstrained CVaR.

BIBLIOGRAPHY

[1] M. T. Al-Khalifa, A. T. Mishkhes, K. N. Baruah, and N. M. al Otaibi. Smart well completion utilization to optimize production in MRC well - a case study. In *Proccedings of the SPE Saudi Arabia section Annual Technical Symposium and Exhibition, Khobar, Saudi Arabia, 19-22 May*, 2013.

[2] H. A. Al-Muailu, M. Al-Suwailem, and S. Aldawsari. Evaluating flow contributions and enhancing the design of smart well completions. In *Proccedings of the SPE Middle East Oil and Gas Show and Exhibition, Manama, Bahrain, 10-13 March*, 2013.

[3] Ahmed H. Alhuthal, Akhil Datta-Gupta, Bevan Yuen, and Jerry P. Fontanillai. Field applications of waterflood optimization via optimal rate control with smart wells. *SPE Reservoir Evaluation & Engineering*, 13(3):406–422, June 2010.

[4] A.H. Alhuthali, D. Oyerinde, and A. Datta-Gupta. Optimal waterflood management using rate control. In *Proceedings of the SPE Annual Technical Conference and Exhibition*, 2006.

[5] S. Alsyed and K. Yateem. Testing methodology for smart wells completion toward attaining optimal production rate setting for maximum hydrocarbon recovery. In *Proccedings of the SPE Intelligent Energy International, Utrecht, The Netherlands, 27-29 March*, 2012.

[6] M. E. Amin, A. Y. Zekr, R. Almehaideb, and H. Al-Attar. Optimization of CO_2 WAG processes in a selected carbonate reservoir: an experimental approach. In *Proceedings of the Abu Dhabi International Petroleum Exhibition & Conference, Abu Dhabi, UAE, 11-14 Novermber*, 2012.

[7] D. N. T. Bahagio. Ensemble optimization of CO_2 WAG EOR. Master's thesis, Delft University of Technology, Delft, Netherlands, 2013.

[8] William J Bailey, Benoît Couët, and David Wilkinson. Framework for field optimization to maximize asset value. *SPE Reservoir Evaluation & Engineering*, 8(1):7–21, 2005.

[9] S. Bender and M. Yilmaz. Full-field simulation and optimization study of mature IWAG injection in a heavy oil carbonate reservoir. In *Proceedings of SPE Imporved Oil Recovery Symposium, Tulsa, Oklahoma, USA, 12-16 April*, 2014.

[10] D. R. Brouwer, Geir Nævdal, J. D. Jansen, Erland H. Vefring, and C. P. J. W. van Kruijsdijk. Improved reservoir management through optimal control and continuous model updating. In *Proceedings of the SPE Annual Technical Conference and Exhibition, Houston, Texas, 26-29 September*, number SPE 90149, 2004.

[11] D.R. Brouwer and J.D. Jansen. Dynamic optimization of water flooding with smart wells using optimial control theory. *SPE Journal*, 9(4):391–402, 2004.

[12] D.R. Brouwer and J.D. Jansen. Dynamic optimization of water flooding with smart wells using optimial control theory. *SPE Journal*, 9(4):391–402, 2004.

[13] Andrea Capolei, Erling Halfdan Stenby, and John Bagterp Jørgensen. High order adjoint derivatives using ESDIRK methods for oil reservoir production optimization. In *Proccedings of the 13th European Conference on the Mathematics of Oil Recovery (ECMOR XIII), Biarritz, France, 10–13 September*, 2012.

[14] Andrea Capolei, Eka Suwartadi, Bjarne Foss, and John Bagterp Jørgensen. Waterflooding optimization in uncertain geological scenarios. *Computational Geosciences*, 17(6): 991–1013, 2013.

[15] Andrea Capolei, Bjarne Foss, and John Bagterp Jørgensen. Profit and risk measures in oil production optimization. *IFAC-PapersOnLine*, 48(6):214–220, 2015.

[16] Andrea Capolei, Eka Suwartadi, Bjarne Foss, and John Bagterp Jørgensen. A mean–variance objective for robust production optimization in uncertain geological scenarios. *Journal of Petroleum Science and Engineering*, 125:23–37, 2015.

[17] K. S. Chan, R. Masoudi, H. Karkooti, R. Shaedin, and M. B. Othman. Production integrated smart completion benchmark for field re-development. In *Proccedings of the International Petroleum Technology Conference, Doha, Qatar, 20-22 January*, 2014.

[18] Yuqing Chang, Zyed Bouzarkouna, and Deepak Devegowda. Multi-objective optimization for rapid and robust optimal oilfield development under geological uncertainty. *Computational Geosciences*, 19(4):933–950, 2015.

[19] Bailian Chen and Albert C. Reynolds. Ensemble-based optimization of the water-alternating-gas-injection process. *SPE Journal*, 21(3):786–798, October 2016.

[20] C. Chen. *Adjoint-gradient-based production optimization with the augmented Lagrangian method*. Ph.D. thesis, University of Tulsa, Tulsa, Oklahoma, USA, 2011.

[21] C. Chen, G. Li, and A. Reynolds. Closed-loop reservoir management on the Brugge test case. *Computational Geosciences*, 14(4):691–703, 2010.

[22] C. Chen, G. Li, and A. C. Reynolds. Robust constrained optimization of short- and long-term net present value for closed-loop reservoir management. *SPE Journal*, 17(3): 849–864, 2012.

[23] S. Chen, H. Li, D. Yang, and P. Tontiwachwuthikul. Optimal parametric design for water-alternating-gas (WAG) process in a CO_2-miscible flooding reservoir. *JCPT*, 49 (10):75–82, June 2010.

[24] Yan Chen and Dean Oliver. Ensemble-based closed-loop optimization applied to Brugge field. *SPE Reservoir Evaluation & Engineering*, 13(1):56–71, 2010.

[25] Yan Chen, Dean S. Oliver, and Dongxiao Zhang. Efficient ensemble-based closed-loop production optimization. *SPE Journal*, 14(4):634–645, 2009.

[26] J. R. Christensen, E. H. Stenby, and A. Skauge. Review of WAG field experience. *SPE Reservoir Evaluation & Engineering*, 4(2):97–106, June 2001.

[27] CMG. *User's Guide: GEM. Advanced Compositional and GHG Reservoir Simulator.* Computer Modelling Group Ltd., Calgary, Canada www.cmgroup.com, version 2009 edition, 2009.

[28] CMG. *User's Guide: IMEX. Advanced Oil/Gas Reservoir Simulator.* Computer Modelling Group Ltd., Calgary, Canada www.cmgroup.com, version 2009 edition, 2009.

[29] S. T. Do and A. C. Reynolds. Theoretical connections between optimization algorithms based on an approximate gradient. *Computational Geosciences*, 17(6):959–973, August 2013.

[30] F. M. Dossary, S. A. Dawsari, and R. S. Anazi. Production gain and optimization through the implementation of smart well completion technology in Saudi Aramco, case study. In *Proccedings of the SPE Intelligent Energy International, Utrecht, The Netherlands, 27-29 March*, 2012.

[31] Alexandre A Emerick and Albert C Reynolds. Ensemble smoother with multiple data assimilation. *Computers & Geosciences*, 55:3–15, 2013.

[32] Geir Evensen. Sequential data assimilation with a nonlinear quasi-geostrophic model using monte carlo methods to forecast error statistics. *Journal of Geophysical Research: Oceans*, 99(C5):10143–10162, 1994.

[33] Geir Evensen. *Data assimilation: the ensemble Kalman filter.* Springer Science & Business Media, 2009.

[34] R. M. Fonseca, S. S. Kahrobaei, L. J. T. van Gastel, O. Leeuwenburgh, and J. D. Jansen. Quantification of the impact of ensemble size on the quality of an ensemble gradient using principles of hypothesis testing. In *Proccedings of the SPE Reservoir Simulation Symposium, Houston, Texas, USA, 23-25 February*, 2015.

[35] R. M. Fonseca, O. Leeuwenburgh, , E. Della Rossa, P. M. J. Van den Hof, and J. D. Jansen. Ensemble-based multi-objective optimization of on-off control devices under geological uncertainty. In *Proccedings of the SPE Reservoir Simulation Symposium, Houston, Texas, USA, 23-25 February*, 2015.

[36] R. M. Fonseca, O. Leeuwenburgh, P. M. J. Van den Hof, and J. D. Jansen. Improving the ensemble-optimization method through covariance-matrix adaptation. *SPE Journal*, 20(1):155–168, 2015.

[37] R. M. Fonseca, B. Chen, J. D. Jansen, and A. C. Reynolds. A stochastic simplex approximate gradient (StoSAG) for optimization under uncertainty. *International Journal for Numerical Methods in Engineering*, 109(13):1756–1776, 2016.

[38] Fahim Forouzanfar, Ernesto Della Rossa, Roberta Russo, and Albert C. Reynolds. Life-cycle production optimization of an oil field with an adjoint-based gradient approach. *Journal of Petroleum Science and Engineering*, 112:351 – 358, 2013.

[39] Golub G., Van Loan C., and Charles F. *Matrix computations*, volume 3. The Johns Hopkins University Press, 2012.

[40] Guohua Gao and A. C. Reynolds. An improved implementation of the LBFGS algorithm for automatic history matching. *SPE Journal*, 11(1):5–17, 2006.

[41] S. M. Ghaderi and C. R. Clarkson. Optimization of WAG process for coupled CO_2 EOR-storage in tight oil formations: an experimental design approach. In *Proceedings of the SPE Canadian Unconventional Resources Conference, Alberta, Canada, 30 October-1 November*, 2012.

[42] Kristian G Hanssen and Bjarne Foss. On selection of controlled variables for robust reservoir management. *Journal of Petroleum Science and Engineering*, 147:504–514, 2016.

[43] Jincong He, Jiang Xie, Pallav Sarma, Xian-Huan Wen, Wen H Chen, and Jairam Kamath. Proxy-based work flow for a priori evaluation of data-acquisition programs. *SPE Journal*, 2016.

[44] Jincong He, Pallav Sarma, Eric Bhark, Shusei Tanaka, Bailian Chen, Xian-Huan Wen, and Jairam Kamath. Quantifying value of information using ensemble variance analysis. In *SPE Reservoir Simulation Conference*. Society of Petroleum Engineers, 2017.

[45] C.W. Hewson and O. Leeuwenburgh. CO_2 water-alternating-gas flooding optimization of the Chigwell Viking I Pool in the western Canadian sedimentary basin. In *SPE Reservoir Simulation Conference*. Society of Petroleum Engineers, 2017.

[46] Obiajulu J Isebor and Louis J Durlofsky. Biobjective optimization for general oil field development. *Journal of Petroleum Science and Engineering*, 119:123–138, 2014.

[47] J. D. Jansen, S. D. Douma, D. R. Brouwer, , P. M. J. Van den Hof, and A. W. Heemink. Closed-loop reservoir management. In *Proceedings of the SPE Reservoir Simulation Symposium*, 2009.

[48] Jan Dirk Jansen. *A systems description of flow through porous media*. Springer, 2013.

[49] Jan-Dirk Jansen, DR Brouwer, G Naevdal, and CPJW Van Kruijsdijk. Closed-loop reservoir management. *First Break*, 23(1):43–48, 2005.

[50] Jan Dirk Jansen, Roald Brouwer, and Sippe G Douma. Closed loop reservoir management. In *Proccedings of the SPE Reservoir Simulation Symposium, The Woodlands, Texas, USA, 2–4 February*, 2009.

[51] JD Jansen. Adjoint-based optimization of multi-phase flow through porous media–a review. *Computers & Fluids*, 46(1):40–51, 2011.

[52] R. T. Johns, L. Bermudez, and H. Parakh. WAG optimization for gas floods above the MME. In *Proceedings of the SPE Annual Technical Conference and Exhibition, Denver, Colorado, 5-8 October*, 2003.

[53] A. Journel and C. J. Huijbregts. *Mining Geostatistics*. Academic Press: New York, 1978.

[54] J. F. B. M. Kraaijevanger, P. J. P. Egberts, J. R. Valstar, and H. W. Buurman. Optimal waterflood design using the adjoint method. In *Proceedings of the SPE Reservoir Simulation Symposium, Houston, Texas, USA, 26-28 February*, 2007.

[55] JFBM Kraaijevanger, PJP Egberts, JR Valstar, and HW Buurman. Optimal waterflood design using the adjoint method. In *Proccedings of the SPE Reservoir Simulation Symposium, Houston, Texas, USA, 26–28 February*, 2007.

[56] Duc H Le and Albert C Reynolds. Estimation of mutual information and conditional entropy for surveillance optimization. *SPE Journal*, 19(04):648–661, 2014.

[57] Duc H Le and Albert C Reynolds. Optimal choice of a surveillance operation using information theory. *Computational Geosciences*, 18(3-4):505–518, 2014.

[58] Olwijn Leeuwenburgh. *Private communication*, 2016.

[59] R Li, AC Reynolds, DS Oliver, et al. Sensitivity coefficients for three-phase flow history matching. In *Canadian International Petroleum Conference*. Petroleum Society of Canada, 2001.

[60] Z. Li and D. Zhu. Optimization of production performance with icvs by using temperature-date feedaback in horizontal wells. *SPE Production & Operations*, 26(3): 253–261, August 2011.

[61] C. Liao, X. Liao, X. Zhao, N. Lu, H. Ding, H. Wang, and Y. Liu. Study on enhanced oil recovery technology in low permeability heterogeneous reservoir by water-alternate-gas of co2 flooding. In *Proceedings of the SPE Asia Pacific Oil & Gas Conference and Exhibition, Jakarta, Indonesia, 22-24 October*, 2013.

[62] Xin Liu and Albert C Reynolds. Gradient-based multiobjective optimization with applications to waterflooding optimization. In *Proccedings of the 14th European Conference on the Mathematics of Oil Recovery (ECMOR XIV), Sicily, Italy, 8–11 September*, 2014.

[63] Xin Liu and Albert C Reynolds. Augmented Lagrangian method for maximizing expectation and minimizing risk for optimal well-control problems with nonlinear constraints. *SPE Journal*, 21(5):1830–1842, 2016.

[64] Xin Liu and Albert C Reynolds. Gradient-based multiobjective optimization for maximizing expectation and minimizing uncertainty or risk with application to optimal well-control problem with only bound constraints. *SPE Journal*, 21(5):1813–1829, 2016.

[65] R. J. Lorentzen, A. M. Berg, G. Nævdal, and E. H. Vefring. A new approach for dynamic optimization of waterflooding problems. In *Proceedings of the SPE Intelligent Energy Conference and Exhibition*, 2006.

[66] S. M. M. M. Mirkalaei, S. J. Hosseini, R. Masoudi, A. Ataei, B. M. R. Demiral, and H. Karkooti. , investigation of different I-WAG schemes towards optimization of displacement efficiency. In *Proceedings of the SPE Enhanced Oil Recovery Conference, Kuala Lumpur, Malaysia, 19-21 July*, 2011.

[67] G. Naroso, ADCO, and J. Hofland. How smart completion can maximize oil production and recovery factor in stacked-marginal reservoir. In *Proccedings of the Abu Dhabi International Petroleum Exhibition& Conference, Abu Dhabi, UAE, 1-4 November*, 2010.

[68] M. M. J. J. Naus, N. Dolle, and J. D. Jansen. Optimization of commingled production using infinitely variable inflow control valves. *SPE Production & Operations*, 21(2): 293–301, May 2006.

[69] Jude Nwaozo. Dynamic optimization of a water flood reservoir. Master's thesis, University of Oklahoma, Norman, Oklahoma, 2006.

[70] Diego F Oliveira and Albert Reynolds. An adaptive hierarchical multiscale algorithm for estimation of optimal well controls. *SPE Journal*, 19(05):909–930, 2014.

[71] Diego Felipe Barbosa de Oliveira. *A new hierarchical multiscale optimization method: gradient and non-gradient approaches for waterflooding optimization.* THE UNIVERSITY OF TULSA, 2014.

[72] Dean S. Oliver, Albert C. Reynolds, and Ning Liu. *Inverse Theory for Petroleum Reservoir Characterization and History Matching.* Cambridge University Press, Cambridge, UK, 2008.

[73] M. Nadri Pari and A. H. Kabir. Viability study of implementing smart/intelligent completion in commingled wells in an australian offshore oil field. In *Proccedings of the SPE Digital Energy Conference & Exhibition, Houston, Texas, USA, 7-8 April*, 2009.

[74] E. Peters, R.J. Arts, G.K. Brouwer, and C.R. Geel. Results of the brugge benchmark study for flooding optimisation and history matching. In *Proceedings of the SPE Reservoir Simulation Symposium, 2-4 February*, 2009.

[75] L. Peters, R.J. Arts, G.K. Brouwer, C.R. Geel, S. Cullick, R.J. Lorentzen, Y. Chen, K.N.B. Dunlop, F.C. Vossepoel, R. Xu, P. Sarma, A.H. Alhuthali, and A. Reynolds. Results of the Brugge benchmark study for flooding optimisation and history matching. *SPE Reservoir Evaluation & Engineering*, 13(3):391–405, 2010.

[76] Jorion Philippe. Value at risk: the new benchmark for managing financial risk. *NY: McGraw-Hill Professional*, 2001.

[77] S. Raniolo, L. Dovera, and A. Cominelli. History match and polymer injection optimization in a mature field using the ensemble kalman filter. In *Proceedings of the 17th European Symposium on Improved Oil Recovery, St. Petersburg, Russia, 16-18 April*, 2013.

[78] R Tyrrell Rockafellar and Stanislav Uryasev. Optimization of conditional value-at-risk. *Journal of risk*, 2:21–42, 2000.

[79] William Richard Rossen, Christian S Boeije, et al. Fitting foam simulation model parameters for sag foam applications. In *SPE Enhanced Oil Recovery Conference*. Society of Petroleum Engineers, 2013.

[80] P. Sarma, L.J. Durlofsky, and K. Aziz. Implementation of adjoint solution for optimal control of smart wells. In *Proceedings of the SPE Reservoir Simulation Symposium*, 2005.

[81] P. Sarma, L.J. Durlofsky, K. Aziz, and W.H. Chen. Efficient real-time reservoir management using adjoint-based optimal control and model updating. *Computational Geosciences*, 10:3–36, 2006.

[82] S. R. M. Shafian, R. Z. K. Bahrim, and P. A. Hamid. Enhancing the efficiency of immiscible water alternating gas (WAG) injection in a matured, high temperature and high CO_2 solution gas reservoir a laboratory study. In *Proceedings of the SPE Enhanced Oil Recovery Conference, Kuala Lumpur, Malaysia, 2-4 July*, 2013.

[83] Mehrdad G Shirangi and Louis J Durlofsky. A general method to select representative models for decision making and optimization under uncertainty. *Computers & Geosciences*, 96:109–123, 2016.

[84] M Mohsin Siraj, Paul MJ Van den Hof, and Jan Dirk Jansen. Risk management in oil reservoir water-flooding under economic uncertainty. In *Proccedings of the 54th IEEE Conference on Decision and Control (CDC)*, pages 7542–7547, 2015.

[85] M Mohsin Siraj, Paul MJ Van den Hof, and Jan Dirk Jansen. Robust optimization of water-flooding in oil reservoirs using risk management tools. In *Proccedings of the 11th IFAC Symposium on Dynamics and Control of Process Systems*, pages 133–138, 2016.

[86] J. P. Srivastava and L. Mahli. Water-alternating-gas (WAG) injection a novel EOR technique for mature light oil fields a laboratory investigation for GS-5C sand of Gandhar field. In *proceedings of the* 9^{th} *Biennial International Conference & Exposition on Petroleum Geophysics, Hyderabad, India*, 2012.

[87] Andreas S Stordal, Slawomir P Szklarz, and Olwijn Leeuwenburgh. A theoretical look at ensemble-based optimization in reservoir management. *Mathematical Geosciences*, 48(4):399–417, 2016.

[88] Davi M Valladao, Ruben R Torrado, Bruno Flach, and Sonia Embid. On the stochastic response surface methodology for the determination of the development plan of an oil & gas field. In *Proccedings of the SPE Middle East Intelligent Energy Conference and Exhibition, Manama, Bahrain, 28–30 October*, 2013.

[89] G. M. van Essen, M. J. Zandvliet, P. M. J. Van den Hof, O. H. Bosgra, and J. D. Jansen. Robust waterflooding optimization of multiple geological scenarios. *SPE Journal*, 14(1): 202–210, 2009.

[90] G. M. van Essen, J. D. Jansen, D. R. Brouwer, S. G. Douma, M. J. Zandvliet, K. l. Rollett, and D. P. Harris. Optimization of smart wells in the St. Joseph field. *SPE Reservoir Evaluation & Engineering*, 13(4):588–595, 2010.

[91] Chunhong Wang, Gaoming Li, and Albert C. Reynolds. Production optimization in closed-loop reservoir management. *SPE Journal*, 14(3):506–523, 2009.

[92] Yudou Wang, Gaoming Li, and Albert C. Reynolds. Estimation of depths of fluid contacts by history matching using iterative ensemble-Kalman smoothers. *SPE Journal*, 15(2), 2010.

[93] X. Yan and A. C. Reynolds. Optimization algorithms based on combining fd approximations and stochastic gradients compared with methods based only on a stochastic gradient. *SPE Journal*, 19(5):873–890, 2014.

[94] Burak Yeten, Louis J Durlofsky, and Khalid Aziz. Optimization of nonconventional well type, location and trajectory. In *Proccedings of the SPE annual technical conference and exhibition, San Antonio, Texas, USA, 29 September–2 October*, number SPE 77565, 2002.

[95] Mohammad Zafari and Albert Coburn Reynolds. Assessing the uncertainty in reservoir description and performance predictions with the ensemble kalman filter. *SPE Journal*, 12(03):382–391, 2007.

[96] M.J. Zandvliet, O.H. Bosgra, J.D. Jasen, P.M.J. Van den Hof, and J.F.B.M. Kraaijevanger. Bang-bang control and sigular arcs in reservoir flooding. *Journal of Petroleum Science and Engineering*, 58:186–200, 2007.

[97] Kai Zhang, Liming Zhang, Jun Yao, Yuxue Chen, and Ranran Lu. Water flooding optimization with adjoint model under control constraints. *Journal of Hydrodynamics, Ser. B*, 26(1):75–85, 2014.

[98] Kai Zhang, Xiaoming Zhang, Wei Ni, Liming Zhang, Jun Yao, Lixin Li, and Xia Yan. Nonlinear constrained production optimization based on augmented Lagrangian function and stochastic gradient. *Journal of Petroleum Science and Engineering*, 146:418–431, 2016.

[99] D. Zhou, M. Yan, and W. M. Calvin. Optimization of a mature CO_2 flood from continuous injection to WAG. In *Proceedings of the SPE Improved Oil Recovery Symposium, Tulsa, Oklahoma, USA, 14-18 April*, 2012.